Active Control of Large-scale Structures in High Reynolds Number Turbulent Boundary Layers

Zhoushun Ruan

Submitted in total fulfilment of the requirements of the degree of

Doctor of Philosophy

Department of Mechanical Engineering
THE UNIVERSITY OF MELBOURNE

February 2021

Declaration

This is to certify that

- the thesis comprises only my original work towards the PhD,
- due acknowledgement has been made in the text to all other material used,
- the thesis is less than 100,000 words in length, exclusive of tables, maps, bibliographies and appendices.

Signed: 

Date: 15/11/2021

Nomenclature

α	Accuracy of the real-time flow estimation
$\Delta\overline{u^2}^+$	Variation of the streamwise turbulent energy
$\Delta\overline{u_l^2}^+(\%)$	Percentage change of the large-scale streamwise turbulent energy
$\Delta\overline{u_s^2}^+(\%)$	Percentage change of the small-scale streamwise turbulent energy
$\Delta\overline{U}^+(\%)$	Percentage change of the mean streamwise velocity
$\Delta\overline{U}^+$	Variation of the mean streamwise velocity
$\Delta\overline{w^2}^+$	Variation of the wall-normal turbulent energy
$\Delta\overline{W}^+$	Variation of the mean wall-normal velocity
ΔE_l	Spatial-averaged large-scale energy reduction of the active flow control
ΔE_s	Spatial-averaged near-wall small-scale energy reduction of the active flow control
Δx_a	Streamwise separation between detection and actuation arrays
Δx_m	Streamwise separation between measurement and actuation arrays
δ	Boundary layer thickness
γ_L	Spectral coherence correlation between the friction velocity and streamwise velocity fluctuations
κ	Von Kármán constant

λ_x Streamwise wavelength of the coherent structures

λ_y Spanwise wavelength of the coherent structures

$\lambda_{x,hi}$ Streamwise wavelength of the i^{th} hierarchy of the coherent structures

$\lambda_{x.coh}$ Minimum streamwise wavelength of the coherent structures maintain coherence between two positions

$\lambda_{x.c}$ Streamwise cut-off wavelength of the real-time filter

$\lambda_{y.c}$ Spanwise cut-off wavelength of the real-time filter

$\langle u_h^+ \rangle$ Conditional high-speed streamwise velocity fluctuations

$\langle u_l^+ \rangle$ Conditional streamwise velocity fluctuations based on zero-crossings of large-scale friction velocity

$\langle u_{\tau_h}^+ \rangle$ Conditional friction velocity fluctuations based on zero-crossings

$\langle u_{\tau_l}^+ \rangle$ Conditional friction velocity fluctuations based on zero-crossings of large-scale friction velocity

$\langle u_{p.i}^+ \rangle$ Phase-averaged streamwise velocity fluctuation in the i^{th} binned phase

$\langle U_{jet} \rangle$ Conditionally averaged wall-normal jet exit velocity

$\langle w_h^+ \rangle$ Conditional high-speed wall-normal velocity fluctuations

$\langle w_{p.i}^+ \rangle$ Phase-averaged wall-normal velocity fluctuation in the i^{th} binned phase

$\left\langle \overline{-uw}^+ \right\rangle$ Conditional averaged streamwise and wall-normal Reynolds shear stress

$\langle DR \rangle$ Conditional drag reduction

$\mathscr{B}_{i.l}$ Lower bound of the laser delay for the i^{th} binned phase

$\mathscr{B}_{i.u}$ Upper bound of the laser delay for the i^{th} binned phase

$\mathscr{B}_i$ The i^{th} binned phase

Nomenclature

$\mathscr{W}$	Average spanwise width of the coherent structures
μ	Dynamic viscosity of the free-stream flow
ν	Kinematic viscosity of the free-stream flow
$\overline{-uw}^{+}$	Streamwise and wall-normal Reynolds shear stress
$\overline{\tau_h}$	Averaged time delay between the laser firing and the previous positive temporal zero-cross of large-scale friction velocity
$\overline{u^2}$	Turbulent energy of the streamwise velocity components
$\overline{u_l^2}$	Turbulent energy of the large-scale streamwise velocity components
$\overline{u_s^2}$	Turbulent energy of the small-scale streamwise velocity components
$\overline{u^2_{\mathrm{IOI}.s}}^{+}$	Small-scale turbulent energy of the fluctuating streamwise velocity predicted from IOI model
$\overline{U}$	Mean streamwise velocity
$\overline{V}$	Mean spanwise velocity
$\overline{w^2}$	Turbulent energy of the wall-normal velocity components
$\overline{W}$	Mean wall-normal velocity
$\phi_{u_\tau u_\tau}$	Pre-multiplied energy spectra of friction velocity fluctuations
$\Phi_{u_\tau u}$	Pre-multiplied co-spectra between the friction velocity and streamwise velocity fluctuations
ϕ_{uu}	Pre-multiplied energy spectra of streamwise velocity fluctuations
ρ	Density of the free-stream flow
σ_{u_l}	Standard deviation of the large-scale streamwise velocity fluctuation
$\sigma_{u_{\tau_l}}$	Standard deviation of the large-scale friction velocity fluctuation

τ Time shift in temporal two point cross-correlation

τ_a Time delay between the actuation and detection

τ_c Time delay due to streamwise convection

τ_e Time required for the solenoid valve to close

τ_f Time delay due to real-time filtering and computation

τ_h Time delay between the laser firing and the previous positive temporal zero-cross of large-scale friction velocity

τ_i Time delay due to structural inclination

τ_l Time delay between the laser firing and the previous negative temporal zero-cross of large-scale friction velocity

τ_m Time delay due to the mechanical response of the wall-normal jet

τ_w Mean wall-shear stress

τ_{TET} Time delay for a single step computation in Speedgoat target machine

τ_{max} Time shift of the peak two point cross-correlation

HF_{Di} The i^{th} hot-film in the downstream measurement array

HF_{Ui} The i^{th} hot-film in the upstream detection array

Jet_i The i^{th} wall-normal jet in the actuation array

Re_τ Friction Reynolds number of the flow

Re_θ Momentum thickness Reynolds number of the flow

θ Inclination angle of the coherent structures

$\widetilde{U_\tau}$ Total fluctuating friction velocity

A Universal constant of the mean velocity profile

Nomenclature

A_{JR}	Gain constant for the jet penetration trajectory
AR	Aspect ratio of the coherent structure
B	Binary control signal
B_e	Binary control signal computed from the estimated large-scale velocity fluctuation
B_t	Binary control signal computed from the true large-scale velocity fluctuation
B_{JR}	Exponential constant for the jet penetration trajectory
C	Coles-Fernholz relation constant
C_1	Exponential constant for the relationship equation 4.3
C_2	Offset constant for the relationship equation 4.3
C_f	Skin-friction coefficient of the flow
C_p	Pressure coefficient of the free-stream flow
d_{hw}	Thickness of the hot-wire sensing section
DR	Mean wall-shear stress measured in active large-scale flow control measurements
E	Voltage reading for the constant temperature anemometry
e_L	Laser signal in the PIV measurement
f	Frequency of a signal
f_{HF}	Sampling frequency of the hot-film probes
f_{HW}	Sampling frequency of the hot-wire probes
f_B	Sampling frequency of binary control signal
h_f	Wall-normal height of the PIV field of view
H_L	Linear transfer kernal between the friction velocity measured at detection array and streamwise velocity measured at actuation array

JR	Ratio between the jet exit velocity and the free-stream velocity
k_x	Streamwise wavenumber of the velocity signals
l_j	Spanwise width of the exit cross-section of wall-normal jets
l_{hw}	Length of the hot-wire sensing section
P_{reg}	Outlet pressure of the pressure regulators
r	Effective jet radius
$r_{u_\tau u_\tau}$	Temporal two-point correlation between friction velocities
$r_{u_\tau u}$	Temporal two-point correlation between friction velocity and streamwise velocity fluctuations
T	Ambient temperature during the measurement
t	Time instant
T_a	Actuation duration of the intermittent control
T_p	Pause duration of the intermittent control
T_s	Sampling time of a single measurement
U_∞	Free-stream velocity of the flow
U	Total fluctuating streamwise velocity signal
u	Zero-mean fluctuating streamwise velocity signal
U_τ	Mean friction velocity
u_τ	Friction velocity fluctuation
u_l	Large-scale streamwise velocity fluctuations
u_s	Small-scale streamwise velocity fluctuations
u_{τ_l}	Large-scale friction velocity fluctuation

Nomenclature

$u_{\tau_{th}}$	Actuation threshold for the proposed modified proportional control
$u_{\mathrm{IOI}.s}$	Small-scale fluctuating streamwise velocity predicted from IOI model
$U_{c_{jet}}$	Local streamwise convective velocity of the jet flow
U_c	Convective velocity of the coherent structures
U_{jet}	Wall-normal jet exit velocity
u_{l_k}	Large-scale fluctuating streamwise velocity scaled by $\sqrt{k}$
V	Total fluctuating spanwise velocity signal
v	Zero-mean fluctuating spanwise velocity signal
W	Total fluctuating wall-normal velocity signal
w	Zero-mean fluctuating wall-normal velocity signal
w_a	Spanwise separation between the hot-films and wall-normal jets
W_b	Box filtered PIV wall-normal velocity fields
w_f	Streamwise length of the PIV field of view
w_j	Streamwise length of the exit cross-section of wall-normal jets
x	Spatial position in the streamwise direction
x_b	Streamwise length of the box-filter used in PIV post processing
y	Spatial position in the spanwise direction
z	Spatial position in the wall-normal direction
z_b	Wall-normal height of the box-filter used in PIV post processing
z_p	Wall-normal jet penetration height
z_{GC}	Wall-normal position of the geometric center of the logarithmic region

z_{LB} Wall-normal position of the lower bound of the logarithmic region

z_{min} Minimum wall-normal position of the PIV field of view

z_{UB} Wall-normal position of the upper bound of the logarithmic region

Glossary

2D2C	Two-dimensional Two-component
AEH	Attached Eddy Hypothesis
DBD	Dielectric Barrier Discharge
DNS	Direct Numerical Simulation
FOV	field of view
HRNBLWT	High Reynolds Number Boundary Layer Wind Tunnel
HWA	hot-wire anemometry
IOI	Inner-Outer Interaction
LEBU	Large Eddies Break Up
LES	Large-Eddy Simulation
LSE	Linear Stochastic Estimation
LSMs	Large Scale Motions
MUCTA	Melbourne University Constant Temperature Anemometer
PIV	Particle Imaging Velocimetry
QSQH	Quasi-Steady Quasi-Homogeneous
RANS	Reynolds Averaged Navier Stokes
TBL	turbulent boundary layer
TET	Task Execution Time
TTL	Transistor-Transistor Logic
UB	Uniform Blowing

US	Uniform Suction
VICA	Variable Interval Conditional Average
VLSMs	Very Large Scale Motions

Abstract

Experimental investigations are carried out to study the effect of manipulating large-scale coherent structures in high Reynolds number turbulent boundary layers. In canonical uncontrolled boundary layers, the large-scale motions interact with the near-wall small-scale structures via modulation and superposition effects. In this dissertation, we actively manipulate these large-scale structures in the logarithmic region using a spanwise array of wall-normal jets to explore their influence on the dynamics of near-wall turbulence in the perturbed boundary layer and, in turn, evaluate the feasibility of reducing skin-friction drag via controlling the large-scale structures.

The evolution of the large-scale coherent structures in the uncontrolled canonical boundary layers is examined using simultaneous (upstream) hot-film and (downstream) hot-wire measurements with increasing streamwise separation. The deterioration of the spectral correlation between the streamwise velocity and friction velocity measured by both probes with increasing separation infers that the traceable distance (lifetime) of these coherent motions is exponentially proportional to their streamwise wavelengths. Through the temporal correlation function between the friction and streamwise velocity signals, the convective velocities of the large-scale structures with different wavelengths are shown to be equivalent to the mean streamwise velocity at their geometric center, which indicates a strong scale-dependence. Based on the convective velocity and the traceable distance of the structures, an approach to systematically design the flow observation of the real-time flow control is proposed such that only coherent information is actuated upon.

Via assigning actuation on the different phases of the estimated large-scale velocity fluctuations (through opposing, reinforcing, and desynchronized control strategies), it is revealed that the percentage of high-speed structures successfully manipulated by the actuation is linearly proportional to the resulting drag reduction measured at 1.7δ downstream of the control. The underpinning physics is that the low momentum jet flow counteracts the wall-ward motions and deceler-

ates the positive streamwise velocity fluctuations associated with targeted high-speed large-scale events, which attenuates the large-scale turbulent energy in the log region. It is estimated that the large-scale motions with a streamwise wavelength greater than 1.6δ contribute to 5.4% of frictional drag. The large-scale superposition and amplitude modulation effect on the near-wall turbulence is shown to be valid in the perturbed boundary layers. Three-dimensional conditional averaged structures show that the modification on the velocity fluctuation in the log region correlates with control impacts on the large-scale footprints. Further, in keeping with the Quasi-Steady Quasi-Homogeneous (QSQH) hypothesis of Chernyshenko et al. (2012), small-scale turbulent energy responds to the local (spatial) large-scale friction velocity variation induced by the control.

The manipulated spatial streamwise/wall-normal instantaneous velocity fields are simultaneously acquired by a multi-camera double exposure PIV. In the controlled cases, both cross-flow and jet flow are separately seeded. This novel experimental set-up provides the opportunity to visualize the interaction between the jet flow and the targeted structures for an improved understanding of the drag-reduction mechanism due to large-scale manipulation. In mean flow statistics, perturbing the low-speed events allows the jet flow to penetrate to a higher wall position than tailoring the high-speed events. A phase averaged analysis reveals that the interaction between the jet flow and the high-speed large-scale motions can be separated into four phases, namely, penetrating, lifting, mixing, and recovery stages. The maximum skin-friction drag reduction and streamwise turbulent intensity attenuation concurrently occur at the mixing phase, which occurs 1.5δ to 2.2δ downstream of the actuation, and the control effects decay further downstream. Conversely, the evolution of the control impacts on the low-speed structures lasts longer, as the recovering stage appears to occur beyond 2.5δ downstream of the control. The recovery of control effect and the difference between the control persistence are both explained by the mismatched convective velocity between the jet flow and targeted LSMs. Finally, a strong correlation between the conditional Reynolds shear stress variation and conditional drag reduction is observed, which might suggest that in achieving drag reduction the attenuated large-scale energy suppresses the near-wall Reynolds shear stress.

Acknowledgements

I would like to sincerely express my utmost gratitude to my supervisors Prof. Nicholas Hutchins and Prof. Ivan Marusic for their continuous and patient suggestions and encouragements throughout my entire PhD study. Their professional understanding and enthusiasm in fluid mechanics immensely motivated and guided me in the course of my PhD journey.

I would also like to extend my gratefulness to the chair of my PhD committee Dr. Jimmy Philip and committee member Dr. Simon Illingworth for their insightful comments and discussions in the progress reviews. I also thanks Dr. Reza Abbassi for his invaluable mentorship in the first year of my PhD. Special thanks must go to Dr. Woutijn Baars, Dr. Charitha deSilva, Dr. Rio Baidya, and Dr. Mogeng Li who generously shared their expertise in the research. Technical support from Mr. Geoff Duke on constructing and manufacturing the experimental components is highly appreciated. I would also acknowledge the administrative assistance from Ms. Kim Robinson and Ms. Jan May.

Also, it was my greatest honor and pleasure to undertake the PhD with all my fellow friends in the fluid mechanics group: Mr. Jiwen Gong, Mr. Minghang Li, Mr. Bo Jiang, Mr. Yuan Wang, Dr. Dea Wangsawijaya, Mr. Ryan Newton, Mr. Aditya Ramani, and too many other names to be listed here, for their helpful supports and friendships during this challenging period in my life.

I would like to appreciate all the constant supports and encouragement from my parents not only during the PhD study but throughout the entire life. Finally, I would like to thank my wife, Min Wu for her love, for her physical and mental care during the thesis-writing (COVID-19 lockdown) stage, and for her giving me a lovely boy.

Contents

List of Figures

List of Tables

Chapter 1

Introduction

This thesis details an experimental study on the control of large-scale coherent structures in a high Reynolds number turbulent boundary layer. A series of experiments are designed to investigate the dynamics of long and very long streaky features that have been noted to populate the log regions of high Reynolds number boundary layers. In particular, this study focuses on the streamwise evolution and relationship of these structures with the near-wall turbulence in both canonical and perturbed boundary layers. Specifically, the large scale motions (LSMs) and very large scale motions (VLSMs) in the logarithmic region are actively manipulated using wall-normal jets in real-time. Hot-film and hot-wire anemometry along with Particle Imaging Velocimetry (PIV) are utilized to examine the control effects on the boundary layer and the resulting skin-friction drag reduction. *The aims are to use the manipulation on large-scale coherent structures to reduce the viscous friction and to enhance the performance of the control through improved understandings of the connections between the LSMs and the near-wall turbulence. Ultimately, we test the potential of manipulating large-scale coherent structures to achieve skin-friction drag reduction in high Reynolds number turbulent boundary layers and, hence, the feasibility of employing such control strategies in practical engineering applications*

Prior to the investigation on the large-scale control, the growth, evolution, and convection velocity of the coherent structures in canonical turbulent boundary layers are studied using spectral coherence analysis on experimental data acquired with varying streamwise separations. These results are subsequently used to design the wall-based flow observation system for real-time flow control (Chapter 4). Different control schemes are employed in real-time, which provides insights on the interaction between the LSMs in the logarithmic region and the near-wall dynamics in perturbed boundary layers (Chapter 5). The evolution of the control effect is further examined via

a series of hot-wire and hot-film measurements at a range of streamwise locations downstream of the control. Based on the findings, some improvements on the present flow control are proposed to seek the potential of enhancing control efficacy. For the first time, a PIV experiment with a large field of view (FOV) and multiple seeding sources is carried out to reveal how the injected jet flow alters the large-scale coherent structures (Chapter 6). The underpinning drag reduction mechanism of the large-scale control strategy is studied using conditional and phase average analysis on the simultaneous PIV and hot-film measurements.

1.1 Motivation

A turbulent boundary layer (TBL), formed when fluid flows over a solid surface, is a thin turbulent region immediately adjacent to the wall, where fluid velocity approaches the velocity of the wall due to the no-slip condition. Such phenomena are observed in a wide range of engineering and natural applications, ranging from the atmospheric flows to the flow of blood through arterial stents or flows around the fuselage of airplanes or hulls of ships. The sharp velocity gradients due to the no-slip condition lead to viscous shear stress in the direction of the fluid motion, which induces skin-friction drag on the surface leading to significant energy expenditure in engineering applications. For example, over half of the total drag experienced by a modern aircraft is comprised of skin-friction due to the viscous shear produced by TBLs, and this ratio is even higher for submarines and pipelines (Gad-el Hak, 1994). The estimations from both Leschziner et al. (2011) and Peeters et al. (2005) suggest a single percent reduction in skin-friction drag annually could save around 3 million tonnes of fuel consumption and 9 millions tonnes of greenhouse gas emission in the global aviation industry. This combination of economic, environmental, and social factors motivates research on alleviating the viscous wall shear stress in the TBLs.

Over the last century, tremendous efforts have been devoted to the research of wall-bounded turbulence. However, the non-linear dynamics, broad range of length-scales, and chaotic nature of turbulent fluid motions leave wall-bounded turbulence as one of the most outstanding unsolved classic physics problems. Despite limited analytical solutions, research has revealed highly organized coherent structures existing in turbulent boundary layers, which contribute to a significant amount of turbulent production and in turn the skin-friction drag. The presence of these recurrent

features in TBLs, which had previously been viewed as random and uncontrollable, stimulated efforts at flow control to mitigate skin-friction darg via controlling these structures. Based on ever-improving understandings of the dynamical features of these coherent motions, different control strategies have been proposed. The majority of previous work focused on tailoring the near-wall coherent structures. These structures increase the turbulence intensity in the near-wall regime and play a major role in turbulent production (dominating low Reynolds number TBLs) making them obvious control targets. However, the length scale of the near-wall structures is proportional to the viscous length-scale which becomes challengingly small at high Reynolds numbers. As an example, at Reynolds numbers of typical flow over the fuselage of an aircraft, the characteristic length of the near-wall structures is $\mathcal{O}[100\mu\text{m}]$ with a characteristic passing frequency of $\mathcal{O}[10k\text{Hz}]$, which severely limits the practical implementation of the near-wall control schemes.

Rather than targeting the near-wall structures, a probably more promising category of control approach aims to manipulate the LSMs and VLSMs. As a result of the improvements in computational capability and experimental techniques, these large-scale structures with a length scale of $\mathcal{O}[\delta]$ have been revealed over the last few decades. At higher Reynolds numbers, the turbulent production of these LSMs and VLSMs becomes increasingly comparable to that of the near-wall structures. It has also been revealed that these LSMs interact with the near-wall turbulence. Together, these findings suggest that large-scale features may also be a suitable target for control. A clear benefit of these large-scale control is that the scale and characteristic frequency of these events create fewer obstacles to the practical realization of control. Thus, this thesis aims to experimentally investigate the feasibility of alleviating the skin-friction drag via manipulating the large-scale structures in a turbulent boundary layer at a practical Reynolds number (i.e. $\text{Re}_\tau \sim \mathcal{O}[10^5]$). The precursor of this project successfully utilized a spanwise array of wall-normal slotted jets to selectively mitigate the large-scale structures in a high Reynolds number wall-bounded turbulent boundary layer at $\text{Re}_\tau \approx 14400$ (Abbassi et al., 2017). By firing at the large-scale high-velocity events detected 1.7δ upstream of the actuator, the large-scale turbulence intensity has been alleviated by over 35% at 1.7δ downstream of the jets, and a 3.2% local skin-friction reduction was observed at the same measuring point, which verified the concept of achieving drag-reduction through altering LSMs. However, though almost a third of the large-scale energy is attenuated, the resulting skin-friction drag was limited. Motivated by the factors addressed above, this thesis is a

continuation of this previous work with the following objectives

1. Optimize the large-scale active flow control strategies. This optimization is approached via enhancement of the observation and actuation systems of the control. Through the study of the coherent structures in canonical turbulent boundary layers, an improved real-time flow estimator has been designed which permits us to better understand the limitations and potential of the current control strategy. In terms of improved actuation, the feasibility of selectively restricting control to specific subsets of the targeted events is investigated to increase the net control outcome.

2. Investigate the control effects on the inner and logarithmic regions of the boundary layer and, hence, understand the relationship between the perturbed large-scale coherent structures and the near-wall turbulence. While the evidence on inner-outer interaction between the LSMs in the log region and the small-scale structures near the wall in the canonical boundary layer is convincing, this dissertation tests the veracity of this interaction in actively perturbed boundary layers. As an additional motivation, it is expected that quantitative analysis of the inner-outer interaction can be used to estimate the contribution of the LSMs to the mean wall-shear-stress.

3. Use snapshot PIV to reveal in higher fidelity the interaction of the jet actuator with the targeted large scale structure. The ultimate target is to reveal the drag reduction mechanism for the present outer-region large-scale flow control via simultaneously considering the perturbed large-scale structures and the friction velocity signals. The intention or goal of this research is to be able to make informed recommendations on the design of future large-scale flow control attempts.

1.2 Thesis Outline

Chapter 2 is a literature survey of research on coherent structures in wall-bounded turbulent flows and boundary layer control techniques. In specific, the review focuses on the dynamics of LSMs and VLSMs, their connection with the near-wall turbulence, and the estimation methodology of these structures from previous studies. Due to the scope of this thesis, the discussion on the

existing flow control strategies is restricted to either active or large-scale boundary layer flow control techniques. The flow control set-up, control outcomes, and the underpinning drag reduction mechanisms of the previous work are summarized. This knowledge forms the basis for the improvements of the large-scale flow control strategy investigated in this thesis.

Chapter 3 discusses the experimental facility, including the wind-tunnel, control set-up, and measurement techniques, for the measurements conducted in the present project. The layout of the control infrastructure is documented, which includes the sensing system, the specifications and air-supply system of the wall-normal jets, and the real-time target controller. The unique calibration process and data acquisition methodology of the constant temperature (hot-wire and hot-film) anemometry are introduced. The coordinate system and the notation for different velocity components and conditional average quantities throughout the entire thesis are defined in this chapter to reduce the repetitiveness.

Chapter 4 demonstrates an approach to design the real-time flow observation system for active flow control. Spectral coherence analysis is performed on simultaneously acquired fluctuating streamwise velocity and fluctuating friction velocity, which, by varying the streamwise separation between the two signals, provides information on the scale-dependent streamwise evolution and convective velocity of the coherent structures. With the aim of maximizing the estimation accuracy of flow observation, the real-time filter of the large-scale control is configured through linear stochastic estimation using the coherence spectrum. The procedure to select the optimal combination of the sensor actuator separation and the length-scale of the targeted structures is reported in this chapter. The performance of the active control with different flow observation accuracy is examined using various control schemes and real-time filters. Extrapolation of these results provides an estimate of the potential maximum drag reduction using the current large-scale flow control strategy.

Chapter 5 describes the role of the large-scale structures on the near-wall turbulence and skin-friction drag. In particular, we estimate the contribution of the LSMs to the mean wall-shear-stress and inspect the scale interaction between the large-scale coherent structures in the outer region and the near-wall small-scale structures in the perturbed boundary layers. Another important feature of the large-scale flow control is the streamwise persistence which is tested through simultaneous hot-wire and hot-film anemometry measurements at different streamwise locations downstream

of the control. The conditional analysis outlines the evolution of the manipulated LSMs and the resulting drag reduction. Based on the conditional analysis, adjustments are implemented on the control strategy to alter the most effectively controlled portion of the large-scale structures aiming to enhance the overall net control efficacy.

Chapter 6 further investigates the drag reduction mechanism of the large-scale control via a flow visualization experiment designed to observe the interactions between the active jet flow induced by the wall-normal jets and the targeted large-scale coherent structures. These novel simultaneous PIV and hot-film measurements utilize two seeding sources with the field of view exceeding 2.5δ in the streamwise direction to capture the behaviors of both jet flow and oncoming turbulent structures. The effect of the jet flow on the boundary layer, including the streamwise/wall-normal mean flow statistics and penetration trajectory, are demonstrated. The spatial evolution of the interaction process is clearly illustrated using phase average analysis. The PIV dataset provides the opportunity to compare the variations of large-scale energy, Reynolds shear stress, and drag-reduction, which gives further information on the drag reduction mechanism of the large-scale flow control strategy.

Chapter 7 concludes the key findings from the previous chapters in the thesis. This study is a continuation of a long-term project (active for more than a decade) on large-scale active flow control. In contrast to the preceding work, this study focuses on analyzing the drag reduction mechanism and the evolution of the large-scale coherent structures in both the canonical and perturbed boundary layers. This study provides insight on the physical and technical feasibility to further refine such a strategy. With the ultimate target of raising the drag reduction potential while retaining the practical advantages of large-scale control, this chapter suggests several possible research avenues, which could be studied as an extension of this work.

Chapter 2
Literature Review

This literature review covers three major aspects. The first section §2.1 surveys the history of the research on coherent structures in the wall-bounded turbulent boundary layers. In §2.2, a more comprehensive review is conducted on the LSMs and VLSMs, which includes their formation, estimation, and interaction with the small-scale structures. Finally, an overview of the underpinning physics and the evolution of the existing boundary layer flow control strategies is provided in §2.3.

2.1 Coherent Structures

The word "Turbulence" from *Latin 'Turba'* means disorder and tumult. In the fluid mechanics society, due to the restrictions in flow observation techniques in the early era, fluid motions in turbulent boundary layers were long regarded as random phenomena in accordance with the flow statistics. Moreover, the governing Navier-Stokes equation transfers perturbations in the flow into disorder under nonlinear complex procedures (Landau and Lifshitz, 1959). However, during the past several decades, there has been a growing acceptance that despite this apparent randomness, turbulence can consist of certain recurrent features, known as coherent structures. The majority of the community has achieved a consistent acceptance that a turbulent boundary layer is constructed from a hierarchy of coherent structures populating both the near-wall and outer-regions. The first documentation of coherent motions can be tracked to the pioneering "Mechanisms of turbulence" of Theodorsen (1952). A further seminal study saw the introduction of the "*Attached Eddy Hypothesis (AEH)*" of Townsend (1961, 1976). However, there is no unanimously accepted definition of a coherent structure adapted in the fluid mechanics community. In this review, the definition proposed by Hussain (1986) is endorsed, which stated that coherent structures are turbulent fluid

motions with their instantaneous vorticity correlated over a certain spatial range. Another description that is taken into consideration is that suggested by Robinson (1991), which added generality to the previous definition and proposed a coherent motion should possess at least one fluid property highly correlated with itself over a spatial or temporal range much larger than the length scale of its smallest scale of the flow.

The definition of Robinson (1991) broadens the meaning of "coherence" without limiting the structure to certain spatial regions or geometric sizes, and without limiting the study to vorticity. Focusing on only zero-pressure-gradient wall-bounded turbulence, Kline (1989) classified the coherent structures into eight categories, which are observed from different experimental flow observation techniques. The attributes of all these different organized structures in a turbulent boundary layer are finely described by Cantwell (1981). A more concise grouping by Smits et al. (2011) divides the structures in terms of their principal characterizations into, **(1).** quasi-streamwise vortices streaking near the wall (Kline et al., 1967); **(2).** Hairpin or Λ-vortex higher than a hundred viscous wall units (Perry and Chong, 1982, Theodorsen, 1952); **(3).** LSMs and **(4).** VLSMs populating the logarithmic region of the boundary layers (Kim and Adrian, 1999). Panton (2001) suggested that the near-wall coherent structures are strongly correlated with either instantaneous or time-averaged turbulence skin-friction drag and hence these have traditionally been the target of flow control schemes. In this thesis, we will investigate the control of (3) LSMs and (4) VLSMs as a method of reducing drag. The subsequent contents follow the classification of Smits et al. (2011), with the near-wall coherent structures and hairpin vortices are discussed in §2.1.1 and §2.1.2, respectively. The survey loosely tracks the timeline of research on coherent structures with a particular focus on the behaviours of organized fluid motions, and more importantly, how these coherent structures affect the turbulence and skin-friction production.

2.1.1 Near-Wall Coherent Structures

In the twentieth century, the history of research on the coherent structures in turbulent boundary layers can be divided into four eras with the progression in flow investigative techniques, which includes the *Discovery Era, Flow-visualization Era, Conditional-sampling Era*, and *Computer-simulation Era* (Robinson, 1991). Conceptual studies via two-point correlation and preliminary conditional statistics in the earliest era revealed the presence of nonrandom and repetitive motions

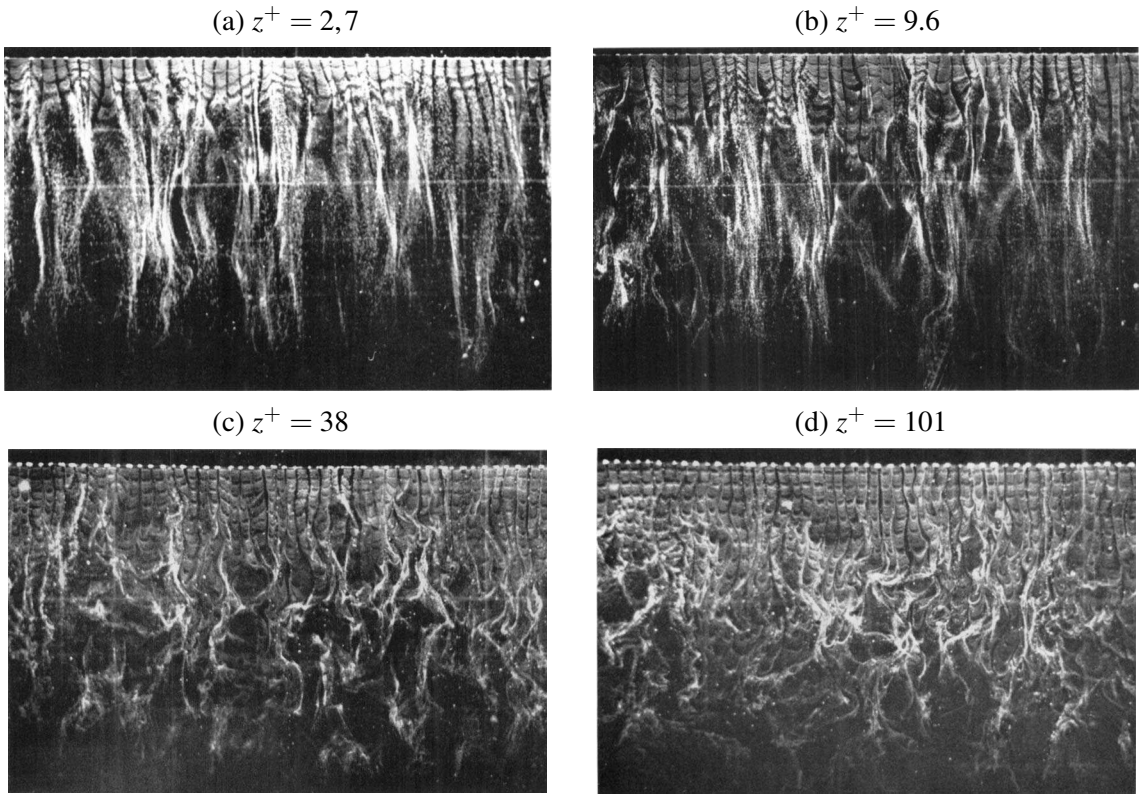

Figure 2.1: Photographs of the low-speed ejection structures taken at a wall normal position z^+ equivalent to (a) 2.7; (b) 9.6; (c) 38; and (d) 101. Adapted and reproduced from Kline et al. (1967).

in the smooth boundary (Einstein and Li, 1956). However, it was the advent of the second era in 1967, where Kline et al. (1967) achieved the very first visualization of these well-organized structures in the near-wall region of the turbulent boundary layer via a hydrogen bubble flow-visualization technique (figure 2.1) which showed a near-wall streaky structure. These flow visualisation results were summarized in the "lifted stretched vortex element" model reproduced here in figure 2.2. (Kline et al., 1967) believed that these assembled low-speed regions grow away from the wall at a certain characteristic angle and velocity. Through combining the hydrogen bubble technique and hot-wire anemometry, Kim et al. (1971) concluded that the low-velocity streaks lift-up, oscillate, burst, and eventually grow away from the surface boundary via vortex induction. Such vortex elements are now widely accepted as quasi-streamwise vortices (Smith and Schwartz, 1983), which are recurring in the viscous sublayer with a spanwise spacing of approximately 100 wall units (Panton, 2001). The significance of these near-wall low-velocity streaks is reflected by their relation with the self-sustaining mechanism of turbulence (Kim et al., 1971). In addition, the

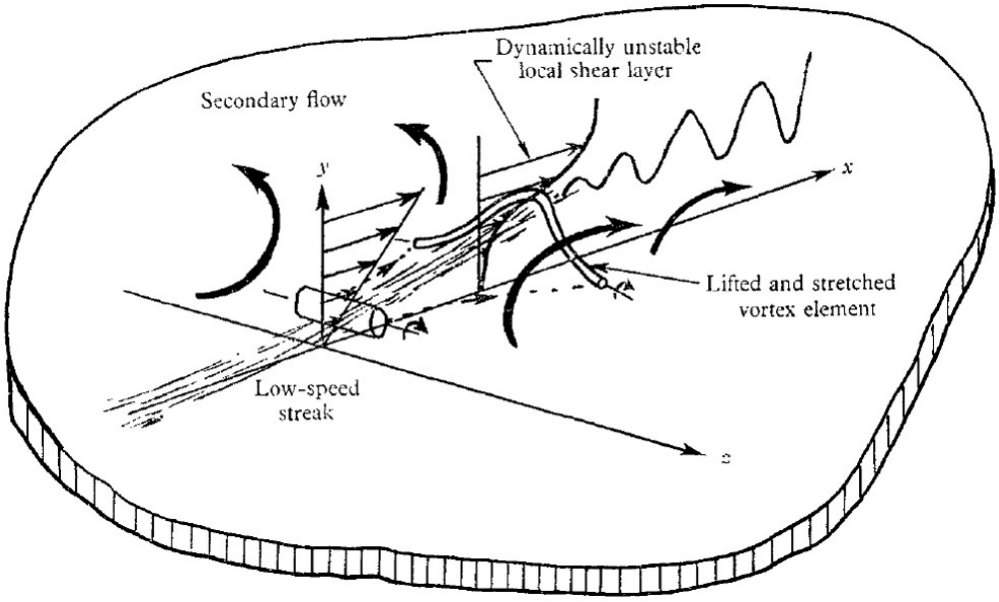

Figure 2.2: A schematic ··lifted stretched vortex element" model for the lifting and break-up mechanism of low-speed streaks. Adapted and reproduced from Kline et al. (1967)

inherent bursting and ejection processes are responsible for a great deal of the turbulent production and transportation of turbulent kinetic energy in the near-wall region (Kim et al., 1971).

Corino and Brodkey (1969) ustilized photographic technique to visualize particles in a turbulent boundary layer and reinforced the understanding of near-wall structures by introducing the motion of "sweep". In comparison with ejections, they recognized that the sweep motion was associated with motions that have grown away from the wall pushing high-speed fluid towards the surface. In addition, Corino and Brodkey (1969) pointed out that the low-speed "ejection" motion contributed to over half of the turbulent production while occupying less than one-fifth of the temporal resource. They also suggested that the interaction between the high-speed sweep motions and the low-speed ejection motions produced the inclined shear layers that had been noted in the near-wall region of a boundary layer. Via hot-film anemometry in an oil channel, Wallace et al. (1972) employed the quadrant splitting method and reported that the Reynolds shear stress resulting from the ejection (Q2) and sweep (Q4) motions are nearly equal at approximately 70% each, whilst the interactions between both structures (i.e. Q1 and Q3 motions) at the maximum turbulent production position ($z^+ = 15$) contributes to negative 20% Reynolds shear stress each. From simultaneous dye streakiness and hydrogen-bubble time-lines, Offen and Kline (1974) revealed

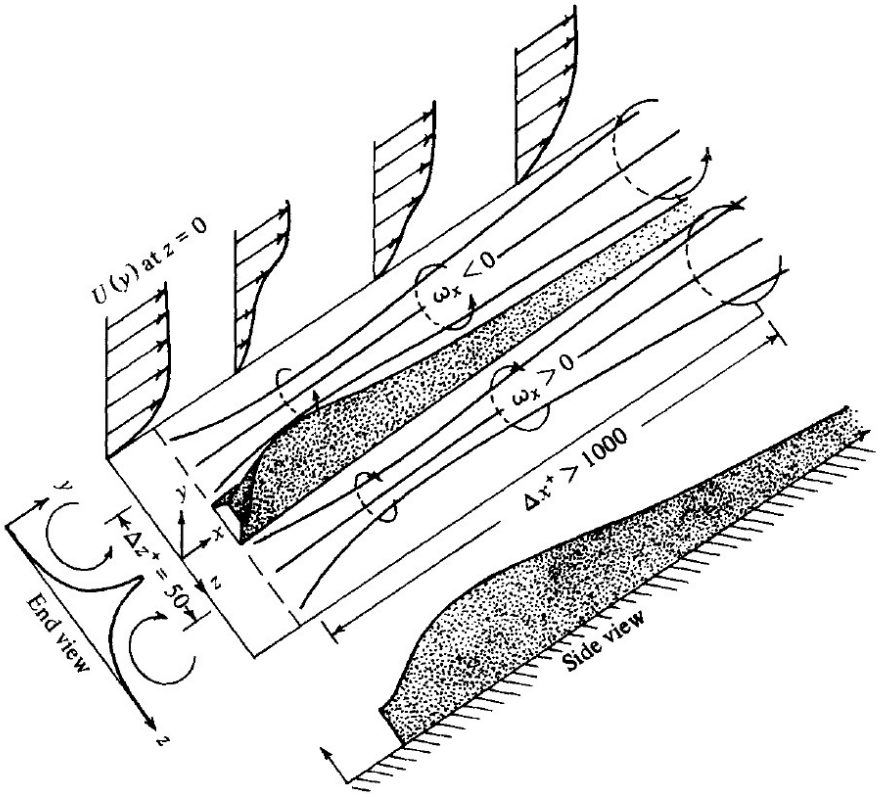

Figure 2.3: A schematic model for the lifting and break-up mechanism of low-speed streaks, which adapted and reproduced from Blackwelder and Eckelmann (1979)

that the low-speed streaks lifting away from the wall always eventually results in the wall-ward "sweep" motions at the higher end of the near wall-region ($20 < z^+ < 200$), and hence forms a *burst-sweep* periodicity in the shear layer. Further evidence or an alternative pattern of high and low-velocity structures is provided by Nychas et al. (1973), who implied that the interactions lead to the appearance of traverse vortices growing from the near-wall to the outer-region. The presence of such traverse vortices was confirmed by Praturi and Brodkey (1978) who obtained a three-dimensional view of the flow structures in the turbulent boundary layer via a stereoscopic camera system maneuvering with the flow. Praturi and Brodkey (1978) further stipulated that these traverse vortices roll the free-stream flow into the bulges of the boundary layer, and suggested that this entrainment initiates the regenerative mechanism of the lifting and sweep motions.

The work of Wallace et al. (1972) opens the gate of the *Conditional-sampling Era* in pursuing the mechanism of the near-wall coherent structures. Blackwelder and Kaplan (1976) utilized a rake of hot-wire probes measuring different velocity components to review the spatial and tempo-

ral organization of structures in the boundary layer. Through the variable interval time-averaging (VITA) method, (a technique to observe the conditional averaged events that occurred when running variance of the velocity fluctuations exceeds a defined threshold), they showed that the originator of low-speed structures meets the implication of Kim et al. (1971), and suggested that low and high-speed structures might be related to different classes of vortices. Applying correlations among the different velocity components, in figure 2.3, Blackwelder and Eckelmann (1979) found that a pair of counter-rotating streamwise vortices flank the low-speed ejection motions (the low-speed streaks). Using a similar VITA technique, Kreplin and Eckelmann (1979) noticed that the convection velocity of the ejections is slightly higher than the local mean velocity in the wall region in the spatial correlation of the coherent structures. During the late twentieth century, with the development of the computational capacity, the coherent structures were successfully captured in a Large-Eddy Simulation (LES) of a turbulence channel flow (Kim and Moin, 1979, Moin and Kim, 1982). The computational results gave well-resolved spatial quantities (including pressure and velocity etc.) of the coherent structures. Most of the studies agreed with the precedent findings on both quasi-streamwise vortex and traverse vortex. However, advanced understandings were raised from the better qualification of their characteristics. For example, Johansson et al. (1991) implement a variable interval spatial averaging (VISA) analysis to a three-dimensional Direct Numerical Simulation (DNS) result of a turbulent channel flow. In comparison with the temporal experimental results, the instantaneous spatial data suggested that the counter-rotating streamwise vortex pairs are largely an artificial artifact of the symmetry imposed by the conditional averaging. Johansson et al. (1991) also argued that the low-speed streaks contribute to turbulent kinetic energy production via their spanwise meandering tendency, which implies a possibility for skin-friction drag reduction via the suppression of such behaviour.

2.1.2 Hairpin Vortex and Outer-Scale Structures

While Kline and his co-workers believed that the ejections and sweeps triggers the self-sustaining turbulent production (Kim et al., 1971, Kline et al., 1967, Offen and Kline, 1974, 1975), some researchers argued that the traverse vortex provokes the mechanism of the near-wall cycles (Nychas et al., 1973, Praturi and Brodkey, 1978). Though the controversy remains debatable, it is long believed that there exists an elementary vortex that connects the quasi-streamwise and tra-

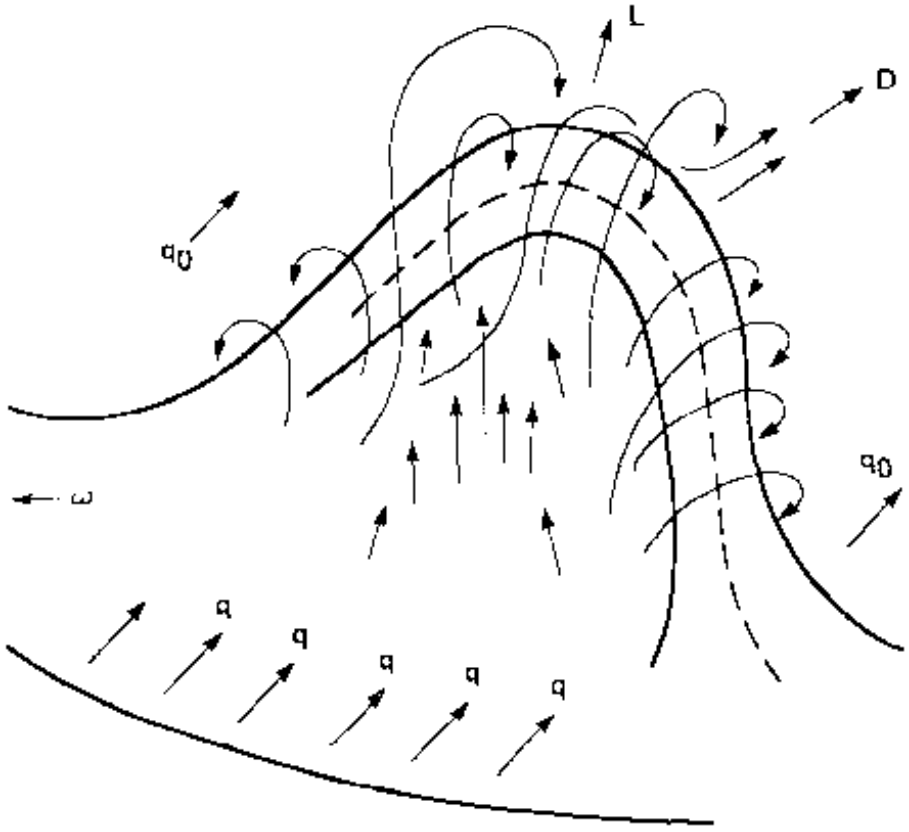

Figure 2.4: Schematic of the horseshoe flow structure proposed by Theodorsen (1952)

verse vortices and transports the turbulent kinetic energy from the near-wall to the outer region of the boundary layer. Deriving from the vorticity transportation, Theodorsen (1952) proposed a hairpin/horse-shoe vortex model, which is shown in figure 2.4. The hairpin vortex contains tornado-shaped vortical structures growing from the near-wall region and straddling on the low-speed structures with an inclination angle of 45°. Independently, Townsend (1956, 1961, 1976) introduced the Attached Eddy Hypothesis, which regards the double-cone eddies as the building blocks of the turbulent boundary layer.

Important evidence supporting these early-era conceptualized models is supplied by Head and Bandyopadhyay (1981), who are widely known as the first to observe the hairpin/horseshoe vortices by conducting a series of synchronized hot-wire anemometry and oil-fog flow visualization experiments on an inclined laser sheet in the zero pressure gradient turbulent boundary layers with $500 < Re_\theta < 17500$. Their results provided insightful knowledge on the structural topology of

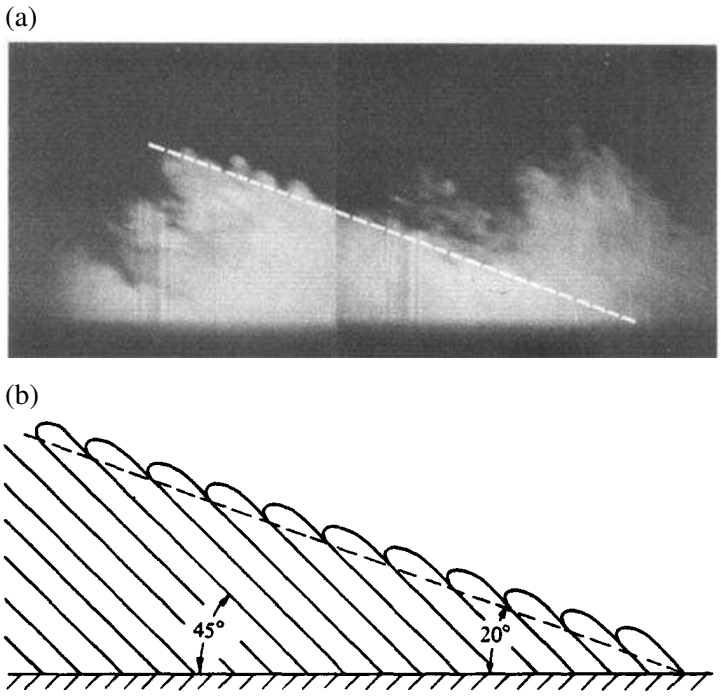

Figure 2.5: (a) An instantaneous snapshot showing the inclination angle of the outer region turbulent-non-turbulent interface. (b) Schematic of the formation of inclined interface from a group of hairpin vortex. Figures are adapted and reproduced from Head and Bandyopadhyay (1981).

the hairpin/horseshoe vortices. As shown in figure 2.5, they verified that the hairpin vortices are forward-leaning at a characteristic angle of approximately 45° against the solid boundary. Such observations on the inclination angle of the hairpin vortices were further confirmed from the LES results of Moin and Kim (1985) and Deshpande et al. (2019) via spectral coherence analysis on high Re_τ turbulent boundary layers. In addition, Head and Bandyopadhyay (1981) visualized that the hairpin vortices tend to arrange together to construct larger coherent structures. These agglomerations of hairpin vortices seemed to lead to larger features with an inclination angle of approximately 20°, despite being composed of individual features with 45° inclination angles (figure 2.5(b)). The legs of these hairpin vortices, located at the wall and pointing upstream, were believed to form the previously observed quasi-streamwise vortices in the near-wall region, which correlates with the high-skin-friction events at the wall (Kravchenko et al., 1993). Perry et al. (1981) also capture the existence of the hairpin-shaped vortex issuing from an oscillating trip wire in a laminar boundary layer but named these structures $\Lambda-$vortex filaments. Robinson (1991)

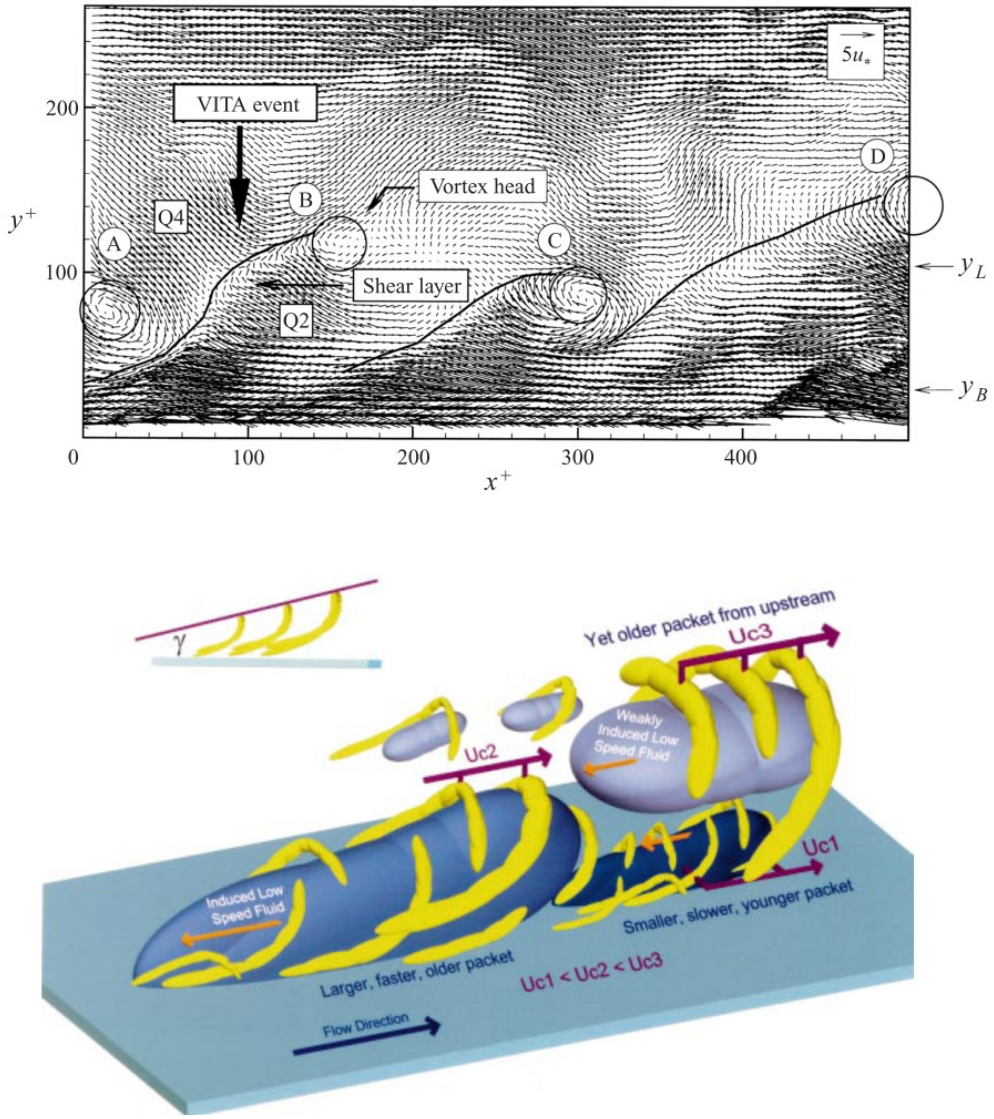

Figure 2.6: (a). Hairpin vortex signatures aligned in the streamwise direction with their vortex heads and inclined shear layers are indicated in a PIV database, which triggers a VITA event. (b). Conceptual scenario of nested packets of hairpins or cane-type vortices growing up from the wall. (Adrian et al., 2000)

combined the previous studies and established a schematic model of vortical structures in a turbulent boundary layer, in which the quasi-streamwise vortices dominates the near-wall region. Hairpin vortices appear at a higher wall-normal position, but remain incomplete, such as no vortex head (i.e. double-cone eddies of Townsend (1956)) or one-legged vortex. The arches of the hairpin vortices eventually locate in the wake region of the boundary layer.

The understanding of the hairpin eddies was further advanced via the advent of PIV measurements and improvements in computational simulations. Smith et al. (1991) postulated that the hairpin vortex is the fundamental basis of the turbulent flow structures. The asymmetric interaction between the hairpin vortices with the crossing shear flow stimulates the regeneration of the secondary new hairpin vortices near the wall. Zhou et al. (1999) carefully studied the transformation process from a single hairpin vortex to an agglomerated packet in a low Reynolds number DNS turbulent channel flow. They termed a hairpin structure with two flanking counter-rotating structures as the primary hairpin vortex. Identical to Smith et al. (1991), they identified that the subsidiary of these primary hairpin vortices forms the agglomerated packet, whose structural geometry is largely affected by the primary hairpins. Adrian et al. (2000) used high-resolution PIV on a wide range of Reynolds number ($930 < Re_\theta < 6845$) turbulent boundary layers, to investigate the behaviour of the hairpins in the streamwise wall-normal velocity fields (figure 2.6(a)). Using VITA analysis, they reported that the vortex head distinguishes each single hairpin vortex along with the low-speed ejection motion, which inclining at approximately 45°. Further, they confirmed that multiple hairpins generate larger hairpin packets via aligning with each other and these hairpin packets occur throughout the entire boundary layer but mainly at the interfaces of the uniform streamwise momentum zone. To summarize their findings, Adrian et al. (2000) proposed the "hairpin packet paradigm", which links the key features of the hairpin packet paradigm. They argued that hairpin packets exist throughout the entire boundary layer, and their different sizes and distances from the wall represent different ages. A typical packet grows as a ramp at a mean inclining angle of 12°. The model, shown in figure 2.6, demonstrates a group of hairpin packets at variable stages and it is obvious that the larger and older structures, convecting at a higher velocity, overtake the smaller and newly-grown structures.

In terms of the outer region, Adrian et al. (2000) noted that the heads of hairpin structures consist of spanwise vortices in the streamwise wall-normal planes (figure 2.6(a)), which forms the turbulent/non-turbulent interface. They suggested that these collections of spanwise vortices, which over a wider spanwise domain form arches, give rise to the three-dimensional bulges at the edge of the boundary layer with the length scale of boundary layer thickness (Tomkins and Adrian, 2005). The flow in the potential core penetrates the turbulent regime through the instantaneous turbulent-non-turbulent interfaces due to the transport effect of these spanwise vortices. When this

penetrating high-speed fluid from the potential core collides with lower speed structures closer to the surface, inclined internal shear layers form.

2.2 Large-scale and Very Large-scale Motions

In the pioneering study, analyzing the auto-correlation functions of the fluctuating streamwise velocity, Townsend (1958) observed that the non-zero tails of the correlation curve stretched to a time delay equivalent to a streamwise length of 1.4δ, which inferred that there are large-scale coherent structures in the turbulent boundary layer. Extending this picture, different correlation techniques confirmed the occurrence of LSMs and added knowledge on the 'large eddy' hypothesis (Blackwelder and Kovasznay, 1972, Favre et al., 1967, Tritton, 1967). For example, Nakagawa and Nezu (1981) employed a fixed V-shaped cross-wire probe and a movable X-shaped cross wire probe in an open channel flow to perform space-time correlations between different velocity components, obtaining the time-averaged scale of the large structures. Considering the pre-multiplied energy spectra of longitudinal velocity fluctuations in a turbulent pipe flow, Bullock et al. (1978) observed that the energy contributed by the low-wavenumber structures was far from being negligible. In specific, while the energy peaks at $\lambda_x^+ \approx 600$ in the near-wall buffer region, they observed that local maximum energy in the wake region ($z = 0.6$ pipe radii) was shifted to λ_x equals one pipe radius. Based on the AEH of Townsend (1976), the theoretical analysis and experimental results of Perry et al. (1986) demonstrated that the streamwise wavelength of the energy-containing structures increases proportionally with the wall distance attaining a maximum at approximately 3 boundary layer thicknesses.

However, the studies on the large-scale structures prior to the invention of PIV were mostly focusing on the formation of turbulent bulges at the edge of the layer, with an averaged wall-normal extension of δ and a longitudinal length of 2δ in the outer region (Brown and Thomas, 1977, Falco, 1977, Laufer and Narayanan, 1971). In the notable taxonomy of the turbulent structures, Robinson (1991) also attributes the large-scale motions to the outer layer features. These flow visualization experiments and DNS data sets at low Reynolds number failed to identify that large-scale streaks are the dominating features within the logarithmic region of a turbulent boundary layer. This is because a minimum friction Reynolds number of 667 (i.e. $Re_\tau > 667$) is required

for the appearance of the logarithmic region spanning $100 < z^+ < 0.15\delta^+$. A simple calculation reflects that a clear observation on the log region (spanning a decade in the wall-normal direction) requires a Reynolds number of 1700 (Hutchins and Marusic, 2007b). With the help of DNS and experimental studies at higher Reynolds number, these large-scale features dominating in the log region becomes another important class of turbulent structures in the boundary layer. In this section, the review is focusing on the LSMs in the logarithmic region, including their geometry and interaction with near-wall turbulence.

2.2.1 Existence and Geometry of LSMs and VLSMs

With the advancement of PIV techniques in the 1990s, the understanding of large-scale structures in the logarithmic region gained significant improvements. Using instantaneous PIV snapshots in the streamwise / wall-normal plane, Meinhart and Adrian (1995) observed that there existed uniform streamwise momentum zones in the near-wall, logarithmic, and wake regions. The largest dimension of these zonal structures is proportional to the boundary layer thickness. They postulated that these uniform momentum regions are induced by the backflow of several aligning hairpin vortices. While the conventional decomposition of the boundary layer is based on the mean velocity profile (i.e. near-wall, logarithmic, and wake regions), these zonal structures provide another characterization of the boundary layer concerning the instantaneous flow dynamics which better reflects the momentum transportation. Zhou et al. (1999) noted that these aligning hairpin vortices in the uniform flow region generate a coherent vortex packet, which was regarded as a unique building structure of the turbulent boundary layer (Panton, 2001). Adrian et al. (2000) refined the study of Meinhart and Adrian (1995) and observed the uniform momentum regions occur in a turbulent boundary layer with momentum thickness boundary layer ranging from 960 to 6845. In specific, as shown in figure 2.7(b), a low-speed uniform flow exists on top of the near-wall low-speed ejection streaks and spanning between the upper bound of the buffer region ($y_B^+ = 30$) and the top of the logarithmic region ($y_L = 0.25\delta^+$). Specifically, Adrian et al. (2000) distinguished such structures from the quasi-streamwise vortex, as these longitudinal velocity deficit regions are considered as the regions within the legs of the aligning hairpin vortices (see the model of Adrian et al. (2000) in figure 2.6). More evidence supporting the existence of these low-speed streakiness features in the logarithmic regions is reported in the studies of streamwise wall-normal

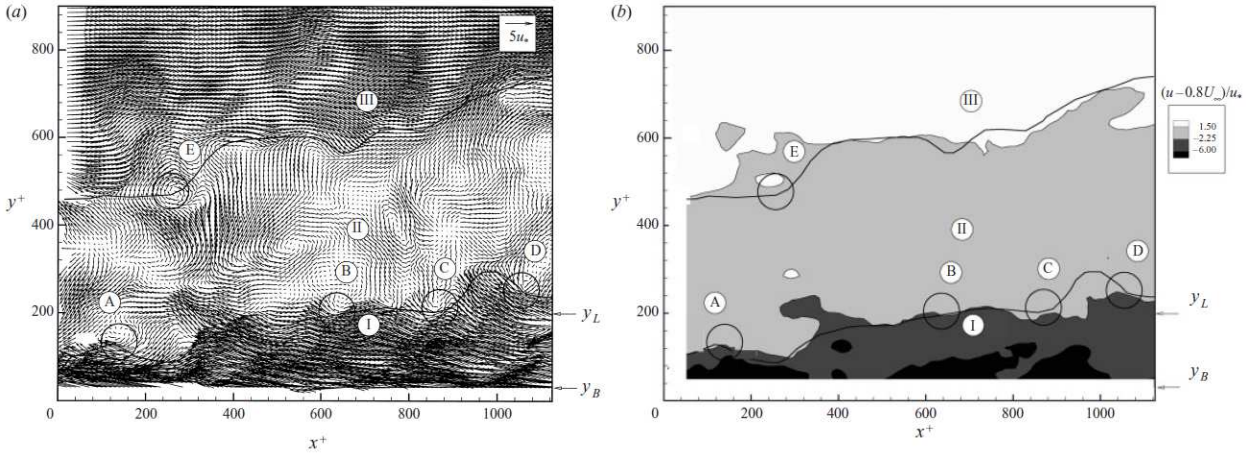

Figure 2.7: (a) Instantaneous velocity vector fields of a turbulent boundary layer with a momentum thickness Reynolds number of 2370. (b) Contours of constant streamwise momentum showing the uniform momentum regions, adapted and reproduced from (Adrian et al., 2000)

PIV (Christensen and Adrian, 2001), streamwise spanwise stereoscopic PIV (Ganapathisubramani et al., 2003), inclined cross-stream stereo PIV (Hutchins et al., 2005b) and DNS channel flow (Del Álamo and Jiménez, 2003). At higher Reynolds number turbulent boundary layer, these LSMs play an important role in turbulent transportation. For example, Ganapathisubramani et al. (2003) demonstrated that the hairpin packets contribute to a significant portion of Reynolds shear stress in the boundary layer. Such a phenomenon was verified by Hutchins et al. (2005b), who observed Reynolds stress concentrations within the large-scale low-speed streaks in the logarithmic region.

Considering the turbulent kinetic energy, Kim and Adrian (1999) observed that the one-dimensional pre-multiplied energy spectrum of the fluctuating streamwise velocities measured by hot-film anemometer in a wide Reynolds number range of fully developed turbulent pipe flows all present a bi-modal distribution. The wavelength of the longer mode increases from the near region to the outer region and is maximized with a value up to 12-14 pipe radii at $0.25 < z/R < 0.45$. Recognizing that this wavelength was an order of magnitude longer than the typical LSMs and the boundary layer thickness which was classically considered to set the largest-scale structures, they termed these structures very large-scale motions (VLSMs). They further postulated that these VLSMs form from the alignment of a series of ordered large-scale hairpin packets in the streamwise direction (see figure 2.8(a)). In DNS channel flow, Del Álamo and Jiménez (2003) also

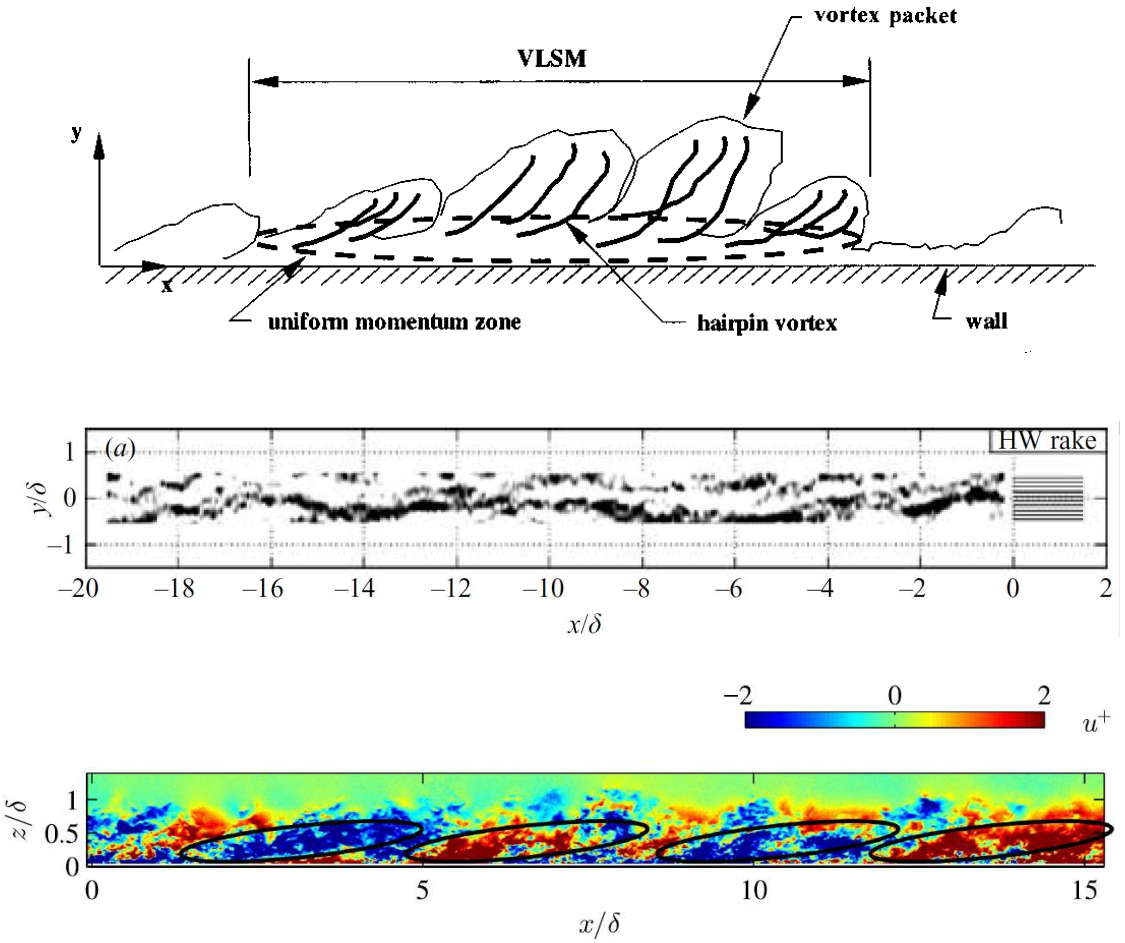

Figure 2.8: (a) Agglomeration of hairpin packets forms VLSMs, adapted from Kim and Adrian (1999) (b) Instantaneous snapshot of VLSMs captured by spanwise hot-wire rake, adapted from (Hutchins and Marusic, 2007a). (c) Large field of view PIV observation of large-scale streamwise periodicity in turbulent boundary layer at $\mathrm{Re}_\tau \approx 2500$, adapted and reproduced from deSilva et al. (2020).

visualized that the longest streamwise modes exceed 10 times the full channel height (i.e. 20 boundary layer thickness) in the two-dimensional energy spectrum. However, due to the restricted field of views of the PIV results at that time, the VLSMs could not be fully captured in experiments. Hutchins and Marusic (2007a) resolved the difficulty by employing a spanwise rake of ten hot-wire probes in the log region of a wall-bounded turbulent boundary layer with Re_τ ranging from 1120 to 19960. Transferring the temporal signals into the spatial domain using Taylor's Frozen Turbulence Hypothesis (Taylor, 1938), they observed VLSMs in an instantaneous velocity

field stretching over 20δ in the principal flow direction, as shown in figure 2.8(b). In addition, they revealed that VLSMs possess spanwise meandering behavior, so that alternating positive and negative fluctuations will align in the streamwise direction such that this meandering can mask the true length of these features from energy spectra. They further claimed that these very large-scale spanwise meandering structures can be observed in the atmospheric boundary layer (Hutchins et al., 2012). By applying a similar azimuthal array of hot-wire probes in a turbulent pipe flow, Monty et al. (2007) reported that the meandering 'superstructures' are a common feature in both internal and external boundary layers.

The significance of LSMs and VLSMs is reflected from their energy contribution in high Reynolds number turbulent boundary layers. Guala et al. (2006) revisited turbulent pipe flow and indicated that the very large energy-containing structures carry more than half of the turbulent kinetic energy, which results in a significant contribution to the Reynolds shear stress. In the external wall-bounded boundary layer, Mathis et al. (2009) conducted a series of experiments using a wall-normal traversing hot-wire probe in turbulent boundary layers with Re_τ ranging from 500 to 19000 and confirmed the observation of Guala et al. (2006). In the energy spectrogram of the streamwise velocity fluctuations across the entire boundary layer, they showed that for Re_τ greater than 2000, the LSMs and VLSMs lead to a second energy peak located at the geometric midpoint of the logarithmic region at $z^+ = \sqrt{15\mathrm{Re}_\tau}$. With the increase in the Reynolds number, a growing portion of the turbulent kinetic energy and Reynolds shear stress contribution is produced by these large-scale structures.

In terms of the geometric appearance of these LSMs, the ramp-like agglomeration of hairpin vortices with a forward-leaning inclination angle of $15^\circ - 20^\circ$ was reported as early as Head and Bandyopadhyay (1981) (see figure 2.4(b)). In the PIV velocity fields, Adrian et al. (2000) considered the conditional averaged hairpin packets and observed the induced shear layer is inclined at approximately 13°. Such forward inclining phenomenon was shown to be independent of Reynolds number based on a two-point correlation between the wall-shear stress fluctuation and the streamwise velocity fluctuations in the log region (Marusic and Heuer, 2007). Using spectral stochastic estimation between the fluctuating velocity signals measured by a fixed hot-wire probe near the wall and a traversing hot-wire in the log region, Baars et al. (2016) found an invariant 14.7° inclination angle for the LSMs and VLSMs with all length scales.

In addition, Tomkins and Adrian (2003) studied the spanwise arrangement of the LSMs in the logarithmic region and present that the high-speed large-scale structures are flanked by the two low-momentum regions. At the same age, Ganapathisubramani et al. (2003) indicated that the high-speed and low-speed LSMs distributed periodically in the spanwise direction in an alternating manner with a width of 0.3 to 0.5 boundary layer thicknesses. Hutchins et al. (2005a) extended the study by applying spanwise Fourier decomposition on the inclined and streamwise-spanwise velocity fields and reported the dominant spanwise length-scale is between 0.5δ to 0.75δ at $z = 0.14\delta$. deSilva et al. (2020) employed a multi-camera PIV configuration processing a field of view reaching 15δ in the streamwise direction. With the availability of this large field of view, they anchored the results from previous studies. Further, in the streamwise wall-normal instantaneous velocity fields, they showed the periodicity of the LSMs occurs in the streamwise direction in figure 2.8(c).

In a DNS of turbulent channel flow with friction Reynolds number of 1900, Del Álamo et al. (2006) also visualized the occurrence of LSMs and VLSMs, which they termed as 'tall clusters' and 'very long streaks', respectively. Based on a conditional average analysis, they reported that the 'tall clusters' have an aspect ratio of $\lambda_x : \lambda_y : z$=6:3:1. Hwang (2015) isolated the LSMs with different spanwise length scales and remarked that the superstructures could have a streamwise-wall-normal aspect ratio at $\lambda_x : z \approx 100$, while the hairpin packets-like large-scale energy-containing structures have a much smaller aspect ratio of 3 to 6. At higher Reynolds number, Baars et al. (2017b) utilized spectral correlation showing the averaged aspect ratio for all LSMs and VLSMs is $\lambda_x : z \approx 14$. From the analysis of the energetic ridge in the two-dimensional energy spectra of the fluctuating streamwise velocity in turbulent boundary layers with Re_τ ranging from 2400 to 26000, Chandran et al. (2017) found that the dominant motions at the high Reynolds number had an average aspect ratio of $\lambda_x : \lambda_y = 7$.

2.2.2 Scale Interaction in Turbulent Boundary Layers

During the flow visualization era, the 'cause-and-effect' relationship between the outer region large-scale motions and the near-wall streaks was controversial. While Nychas et al. (1973) argued the outer region large-scale vortices cause the production of near-wall turbulence, Offen and Kline (1975) debated that near-wall ejections lead to the large-scale outer region structures. In recent

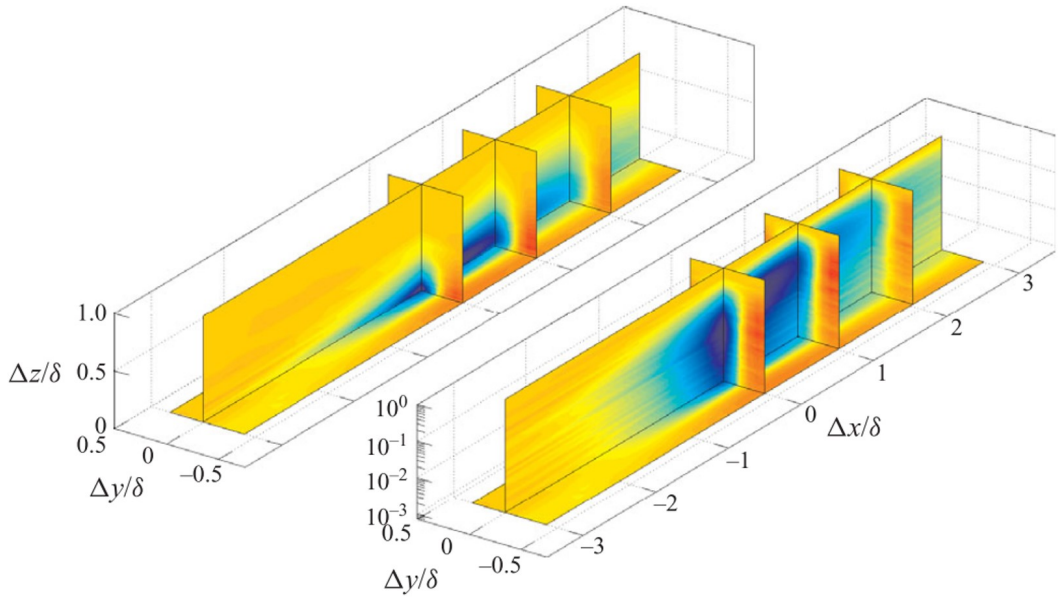

Figure 2.9: A schematic diagram of the three-dimensional conditional averaged low-speed large-scale structure. (Hutchins et al., 2011)

decades, a great deal of studies have provided evidence to suggest that LSMs affect the near-wall dynamics via a modulation and superposition mechanism. Notwithstanding this, there is also strong evidence that the autonomous near-wall cycle can regenerate turbulence in the absence of external influence (Jiménez and Pinelli, 1999).

Based on the AEH, Townsend (1976) predicted that the large-scale structures in the outer layer would leave their footprints on the near-wall region. In a fully developed DNS turbulence channel flow at $\mathrm{Re}_\tau = 640$, Abe et al. (2004) observed very long coherent features existing in the wall shear-stress fluctuations measured in the inner region. These large-scale features are correlated with the structures in the outer region. Such superposition phenomenon between the LSMs in outer layers and the near-wall cycle is, at the same time, reflected by the increased streamwise turbulence intensity in the near-wall region as Reynolds number increases Marusic and Kunkel (2003), Metzger and Klewicki (2001). Hutchins and Marusic (2007b), Hutchins et al. (2009) demonstrated that this increasing energy is solely attributable to a superposition of large-scale energy on the near-wall region. A step further, Baars and Marusic (2020) attributes such phenomenon to the Reynolds dependent superimposition of outer-layer streamwise turbulent intensity

on the viscous sublayer owing to the AEH. By applying a Gaussian filter to streamwise/ spanwise planes of streamwise velocity from a DNS channel flow database, Hutchins and Marusic (2007a) confirmed that the LSMs and VLSMs in the log region superimpose their footprint onto the near-wall coherent structures in the near-wall region. Hutchins et al. (2011) continued their work by using a spanwise array of hot-film sensors and traversing hot-wire probes to investigate the interaction between the inner and outer regions. Conditioned on negative low-pass filtered friction velocity fluctuations at the wall, they constricted a three dimensional conditional averaged low-speed large-scale structure (figure 2.9), which demonstrated that the low-speed LSMs in the outer region is concurrent and well-correlated with the large-scale low friction velocity events at the wall.

In the same study, Hutchins et al. (2011) conducted another conditional average analysis based on the points that instantaneous small-scale friction velocity intensity is smaller than its average. They showed that these near-wall weakened energy regions are associated with negative large-scale streamwise velocity fluctuations in the log region, which implied the modulation effect between the LSMs and the near-wall turbulence. Such scalar interaction is first inferred by Rao et al. (1971), who expressed that the occurrence period of the near-wall quasi-streamwise structures scales with the boundary layer thickness and free-stream velocity. The first investigation on the scalar interaction in the turbulent boundary layer was carried out by Brown and Thomas (1977). They utilized an array of hot-wire probes and wall shear stress sensors and demonstrate that the large-scale structures induced a low-frequency component in the wall shear stress (i.e. superposition effect). In addition, based on the correlation results, they showed these slowly varying fluctuations are associated with the near-wall bursting events. Bandyopadhyay and Hussain (1984) studied the connection between the small and large-scale motions via short-time correlation measurements and reported a strong coherence between the low-frequency large-scale fluctuation and envelope of the high-frequency small-scale velocity fluctuation of the streamwise velocity signal measured in the outer layer. This supports the presence of scalar modulation. However, they noted that there existed a phase delay between the low- and high-frequency fluctuations, and this delay varied with the wall-normal position of the velocity acquired in the outer region.

In the latest century, with the increasing knowledge on the LSMs and VLSMs, it is widely accepted that the amplitude modulation also exists between the long streaky features in the log

region and the near-wall turbulence. In a high Reynolds number boundary layer at $Re_\tau = 7300$, Hutchins and Marusic (2007b) employed a Fourier spectral filter with a cut-off frequency of $\lambda_x = \delta$ to decompose the streamwise velocity into large-scale and small-scale fluctuations, observing that the small-scale fluctuations of all three velocity components and the Reynolds shear stress are weakened during a negative large-scale fluctuating velocity region. Mathis et al. (2009) quantitatively studied this modulation phenomenon by applying a Hilbert transformation to attain the instantaneous modulating wave of the high-frequency velocity components. Through such methods, they were able to show that the degree of amplitude modulation flips from positive values to negative with the increased wall-normal position, which confirmed the varying phase delay observed by Bandyopadhyay and Hussain (1984). Talluru et al. (2014) employed an array of hot-film sensors and traversing cross-wire probes and quantitatively verified the amplitude modulation effect between the large-scale streamwise velocity and small-scale fluctuation of all three velocity components and Reynolds shear stress through both conditional average and correlation analyses. Although concurring with the general concept of amplitude modulation, Agostini and Leschziner (2014) mentioned that the modulation effect on the positive and negative sides of the low-frequency velocity fluctuation is asymmetric.

Ganapathisubramani et al. (2012) conceptualized the frequency modulation effect between the large and small-scale fluctuations. They noticed that the numbers of the local minimum and maximum of the small-scale velocity fluctuations increase during the positive large-scale velocity fluctuations and decrease within the negative part. However, they noted that such an effect is limited under the lower bound of the log region. Baars et al. (2015) refined this study by using wavelet analysis to decompose the velocity fluctuation into the temporal-spectral domain. They reported that the degree of frequency modulation could extend to much higher wall positions agreeing with the trend of the amplitude modulation computed by Mathis et al. (2009). Baars et al. (2017a) extended their previous study in turbulent boundary layers with Reynolds number ranging from 2800 to 13400. Based on the instantaneous amplitude and frequency modulation curves, they observed the intermittent-type scale arrangement in the log region. Summarizing the superposition and modulation effect, Zhang and Chernyshenko (2016) put forward the quasi-steady quasi-homogeneous (QSQH) hypothesis which essentially suggests that the near-wall turbulence will scale with the large-scale fluctuating wall friction velocity and, hence, explains both amplitude and frequency

modulation.

Based on the unique features of these LSMs and perceived importance at high Reynolds numbers, numerous modeling methods have been proposed. Adrian and Moin (1988) utilized linear stochastic method to estimate the conditional large-scale coherent structures based on the two-point spatial correlation functions between the velocity streamwise fields. Multiple studies pursue the use of linearized Navier-Stokes equations to model and estimate the large-scale coherent motions in the fully developed turbulent shear flow (Del Álamo and Jimenez, 2006, Illingworth et al., 2018, McKeon and Sharma, 2010). Based on the observation that the large-scale fluctuations influence the near-wall turbulence via modulating and superposition effects, Marusic et al. (2010) and Mathis et al. (2011a) established a predictive Inner-Outer-Interaction (IOI) model to estimate the less coherent near-wall structures based on the large-scale streamwise velocity fluctuations measured in the log region. In the model, they linearly superimpose the scaled large-scale outer region velocity fluctuations onto the amplitude-modulated universal de-trended small-scale fluctuations to construct the near-wall streamwise velocity fluctuations. Such a method was further extended by Mathis et al. (2013) to estimate the wall-shear-stress fluctuations. Baars et al. (2016) applied spectral linear stochastic estimation between the simultaneously acquired fluctuating streamwise velocity signals acquired in the inner and log regions to refine the amplitude modulation coefficient of the IOI model proposed by Mathis et al. (2011a).

Numerous attempts have been made to relate the LSMs to a mean wall-shear-stress contribution, owing to their substantial turbulent kinetic energy contribution and Reynolds stress transportation roles. In a zonal detached eddy simulated turbulent boundary layer with momentum thickness Reynolds number up to 13650, Deck et al. (2014) decomposed the skin-friction coefficient in accordance to FIK identity and visualized that the structures with a streamwise wavelength larger than δ and 2δ contribute to over 50 percent and 35 percent of the total skin-friction, respectively. From a vorticity perspective, Hwang and Sung (2017) noticed that the vortical motions $-v\omega_z$ are modulated by the large-scale streamwise velocity fluctuations due to the dependent large-scale swirling strength. They predicted that the skin-friction drag resulting from the amplified vortical motions associated with a large-scale fluctuation greater velocity $u_l^+ > 2$ accounts for approximately 15% of the total drag. By decomposing the structures using Empirical Mode Decomposition, Agostini and Leschziner (2018) and Agostini and Leschziner (2019) studied the

connection between large-scales and the skin-friction in a DNS turbulent channel flow. Using joint PDF of the decomposed streamwise and wall-normal velocity components, they used FIK analysis to show that the contribution of large-scale structures is approximately 24%, which is approximately equal to the contribution from the near-wall scales. They also showed that the Reynolds shear stress produced from mixed scale dynamics (e.g. large-scale streamwise and small-scale wall-normal velocity fluctuations) is very limited. However, if an energy balance approach is used to decompose the skin-friction contribution, the contribution from large-scales dropped to only 8% (Agostini and Leschziner, 2019). This value matches the estimation of deGiovanetti et al. (2016), who completely removed the LSMs and VLSMs with a spanwise wavelength larger than 1.5 channel height by confining the computational domain in spanwise direction and observed these very large-scale contributes to only 5%-8% skin-friction drag.

2.3 Boundary Layer Flow Control Techniques

Controlling turbulent flow field in the desired manner and reducing the associated energy consumption benefits a wide range of engineering applications. The consequent environmental and economic profits have inspired significant efforts devoted to the study of skin-friction reduction techniques over the past century. Apart from the researchers studying fluid mechanics, turbulence control endeavours attract scholars from such varied discipline as applied mathematics, classic physics, control theory, and sensor-design (Cattafesta III and Sheplak, 2011). In terms of the control objectives, flow control can be categorized into various domains, including turbulent boundary layer control, separation control (Gad-el Hak and Bushnell, 1991), vortices control (Gursul et al., 2007), bluff body control (Choi et al., 2008), acoustic noise control (Ginevsky et al., 2004). The review in this chapter is limited exclusively to control techniques that attempt to reduce skin-friction drag in wall-bounded turbulent flows. For many engineering applications (for example, the flow of fluid through pipes and conduits, large ships, and transport aircraft) skin friction drag accounts for most of the propulsive energy expenditure. For example, turbulent skin-friction drag contributes to approximately half of the total drag force on an airplane (Gad-el Hak, 1994). Leschziner et al. (2011) estimates that a single percent reduction in skin-friction drag in the modern aviation industry could reduce approximately 3 million tonnes of fuel consumption and 9 million tonnes of

associated greenhouse gas emission in 2030 Peeters et al. (2005). Together, these factors ensure that there is an enduring effort towards turbulent boundary layer control strategies.

According to Gad-el Hak (1994), the history in controlling the boundary layer can be divided into five eras. These commenced from the boundary layer theory of Prandtl (1904), in which several experiments to control the boundary layers are introduced. With the improved understanding of the turbulent structures, boundary layer control strategies transferred from brute-forcing in the early ages to more focused attempts to eliminate/interfere with the coherent structures (Gad-el Hak, 1994). Based on the mechanism, these control strategies could be split into two branches, includes taming the near-wall turbulence and outer-scale control (Corke and Thomas, 2018). Studies in the former category are unanimously focused on tailoring the near-wall cycle by the manipulation of quasi-streamwise vortices to weaken the strength of bursting events (Choi et al., 2011a), which is widely regarded as the key to the self-sustained turbulent boundary layer (Kim et al., 1971). Researchers who study outer layer control usually do so because they believe that the near-wall turbulence production is influenced by the large-scale structures in the outer region (see the discussion in §2.2). Furthermore, based on their control inputs, turbulence control strategies are also classified into passive and active control (Cattafesta III and Sheplak, 2011). A passive control consumes no external input energy during the entire control process, whereas active control requires auxiliary energy during either observation or actuation processes. Catering to the topic of the present project - "Large-scale Active Flow Control", §2.3.1 summarizes some successful near-wall active flow control attempts and §2.3.2 surveys the existing large-scale flow control strategies. Thus, it should be noted that some successful passive inner-region control strategies, such as riblets, are not within the scope of the present study. In addition, a more detailed review is provided on the opposition control strategies in §2.3.3 , since this is closely related to the large-scale control adopted for this thesis. The literature review ends up with a review of the major obstacles that currently prevent the implementation of successful laboratory experiments into real-world engineering applications at practical Reynolds number.

2.3.1 Active Flow Control Strategy

In general, active turbulent flow control strategies are distinguished from other approaches by the required energy input from the actuators. According to the arrangement of sensors and actua-

tors, all active flow control strategies fall into three sub-groups, namely open-loop, feed-forward, and feedback control (MacMynowski and Williams, 2009). Open-loop control schemes request no observation to guide the actuation so that the actuators actively operate either uniformly or periodically under a pre-configured frequency (i.e. spanwise wall oscillation or traveling wave approaches). In comparison, both feed-forward and feedback employ at least one observer to determine the control input signal for the actuation. While the control signal generated from feed-forward control depends only on the sensors upstream of the actuators, the closed-loop system further utilizes information from the downstream observers to rectify the control input. As shown in figure 2.10, three major types of actuators are employed in a majority of active flow control strategies. These contain the fluidic jets injection, moving boundaries, and plasma actuators (Cattafesta III and Sheplak, 2011). The following content surveys the development of flow control strategies involving these three actuation styles in step, but other attempts, typically applicable in liquid flows, using electromagnetic and magneto-hydrodynamic actuators are excluded in this review.

Fluidic Actuators

Active flow control employing fluidic actuators typically perturb the boundary layers via wall blowing and suction. These actuators, ranging from zero-net mass flux synthetic jets to non-zero mass flux jets, capable of producing long-lasting strong perturbations at a relatively large bandwidth response, are arguably the most commonly applied and widely studied actuator in active control (Cattafesta III and Sheplak, 2011). Studies on such control schemes over the past several decades were initialed with the effect of Uniform Blowing (UB) and Uniform Suction (US) on the turbulent boundary layer in the early era. In the 1960s, Stevenson (1963) reported that uniform blowing is a valuable method to reduce turbulent skin-friction drag. Applying flow visualization, Antonia et al. (1988) investigated the effect of a small uniform wall suction (0.07% of the free stream velocity) via a porous boundary to the turbulent boundary layer in both wind and water tunnel facilities. As shown in 2.11, they observed that the ejecting low-speed coherent structures processed higher streamwise coherence and stability due to uniform suction, which attenuates the bursting-ejecting cycles.

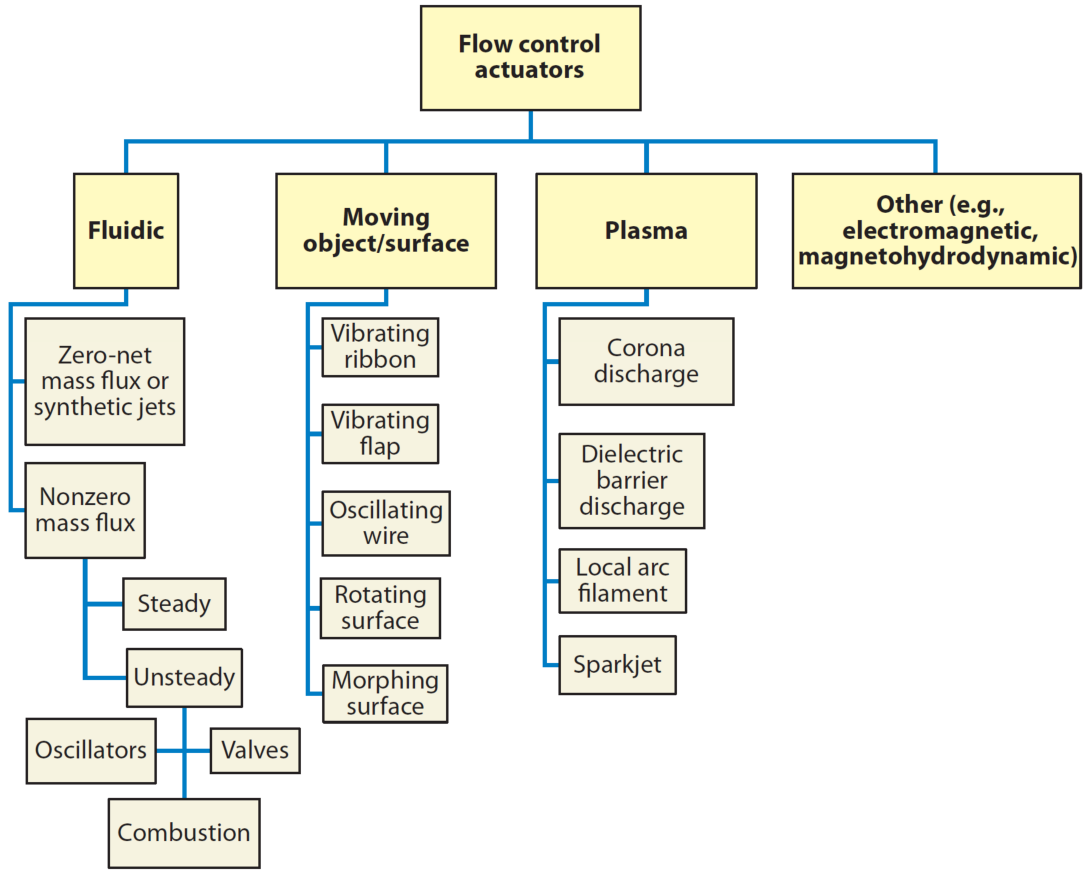

Figure 2.10: Classification of the actuation type, adapted and reproduced from Cattafesta III and Sheplak (2011)

Sumitani and Kasagi (1995) applied wall injection and suction on the top and bottom boundaries of a fully-developed DNS turbulent channel flow, respectively. They validated that US confines the turbulent production which decreases the turbulent intensity in the near-wall region. Conversely, the near-wall turbulence is energized by UB so that velocity fluctuations and Reynolds shear stress is increased by the injection. Despite the increased Reynolds shear stress which would typically be associated with a drag penalty, a reduction in turbulent skin friction is observed on the UB side. This peculiar phenomenon is further verified in DNS turbulent channel flow involving a spanwise slot to solely employ UB and US (Kim et al., 2002, Park and Choi, 1999). As shown in figure 2.12, Park and Choi (1999) indicated that, in UB cases, the near-wall quasi-streamwise vortices are pushed away from the wall by the injected fluid, which resulted in the skin-friction

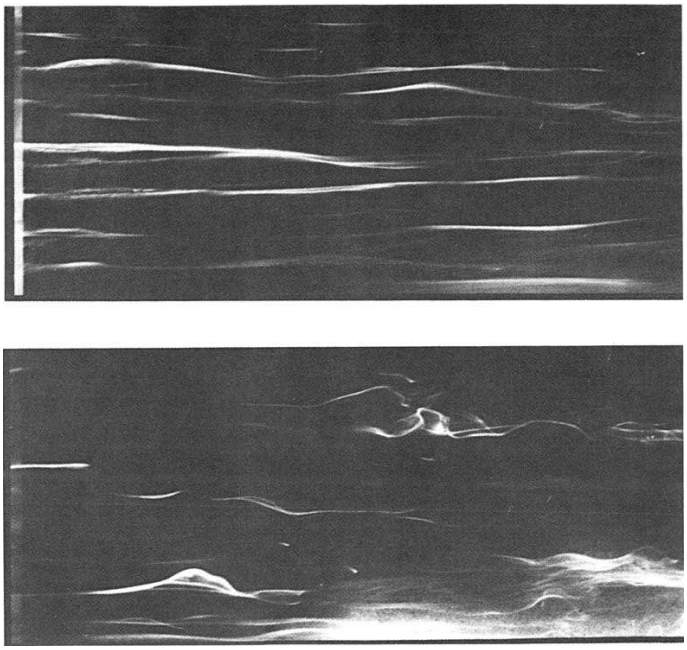

Figure 2.11: The low-speed eject motions in the wall parallel plane with suction (top) and without suction (bottom), adapted and reproduced from Antonia et al. (1988)

reduction. In contrast, US pulled the longitudinal vortices towards the wall which increased the skin-friction drag due to rising interactions between the near-wall structures and the wall. However, in UB case, the lifted streamwise vortices grow during the convection, which increased the turbulence intensity. On the other hand, the near-wall vortices drawn by uniform suction are weakened by diffusive viscous forces, which leads to a deficit in turbulence intensity. Hence, UB initially increases the wall skin-friction, but the effect reduces further downstream (and vice verse for US).

The mechanism of drag reduction in turbulent boundary layers with steady blowing is further explained by Kametani and Fukagata (2011). According to the FIK identity, they argued that the mean streamwise convection term has a most significant impact on frictional drag reduction (Fukagata et al., 2002). Thus, the streamwise velocity deficit induced by the low-speed jet flow overcomes the positive drag contribution from the Reynolds shear stress and turbulent intensity increase. In addition, Noguchi et al. (2016) revisited steady suction control in a Reynolds Averaged Navier Stokes (RANS) simulated turbulent boundary layer at $\mathrm{Re}_\tau \approx 40000$. They reported that US successfully delays the turbulent transition of the boundary layer and, in turn, gained a consider-

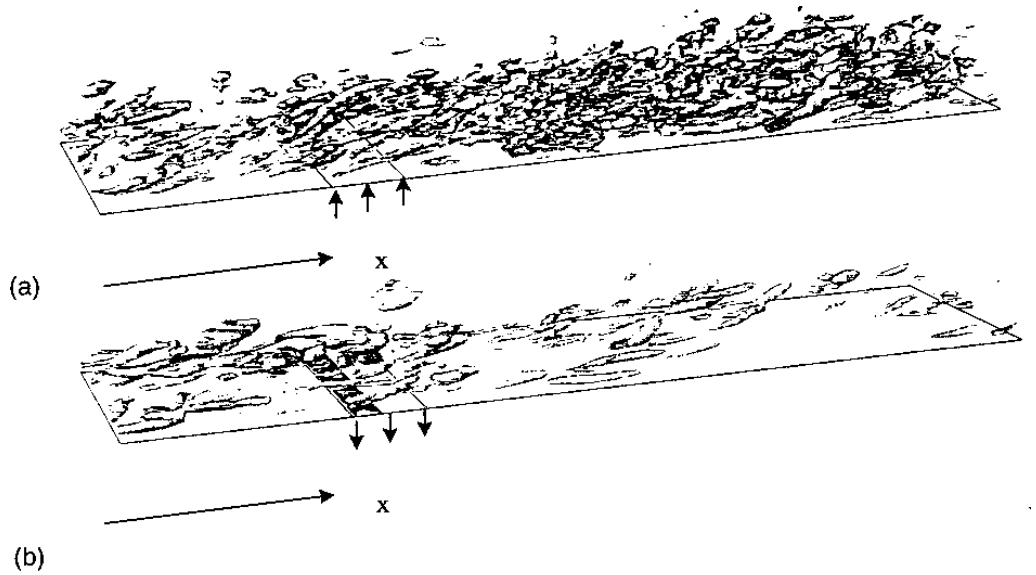

Figure 2.12: Iso-surface of the near-wall quasi-streamwise vortices in the turbulent boundary layers due to (a) UB and (b) US, adapted and reproduced from Park and Choi (1999)

able 44% global skin friction coefficient. Most recently, Kühnen et al. (2018) utilized both radial and wall-parallel jets to consistently perturb a turbulent pipe flow and achieved friction losses by as much as 90% both computationally and experimentally. They indicated the strong forcing produced by both radial and wall-normal jets appropriately distort the mean velocity profile of the turbulent pipe flow, which leads to a sudden collapse of turbulence production and re-laminarized the flow at approximately 40 pipe diameters downstream of the actuators. They also demonstrated that if other forcing strategies are able to tailor the mean velocity profile in the same manner, a similar friction-reduction can be achieved. However, it should be noted that the control strategies of Noguchi et al. (2016) and Kühnen et al. (2018) are mostly related to the effect of transition delay, which only effective at relatively low Reynolds number (i.e. barely turbulent) boundary layers.

The uniform blowing/suction perturbs the turbulent boundary layer with a steady mass flux, while these fluidic jets can be also configured to an unsteady mode, including periodic and selective control. Specifically, periodic actuation is accomplished by spatially or temporally injecting air into the turbulent boundary layer at a certain wavelength or frequency. Tardu (1998) explored a periodic blowing/suction through a streamwise series of six spanwise rectangular slots to manip-

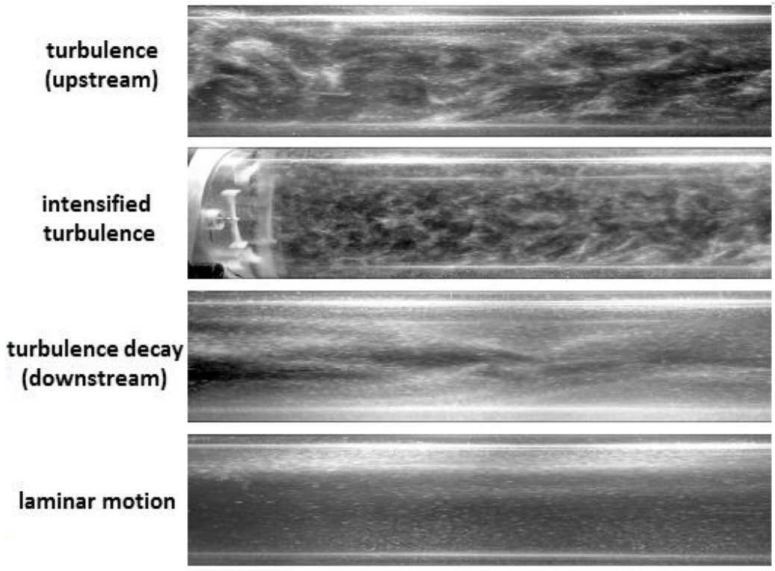

Figure 2.13: Visulized flow field upstream and downstream of the radial jets. Adapted and reproduced from Kühnen et al. (2018)

ulate the near-wall turbulent characteristics. These slots, acting as synthetic jets in the temporal domain, are arranged to perform blowing and suction alternatively at any given instant in the spatial domain. Tardu (1998) concluded that the unsteady blowing/suction successfully breaks down the vorticity generation mechanism, whereas it failed to tailor the quadrant motions associated with the near-wall coherent motions. Tardu and Doche (2009) extended the previous research on periodic blowing/suction by considering an antisymmetric temporal periodic blowing strategy. The periodic jet exit velocity was designed to have a rapid acceleration and a slower deceleration phase. Over 50% skin-friction drag reduction is claimed, which 40% more effective than UB. They argued that this is because the selected period was optimized to prevent the spanwise counter-rotating vortices induced by uniform blowing, which reduced the corresponding Reynolds shear stress.

In terms of spatial periodicity, Quadrio et al. (2007) examined a DNS turbulent channel flow controlled by a steady wall-transpiration, with the transpiration strength sinusoidally distributed in the streamwise direction at different wavelengths. The skin-friction drag is increased for long wavelengths while the shorter wavelengths reduce the drag. The wavelengths achieving these two opposite effects are shown to be separated by the wavelength comparable to the near-wall bursting

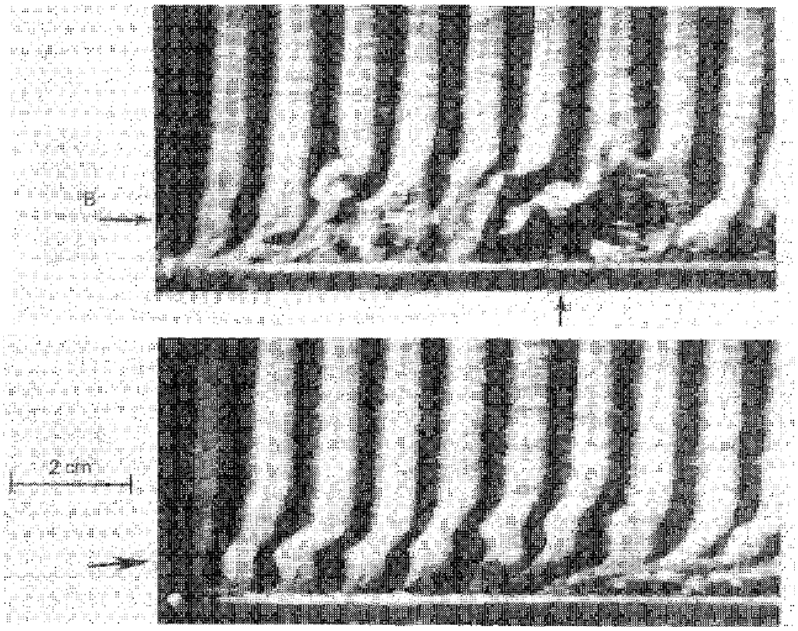

Figure 2.14: Artificially generated bursting events in (a) canonical boundary layer, (b) boundary layer with selective suction, adapted and reproduced from Gad-el Hak and Hussain (1986)

cycle. Quadrio et al. (2007) noticed that any net drag reduction resulted from the balance between the drag reduction obtained from the controlled near-wall turbulence due to the injected flow and the pressure drag created by the transpiration, and the former overwhelms the latter at shorter wavelengths. Eventually, by a parametric study, the optimized sinusoidal transpiration provides over 13% drag reduction. Kametani et al. (2016), on the other hand, compared the boundary layer control effect between spatially periodic blowing and UB with identical total mass flux. To determine the effect of the spatial arrangement of the jets on the control outcome, they separated the jets into an increasing amount of spanwise slots with shorter streamwise offsets. It is reported that the skin-friction oscillated due to the periodic blowing section, which follows the pattern of the jet locations in the streamwise direction. However, regarding the net total energy saving, periodic blowing stands at almost the same level as US (with net energy saving dropping from 18% for UB to 16% for periodic blowing).

While the majority of uniform and periodic blowing/suction employs no observation efforts, selective schemes activate either blowing or suction to intervene in a specific group of fluid structures (usually, the sweep-burst near-wall cycles) within the turbulent boundary layers. Inspired

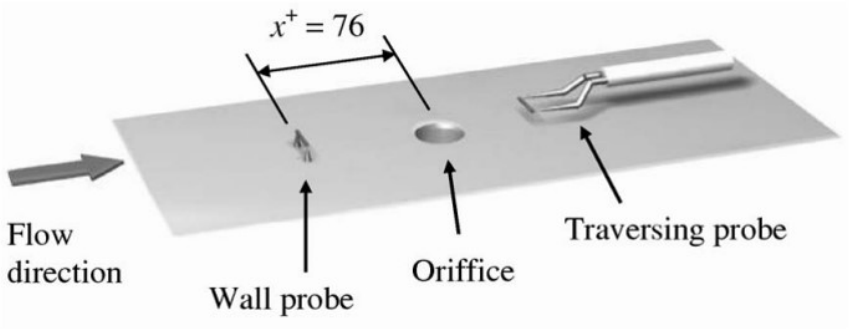

Figure 2.15: Schematic diagram of the experimental set-up for the real-time opposing control conducted by Rebbeck and Choi (2006)

by the correlation between the Reynolds shear stress production and the quasi-streamwise near-wall vortices, Gad-el Hak and Blackwelder (1989) first examined the possibility of eliminating the near-wall burst events in the boundary layer via applying selective suction on these events using a streamwise suction slot. In their experiments, VITA techniques are used on the hot-film signals to observe the burst events which were artificially generated by two impulsive suction holes in a laminar boundary layer (Gad-el Hak and Hussain, 1986). In figure 2.14, they reported the turbulence production due to the burst-ejection motions is reduced by approximately 80% with a selective wall suction The potential to combine selective blowing and suction is investigated by Choi et al. (1994). In a DNS channel flow, they applied wall blowing and suction to suppress the coherent motions in the near-wall region. Specifically, positive and negative wall-normal velocity inputs are actively imposed on the flow field to counteract the sweep (moving towards the wall) and ejection (moving away from the wall) motions detected at a "detection plane" located at $z^+ = 10$. The control achieved 20% drag reduction by purely controlling the wall-normal velocity components to modify the near-wall coherent motions. At the same time, by affecting the spanwise velocity components accompanying the near-wall structures in the same manner, the drag reduction increased to 30%. Choi et al. (1994) noticed that such control schemes are impractical in real applications due to zero time delay sensing and reported that the optimized drag reduction under a sensible detection criterion would drop to only 6%.

Rebbeck and Choi (2006) implemented the control strategy proposed by Choi et al. (1994) in a wind-tunnel turbulent boundary layer at $\mathrm{Re}_\theta \approx 800$. They used a protruding wall-probe 76 wall units upstream of a circular jet as shown in figure 2.15. The injections were performed only

when the upstream hot-wire probe detected sweep events (i.e. the running standard deviation of the velocity fluctuation exceeds a certain threshold). Rebbeck and Choi (2006) indicated that the opposition wall-normal velocity control constructed a "virtual wall" in the middle of the detection point and the wall, which successfully prevents the sweep events from reaching the wall and imparting a high friction footprint. They further claimed that the low streamwise velocity fluid injected by the jets would be beneficial to the effectiveness of opposition control since the reduction of streamwise momentum also reduces the mean velocity gradient at the wall. However, it was also realized that the low-speed fluid from the jet was overtaken by the targeted event due to the difference in convection velocity, which limited the streamwise coverage of the opposition control. The study of Choi et al. (1994) and the following experiments of Rebbeck and Choi (2006) stimulated the research on opposition control strategies, which are specifically reviewed in §2.3.3. For example, instead of targeting at the high-speed sweep events, Kang et al. (2008) positioned a nozzle outside of the boundary layer to generate a local downward jet towards the wall which was activated whenever an ejection motion associated with the quasi-streamwise near-wall vortices was detected. The measurement result is off-line post-processed and they predicted that if hairpin vortices were hit by the jet correctly, the control has the possibility to reduce the skin-friction drag.

Moving Surfaces

Flow control via moving surfaces involves the wall-deformation in both wall-normal and spanwise directions. Specifically, the spanwise deformation controls the turbulent boundary layer via in-plane spanwise wall oscillation with a pre-determined viscous scaled frequency and amplitude. Initiated in the 1990s, the flow control schemes using spanwise moving walls are derived from the knowledge that a sudden spanwise pressure gradient in the turbulent boundary layer suppresses the near-wall turbulent production mechanism (Moin et al., 1990). Jung et al. (1992) investigated the wall-oscillation turbulence control by through a DNS of turbulent channel flow with both upper and lower boundaries vibrating at periods from 25 to 500 viscous time steps. By comparing with a canonical turbulent channel flow, the occurrence frequency of bursting events and spanwise coherence of near-wall structures were both reduced in the controlled boundary layers. Their optimized case was reported at a vibration period of 100 viscous time units, in which the streamwise Reynolds shear stress ($-\overline{uw^+}$) reduced by 40% without exciting the spanwise Reynolds shear

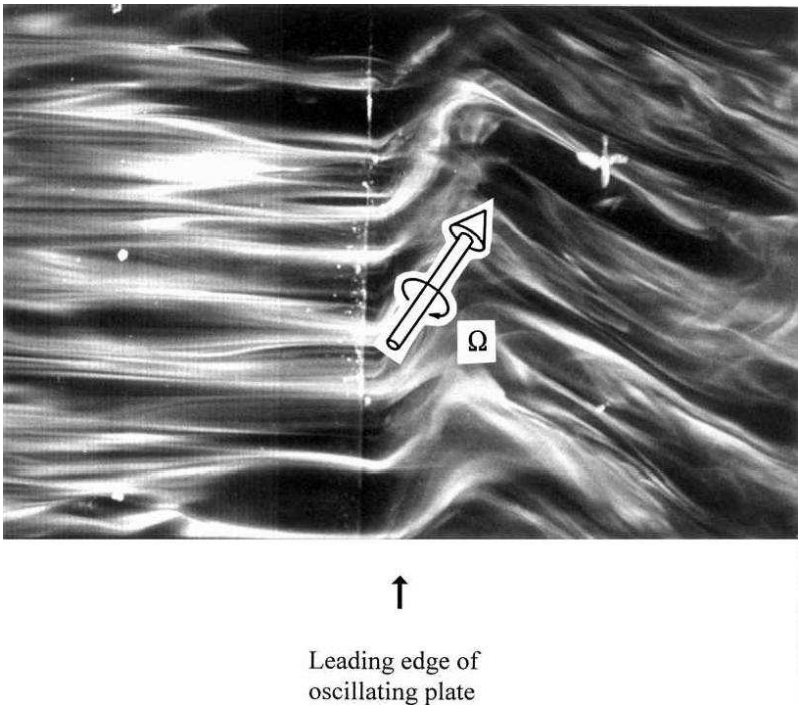

Figure 2.16: Flow visualization of the turbulent boundary layer controlled by the spanwise oscillation at the leading edge of the plate, which is reproduced from Choi et al. (1998).

stress ($-\overline{vw^+}$). At the same time, the wall-normal and spanwise velocity fluctuations are significantly decreased by 35% and 30%. However, they suggested that the effect of oscillation remains only at the region immediately adjacent to the oscillating walls. This simulation study is experimentally repeated by Trujillo et al. (1997), who used a steady lateral-oscillated wall to record a maximum 25% drag reduction measured by hot-film sensors. These results are confirmed in multiple succeeding studies (Choi and Clayton, 2001, Choi et al., 1998, Dhanak and Si, 1999).

Through hot-wire anemometry and flow visualization measurements in a wind tunnel, Choi et al. (1998) noted that, at a slightly higher oscillation frequency, the optimized local skin-friction reduction reached 45% at five boundary layer thicknesses downstream of the leading edge of wall-oscillation. They argued that the stokes layers due to the periodic spanwise oscillation created spanwise vortices, which decrease the mean velocity gradient by extending the local viscous sublayer. In addition, the spanwise wall-oscillation re-orients the streamwise vortices (figure 2.16) and attenuates the streamwise turbulence intensity. In the same year, Choi and Graham (1998) adapted this control strategy to a pipe flow by oscillating the pipe wall in the azimuthal direction.

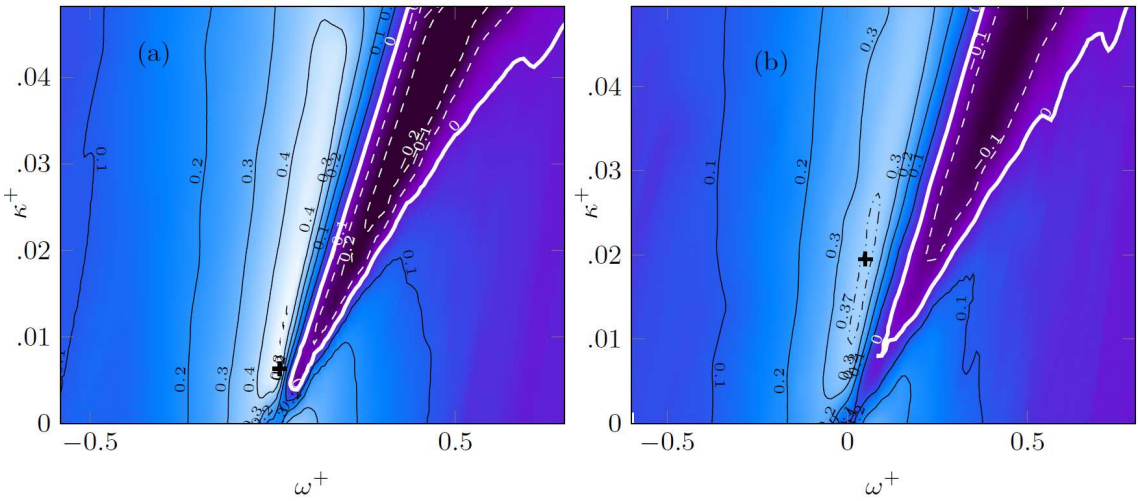

Figure 2.17: Iso-contour of skin-friction drag reduction as a function of spatial wavelength of streamwise travelling wave and temporal frequency of spanwise oscillation at (a) $\mathrm{Re}_\tau = 200$ and (b) $\mathrm{Re}_\tau = 1000$, adapted and reproduced from Gatti and Quadrio (2016)

They also observed a significant reduction in spanwise vorticity and streamwise turbulence intensity, along with a 25% skin-friction drag reduction. Summarizing the previous works, Choi and Clayton (2001) attributed the decrease in skin-friction to the manipulation of the mean velocity profile. Burst events are weakened since the longitudinal vortices are stretched in the spanwise direction over the oscillating walls, which results in a lower skin-friction. Though the percentage skin-friction drag reduction achieved via spanwise wall oscillation is promising, activation of the oscillating wall requires a large amount of power input which leads to net-energy savings that are much less than the stated drag reductions (Baron and Quadrio, 1995). In a DNS of turbulent channel flow, Quadrio and Ricco (2004) studied the dependency of the drag reduction on oscillation frequency and reported that the benefits of drag reduction outweigh the energy expended to oscillate the wall by 7.3% at the optimized condition.

Motivated by the idea remove the need for wall oscillation from the spanwise oscillation technique, Quadrio et al. (2009) introduced a streamwise spatial-traveling sinusoidal wave modulating the spanwise oscillation velocity, which is governed by $v_w = Asin(\kappa x - \omega t)$. Here, V_w is the spanwise velocity at a given time and streamwise location, with the key parameters A, κ, and ω notating the amplitude of oscillation, the wavenumber of streamwise waves, and the angular frequency of spanwise oscillation, respectively. Quadrio et al. (2009) investigated the effect of

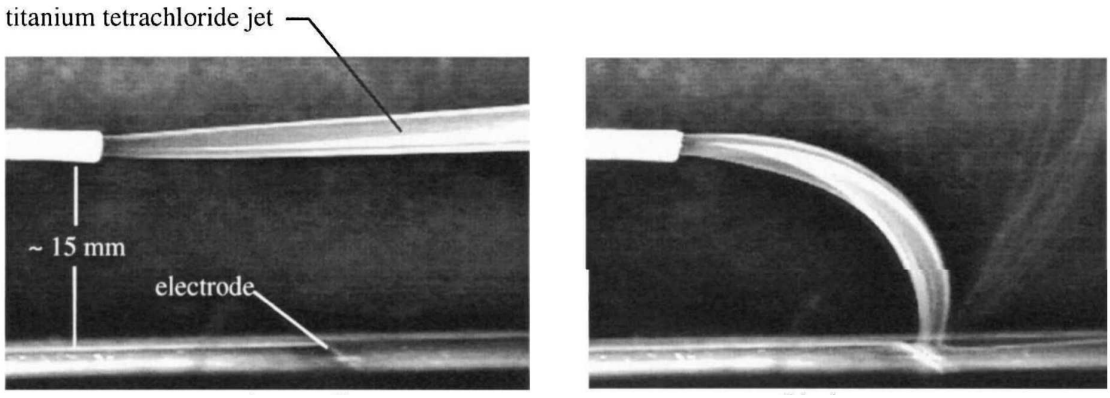

Figure 2.18: Flow visualization of titanium tetrachloride jet flow in a flat-plate boundary layer (a) without and (b) with plasma on, adapted and reproduced from Roth et al. (2000)

the wavenumber (κ) and temporal frequency (ω) of the oscillation on skin-friction reduction and observed a 52% drag reduction under streamwise spatial forcing with amplitude and streamwise wavelength at 20 and 1250 wall units, respectively. A more comprehensive parametric space study on such a control strategy was carried out by Gatti and Quadrio (2016) to examine the effects of spatial wavelength and temporal frequency on the drag reduction. Figure 2.17 summarizes the iso-contour of drag reduction at two different Reynolds number ($\mathrm{Re}_\tau = 200$ and 1000) with varying κ and ω. They showed that if the temporal frequency was located in the backward-traveling wave regime, a sudden increase of the skin-friction drag was visualized in both cases. The maximum net power saving reaches 31%, but this value is found to exponentially deteriorate with the increased Reynolds number. However, using the assumption that the skin-friction reduction is related to the vertical shift of the logarithmic region, they estimate the maximum drag reduction employing the streamwise traveling spanwise oscillation wall could still reach 23% at $\mathrm{Re}_\tau = 10^5$. In contrast, the other category of the moving surfaces, wall deformation in the wall-normal direction, often acts as a body forcing to oppose certain flow motions (similar to opposition control, which will be reviewed in §2.3.3.

Plasma Actuators

In the recent decade, Dielectric Barrier Discharge (DBD) plasma actuators have received considerable attention in flow control strategies because of their outstanding features. These purely

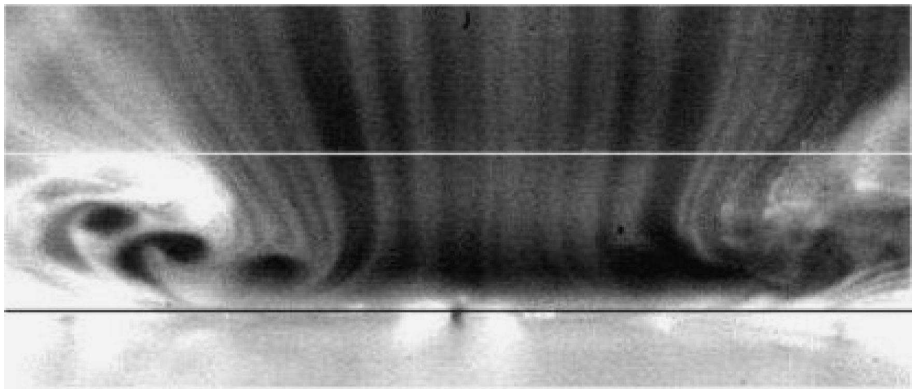

Figure 2.19: Smoke wire visualization of the spanwise ocillation induced by the DBD plasma actuator set-up. adapted and reproduced from Jukes et al. (2006)

electrical and low weight actuators contain no moving components and can be non-intrusively adhered to the surface boundary (Corke et al., 2010). During operation, DBD plasma directly transfers voltage input to the desired body forces onto the flow field. In specific, DBD plasma actuators consist of two electrodes connected by a high voltage supply and separated by the dielectric layer. The overall thickness of the actuator is approximately 1mm, with the top electrode exposed directly to the flow field and the other covered by the dielectric layer. The effect of plasma actuators on the zero-pressure gradient boundary layers was first investigated by Roth et al. (2000), who used a glass-epoxy board to separate an array of electrodes to manipulate the boundary layer with different free-stream velocities. Using flow visualization technique, they observed that the electrode attracts the titanium tetra-chloride jet flow injected aligning parallel to the wall (figure 2.18). They concluded that the behavior of plasma actuators is similar to that of the wall-normal jets, which provides a wall-normal forcing on the crossflow using a reversed polarity in figure 2.18.

Multiple studies reveal that plasma actuators have convincing performance in stabilizing the laminar boundary layer and delaying the laminar-to-turbulent transition (Joussot et al., 2010, Magnier et al., 2009, Seraudie et al., 2011). Wilkinson (2003) first investigated the possibility of using spanwise DBD plasma pairs to generate spanwise oscillation in the same manner as oscillating walls. Jukes et al. (2006) extended the study and used two sets of asymmetric plasma actuators to successfully create the spanwise oscillating layers without the accompanying wall-normal velocity components, as shown in figure 2.19. Jukes et al. (2006) further conducted an experimental

study on turbulent skin-friction reduction via plasma actuators. With the optimized combination of the oscillation frequency and the actuation strength, the maximum drag reduction reaches 45% based on the near-wall velocity gradients acquired by hot-wire and cold-wire anemometry. In a later report, they claimed that the plasma produces spanwise alternating jets, which lead to negative spanwise vorticity and consequently a lower mean velocity gradient near the wall (Choi et al., 2011b). Whalley and Choi (2014) further examine the spanwise traveling waves via the DBD plasma actuators and observed that the spanwise traveling waves group the near-wall coherent vortices to a signal streamwise vortex, which transports the low-speed fluid to a larger low-speed band. Such behaviour is similar to the effect of spanwise traveling wall oscillation on the turbulent boundary layer as reported by Du and Karniadakis (2000). Most recently, Duong et al. (2019) configured a spanwise array of pulsed plasma actuators to generate a single direction spanwise blowing. They reported the control effect is confined near the wall by preventing the lift-up of low-speed streaks. With the optimized exposed electrode spacing ($\lambda_y^+ = 300$), the drag reduction could reach 68% in a low-speed flow environment.

2.3.2 Large-scale Flow Control Strategies

Previously discussed boundary layer control strategies manipulate the near-wall coherent structures to affect the near-wall turbulent regeneration cycles and, eventually, influence the outer-region structures as this effect percolates outwards from the wall (this is very much a 'bottom-up' view). In contrast, Praturi and Brodkey (1978) suggested that the outer-region transverse vortices resulted in the entrainment of free-stream flow into the boundary layer and initiated the regeneration of near-wall cycles (a 'top-down' model). Gad-el Hak (1996) suggested that the distribution of Reynolds shear stress within a turbulence boundary layer concentrated in a relatively small area where vortex packets reside. Furthermore, recent studies in high Reynolds number turbulent boundary layer have revealed the interaction between the large-scale structures in the outer region and the near-wall turbulence (discussed in §2.2). Therefore, in contrast to the 'bottom-up' near-wall control strategies, in this section, we review the distinct category of flow control strategies that aim to tame the turbulence through manipulating the outer-region large-scale motions through the 'top-down' effect.

LEBUs

A LEBU device aims, as its name suggests, to break the large-scale eddies in the outer region in turbulent boundary layers for skin-friction drag reduction. These LEBU devices mainly contain systems of plates placed at specific wall-normal positions aligning with the flow direction. The first study of LEBU can be tracked to the work of Loehrke and Nagib (1972), who used a set of screens, grids, and honeycombs to decrease the free-stream turbulence, but no skin-friction drag reduction is calculated. Yajnik and Acharya (1977) continued the effect of these honeycomb meshgrids on the boundary layer control. Though a 50% reduction of the skin-friction coefficient is obtained downstream of the screens, the pressure drag reaches four times the total skin friction drag of the uncontrolled boundary layers.

To pursue an optimized balance between the skin-friction and pressure drag, later studies employed LEBU systems with simpler geometries (Corke et al., 1981, Hefner et al., 1983, Zheng and Longmire, 2014). The skin-friction reduction attained from these devices generally reached a streamwise extension over 150 boundary layer thicknesses. Corke et al. (1981) utilized four wall-parallel panels with closer spacing near the wall (shown in figure 2.20) and observed a deficit in streamwise velocity fluctuation for wall-normal position smaller than 0.1δ. In figure 2.20(b,c), the large-scale structures in the outer part of the boundary layer are completely suppressed by the four-plate LEBU. Their results indicated that the reduction of the turbulence intensity was related to a decreased frequency of burst events caused by the suppressed large-scale structures. In this study, they also tested two other LEBU systems containing single and double plate configurations. The single plate device was located at a wall-normal position of 0.6δ and the double plate device (tandem device) featured one additional added flat plate at 0.2δ. While the double plate system showed the same level of effectiveness in the suppression of outer-layer structures, the control efficacy of the single-layer device deteriorated significantly. They reported the two-plate LEBU system leads to a 19% reduction in the streamwise velocity fluctuation and a 17% reduction of the bursting frequency. Corke et al. (1982) extended their study investigated a different configuration of two-plate LEBU arranged in series 8δ apart in the streamwise direction and at a wall-normal distance of 0.8δ in the turbulence boundary layer. By using such a device, they reported a total skin-friction drag-reduction of 22% and explained the selection of the streamwise separation distance as being matched to the life span of the large-scale structures, which results in a better

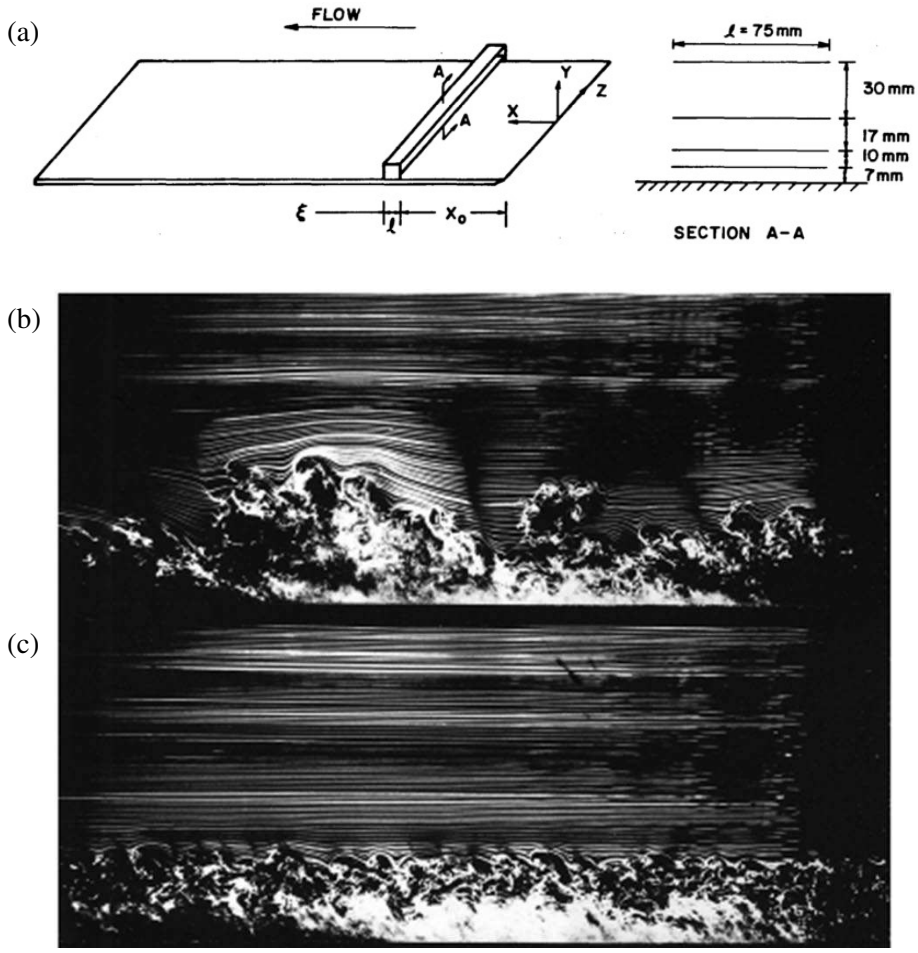

Figure 2.20: (a) A schematic diagram of the experimental set-up for the LEBUs employed by Corke et al. (1981). Visualized outerscale structures in the boundary layers (b) without and (c) with LEBU. Adapted and reproduced from Corke et al. (1981)

suppression effect on these large eddies.

Savill and Mumford (1988) conducted a series of experiments to measure the skin-friction drag with various configurations of flat plates. They added a second drag reduction mechanism to the traditional large-eddies suppression perspective. The interactions between the vortices in the wake of LEBU devices and the near-wall vortices counteracted each other and, eventually, reduced the turbulence fluctuations near the wall. The local skin-friction reported by Walsh and Anders (1989) using a different LEBU configuration reaches approximately 10%. In a recent study, Chin et al. (2017) investigated the skin-friction drag reduction in an LES of wall-bounded turbulent flow with a single flat plate LEBU, reporting a skin-friction reduction equivalent to the single plate con-

figuration of Corke et al. (1981), persisting to 180 boundary layer thicknesses downstream of the device with a maximum drag reduction of 12%. However, in terms of total drag reduction, Sahlin et al. (1988) and Anders (1990) both noted limited potential in obtaining a net drag reduction with implementation of LEBU systems in high Reynolds number turbulent boundary layers. Similar results were concluded by Chin et al. (2017), who disappointingly observed no total drag reduction in their simulation results. However, to date, LEBU is one of the few examples of an attempt to directly force the large-scale structures away from the near-wall region.

Large-scale Vortex Flow

Another large-scale control strategy involves using vortical flow (i.e. wall-normal jets) to artificially introduce large-scale streamwise vortices into the crossflow to reduce the skin-friction drag, which was first simulated by Schoppa and Hussain (1998) in a DNS of turbulent channel flow at friction Reynolds number of approximately 180. They investigated two different forcing schemes including counter-rotating streamwise vortices and spanwise colliding jets mounted on the wall and reported a skin-friction reduction of 20% and 50% respectively. Contrary to the proposed mechanism for LEBU devices, Schoppa and Hussain (1998) suggested that the large-scale vortical flow achieves skin-friction reduction via forcing the near-wall streaks together into one large stable streak to interrupt the regenerative cycle of the near-wall turbulence. Consequently, the strength of quasi-streamwise vortices near the wall is decayed and the underlying low-speed streaks become more stable, which leads to the observed large skin-friction reduction. In addition, Schoppa and Hussain (1998) announced that at higher forcing magnitude, an increased skin-friction was detected. Hence, they concluded that the strength of these vortical flow must be precisely tailored to counteract the pairing longitudinal vortices and stabilize the near-wall streaks.

Iuso et al. (2002) carried out a large-scale flow control experiment in a fully developed turbulent channel flow tunnel at $Re_\tau = 180$. By utilizing an array of transversal inclined vortex generator jets, Iuso et al. (2002) verified the results of Schoppa and Hussain (1998) and observed substantial skin-friction reduction of approximately 30%. At the same time, the fluctuation of the skin-friction was halved. In line with the simulation results of Schoppa and Hussain (1998), the vortex generator jets thickened the viscous sublayer of the boundary layer, increased the coherence of the longitudinal vortices, and eventually reduced the frequency and strength of the

near-wall burst events. However, a recent study carried out by Canton et al. (2016) suggested that the effectiveness of the large-scale vortical flow control will deteriorate significantly for a higher Reynolds number. After a thorough investigation on the control parameters suggested by Schoppa and Hussain (1998), Canton et al. (2016) attributed the success of Schoppa and Hussain (1998) to the relatively low Reynolds number flow, at which the turbulent boundary layer still possesses its transient nature. Yao et al. (2018) further elaborated that the performance degradation observed by Canton et al. (2016) is because the channel half-height is selected as the center of the imposed large-scale vortical control. They demonstrated that if by carefully confining the spanwise vortical forcing to the viscous sublayer, the skin-friction drag 14.5% is still achievable at $Re_\tau = 550$. Based on the observation of Yao et al. (2018), Thomas et al. (2019) extended the studies of Schoppa and Hussain (1998) by experimentally utilizing a spanwise array of pulsed-DC DBD plasma actuators to intervene the automous near-wall turbulence production mechanism in turbulent boundary layers with Mach number ranging between 0.05 and 0.15 and observed a drag reduction over 70%. They further estimated that the drag reduction could reach 45% with a positive net energy saving in the controlled boundary layers at a Mach number of 0.5. Most recently, Duong et al. (2021) explained the mechanism of drag reduction associated with this DBD control as a stabilization of the transient streak growth associated with the autonomous near-wall turbulence generation cycle proposed by Schoppa and Hussain (2002).

2.3.3 Opposition Control Strategy

Opposition boundary layer control generally involves counteracting the inherent features (Q2 and Q4 motions) of the targeting coherent structures, which exemplified as the study of Choi et al. (1994). As shown in figure 2.21, they investigated two different opposition control strategies in DNS of turbulent channel flow. The first one applies a positive wall-normal forcing on the wall-ward motions (w-control) associated with the near-wall streamwise vortices, while the second one uses spanwise forcing to control the $+v$ components of the streamwise vortices (v-control). Through breaking the sweep motions and suppressing the regenerative mechanism of the near-wall vortices, 20% and 30%skin-friction drag reduction are achieved for w- and v-control, respectively.Hammond et al. (1998) extended the study and reported that the drag reduction of $w-control$ could be improved to 25% via optimizing the detection plane to $z^+ = 15$. Rebbeck

and Choi (2006) carried out an experimental investigation on the opposition control concept of Choi et al. (1994) by using wall-normal blowing and suction to fulfill the selective forcing tasks. The near-wall streamwise vortices are observed by a hot-wire probe protruded from the wall at $x^+ = 76$ upstream of the actuator. Although no skin-friction drag reduction is reported, they observed an apparent streamwise turbulent energy reduction downstream of the control. In other flow geometries, Fukagata and Kasagi (2003) performed the opposition control in a turbulent pipe flow and visualized that the control effect lasts for more than 10 pipe radius downstream of the actuation. Stroh et al. (2015) compared the opposition control in the wall-bounded turbulent boundary layer and turbulent channel flow. They observed the same level of skin-friction drag reduction but the underpinning dynamics that contribute to the drag reduction in both cases are different. Via FIK decomposition of the skin friction, they reported that a majority of the skin-friction reduction in turbulent channel flow is contributed by the decreased Reynolds shear stress, modification of the spatial flow development becomes the dominating factor in the wall-bounded flow. This result is independently verified by Xia et al. (2015), who observed a maximum of 20% drag reduction in a DNS spatially developing turbulent boundary layer.

Apart from the fluidic jet flow, the feasibility of opposition control is also examined using other actuators. One of these attempts utilized selective wall deformation against the near-wall coherent structures in the wall-normal direction. Carlson and Lumley (1996) introduced an opposition control to a numerically simulated minimal turbulent channel flow, which consists of a pair of near-wall coherent events (one high and one low). They attempted to reduce the skin-friction by actively employing a Gaussian bump with a maximum height of twelve wall units onto different structures. When the wall is raised below a low-speed ejection motion, the nearby high-speed events spread to a larger domain and increased the drag. Conversely, activating the control beneath the low-speed sweep motion, will enlarge the adjacent low-speed structures and, hence, results in a drag reduction. In advance, Kang and Choi (2000) utilized a local wall deformation to counteract the near-wall streamwise vortices, in a manner similar to that of Choi et al. (1994). Such actuation breaks the near-wall streamwise vortices which significantly weakens the turbulence intensity and results in a 13%-17% skin-friction drag reduction. The associated skin-friction mechanism matches that of Choi et al. (1994), which breaks the quasi-streamwise vortices and weakens the turbulence intensity near the wall. Yoshino et al. (2008) implements the idea of Kang and Choi

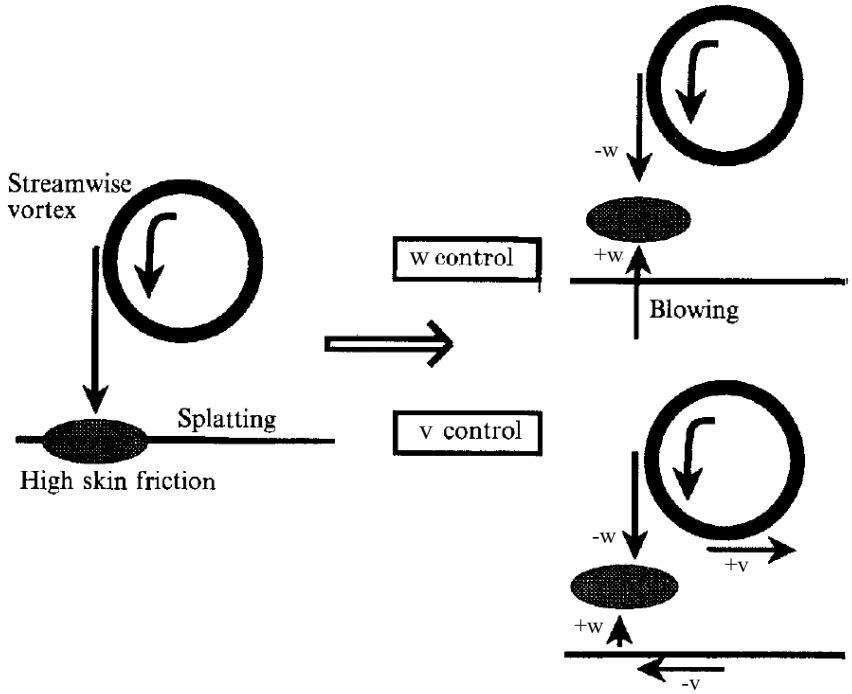

Figure 2.21: The wall-normal and spanwise schematic of the near-wall vortices and the corresponding opposition control via spanwise and wall-normal forcing. Modified based on Choi et al. (1994)

(2000) into a fully developed turbulent channel flow with $\mathrm{Re}_\tau = 300$. They employed four rows of hot-film sensors and three rows of wall-deformations magnetic alternatively placed in spanwise direction to perturb the estimated high-friction events through feedback control. However, the resulting skin-friction reduction was only 6%.

Using LES simulation, Chang et al. (2002) investigated the Reynolds dependence of the opposition boundary layer control strategy. They reported that, due to the viscous effects, skin-friction drag reduction attained from the opposition control deteriorates from 30% at $\mathrm{Re}_\tau = 100$ to 19% at $\mathrm{Re}_\tau = 720$. Thus, multiple studies attempted to improve the effectiveness of the opposition control at a higher Reynolds number. Pamiès et al. (2007) changed the classical opposition control to a one-sided opposition control, such that the actuators only blow away the high-speed sweep motions. In a boundary layer at $\mathrm{Re}_\tau = 960$, they announced a skin-friction drag reduction over 60% is achieved from their modification. In contrast, other improvements mainly focus on optimizing the sensor location and detection accuracy. For example, Luhar et al. (2014) applied the opposition

control by tuning the gain of the most energetic turbulent modes decomposed from the resolvent analysis. They showed that the low-speed modes near the wall are suppressed by the control. However, at higher Reynolds numbers, the high-speed modes become much more energetic and tend to detach from the wall. They concluded that a better determination of the control modes and sensor location is capable to enhance the control effectiveness. Extending the picture, Lee (2015) conducted a comprehensive study on the sensor location and measured a maximum drag reduction of 29% when the sensor is placed at 25.2 wall units upstream of the actuator with a wall-normal height of 20 wall units. Toedtli et al. (2019) carried out a varying-phase opposition control on low-order resolvent modeled flow structures with a varying phase delay. A drag reduction of 21% is reported, which indicated the potential of using the resolvent analysis to simplify the control design process.

Similarly, opposition control can be also occupied in large-scale control. Rathnasingham and Breuer (2003) attempted to utilize a rectangular slotted synthetic jet to counteract the near-wall large-scale motions in a turbulent boundary layer at $\mathrm{Re}_\theta = 1960$. The real-time large-scale fluctuation near the wall was predicted by a linear model between the streamwise velocity fluctuations at the detecting sensors and large-scale fluctuation above the actuators. They announced that by counteracting the predicted near-wall large-scale velocity fluctuation, they managed to obtain a 7% reduction in skin-friction drag and a 30% attenuation on turbulence fluctuation. It is first proposed by Marusic et al. (2014) that, due to the interactions between the large-scale structures between the inner- and outer-regions Marusic et al. (2010), one can apply an opposition control to the very large-scale structures in the log region to control a high Reynolds number turbulent boundary layer in real-time. Abbassi et al. (2017) conducted a real-time opposition control in a high Reynolds number turbulent boundary layer at $Re_\tau = 14400$ and achieved a maximum local skin-friction reduction of 3.2% at 1.7 downstream of a spanwise of rectangular jets. They noticed that if the opposition control is inverted to a reinforcing control, such that the jets will be activated while a low-velocity large-scale event has been detected, they were still able to measure a maximum local skin-friction reduction up to 1.2%. They contributed this to a combination of two mechanisms. First, while the low streamwise velocity jets injected into the boundary layer created an area of low-streamwise momentum. Second, by activating the jets against the high-speed large-scale structures, they managed to manipulate the large-scale structures inhibited in

the log region and diminished 30% of their associated energy. While the former mechanism created a skin-friction reduction for all their examined control schemes, the attenuation of large-scale energy lead to the difference between the opposition and reinforcing controls.

2.3.4 Challenges in Practical Implementations

All the boundary layer control strategies introduced above achieved a certain degree of local skin-friction drag reduction, in numerical simulations and laboratory experiments, often at Reynolds numbers that were much lower than those of a typical application. Moreover, in terms of the net power saving, the pressure drag induced by the passive device and the input energy of the active actuators can often exceed the energy-saving from the viscous drag reduction (Corke and Thomas, 2018). Thus, the practical implementation of these strategies encounters various challenges. One of the very few successes of in-flight drag reduction utilized riblet surfaces on the fuselage of an airplane and achieved a total 2%-3% drag reduction energy-saving (McLean et al., 1987). The difficulties that currently prevent the widespread uptake of boundary layer control strategies in real-world applications ranging from the Reynolds number dependency of control strategies to the huge computational requirements required for real-time high-frequency flow estimation and control, and manufacturing of the sensors and actuators with sufficient frequency response and control authority.

The development of a boundary layer control scheme usually undergoes a four-step procedure: physical understanding, computational LES/DNS simulation, laboratory experimental validation, and engineering application tests. However, due to the computational expenses and capacity, the available DNS zero-pressure-gradient turbulent boundary layer database has a maximum friction Reynolds number $\mathrm{Re}_\tau = \mathscr{O}[10^3]$ (Sillero et al., 2011) and the simulation of controlled boundary layers are at an even lower order, $\mathrm{Re}_\tau = \mathscr{O}[100]$ (Choi et al., 1994, Jung et al., 1992, Schoppa and Hussain, 1998). Though laboratory wind-tunnels can produce turbulent boundary layers with friction Reynolds number of $\mathscr{O}[10^4]$, it is still approximately one-tenth of the Reynolds number of the turbulent boundary layers in real-world engineering applications (Deck et al., 2014, Smits and Marusic, 2013). Researches attempt to extrapolate the performance of the control strategies at lower Reynolds numbers to understand the Reynolds number dependency of the control effect and, in turn, to estimate the potential drag reduction at practical Reynolds number boundary layers. For

example, Iwamoto et al. (2005) studied the controlled boundary layer at $\mathrm{Re}_\tau = 642$ and estimated that a 35% frictional reduction can be achieved at $\mathrm{Re}_\tau = 10^5$ by eliminating all the turbulent energy below $z^+ = 10$. However, other studies have pointed out that control strategies based on the manipulation of the viscous-scaled near-wall structures can have a drag reduction that scales unfavorably with the Reynolds number Chang et al. (2002). Gatti and Quadrio (2016) estimated that the frictional drag reduction achieved using streamwise traveling spanwise oscillation walls in a turbulent boundary layer at $\mathrm{Re}_\tau = 10^5$ is approximately 23%, as opposed to an impressive 58% drag reduction at $\mathrm{Re}_\tau = 200$. However, Corke and Thomas (2018) noticed that, under an actual flight condition, the oscillation frequency in physical space would reach 10^6Hz for the optimized parameters nominated by Gatti and Quadrio (2016). The main reason for this drop in effectiveness at higher Re_τ is that the near-wall turbulence only contributes the majority of the turbulence production in low Re_τ boundary layers, while high *Re* boundary layers are governed by dynamics in both the near-wall and logarithmic regions (Gad-el Hak, 1994), with increasing amounts of turbulence production due to large-scale structures in the logarithmic region (Deck et al., 2014, Mathis et al., 2009).

At the same time, the active boundary layer control techniques require the employment of sensors and actuators. In the concept proofing process, the architectures of these control algorithms are designed based on laboratory set-ups at relatively low Reynolds numbers. Since these active control schemes are mainly focused on attenuating the near-wall turbulence energy, the characteristic length scale of actuators and sensors will be in the order of micrometers, and around ten million sensor-and-actuator pairs will be required to cover an area of one square meter on the fuselage of a cruising commercial aircraft (MacMynowski and Williams, 2009). As suggested by Kreplin and Eckelmann (1979), the near-wall quasi-streamwise vortices have a streamwise length-scale of 300 wall units and convect at approximately $U^+ = 12$. Thus, the passing frequency of these structures is approximately 70kHz, which leads to a requirement of micro-electro-mechanical systems in the flow control of higher Reynolds number boundary layers (Gad-el Hak, 1994). The combination of these two factors dramatically limits the opportunities to apply current active control strategies to practical engineering applications.

Apart from the cost of building these control infrastructure, Brunton and Noack (2015) stated that another important challenge faced when attempting to transplant a DNS control scheme into

the real experimental measurement is the time delay for actuation. All experimental real-time control requires a benchmark signal (either large-scale structure or the running standard deviation) to determine the control signal, which is filtered from detected flow quantities. The use of filters in real-time induce a lag between the detection of flow fields and the generation of control signals so that the actuation will also be half filter length later than the detection (Brunton and Noack, 2015). At higher Reynolds numbers, as the convective velocity becomes higher the targeted structures will travel for a longer streamwise distance during this time delay, which means a larger sensor-actuator separation becomes inevitable. By using spectral coherence analysis, Baars et al. (2016) visualized a total loss of the small-scale coherence of the near-wall dynamics between the friction velocity measured by the wall-based sensor and the streamwise velocity right above at $z^+ = 10$. They hypothesized that this may be owing to a misalignment of the sensors in the spanwise direction. Applying an identical analysis method, Baidya et al. (2019) confirmed the hypothesis by artificially adding a spanwise offset between the friction velocity and streamwise velocity sensors. In other words, for the real-time control strategy taming the near-wall coherence structures, an extremely high degree of spanwise alignment (in the order of 10 viscous wall units) is required to capture the informative signal from the detection sensors for actuation downstream. Furthermore, in a recent study, Samie et al. (2020) observed a loss of coherent from the near-wall turbulence by adding a very small streamwise offset between the friction velocity and streamwise velocity signals. They predicted that even with perfect spanwise alignment, the coherence level between the actuation and detection points is the only 55%.

A plausible methodology to resolve these difficulties associated with controlling the near-wall coherent structures is to target the LSMs and VLSMs. As reviewed in 2.2, these long streaky structures have a streamwise extension with an order of boundary layer thickness, and their contribution to turbulent kinetic energy increases with the Reynolds number. In turn, it is reasonable to believe the large-scale control strategies may obtain a more favorable scaling of drag reduction with respect to the Reynolds number. Further, due to the geometric size of these LSMs, the requirement on the frequency responses of the sensors and actuators will be less strict. Although this long streamwise extension inevitably leads to a longer real-time filter and, consequently, a larger sensor-actuator separation, the impact on the estimation accuracy of the real-time LSMs observation is limited. This is mainly because of the high coherent magnitude of such structures (Baars

et al., 2016). Thanks to this high spatial correlation feature, the control effect on the LSMs are expected to be more long-lasting. Hence, the total amount of sensor/actuator pairs per square meter is decreased. Thus, large-scale control largely relieves the financial and technical burdens on the manufacturing of the sensors and actuators. In summary, all of these considered factors highlight the significance of the idea to actively control the large-scale or very large-scale structures that resides in the outer layer of a high Reynolds number turbulent boundary layer.

Chapter 3
Experimental Set-up

In this chapter, the experimental set-up utilized in the current study is described, which includes:

- §3.1: Wind-tunnel facility
- §3.2: Active flow control arrangement
- §3.3: Measurement Techniques

3.1 Wind-tunnel Facilities

3.1.1 Wind Tunnel

All experiments in the study are conducted in the High Reynolds Number Boundary Layer Wind Tunnel (HRNBLWT) at the University of Melbourne. Figure 3.1 shows a schematic diagram of the open-return tunnel, which possesses a working section of total length 27m with a cross-section of 1.89m$\times$0.9m. Measurements are made in the turbulent boundary layer that develops over a 27m long polished aluminium plate on the bottom floor of the working section. The flow enters the tunnel via a bell mouth inlet before experiencing two 90 degrees turns facilitated by vertical turning vanes. A flow conditioning section consists of a honeycomb followed by a series of six mesh screens. Immediately after the two-dimensional contraction with a ratio of 6.2:1, the boundary layer is tripped by a strip of P40 grit sandpaper. The careful design of this wind tunnel guarantees low free-stream turbulence intensity, which is defined as the variance of the velocity fluctuations normalized by the square of free stream velocity, $\overline{u^2}/U_\infty^2$. Free stream intensity is less than 0.15% for U_∞ ranging from 20m/s to 40m/s. Even with these moderate free-stream

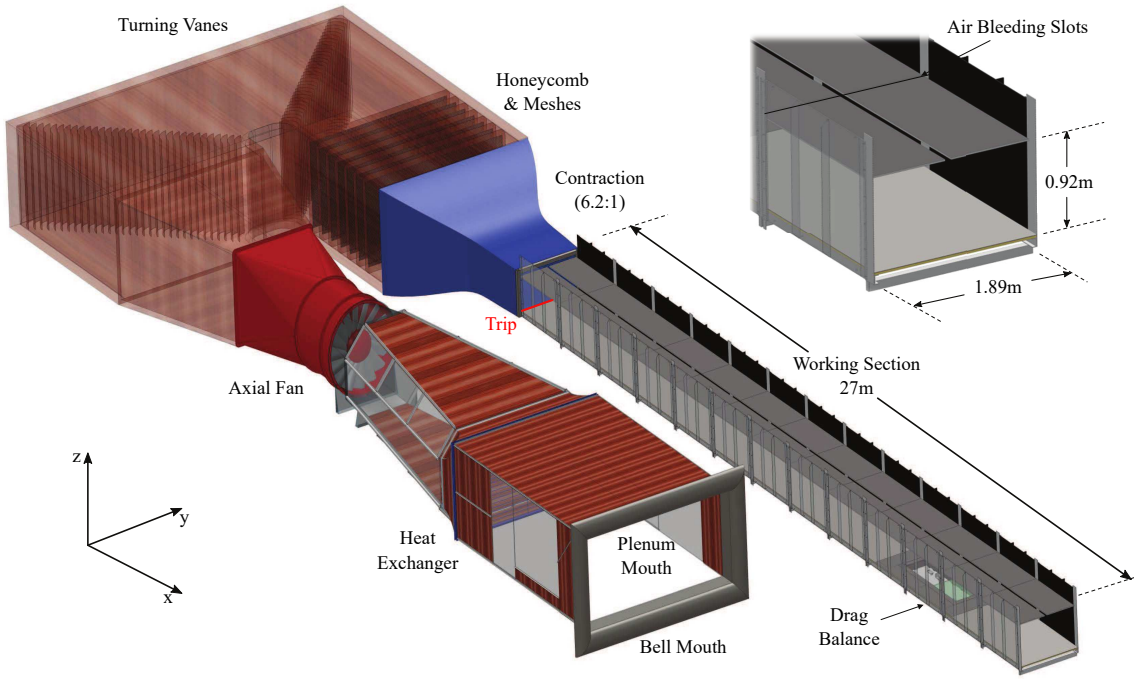

Figure 3.1: A three dimensional overview of the HRNBLWT. Adapted and reproduced from Talluru (2013).

velocities, the large streamwise extent of the working section enables the development of a high Reynolds number turbulent boundary layer within the HRNBLWT. Because the boundary layer thickness reaches beyond 0.3m at the downstream end of the working section (27m downstream of the trip), air bleeding slots are employed in the ceiling of the working section to depressurize and ensure a nominally zero-pressure-gradient boundary layer. Via measuring U_∞ along the streamwise direction, the percentage variation of the pressure coefficient, defined as $C_p = \frac{\Delta P}{0.5\rho U_\infty^2}$, where ΔP is the pressure difference between the reference position (inlet to the working section) and a position anywhere along the length of the working section, is limited to $\pm 0.7\%$ at the nominal flow velocity of 20 m/s (Hutchins et al., 2011). On the other hand, the combination of the thick boundary layers and low free stream velocities (low friction velocity, U_τ) provides the opportunity to acquire measurements with excellent spatial resolution in the wall-normal direction. Further information associated with the detailed specifications of HRNBLWT is available in Nickels et al. (2005).

Throughout the report, the coordinate system adopted for the experimental set-up and the measurement results is as illustrated in figure 3.1, where x, y and z denote the streamwise, spanwise, and wall-normal directions, respectively. Capital U,V and W represent the total velocity fluctua-

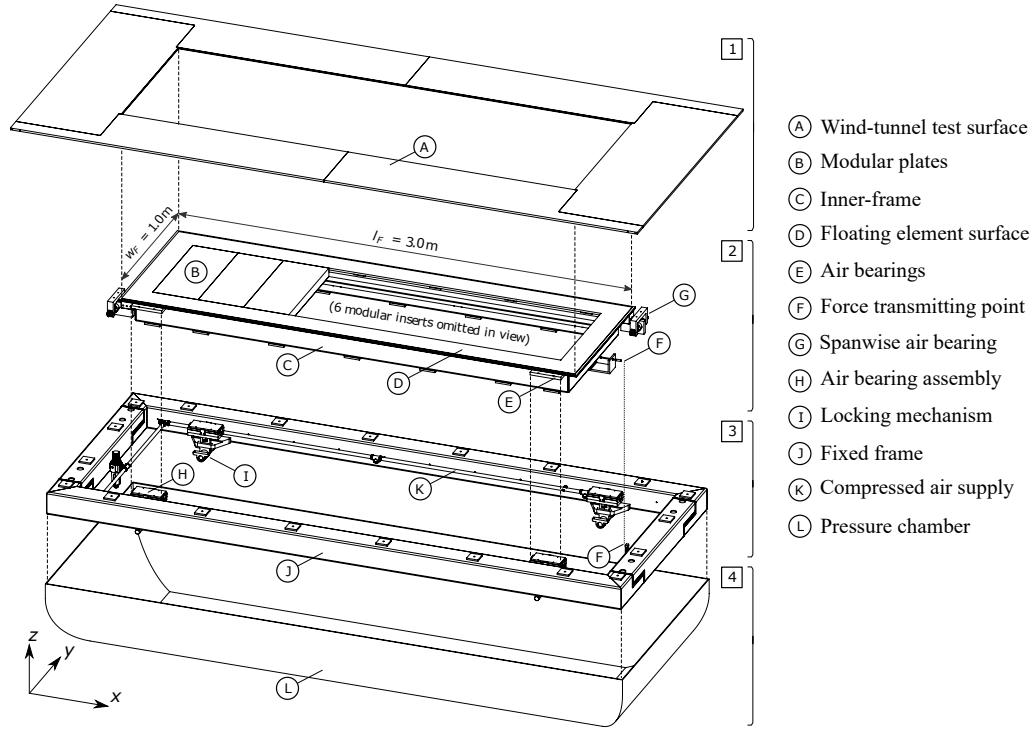

Figure 3.2: A three dimensional explosive view of the drag balance facility. Adapted and reproduced from Baars et al. (2016).

tions in the x, y, and z directions, respectively, while lower-cased u, v and w are the corresponding turbulent fluctuations about the mean. $\overline{U}$, $\overline{V}$, and $\overline{W}$ are the time-averaged velocity components, which means $U = \overline{U} + u$ and the angled bracket $\langle\rangle$ denotes the conditionally averaged quantity. The superscript $+$ denotes normalization with viscous scaling for the uncontrolled boundary layer (i.e. $U^+ = U/U_\tau$ and $z^+ = zU_\tau/\nu$, where ν is the kinematic viscosity of the flow). Here, U_τ is the mean skin-friction velocity, which is defined as $U_\tau = \sqrt{\tau_w/\rho}$ (where ρ is the density of the cross-flow). The subscript "l" and "s" represents the large-scale and small-scale fluctuations of the velocity signals. In addition, the subscript "un" and "co" represent the physical quantities obtained in uncontrolled and controlled boundary layers, respectively.

3.1.2 Drag Balance

The main measurement campaign carried out in this study take place at a streamwise location between 19.8m and 21.0m downstream of the boundary layer trip, which coincides with the location of drag-balance shown in figure 3.1. This drag balance is a direct skin-friction drag measurement

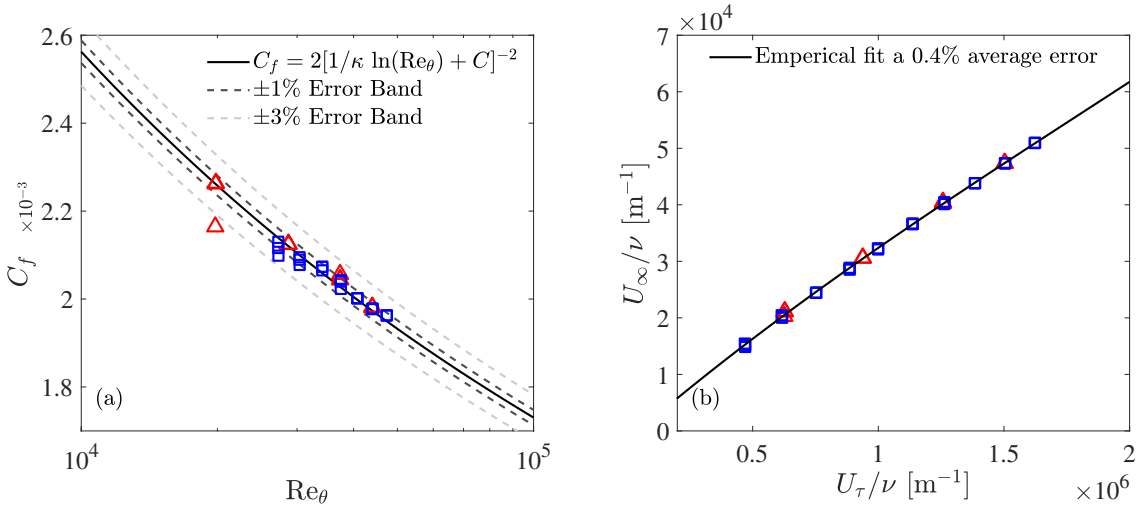

Figure 3.3: (a) Blue squares (□) and red triangles (△) are the skin-friction coefficient measured by the drag balance at different friction Reynolds numbers, and the black solid line shows the empirical Coles-fernholz relation with $\kappa = 0.384$ and $C = 3.7$. (b). Empirical relation between U_∞/ν and U_τ/ν at the measurement campaign based on drag balance results.

device with a large floating element of 3m × 1m, with which to measure the wall shear stress. An exploded view of the drag balance assembly is shown in figure 3.2. Sub-assembly [1] is the wind-tunnel test-surface, which aligns with the main floating element (sub-assembly [2]) during the measurement. Four air bearing pads (H) are equipped on the outer frame (sub-assembly [3]) mounted on the bottom of the tunnel. When connected to a compressed air supply, the air bearings slightly lift and allow the frictionless motion of the floating element. At the leading and trailing edges of the floating element, two spanwise air bearings (G) restrict the movement of the floating element happens to the streamwise direction. The floating element contains nine 0.3m × 0.7m wide interchangeable plates (B) that form the test surface within the inner floating frame. Such a modular design ensures the control architectures and the measurement equipment required by the current project can be easily embedded into the surface of the wind tunnel. In the current project, the results acquired by the drag balance are applied to calibrate the constant temperature hot-film anemometry. Figure 3.3(a) shows the skin-friction coefficient measured by the drag balance as a function of the Reynolds number on two independent days. Here, the skin-friction coefficient is defined as $C_f = \frac{\tau_w}{0.5\rho U_\infty^2}$, where τ_w is the mean wall-shear stress measured over the entire floating element. This is calculated from the ratio between the total skin-friction force determined by the drag balance and the surface area of the floating element. Figure 3.3(a) demonstrates the accuracy

and repeatability of the skin-friction measured by the drag balance, which resides within $\pm 1\%$ error band of the empirical Coles-Fernholz relation with $\kappa = 0.384$ and $C = 3.7$, at momentum thickness Reynolds number $\mathrm{Re}_\theta > 38000$. The error at $Re_\theta \approx 20000$ is slightly higher $(> 3\%)$, which is due to the lower signal-to-noise ratio of the shear stress measurement at lower freestream velocities. However, the majority of data reported in this study are conducted at $Re_\theta = 44000$, where the accuracy of the device can be assumed to be $\pm 0.4\%$. Since the development of C_f along the 3m length of the floating element is close to linear, it can be assumed that the skin-friction at the streamwise mid-point of the floating elements is approximately identical to the mean skin-friction coefficient over the entire testing surface. Based on this assumption, an empirical fit is obtained to connect free-stream velocity and the mean skin-friction velocity at the streamwise midpoint of the floating elements in figure 3.3(b). This empirical fit is used to calibrate the hot-film sensors, which will be described in §3.3. Full details on the design and error analysis related to the drag balance are available in (Baars et al., 2016).

Three different classes of measurements are performed within the current project, which include **(i).** a series of system identification experiments preceding to the application of active flow control strategy (see Chapter 4); **(ii).** simultaneous hot-film and hot-wire anemometry experiments (see Chapter 5); and **(iii).** simultaneous hot-film and PIV experiments with the active control strategy employed (see Chapter 6). Without special nomination, these measurements all have a nominal free-stream velocity at $U_\infty = 20$m/s at the drag balance position, which resulted in a nominal composite boundary layer thickness $\delta = 0.36$m and a mean friction velocity around 0.65m/s. In turn, the friction Reynolds number, $Re_\tau = U_\tau \delta / \nu$, predicted from a composite velocity fit with $\kappa = 0.384$ and $A = 4.17$ is approximately 14000 and the momentum thickness Reynolds number is 44000. More detailed flow parameters for each measurement is specified in the corresponding Chapters.

3.2 Active Flow Control Arrangement

In this section, the active flow control infrastructure is introduced on the basis of the simultaneous hot-film and hot-wire measurement set-up. In addition, the hardware and software for the real-time control signal processing as well as the specifications associated with the actuators are presented.

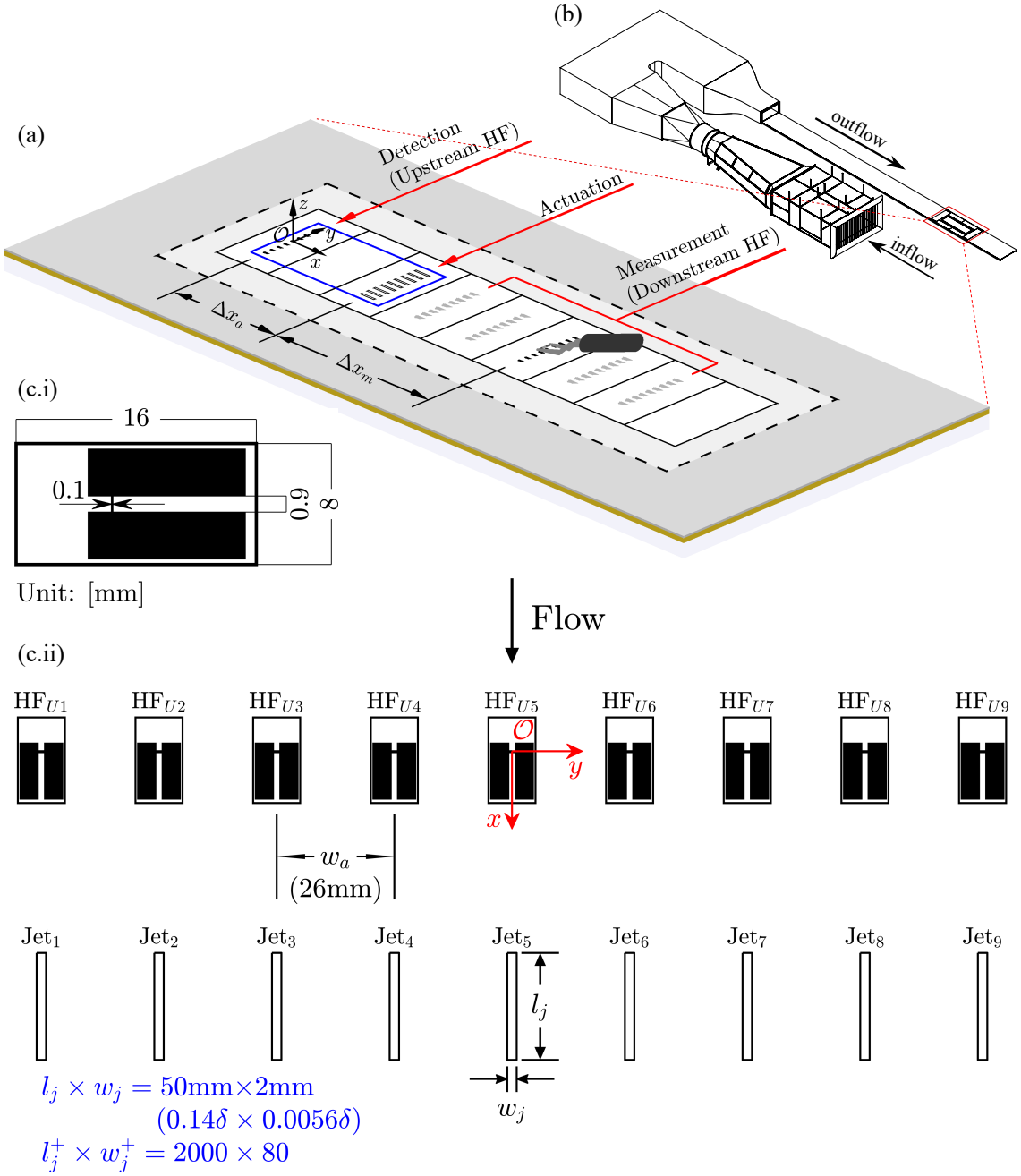

Figure 3.4: (a) Three dimensional layout of the control infrastructures. (b) Location of the control infrastructure in HRNBLWT. (c.i) Specification of the hot-film probe used in the experiments, (c.ii) Arrangement of the upstream hot-film (detection) array and the wall-normal jets (actuation array)

It should be noted that an almost identical control architecture is employed throughout this thesis, but the detailed experimental measurement apparatus does vary and is described in §4.1 and §6.1,

respectively.

The active flow control infrastructure is placed at the drag balance position as highlighted by the red box in figure 3.4(b) and a zoomed view of this is given in figure 3.4(a). In general, the modular control surface consists of detection, actuation, and measurement arrays. Specifically, the detection array contains a spanwise array of nine Dantec 55R47 glue-on hot-film probes, which are fixed at the leading modular panel slot of the drag balance (i.e. 19.8 meters downstream of the trip of the boundary layer). The arrangement of the hot-film sensors is shown in the magnified view of the detection array in figure 3.4(c). These hot-films sensors are known to possess limited temporal response due to the temperature drift. In the current project, the hot-film sensors in the detection (upstream) and measurement (downstream) arrays mainly measure the large-scale friction velocity fluctuation and the mean wall-shear-stress. Thus, the unreliable high-frequency response is acceptable. More details on the measures undertook to resolve such problems and the associated validations are discussed in §3.3. The spanwise separation between the adjacent hot-film sensors, $w_a = 0.026\text{m}$ ($w_a^+ = 1000 = 0.075\text{Re}_\tau$), is constant for all measurements. The selected w_a value ensures that the detection array is able to capture LSMs with a spanwise wavelength $\lambda_y > 0.075\delta$. Based on the streamwise-spanwise aspect ratio of the LSMs the coherent structures with a streamwise wavelength λ_x greater than δ is observable under this configuration (Baidya et al., 2019). It should be noted that the origin of the coordinate system is set on the middle hot-film sensor in the detection array throughout the project, which lies on the centreline of the wind-tunnel workings section. The order of the hot-film sensors is counted from the negative y-axis towards the positive positions. The first hot-film in the detection array is denoted as HF_{U1}, which has a coordinate position of $x_{\text{HF}_{U1}} = 0$ and $y_{\text{HF}_{U1}} = -0.104\text{m}$.

Downstream of the detection array, an actuation array containing nine rectangular wall-normal jets are assigned to manipulate the boundary layer with the spanwise position of the jets aligned perfectly with the corresponding upstream hot-film sensors. The streamwise separation between the detection and actuation array, referred to as sensor-actuation separation Δx_a, is adjusted to accommodate the real-time actuation delay. The value of Δx_a is specified as 1.7δ, with the optimization process explicitly discussed in Chapter 4 via the system identification measurements. In order to examine the effect of the current active flow control strategy, a measurement array is included downstream of the actuation array, which consists of a further spanwise array of nine hot-

film sensors, identical to the upstream detection array, and also a wall-normal traversing hot-wire probe. The arrangement of the downstream hot-film array HF_D is the same as the upstream detection array, but the downstream hot-films are mainly used to provide a record of skin-friction drag modification due to the control. Simultaneously, a wall-normal traversing hot-wire probe is placed on top of HF_{D5} to acquire the boundary layer profile simultaneously with the hot-film acquired skin-friction velocity fluctuations. It should be noticed that the components in each array are located at the center of the modular panels so that the streamwise distance between the arrays can be simply changed via switching the order of the modular panels. Thus, the streamwise separation between the actuation and measurement arrays, Δx_m, is adjustable to evaluate the control effect at multiple desired streamwise positions. Detailed Δx_m values are specified in the later chapters.

The real-time execution of the control infrastructure is designed based on the Speedgoat Performance real-time target machine. The Speedgoat target machine is triggered and monitored by a MathWorks Real-Time Simulink model running on a host computer (Microsoft Windows 10 operating system). The target machine uses an Intel Core 2 Duo 3.33GHz processor, with a 4GB DDR2 memory. The data from the hot-films and hot-wire probe are sampled by 16-bit A/D Speedgoat IO106 modules embedded in the machine, with a maximum of 34 data sampling input ports available in each time step. The target machine temporarily transfers the collected data in near real-time to the host computer. Various computations performed on the hot-film signals from the detection array by the real-time host computer Simulink program to generate the Transistor-Transistor Logic (TTL) binary signals, which provide the actuation commands for the actuation array when transferred to an IO205 Speedgoat D/A converter module.

Figure 3.5(a) shows a clip of the mean-subtracted fluctuating wall friction velocity fields u_τ attained from the detection array of hot-film sensors. The mean running-averaged skin-friction velocity over five seconds, which is equivalent to approximately 200 boundary layer turnovers (i.e. $tU_c/\delta \approx 200$), is used to compute the fluctuating component u_τ so that it provides sufficient convergence. Here, U_c is the convective velocity of the large-scale skin-friction footprints on the wall. Since the aim of the current project is to control the boundary layer via manipulation of the LSMs, a low-pass filter is convolved the u_τ fields in real-time to obtain a large-scale fluctuating skin friction footprint u_{τ_l}. In chapter 4, a systematic approach is introduced to shape the filter so that it leaves a large-scale component that is statistically most likely to retain coherence over

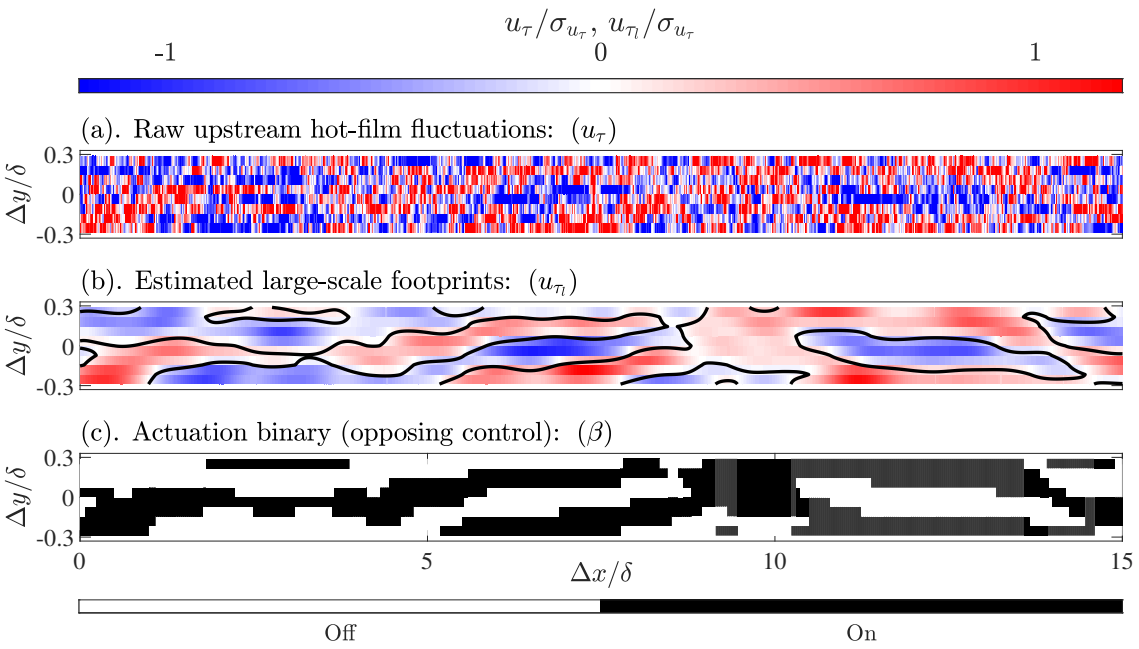

Figure 3.5: (a) A sample of zero-mean skin-friction velocity fluctuation measured by the upstream detection array. (b) Low-pass filtered large-scale skin-friction velocity from the raw u_τ fields in (a). (c) Opppsoing control binary signals based on the estimated large-scale skin-friction velocity fluctuations.

the streamwise separation between the detection and actuation array. In the rest of the report, the real-time filter comprises a streamwise LSE filter and a spanwise low-pass Fourier filter with cut-off wavelengths $\lambda_{x.c} \times \lambda_{y.c} = 1.6\delta \times 0.3\delta$ (see §4.3). The large-scale fluctuating friction velocity fluctuation fields u_{τ_l} resulting from the sampled u_τ data is shown in figure 3.5(b). Black solid lines indicate the zero iso-contour of the large-scale skin-friction velocity field, which separates the positive (red) and negative (blue) u_{τ_l} regions. In this report, these positive u_{τ_l} regions are named as high-speed structures, high-speed events, and high-speed footprints interchangeably. Conversely, the low-speed events indicate the negative u_{τ_l} regions. As regards the estimated u_{τ_l} fields, three different control schemes are attempted to investigate the effect of the wall-normal jets at perturbing different large-scale events. These include:

Opposing control the jets are activated on the estimated large-scale high-speed events

Reinforcing control the jets are activated on the estimated large-scale low-speed events

Dessynchronized control the jets operating upon a pre-determined duty cycle.

Consequently, the actuation within the desynchronizing control is randomly distributed in either high-speed or low-speed events. In all control schemes, the jets are active consistently engaging for 50% of the total measurement duration. As an example, figure 3.5(c) illustrates the case of opposing control binary control where the jets are switched on during the positive u_{τ_l} regions.

The averaged Task Execution Time (TET) to complete one computation cycle, initiating from obtaining one skin-friction velocity data point applying the filter and then outputting the binary control signal, is approximately 0.2ms. In the Speedgoat system, one frame is processed in real-time at each time step. Thus, to permit adequate execution time between samples, a sampling period of 0.25ms is used. Since the data acquired by the detection hot-film probes are utilized in the Speedgoat real-time numerical processing, one data-point is sampled for each hot-film sensor per frame. In turn, the sampling frequency of these hot-films is equivalent to the execution frequency of Speedgoat at $f_{\mathrm{HF}} = 4\mathrm{kHz}$. This sampling frequency corresponds to a 0.01 boundary layer turnovers, which is sufficient for the detection array to capture the large-scale footprints with $\lambda_x > 1.6\delta$. In contrast, the velocity signals from the traversing hot-wire sensor are not further processed in real-time. Therefore, for the hot-wire sensor, five data points are collected at each execution frame with a resulting sampling frequency $f_{\mathrm{HW}} = 20\mathrm{kHz}$, which provides more information on the small-scale velocity fluctuations of the controlled boundary layers.

The TTL binary signal is transmitted to a Festo MPAL-VI valve terminal and then distributed to nine solenoid valves ([7] in figure 3.6(a)) integrated into the valve terminal with each of them connected to one wall-normal jet [8]. While a 'low' signal is received the solenoid valves remain closed. When a 'high' binary signal is received, the valves open under a mechanical spring-return system, so that the air-flow can be delivered into the jet cavity. Figure 3.6(a) shows a more detailed schematic diagram of the air-supply system of the wall-normal jets. The source of the air generated by an industrial compressor [1] has a static pressure between 8.5bar to 9bar. The compressed air is then delivered to a ten-liter pressure vessel [2], which provides a buffer or stability of the working pressure during the long-term measurements. Prior to regulation, a 40µm (Festo MS6-LF-1/2-ERV) filter [3] and a 5µm (Festo MS6-LF-1/2-CRV) filter [4] are placed in series to remove contamination and moisture from the compressed air. There are two pressure regulators applied to the purified air in parallel PR-1 [5] and PR-2 [6]. The outlet pressure from the first regulator (PR-1) is directly connected to the air-supply system of the jets at 0.9bar. A

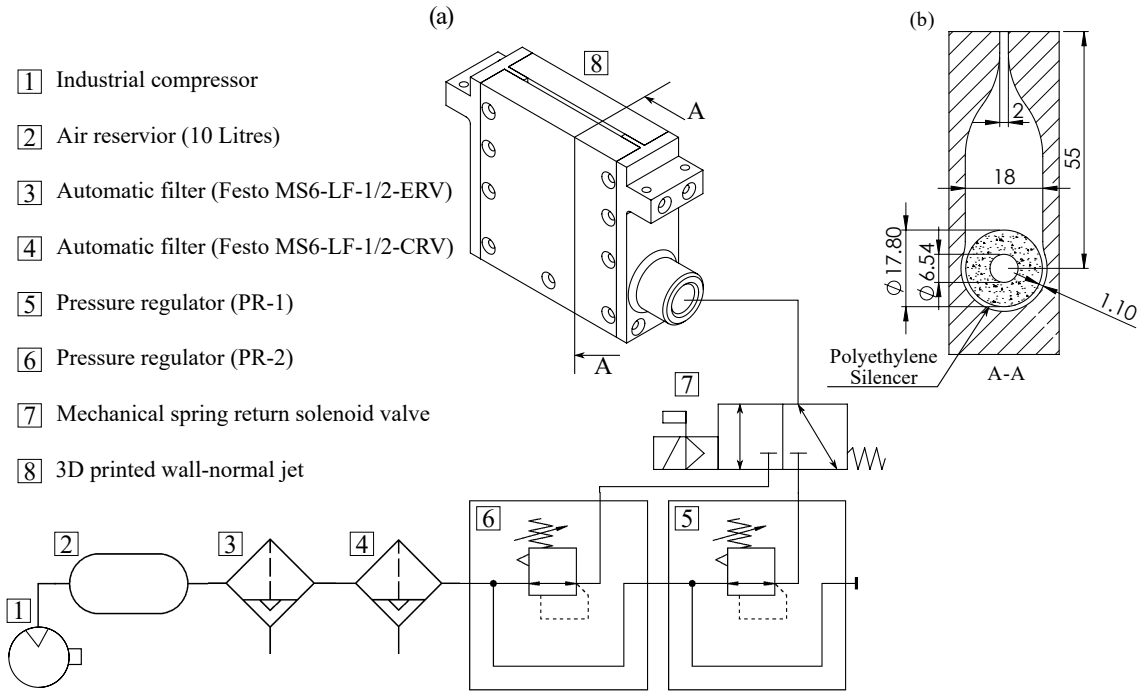

Figure 3.6: (a) Schematic diagram of the air-supply system of the wall-normal jets in the present real-time control. (b) Cross-sectional view of the 3D-printed wall-normal jet with the key dimension labeled.

further pressure regulator (PR-2) regulates the supply to a higher pressure (4bar), which aids the spring-return system of the solenoid valves during their closure processes. Within each individual wall-normal jet assemble (see figure 3.6(a)), a polyethylene silencer, working as a throttling valve, is connected to the solenoid valve to ensure uniform delivery of air into the jet cavity (to ensure a jet profile that is close to two-dimensional along the length of the slot). The components of the wall-normal jets are 3D-printed using an Objet EDEN 260V polymer 3D printer, which guarantees that the dimensions of the jet cavity (depicted in figure 3.6(b)) are consistent over the entire actuation array. The jets are assembled using a series of through bolts and nuts, with the gaps between the components sealed with super-glued cloth tape to minimize leakages.

The behaviour of the jets without cross-flow is examined via placing a hot-wire probe exactly at the geometric center of the jet exit slit, which has a rectangular $l_j \times w_j$ =50mm $(0.14\delta) \times$2mm 0.0056δ ($l_j^+ \times w_j^+ = 2000 \times 75$, see figure 3.4(c)) cross-section area. As shown in figure 3.7(a), the mean jet exit velocity increases proportionally with the outlet pressure P_{reg} of the pressure regulator (PR-1). The jet exit velocity U_{jet} at the selected $P_{reg} = 0.9$bar is 13.6m/s, which corresponds to

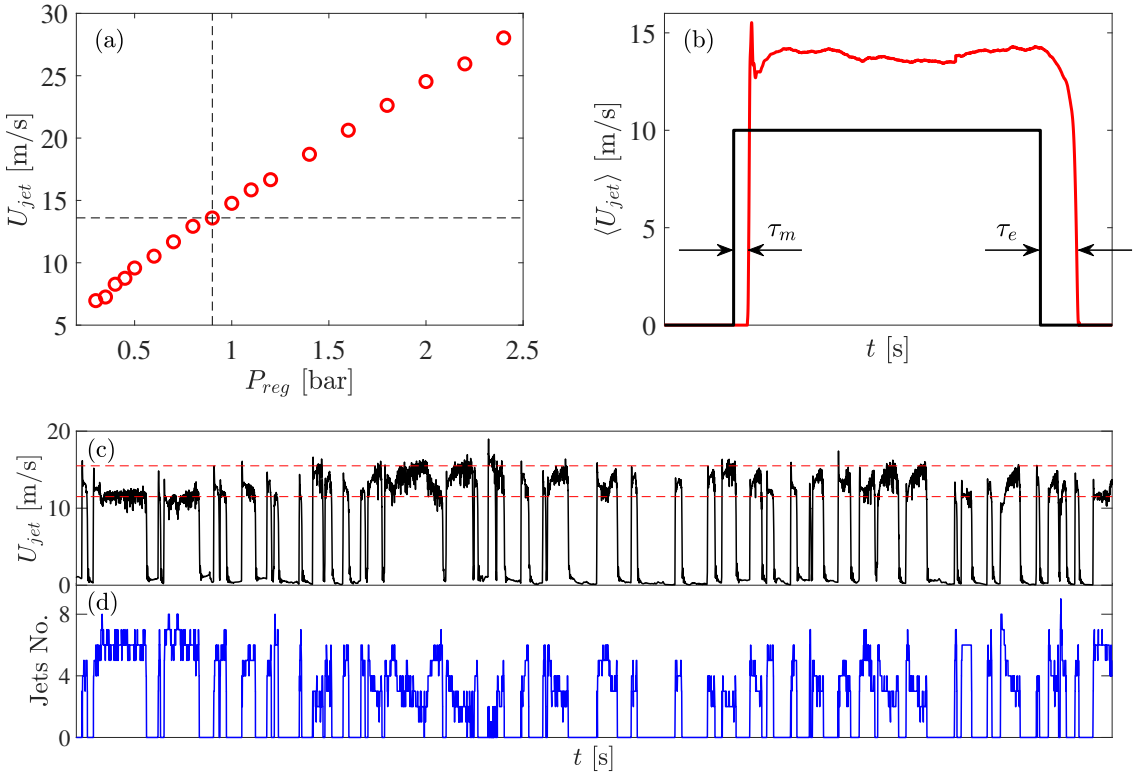

Figure 3.7: (a) Mean jet exit velocity at different outlet pressure of the pressure regulator (PR-1). (b) Conditionally averaged jet exit velocity (red solid line) over one period of actuation (black solid line). (c) Instantaneous jet exit velocity acquired by hot-wire sensor with the corresponding number of jets activated shown in (d).

a nominal jet ratio $U_{jet}/U_\infty = 0.68$ at the operating conditions of the majority of experiments reported here ($U_\infty = 20m/s$, $\mathrm{Re}_\tau = 14000$). It is worth noting that for this study we have only binary (on/off) control of the jet array, and therefore the jet actuation is the same strength regardless of the strength of the detected turbulent event. However, figure 3.7(c) shows the instantaneous U_{jet} of the middle jet, which is operating under a series of binary signals adapted from real-time control measurements. The jet exit velocity is nearly zero while the jet is closed, but it is obvious from figure 3.7(c) that U_{jet} is varying between 11.5m/s to 15.5m/s during the actuation. This is because, as shown in figure 3.7(d), the number of wall-normal jets engaged at each time step changes in real-time measurements. Since the volume flow rate of the air-supply system is restricted in the hose due to choking, the jet-exit velocity is reduced while a larger amount of jets are activated. As a benchmark, the mean U_{jet} in figure 3.7(a) is measured while five jets are activated throughout the entire realization. This issue means that U_{jet} varies by $\pm 20\%$ about the nominal mean value

based on the number of active jets. However, it is deemed reasonable for the current experiments, especially since the possibility of these extreme cases is low. It is calculated that the possibility of $3 \sim 7$ jets engaging at a given time instance is approximately 84%.

One important feature of the current control infrastructure is the delay of the actuation (τ_a), which is defined as the temporal difference between the passage of a target structure at the detection array and the successful injection of the jet flow into the boundary layer. Such delay is contributed by the computational delay due to real-time filtering and data processing, and the mechanical delay owing to the air-supply system and solenoid valves. Temporal convolution between the low-pass filter and the u_τ signals from the detection array in real-time results in a computational delay (τ_f) equivalent to half of the streamwise cut-off wavelength plus the time required to process one single frame in Speedgoat target machine (τ_{TET}) as equation 3.1.

$$\tau_f = \frac{1}{2}\frac{\lambda_{x.c}}{U_c} + \tau_{\mathrm{TET}} \approx 20.8 \text{ ms} \tag{3.1}$$

For typical conditions reported here where the convection velocity $U_c = 14.2$m/s and the processing time $\tau_{\mathrm{TET}} = 0.2$ms, the total computational delay is $\tau_f = 21$ms. In terms of the mechanical delay, the temporal jet response is determined by measuring the jet exhaust velocity with a hot-wire sensor with the jet actuated by a periodic square-wave binary control signal. Figure 3.7(b) shows the conditionally averaged jet exit velocity $\langle U_{jet} \rangle$ over one period of actuation. The jet velocity rises from 0 to full speed with a mechanical delay of $\tau_m = 14.3$ms from the rising edge of the binary control signal. Shutting of the solenoid valve takes a longer time (i.e. $\tau_e = 39.8$ms) as the pressure in the jet cavity and tubes equalize to tunnel conditions. The summation of the computational and mechanical delay can be accommodated in the experiment design by adjusting the separation distance between the detection and actuator array Δx_a, which adjusts the time taken for the detected structure to convect to the actuator array. Detailed discussion on optimizing such values are in Chapter 5. Since the current large-scale control strategy aims to perturb the LSMs in the log region, the forward-inclination feature of these LSMs results in an inclination delay due to the wall-based estimation ($\tau_i = 8$ms). As a summary, the total time delay that should be introduced between detection and actuation (τ_a) can be calculated from the following equation.

$$\tau_a = \frac{\Delta x_a}{U_c} - (\tau_f + \tau_m + \tau_i) = -0.1 \text{ ms} \tag{3.2}$$

The negative sign in the result implies that the actuation is, indeed, 0.1ms later than expected. However, this deviation is regarded as insignificant because 0.1ms is less than half of a single time-step under the current control architecture. Consequently, for the majority of results reported here, we actuate immediately following a confirmed detection in the filtered signal without any added time delay.

3.3 Measurement Techniques

As discussed before, three major measurement techniques are employed in this project, which includes hot-wire and hot-film anemometry and PIV. This section introduces only the information associated with the constant temperature anemometry (hot-wire and hot-film), ranging from the specification of the probes to the calibration processes. Details of the PIV techniques are provided in §6.1.

3.3.1 Hot-wire Anemometry

All hot-wire anemometry conducted in the three measurement classes involves only one single-normal hot-wire probe mounted to a two-axis (streamwise/wall-normal) traversing system, which is shown in figure 3.8. This traversing system has an aerofoil-shaped cross-section to prevent disturbance to the flow at the measurement position. A custom-designed sting (hot-wire probe holder) is placed at 0.55m upstream of the leading edge of the traverse system and it is positioned at the centerline of the HRNBLWT so that the tip of the hot-wire is aligned perfectly with HF_{U5} in the span. A single Dantec 55P15 boundary layer hot-wire probe is mounted on the hot-wire probe holder, which is fixed at the leading edge of the traversing system with an angle of 10 from against horizontal towards the wall (to assist with near-wall measurements). Though the traverse can be moved in x and z, for boundary layer traverses at a given x location a pneumatic foot from the bottom of the sting is actuated onto the tunnel flow to avoid flow-induced vibration of the traverse. The wall-normal traversing of the hot-wire probe is driven by a servo motor and transmitted by a ball screw with a gear ratio of 60:1. Fully automated traversing during the measurements is achieved via wireless interfacing between the host computer and the servo-controller. Through the use of an optical encoder in the servo-controller, the spatial resolution of the wall-normal traversing

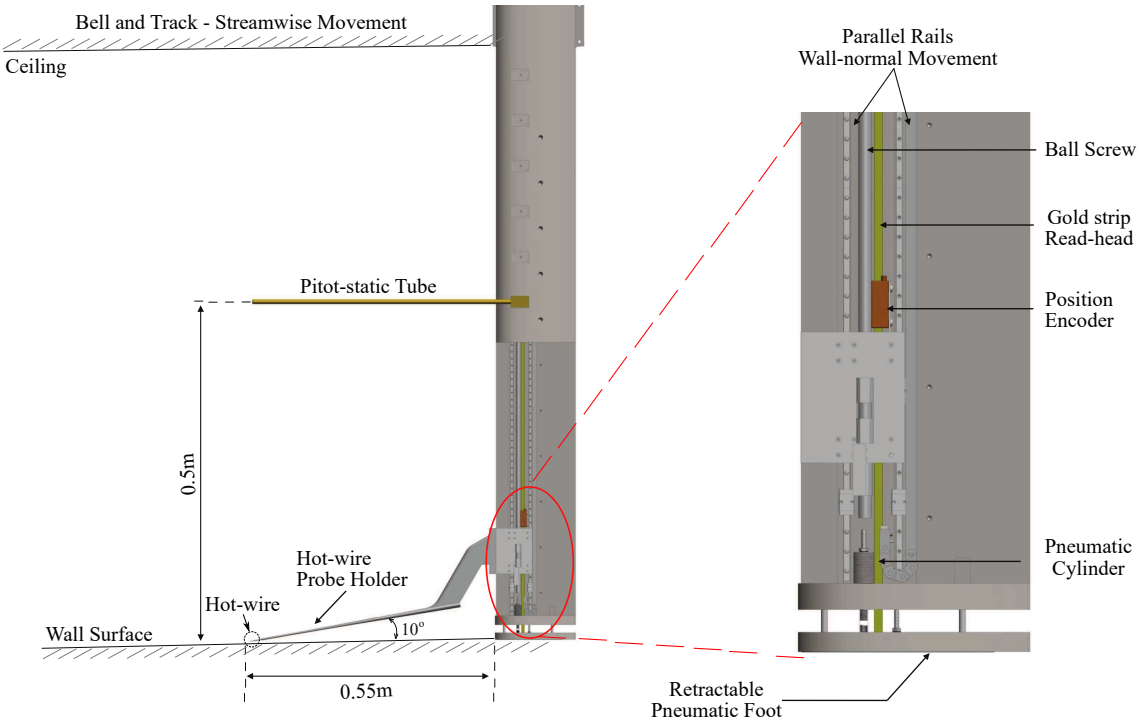

Figure 3.8: Schematic of the streamwise/wall-normal traversing system used for hot-wire anemometry.

of the hot-wire probe is within reaches 0.5µm (approximately one-fifth of a viscous unit for the current study). A pitot-static tube is fixed on the sting at $z = 0.5$m to measure the free-stream velocity. Hot-wire measured boundary layer traverses are obtained for both uncontrolled and controlled boundary layers at the designated streamwise positions downstream of the actuation array. Each boundary layer traverse consists of forty logarithmically spaced points covering a range from 325µm$< z <$ 525mm, which equations to $10 < z^+ < 1.45\delta^+$. At each wall position, the hot-wire probe alternatively acquires two sets of voltage signals for uncontrolled (without control) and controlled boundary layers, so that the data will be more comparable.

The Dantec 55P15 boundary layer hot-wire probe has a 1mm prong spacing and a Platnum-Wollaston wire with 2.5µm core is soldered in-house spanning the tips of the prongs. The middle section of the Wollaston wire is etched to a length of 0.5mm (25 wall units) to ensure a length to diameter ratio l_{hw}/d_{hw} of around 200 for the exposed Platinum sensor at the nominal experimental conditions. Such values are recommended by Hutchins et al. (2009) to minimise heat loss due to end-conduction. The etched length of $l^+_{hw} = 25$ provides sufficient spatial resolution to capture

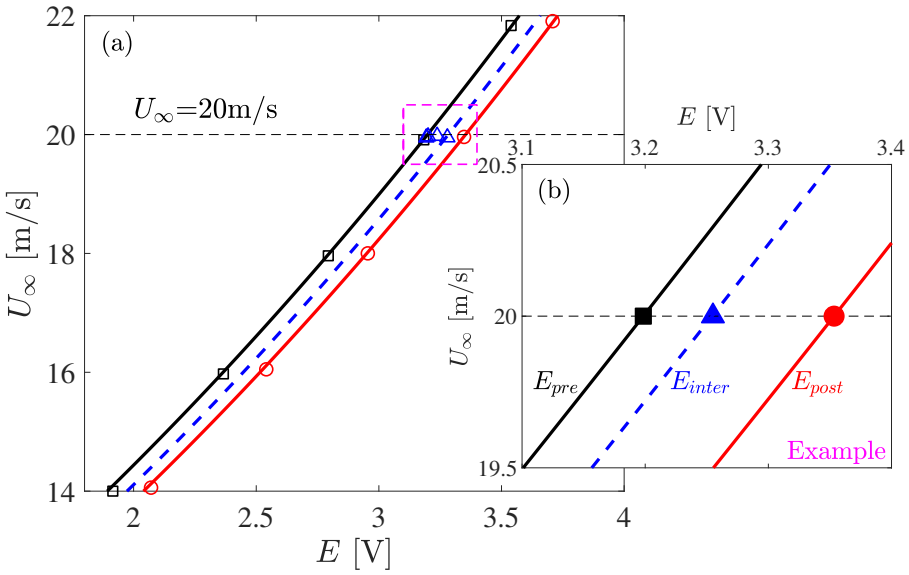

Figure 3.9: (a) Pre-calibration (□) and post-calibration (○) points measured before and after the measurement. Black (−) and red (−) lines are the third-order polynomial fit of the calibration points. Blue triangle markers are the intermediate calibration points measured during the measurement, and the blue dashed line is the interpolated intermediate calibration curve. (b) A zoomed view of the pre, post and intermediate calibration points.

the small-scale dynamics from the hot-wire results (Hutchins et al., 2009). The hot-wire probes are operated with a Melbourne University Constant Temperature Anemometer (MUCTA) with an over-heat ratio of 1.75. Fluctuating voltage signals from the CTA are sampled with the 16bit Speedgoat IO106 analog-digital converter at a sampling frequency of 20kHz which corresponds to a viscous scaled time-step between samples of $\Delta t^+ = 1.3$. The sampling time at each wall-normal location is set to $T_s = 360$s which equates to a boundary layer turnover time of $T_s U_c / \delta \sim \mathcal{O}[10^5]$ for a statistically converged result.

Calibration of the hot-wire is performed by traversing the probe to $z = 525$mm, such that the hot-wire sensor is placed adjacent to the Pitot-static tube that is mounted statically to the sting and so that both probes are within the potential core of the flow. Calibration is performed before (pre-calibration) and after (post-calibration) the actual boundary layer measurements. Both calibrations contain 16 calibrating points acquired at different free stream velocities ranging from 0m/s to 24m/s, where the zero velocity point is utilized to correct the offset of the pitot-static tube. At each calibration velocity, the two probes are sampled for 40 seconds which provides adequate first-order convergence of the signals. Figure 3.9 shows the sampled pre-calibration (○)

and post-calibration (□) points for U_∞ between 14m/s to 22m/s. Third-order polynomials fit the mean voltage (E) obtained from the hot-wire sensor and the free-stream velocity (U_∞) measured from the Pitot-static tube for all 16 realizations to compute the calibration curve. However, a clear deviation occurs between the two calibration curves in figure 3.9 due to the change in the ambient temperature T and also other sources of hot-wire drift (Hutchins et al., 2009). To take the variation into account, a single point re-calibration method is employed (Talluru et al., 2014). During boundary layer measurement, for every eighth measurement (approximately 1.5hrs) the hot-wire probe is maneuvered to the free-stream position adjacent to the Pitot-static probe ($z =$ 0.525m) a single calibration point is acquired in the free-stream at U_∞ (△ in figure 3.9 where $U_\infty \approx$ 20m/s). Using the voltage from the pre-and-post-calibration curve fits and the single intermediate calibration points at U_∞, a linear interpolation ratio η is calculated. Based on the pre-calibration and post-calibration curves, the value of η permits the construction of an intermediate calibration curve (blue dashed line) that is considered to be valid at the time of the single point calibration measurement in accordance with equation 3.3.

$$E_{inter} = E_{pre} + \eta(E_{post} - E_{pre}), \text{ where } \eta = \frac{E_{inter@U_\infty} - E_{pre@U_\infty}}{E_{post@U_\infty} - E_{pre@U_\infty}} \tag{3.3}$$

$$U = U_{pre} + \frac{T - T_{pre}}{T_{inter_1} - T_{pre}}(U_{inter_1} - U_{pre}) \tag{3.4}$$

Here, as shown in figure 3.9(b), $E_{pre@U_\infty}$, $E_{post@U_\infty}$, and $E_{inter@U_\infty}$ are hot-wire voltage reading at the measurement free-stream velocity for pre-calibration (■), post-calibration (●) and intermediate-calibration (▲), respectively. Since the single point, intermediate calibration is performed every eight measurement realizations, a total of six calibration curves, including four intermediate, one pre, and one post are obtained. Finally, the measurement voltage signals acquired from hot-wire anemometry are converted to the velocity signals based on the adjacent calibration curves via interpolating based on temperature. For example, for the realizations measured between pre-calibration and first intermediate calibration (i.e. the first eight measurement points), the velocity signal can be calculated as 3.4. In the equation, U_{pre} and U_{inter_1} are the velocity signals calibrated based on pre-calibration and the first intermediate calibration curves. T_{pre} and T_{inter_1} the temperature at the measurement free-stream velocity for the pre-calibration and the first in-

termediate calibration. T is the ambient temperature during the measurement, which is used to interpolate U_{pre} and U_{inter_1} to eventually get the final calibrated velocity signal U.

3.3.2 Hot-film Anemometry

For the measurement and detection arrays (see figure 3.4), two spanwise arrays of nine Dantec 55R47 glue-on-type hot-film sensors are operated by AA-lab AN1103 constant temperature anemometers with an overheat ratio of 1.2. Though the probes are nominally flush-mounted, the thickness of the flexible KaptonT foil (50µm) and the thickness of the adhesive layer (30µm) sums to approximately 80µm, which is maximized at approximately 4 viscous wall units for the experimental conditions reported in this thesis. The small step is considered to be dynamically "smooth" for the current experiments. This is especially so since these sensors are used to measure the passage of large-scale structures (via their skin friction footprint) which are unlikely to be modified by such small non-smooth topographies. Since the measurement are conducted at a constant free-stream velocity, the resulting friction velocity measured by the hot-film sensors has a constant probability distribution. Thus, as shown in figure 3.10(a), the calibration of the hot-film probes is performed at seven different free-stream velocities (●) increasing from 16m/s to 24m/s, which covers the expected range of the friction velocities that will be encountered during the active control experiments. However, the hot-film anemometry is still considered problematic because of the unreliable high-frequency response and significant temperature drift during long-term measurements. To better account for the temperature drift, the signal point re-calibration method of Talluru et al. (2014) is amended for the on-the-fly re-calibration of the hot-film arrays. For the experiments only measuring the skin-friction drag reduction via hot-film sensors (i.e. no simultaneous hot-wire anemometry and PIV), the intermediate re-calibration are conducted after every five groups of active-control measurements in the same manner as the full calibrations. During the experiment, as the mechanical energy gradually accumulates in the tunnel, the ambient temperature (T) during each intermediate re-calibration increases. Furthermore, each group of active control measurement contains an uncontrolled referencing point (■), which is also considered into calibration. A three-dimensional calibration surface is attained from the mean friction velocity (U_τ), mean ambient temperature (T) and mean hot-wire voltage (E) for all full calibration points and uncontrolled measurement points (equation 3.5).

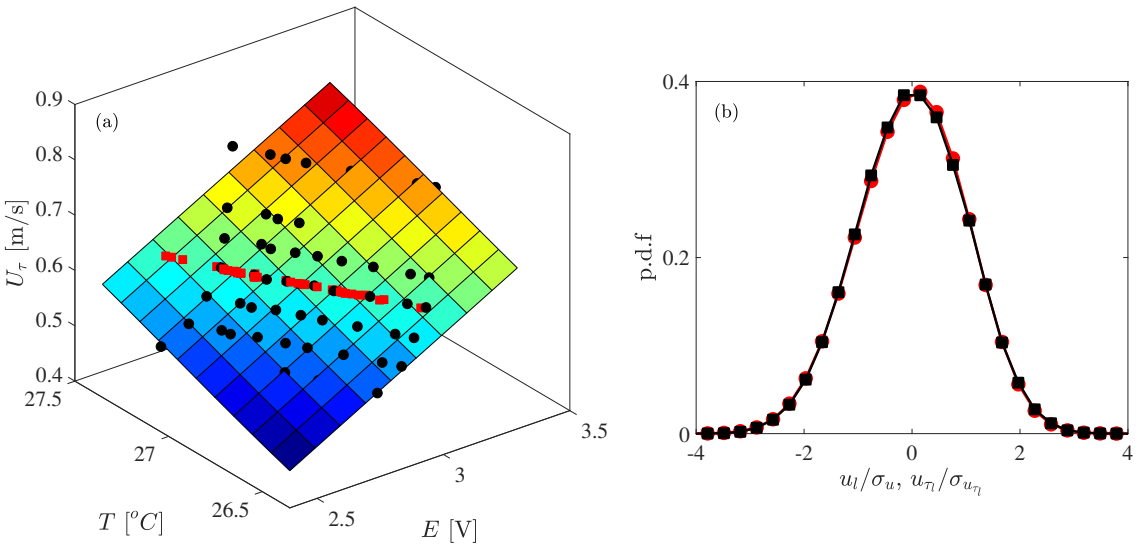

Figure 3.10: (a) An example of the on-the-fly hot-film calibration methodology. Black circles (●) are the full re-calibrations performed every five active control measurements. Red squares (■) are the uncontrolled mean friction velocity points acquired during active control measurements. Color contour is the resulting calibration surface using equation 3.5. (b) Probability density functions of the standardized large-scale friction velocity (■) and streamwise velocity (●) fluctuations measured by hot-film and hot-wire probes

$$U_\tau = (A_1 T + A_0)(B_3 E^3 + B_2 E^2 + B_1 E + B_0) \tag{3.5}$$

where, U_τ is linearly fitted by T, and a third-order polynomial describes the relation between U_τ and E. However, in the simultaneous hot-wire and hot-film measurements, only two full calibrations are performed before (pre-calibration) and after (post-calibration) the boundary layer measurements. In this case, to include the temperature drift, the data points attained in uncontrolled boundary layers during the measurements (■) are utilized as the intermediate calibration points in figure 3.9(b). The friction velocity measured by the hot-films is computed in a similar manner to equation 3.3 and 3.4 via the single-point re-calibration method.

The spatial averaging effect from the relatively large sensing section (0.1mm×0.9mm) together with the limited temporal response of the hot-film result in an unreliable high-frequency friction velocity component. While Alfredsson et al. (1988) reported that the ratio between standard deviation and mean of the skin-friction fluctuations measured by hot-film sensors is approximately 0.1, DNS and highly-resolved PIV measurements revealed that such a ratio is between

0.3 and 0.4 (deSilva et al., 2014). This further indicates that the hot-film sensors are unable to accurately capture the small-scale friction velocity fluctuations. However, as indicated in the previous section, the purpose of the hot-film sensors in the current project is to observe the large-scale friction velocity at the upstream detection array and to determine the mean skin-friction drag reduction at the downstream measurement array. Therefore, our focus here is on the reliability of the low-frequency u_τ fluctuations with streamwise wavelength $\lambda_x > 1.6\delta$ (lower than 25Hz in the spectral domain). The fidelity of the low-frequency friction velocity fluctuations acquired by the hot-film probes is demonstrated in figure 3.10(b) by comparing the probability density function of the low-pass filtered skin-friction velocity and hot-wire acquired streamwise velocity fluctuations with a cut-off wavelength equivalent to 1.6δ. Here, the streamwise velocity fluctuation is obtained by the hot-wire probe placed at a comparable wall-normal position (i.e. $z^+ = 4$) against the hot-film probe. Figure 3.10(b) demonstrates that both probability density functions of the standardized large-scale friction/streamwise velocity fluctuations (u_l / σ_{u_l} and $u_{\tau_l} / \sigma_{u_{\tau_l}}$) measured by hot-film/hot-wire probes agree with each other, where σ_{u_l} and $\sigma_{u_{\tau_l}}$ are the standard deviations of the large-scale friction velocity and streamwise velocity fluctuations. The result indicates the configuration of the hot-film anemometry is capable to accurately capture the large-scale skin-friction fluctuations, which is suitable to fulfill the tasks requested in the current project. In addition, Talluru (2013) and Hutchins et al. (2011) both independently demonstrated other evidence on the reliability of hot-film sensors at low-frequency regimes.

Chapter 4

Optimization of Control Configuration

As reviewed in Chapter 2, many previous attempts at active flow control have tended to be DNS studies, where the implementation of the physical control architecture has not been a concern. The physical implementation of an active flow control strategy encounters two major challenges which are avoidable in simulations, **(i).** real-time flow estimation, **(ii).** actuation latency owing to the real-time flow estimation and the mechanical response of the sensor and actuators. A common solution, as mentioned in §3.3, is to employ a non-intrusive flow observing instrument located a certain physical distance upstream of the actuators. For example, Rathnasingham and Breuer (1997) and Rebbeck and Choi (2001) both utilized a hot-wire probe protruding perpendicularly from the wall to detect the oncoming near-wall flow (to provide real-time flow estimation) and their actuators were positioned 300 and 72.5 viscous wall units downstream, respectively (to account for actuation latency). Similarly, Abbassi et al. (2017) used flush-mounted hot-film sensors to observe the friction velocity 1.65δ upstream of their actuators, which is similar to the configuration used here.

For an accurate actuation, a real-time filter is required to retain the coherent signals between the sensor and actuator pairs. Therefore, the sensor-actuator separations are designed to accommodate the convection of the cross-flow during the actuation latency, which is defined as the combined latency due to the computational delay of the real-time filtering and the mechanical delay of the actuators. Since the structures controlled by Rathnasingham and Breuer (1997) were larger than those targeted by Rebbeck and Choi (2001), the larger filtering delay necessitated that their actuators were placed further downstream to account for the latency. In addition, the sensor-actuator separation in the control architecture of Abbassi et al. (2017) is much longer than those of the previously cited examples since the controller was designed to target outer-scaled (δ-scaled)

structures which required a much larger real-time filter to detect. However, a larger separation inevitably leads to a loss of flow coherence between the detection and actuation positions, influencing the efficacy of the flow estimator and potentially reducing the control efficacy. The study of Abbassi et al. (2017) did not consider the dilemma caused by all these aspects for the optimized control configurations. In this chapter, to address this gap, we take the control architecture introduced in §3.3 as an example to introduce a systematic methodology of optimizing active control configurations. At the end of this chapter, the resulting enhancement in the control effect is demonstrated.

4.1 Simultaneous Hot-film and Hot-wire Measurements

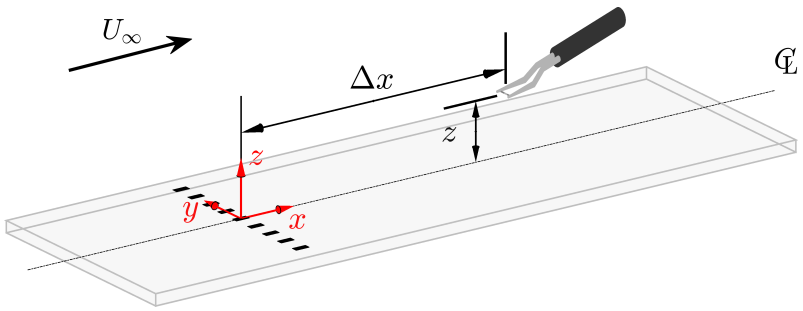
U_∞
Δx
z
z
y
x
$\mathbb{C}\!\!\!

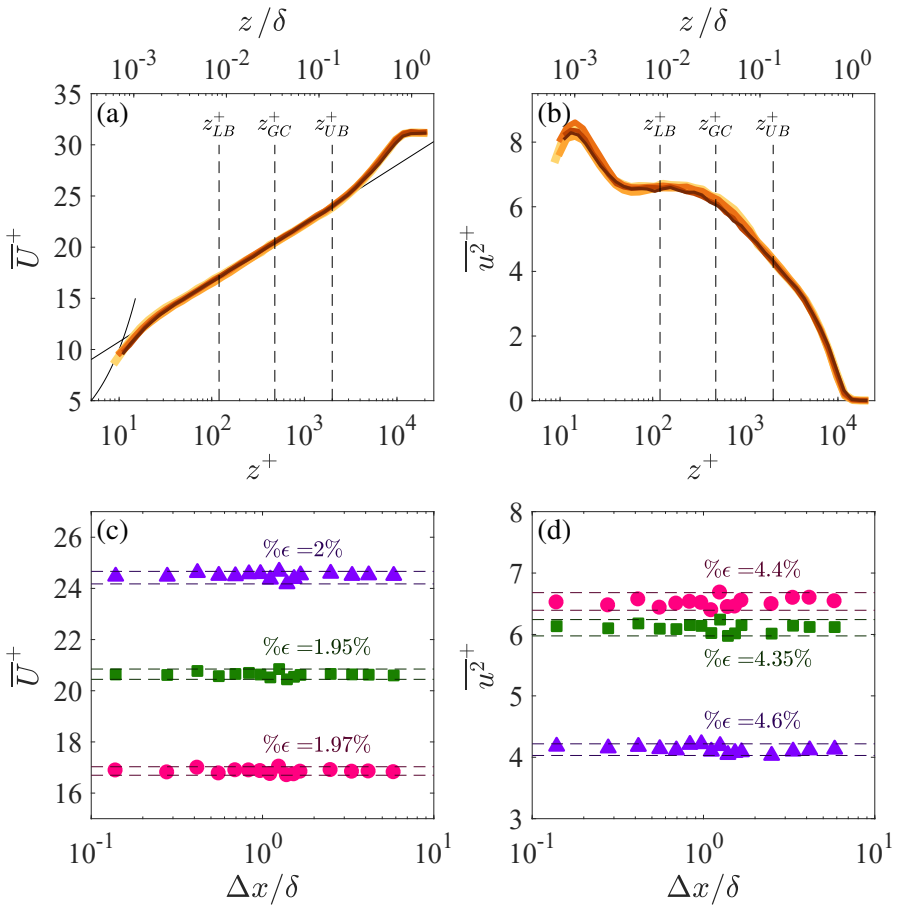

Figure 4.2: Hot-wire acquired inner-scaled mean streamwise velocity and streamwise turbulent intensity profiles (a,b) against z in all *type I* measurements; (c,d) against Δx in all *type II* measurements.

velocity field. The downstream hot-wire probe is aligned with the middle hot-film sensor in the spanwise direction, which locates it at the centreline of the tunnel. The streamwise velocity signal from this traversing hot-wire probe is acquired, simultaneously with the hot-film array, at a grid of streamwise (Δx) and wall-normal positions (z) downstream of the u_τ sensors. Subsequently, the evolution of the coherent structures can be studied by considering the correlation between the u and u_τ signals. The signals are sampled for 360 seconds in each position, which results in over 14000 boundary layer turnovers and ensures converged statistics of the largest scale coherent structures. More detailed specifications of the hot-wire and hot-film can be found in §3.2.

The experiments are categorized into two different types depending on how the hot-wire maneuvers in the boundary layer. For *type I* measurements the hot-wire probe acquires boundary layer

profiles at different streamwise positions downstream of the hot-film array traversing in the wall-normal direction at 40 logarithmically spaced positions between 300μm ($z^+ = 10$) and 0.525m ($z = 1.5\delta$). The streamwise separation Δx between the hot-wire and hot-film array ranges from 0 to almost 6δ to capture the entire life-cycle of the coherent structures especially for the LSMs and VLSMs with a length-scale of $\mathscr{O}[\delta]$. In specific, the values for Δx are chosen as 0, 0.3, 0.6, 0.9, 1.2, 1.5, and 2.1 meters ($\Delta x/\delta = 0$, 0.85, 1.7, 2.5, 3.3, 4.2 and 5.8). Note that the experiments are performed with the hot-film array located 19.8 meters downstream of the boundary layer trip at a relatively low free stream velocity $U_\infty \approx 20$m/s so that the development of the boundary layer in the x direction over $Deltax = 5.8\delta$ is relatively negligible. Thus, we can assume, with little loss of accuracy, streamwise homogeneity to neglect variation of δ and u_τ with Δx. The mean velocity profiles and turbulent intensity curves acquired by the hot-wire in all *type I* experiments are illustrated in figure 4.2(a,b). Good alignment is observed among the boundary layer profiles, especially at the wake region of the mean velocity profiles, which implies an invariant Re_τ at different measurement stations and validates this above assumption of streamwise homogeneity.

To better resolve the evolution of the coherent structures, in *type II* experiments the hot-wire is held at a constant z and traversed in x with a finer 0.05m increment between 0 to 0.6 meters downstream of the hot-film array (i.e. $0 < \Delta x/\delta < 1.7$). A summary of the key experimental parameters and flow conditions, as well as the symbols for each measurement, are available in table 4.1. Since the large-scale active flow control strategy mainly aims to reduce the skin-friction drag via manipulating the LSMs and VLSMs, which are most energetic in the logarithmic region of

Table 4.1: Key experimental parameters and flow conditions for the simultaneous hot-film and hot-wire measurements

Type	U_∞ [m/s]	δ [m]	U_τ [m/s]	Re_τ	Δx [m]	z [mm]
I	20.2	0.36	0.65	14300	0 (—), 0.3 (—), 0.6 (—), 0.9 (—), 1.2 (—), 1.5 (—), 2.1 (—)	40 logarithmically spaced points between 0.3mm to 525mm
II	20.3	0.36	0.64	14200	0 to 0.6m with an increment of 0.05m	2.5 (●), 12 (■), 50.7 (▲)

a turbulent boundary layer, the *type II* measurements are repeated at three significant z positions, namely the lower bound, geometric center and upper bound of the logarithmic region, respectively. The estimation of the log region, especially the lower bound varies significantly in studies (compare for example Hutchins and Marusic (2007a), Klewicki et al. (2007), Marusic et al. (2013)). Here, we adopt the definition by Mathis et al. (2009) that the log region ranges between $z^+_{LB} = 120$ and $z^+_{UB} = 0.15\mathrm{Re}_\tau = 2000$ and centres at $z^+_{GC} = 3.9\sqrt{\mathrm{Re}_\tau} = 480$ and these values are highlighted as the black dashed-lines in figure 4.2(a,b). For other control techniques targeting different parts of the boundary layer, the z value should be adjusted correspondingly. To validate the consistency of the inner-scaled wall positions z^+ throughout each *type II* measurement, figure 4.2(c,d) illustrates how the $\overline{U}^+$ and $\overline{u^2}^+$ changes with respect to Δx. It is observed that the variations of the $\overline{U}^+$ and $\overline{u^2}^+$ reside within 2% and 5% error bands, respectively, which again provides support for the assumption that streamwise homogeneity over the $]deltax$ range in *type II* measurements. The friction velocity here is determined based on the mean skin-friction velocity acquired by the upstream hot-film sensors. Moreover, since the hot-wire probe does not reach the free-stream in *type II* measurements, the mean boundary layer thickness measured from all seven *type I* measurements is adopted as the canonical boundary layer thickness for *type II* measurements.

4.2 Evolution of Large-scale Motions

The underpinning physics of the flow estimation using flush-mounted hot-film sensors is the AEH established by Townsend (1976) and developed by Perry and Chong (1982). This hypothesis suggests that the near-wall flows consist of the superimposed velocity fields due to hierarchies of self-similar eddies. These eddies with length-scales proportional to their wall-positions are attached to the wall. Despite the random spatial distribution, these large eddies are self-similar and persistent in the boundary layer. Based on the self-similarity, the inner-outer interaction model of Marusic et al. (2010) and the refined spectral stochastic estimation model of Baars et al. (2016) successfully predict the velocity fluctuations near the wall using a reference signal measured in the log region. Conversely, an observation of the near-wall turbulence (as is made here via the hot-film array) also carries information on the attached coherent structures in the log region. However, in real-time control, a streamwise separation is inevitably required between the observers

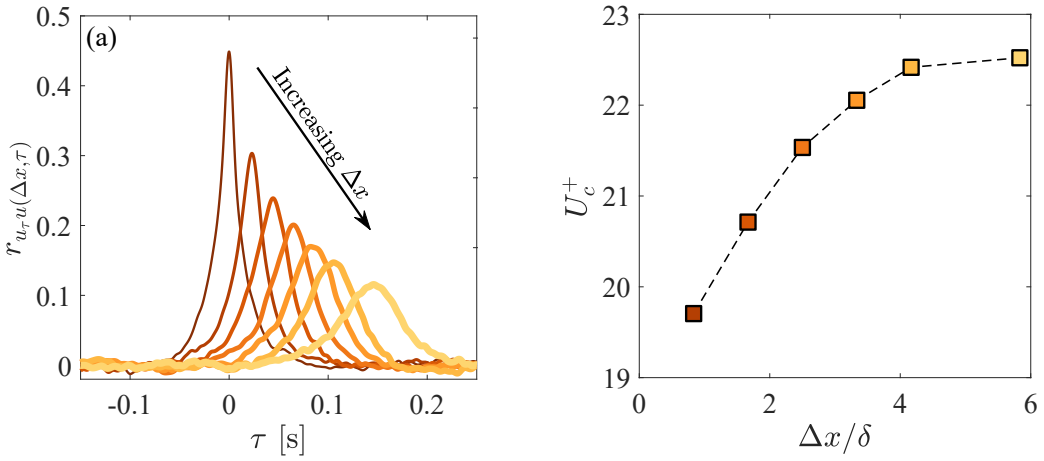

Figure 4.3: (a) Two point cross-correlation, $r_{u_\tau u}$, between u_τ at the centreline of the upstream hot-film array and u measured with increasing streamwise separation, Δx, at fixed $z_i^+ = 10$. (b) The convection velocity U_c of the coherent structures are calculated at each measurement station.

and the point of actuation to account for latency and structural inclination. Hence, prior to the optimization process, the streamwise evolution of the coherent structures is discussed in this section to understand the observability of structures with different length-scales. This is surveyed via the variation of the correlation between the u_τ and the u signals acquired from the measurements listed in table 4.1.

Figure 4.3 shows the temporal two-point correlation function $r_{u_\tau u}(\Delta x, \tau)$ between the hot-film sensor on the centreline and the hot-wire probe at all measurements stations with $z^+ = 10$, which is calculated as equation 4.1

$$r_{u_\tau u}(\Delta x, \tau) = \frac{\overline{u_\tau(t) \cdot u(\Delta x, t+\tau)}}{\sqrt{\overline{u_\tau^2(t)}} \cdot \sqrt{\overline{u^2(\Delta x, t+\tau)}}} \tag{4.1}$$

where τ is the time delay between the signals. Figure 4.3(a) shows that the maximal correlation coefficient decreases as the separation Δx between the hot-wire and the hot-film array increases, which indicates the ejection of certain coherent structures during the convection. The time delay between the peak correlation of $\Delta x = 0$ and all other cases (τ_{max}) are caused by the combination of streamwise convection (τ_c) and the structural inclination angle (τ_i), which is $\tau_{max} = \tau_c + \tau_i$. As the study is interested in the length-scale based information of the coherent structures, it is crucial to determine convection velocities to convert τ_{max} to the spatial domain. Typically assigning the local mean velocity, $\overline{U}(z)$, as the convection velocity of the hot-wire signals will result in decorrelation

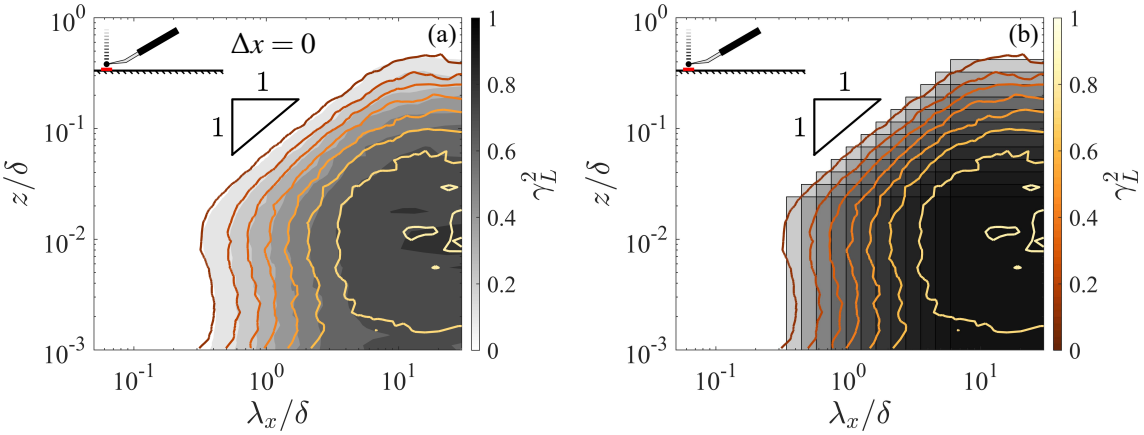

Figure 4.4: (a) Iso-contour (gray-scaled) of the coherent spectrum between two simultaneously measured streamwise velocity fluctuations by a hot-wire near the wall at $z^+_{ref} = 4$ and another hot-wire traversing between $8 < z^+ < 14000$ at the same streamwise location z^+ (Baars et al., 2017a); Iso-contour (coloured solid lines) of the coherent spectrum between simultaneously measured skin-friction velocity $u_\tau(\Delta y = 0)$ by the centre hot-film probe on the wall and the streamwise velocity fluctuation $u(\Delta x, z)$ measured by the hot-wire probe traversing between $8 < z^+ < 14000$ without streamwise separation. (b) Schematic of hierarchy-decomposed coherent spectrum resulted from attached-eddy hypothesis (Baars et al., 2016).

of the structures with increasing Δx, owing to the varying velocity deficit at different wall-normal positions. Instead, a composite method that deploys different convection velocities to τ_c and τ_i respectively is implemented in the current study. In terms of τ_i, Taylor frozen hypothesis is employed, $\Delta x_i(z) = -\tau_i U_c$, since the structures pass through the hot-wire probe positioning at fixed locations (Taylor, 1938). In contrast, τ_c is purely resulted from the physical displacement of the turbulent structures, which can be expressed as $U_c = \Delta x / \tau_c$. Here, U_c is the convective velocity of the coherent motions. Remember that the cross-correlations in figure 4.3(a) are computed between the signals with a limited wall-normal height difference (8 viscous units). Thus, the time delay due to the inclination angle is negligibly small and τ_{max} is predominantly comprised of τ_c. Using the relationship, figure4.3(b) provides a first glimpse on the convection velocity from the *type I* measurement stations. Similar to the observation of Hutchins et al. (2011), the measured convection velocity U_c increases with increasing Δx location. This implies the smaller eddies, which will decorrelate during the streamwise evolution possess a slower convection velocity than the more persistent (presumably larger) structures. Since del Álamo and Jiménez (2009) reported that the convection velocity is positively proportional to the structural streamwise and spanwise wavelengths, we might speculate that a structure with a longer streamwise wavelength is more

enduring and convects at a higher pace in wall-bounded boundary layers.

However, one disadvantage of the temporal two-point correlation is that, as a function of τ, it autonomously mixes the contribution from a broad range of wavelengths and frequencies. Therefore, it is hard to determine which structures predominantly contribute to the degradation of the cross-correlation. In turn, it can only provide qualitative insights on the streamwise evolution of the LSMs. In order to verify the observation and quantitatively formulate its trend, the coherence analysis is further performed in the frequency domain. It employs the spectral linear stochastic estimation (sLSE) to assess the correlation between the upstream skin-friction velocity and the streamwise velocity fluctuations downstream in the entire turbulent boundary layer. Referring to Baars et al. (2017a), such spectral correlation is known as the coherence spectrum, γ_L^2, which is defined as,

$$\gamma_L^2\left(\Delta x,\Delta y,z,\lambda_x\right)=\frac{\left\langle \mathscr{F}\left[u_\tau\left(\Delta y,\lambda_x\right)\right]\mathscr{F}^*\left[u\left(\Delta x,z,\lambda_x\right)\right]\right\rangle \left\langle \mathscr{F}\left[u_\tau\left(\Delta y,\lambda_x\right)\right]\mathscr{F}^*\left[u\left(\Delta x,z,\lambda_x\right)\right]\right\rangle^*}{\left\langle \mathscr{F}\left[u_\tau\left(\Delta y,\lambda_x\right)\right]\mathscr{F}^*\left[u_\tau\left(\Delta y,\lambda_x\right)\right]\right\rangle \left\langle \mathscr{F}\left[u\left(\Delta x,z,\lambda_x\right)\right]\mathscr{F}^*\left[u\left(\Delta x,z,\lambda_x\right)\right]\right\rangle} \tag{4.2}$$

where, $\mathscr{F}\left[\bullet\right]$ is the Fourier transformation of the temporal signals. For example, $\mathscr{F}\left[u\left(\Delta x,z\right)\right]$ is the Fourier transformation of the streamwise velocity fluctuation, $u\left(\Delta x,z\right)$. The asterisk sign $*$ denotes complex conjugate, while the angle bracket $\langle\rangle$ notates the ensemble averaged results. The frequency, f, of the acquired temporal signal is transferred to spatial streamwise wavelength, λ_x using the local mean velocity measured by the hot-wire probe, such that $\lambda_x(z)\equiv\overline{U}(z)/f$. We mention that the numerator of equation 4.2 is the squared magnitude of the co-spectra between the skin-friction and streamwise velocity fluctuations, $\phi_{u_\tau u}$, and the denomenator is the multiplication of their energy spectrum, $\phi_{u_\tau u_\tau}$ and ϕ_{uu}, respectively, which means the coherence spectrum, γ_L^2, is a normalized quantity. Hence, its range will be limited between 0 and 1 across the entire range of λ_x and z and a higher magnitude of γ_L^2 reflects a better scale-based coherence between the $u_\tau(\Delta y)$ and $u(\Delta x,z)$ signals at the corresponding wavelengths and wall-normal location z.

The coloured contour lines in figure 4.4(a) present the coherence spectrum between the u_τ measured by the middle hot-film (HF_5) and u measured by the traversing hot-wire at $\Delta x=0$. As a comparison, the gray-scaled surface contour is the same spectrum at a comparable Reynolds number but computed between the two hot-wire velocity signals measured at a fixed near-wall position

($z^+_{ref} = 4$) and the entire boundary layer, respectively (Baars et al., 2016). Though the temporal response of the hot-film probes is commonly recognized as unreliable at high-frequencies the coherence spectrum in figure 4.4(a) displays good agreement. This is because only the structures with streamwise wavelength $\lambda_x > 0.3\delta$ attain a coherence level greater than 0.1 and the hot-film signal is considered trustworthy at such wavelengths ($f < 120\,\mathrm{Hz}$, corresponding here to $\lambda_x/\delta > 0.3$). This also validates the feasibility to employ hot-film sensors to collect the referencing skin-friction velocity fluctuation on the wall for the spectral analysis. Baars et al. (2017a) argued that the vanishing of the coherence in the range $\lambda_x \leq 0.3\delta$ and $z^+ < 200$ in figure 4.4(a) is because of the misalignment of the sensors in a spanwise direction, due to both the set-up error and spanwise oscillation of the probe near the wall. As reported by Baidya et al. (2019) and Samie et al. (2020), even a small spanwise offset between the skin-friction sensors also leads to a dramatic attenuation in near-wall coherence. Nonetheless, the vanishing small-scale coherence for $z^+ < 200 (z/\delta < 0.015)$ suggests that when the flush-mounted hot-film sensors are used for flow detection, the minimal observable structures in the boundary layer will have $\lambda_x > 0.3\delta$. In turn, for a sensible active flow control strategy, the targeted structures ought to be restricted by this threshold.

Moreover, the key feature reflected by the coherence spectrum shown in figure 4.4 is the self-similarity of the attached eddies, which is implied by the one-to-one slope of the iso-contour within the logarithmic region (i.e. $10^{-2} < z/\delta < 0.3$). In other words, the aspect ratio between streamwise wavelength and the wall-normal height of structures with different length-scales maintains invariant, $AR \approx 14$. Based on the attached eddy hypothesis, Baars et al. (2017b) decomposes the coherent spectrogram into the contribution from the discrete hierarchy of self-similar eddies. Hierarchy 1, corresponding to the smallest structure with the presence of coherence in figure 4.4(a), has a streamwise wavelength of $\lambda_{x,h1} = 0.3\delta$ and a wall-normal extent of $z_{h.1} = 0.023\delta$. Owing to self-similarity, the size of higher hierarchy i amplifies in both streamwise and wall-normal direction by $c^{(i-1)}$, where c is the geometric ratio between the i^{th} and $(i+1)^{\text{th}}$ hierarchy. Due to the random spatial allocation of the attached eddies in the turbulent boundary layer, a selected ith hierarchy will resulted in a uniform contribution to the coherent spectrogram for the region, $\lambda_x > c^{(i-1)}\lambda_{x,h.1}$ and $z < c^{(i-1)}z_{h.1}$. As the self-similar eddies with different hierarchies are considered uncorrelated with each other (Woodcock and Marusic, 2015), the coherent spectrogram

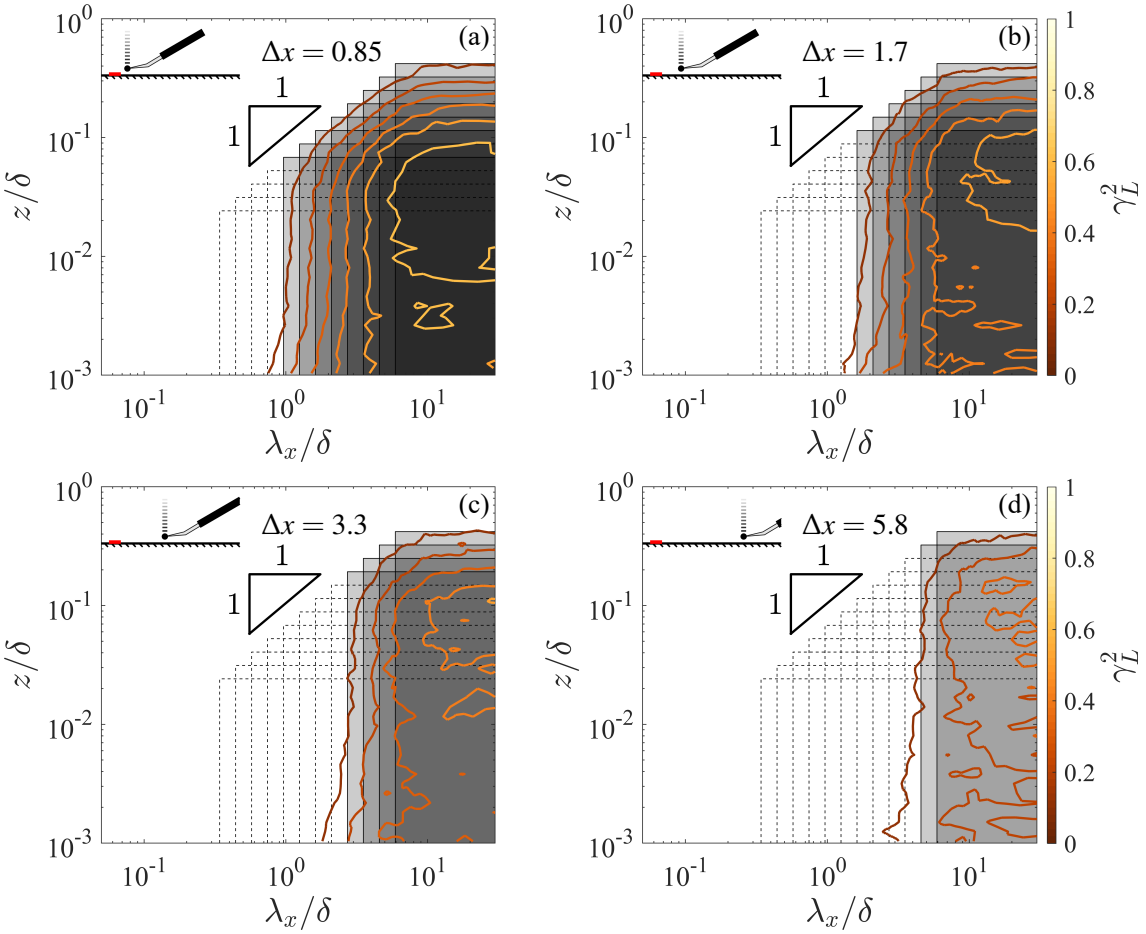

Figure 4.5: Iso-contours (coloured solid lines) of the coherent spectrum between simultaneously measured skin-friction velocity $u_\tau(\Delta y = 0)$ by the centre hot-film probe and the streamwise velocity fluctuation $u(\Delta x, z)$ measured by the hot-wire probe traversing between $8 < z^+ < 14000$ at $\Delta x =$ (a) 0.3, (b) 0.6, (c) 1.2, and (d) 2.1 meters downstream. Gray-scaled blocks is the decomposition of the spectrogram using the same methodology in figure 4.4(b).

could be reconstructed via a linear superposition of the coherence attributed by every single hierarchy. An example of the discretization is performed in figure 4.4(b), using totally 12 hierarchies with the geometric ratio c equivalent to 1.3. Note, the selection of the ratio is arbitrary. While the conventional geometric ratio in most research is 2, the chosen value ($c = 1.3$) is for a clear demonstration of the hierarchical evolution of the γ_L^2 contour.

Figure 4.5 displays the coherent spectrum between the u_τ and u with Δx as 0.85δ, 1.7δ, 3.3δ and 5.8δ, respectively. It is obvious that the minimum wavelength of the structures, which maintains $\gamma_L^2 > 0.1$, increases with increasing streamwise separation $]Deltax$ between the hot-film

array and the traversing hotwire sensor. However, the one-to-one slope is still preserved in figure 4.5(a,b,c), which indicates that the self-similarity still holds within the persisting structures,at least up to $\Delta x/delta = 6$ (Baars and Marusic, 2020, Krug et al., 2019). In figure 4.5(a), by discretizing the coherent spectrogram with the identical $\lambda_{x.h1}$ and c values (as shown by grey filled and dotted contours), we demonstrate that the smallest four hierarchies (shaded grey filled solid contours) become uncorrelated, whereas all remaining higher hierarchies (blocks with black-solid edges) preserves the same level of coherence as in figure 4.4(b). This suggests that the lifetime of coherent structures with a streamwise wavelength, $\lambda_x < 0.8\delta$ limits their trackable streamwise evolution to $Deltax/\delta < 0.8$. Applying the same discretization process for larger streamwise separation in figure 4.5(b,c), more hierarchies disappear, which verifies the hypothesis from the two-point correlation that the lifetime of the LSMs and, hence downstream streamwise coherence increases with the scale of these structures (i.e. increasing λ_x). It is noted that the maximum γ_L^2 contours seem to shift to higher wall-normal positions with increasing Δx. This suggests that the deformation of the LSMs initiates at the near-wall region and propagates to the log region. This is arguably attributed to the mechanism of the formation of the LSMs and VLSMs, which have been suggested to form through a concatenation of hairpin vortices with different length-scales (Adrian et al., 2000). The smaller of these hairpin vortices, which are predominately located closer to the surface, will experience the most rapid decorrelation with increasing Δx. Newly emergent and randomly located smaller-scale hairpin vortices will also affect the coherence for the larger LSMs, but only localized in the near-wall region. When Δx is further increased to 5.8δ, the missing coherence now extends to the highest hierarchy ($\lambda_{x.h12} > 6\delta$) and the one-to-one slope between λ_x and z is in this case barely observed. This is because, as only the largest VLSMs correlate between the upstream hot-film and downstream hot-wire probes, the self-similarity can no longer be captured by the coherence spectrogram (there is no remaining hierarchy of correlated scales).

The results from *type I* measurements are sufficient to verify the conjecture. To further formulate the relationship between Δx and the decay of the scale-based coherence, additional Δx values with finer increments are tested in *type II* measurements. Ultimately, these measurements offer additional insight on the influence of the streamwise wavelength λ_x of LSMs on their lifetime. Figure 4.6(a) demonstrates the variation of the coherent spectrum between the skin-friction velocity fluctuation u_τ and the streamwise velocity fluctuations downstream $u(\Delta x)$ at the lower-bound

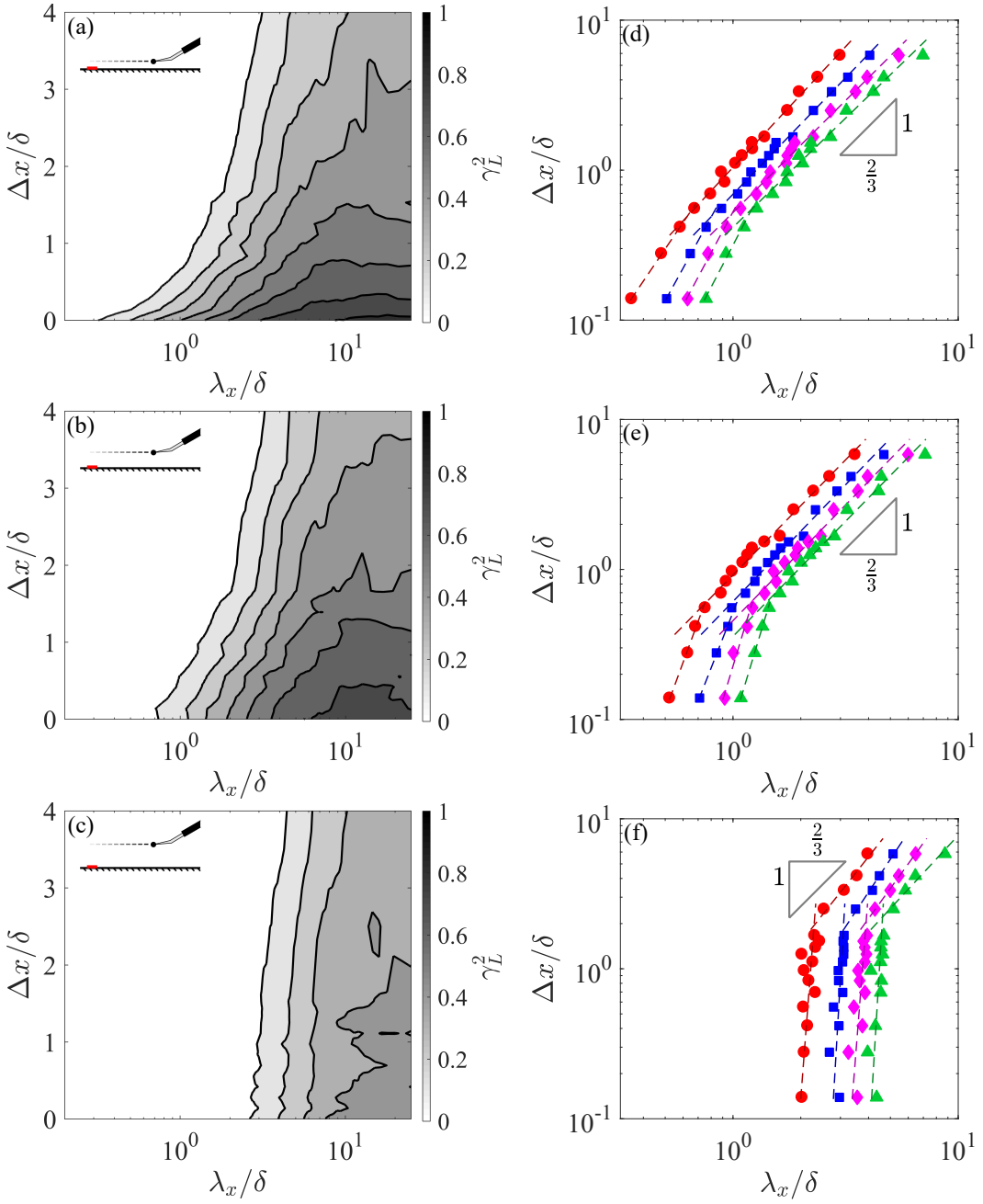

Figure 4.6: Iso-contour of the coherent spectrum between simultaneously measured skin-friction velocity $u_\tau(\Delta y = 0)$ by the centre hot-film probe on the wall and the streamwise velocity fluctuation $u(\Delta x, z)$ measured by the hot-wire probe fixed at (a) $z^+ = 120$, (b) $z^+ = 3.9\sqrt{\mathrm{Re}_\tau} = 480$ and (c) $z^+ = 0.15\mathrm{Re}_\tau = 2000$, respectively. Δx ranges between 0 and 0.6m with a step of 0.05m, additional *type I* data included at $\Delta x = 0.9$, 1.2, 1.5, 2.1m. (d,e,f) Adapted iso-contour lines of $\gamma_L^2 = 0.05$ (●), 0.1 (■), 0.15 (♦) and 0.2 (▲) from the spectrogram in (a), (b) and (c), respectively, and plotted with logarithmic ordinate.

of the log region ($z^+ \approx 100$). Comparable figure are provided for the centre ($z^+ = 3.9\sqrt{\mathrm{Re}_\tau} \approx 480$) and the upper bound ($z^+ = 0.15\mathrm{Re}_\tau \approx 2000$) of the log region in figure 4.6(b,c) respectively. Close to the wall, the coherence of the LSMs deteriorates immediately after a small Δx is engaged. In contrast, at the outer bound of the log region, the coherence remains invariant even for larger streamwise separations, and the decay is only visible after $\Delta x > 1.5\delta$. This further suggests that the structures with larger streamwise wavelength λ_x have a longer lifetime. Owing to the aspect ratio between the streamwise wavelength and the wall-normal extension of the attached eddies, the deformation of the smaller LSMs initiating near the wall is undetectable from the hot-wire probe located at the upper-bound of the log region in figure 4.6(c). Figure 4.6(d,e,f) extract present four extracted contour lines ($\gamma_L^2 = 0.05$, 0.1,0.15 and 0.2) from the coherent spectrogram shown in figure 4.6(a,b,c), respectively. The consistent slope of each contour level indicates that the coherent structures have a time-scale or downstream persistence that is proportional to their streamwise wavelength (λ_x). The minimum length-scale of the intact coherence structures increases exponentially with their streamwise convecting distance. Such a relationship can be described as,

$$\log\left[\frac{\lambda_{x.c}(\gamma_L^2, z^+)}{\delta}\right] = C_1 \log\left[\frac{\Delta x}{\delta}\right] + C_2\left(\gamma_L^2, z^+\right) \tag{4.3}$$

where $\lambda_{x.c}(\gamma_L^2, z^+)$ is the minimum length-scale of the coherent structures that retain a coherence level of $\gamma_L^2 > 0,05$ at the wall-normal position of z^+ and the downstream advection distance δx. The exponential constant between the quantities, $C_1 = \frac{2}{3}$, is invariant at all coherence levels and the examined wall-normal positions. In contrast, C_2 increases with the coherence level and decreases with the selected wall-normal position. With a minimal coherence level ($\gamma_L^2 = 0.05$) near the wall ($z^+ = 100$), C_2 is estimated to be 0 and it has an increment of $4.6\gamma_L^2$. The expression is physically reasonable, as the coherent structures with a streamwise wavelength of 1δ will at least maintain correlation in the boundary layer for over 1 boundary layer turnover during the convection. Owing to the less than unity slope $C_1 = 0.67$, VLSMs are expected to survive much longer than their length-scale in the boundary layer. Since the average λ_x of the VLSMs in a high Reynolds turbulent boundary layer approximately $\lambda_x = 6\delta$ (Hutchins and Marusic, 2007a), it could be predicted that, only when the streamwise separation $\Delta x/\delta$ exceeds a threshold of $\Delta x/\delta \geq 6^{1/C_1} \approx 14$, will no correlation be detected.

Convection velocity of coherent structures is critical in the study of turbulence, especially after

Taylor (1938) expressed the flow field in the boundary layer as a group of frozen eddies. Previous research has demonstrated that the convective velocity of the LSMs increases with the streamwise wavelength of the coherent structures (del Álamo and Jiménez, 2009, Liu and Gayme, 2020). In addition, Hutchins et al. (2011) reported that U_c of large-scale skin-friction footprints in a high Reynolds number turbulent boundary layer can be approximated by the mean streamwise velocity located at the center of the log region (the geometric center of the LSMs and VLSMs).

$$U_c^+ = \frac{1}{\kappa}\log\left(\sqrt{15\mathrm{Re}_\tau}\right) + A \tag{4.4}$$

The value is obtained by equating the U_c of raw u_τ and large-scale filtered u_{τ_l} with a cut-off wavelength of 1δ. Thus, equation 4.4 describes the averaged convection velocity of the LSMs with $\lambda_x \geq \delta$. The measurements of Hutchins et al. (2011) consider a streamwise separation range of $0.1 \leq \Delta x/\delta \leq 0.75$ and a lumped range of scales $\lambda_x > \delta$. However, for a larger Δx, accelerated convection velocity is observed in figure 4.3(b) when the large-scale structures start to lose their coherence. The varying convection velocities reflect the varying streamwise coherence and varying convection velocity of different scales. This suggests that the available data from the *type I* and *type II* measurements affords the opportunity to quantify the scale dependent convection velocity $U_c(\lambda_{x.c})$ for the LSMs have streamwise wavelengths greater than $\lambda_{x.c}$. Using equation 4.3 with the selected coherence level of $\gamma_L^2 = 0.05$, we convert the x-axis of $\Delta x/\delta$ in figure 4.3(a) into λ_x/δ in figure 4.7. Owing to the self-similarity of the coherent structures, the geometric centre of the LSMs increases with increasing λ_x and the local mean velocity at the elevated geometric centre will increase accordingly. As the LSMs with smaller wavelengths detected by the upstream hot-films vanish during the advection, figure 4.7 demonstrates that convection velocity U_c is logarithmically proportional to the minimal length-scale of the correlating structures $\lambda_{x.coh}$ in the boundary layer. This further implies that the convection velocity of the LSMs with different length-scales are equivalent to mean streamwise velocity at their own geometric centre, which can be formulated as equation 4.5,

$$U_c^+(\lambda_{x.c}) = \frac{1}{\kappa}\log\left(\sqrt{15\mathrm{Re}_\tau}\right) + A + \frac{1}{\kappa}\log\left(\frac{\lambda_{x.c}}{\delta}\right) + C_3 \tag{4.5}$$

Here, the value of κ and A are selected as 0.384 and 4.17, respectively. Applying equation 4.4

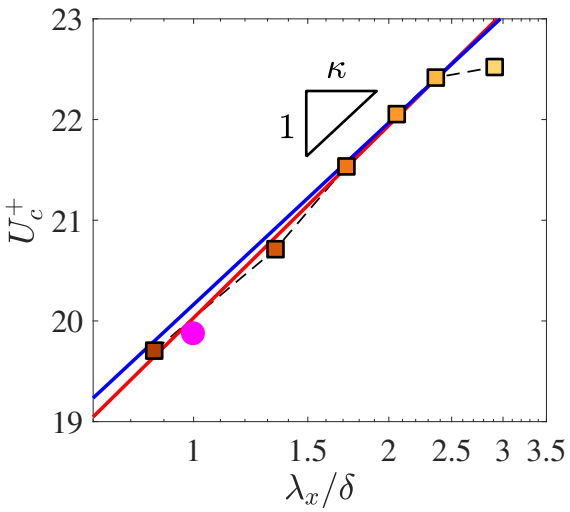

Figure 4.7: Square markers are the convective velocity U_c of the coherent structures with a streamwise wavelength greater than λ_x computed from the simultaneous hot-wire and hot-film measurements. Red solid line (−) is the linear fit of the data points. Magenta circle is the convective velocity reprted by (Hutchins et al., 2011) for coherence structures with $\lambda_x > 1\delta$. Blue solid line is the graphical interpolation of equation 4.5.

as the boundary condition for the estimation (i.e. $U_c^+(\delta) = \frac{1}{\kappa}\log\left(\sqrt{15\mathrm{Re}_\tau}\right) + A$), the constant C_3 is determined to be 0. We present the equation as the blue solid line in figure 4.7, which shows a good agreement with the linear fit of the U_c^+ calculated from all *type I* measurements (red solid line). Such a scale dependence of the convective velocity is also observed by Liu and Gayme (2020) via an input-output based model in a turbulent channel flow. However, it is noticed that this trend from figure 4.7 ceases for structures with $\lambda_x \geq 3\delta$. A similar observation was made by del Álamo and Jiménez (2009), where they noted that eddies with streamwise wavelength large than double of the channel height have a uniform convection velocity. In addition, it has been suggested by Adrian et al. (2000) that the VLSMs with $\lambda_x \geq 3\delta$ are formed by aggregations of LSMs with shorter λ_x. Under this conjecture, we would expect the convection velocity of VLSMs to be bound by the size of the largest LSMs. While the attached eddy model focuses on the geometric and spatial arrangement of the LSMs, equation 4.3 and 4.5 could improve the model by providing information on the life-cycle and temporal evolution of the coherent structures in turbulent boundary layers. More importantly, for this study, in terms of active flow control strategies, the following section introduces how the optimized sensor-actuator separation and the corresponding cut-off wavelength of the real-time filter are derived from the above expressions.

4.3 Optimized Configuration and System Identification

According to the correlation deterioration reported in the previous section, in active flow control strategies, smaller sensor-actuator separation (Δx_a) is preferred to enhance the coherence magnitude between the points of detection and actuation. However, the minimum Δx_a is constrained by the actuation delay τ_a. As discussed in chapter 3, the actuation delay consists of the mechanical response of the actuators τ_m and the computational delay due to the real-time computation and filtering τ_f, which because of the real-time filter will increase with the increasing scale of the targeted structure λ_x. Thus, the lower bound of Δx_a is given by the streamwise distance that the targeting structures travel within the actuation delay, which is expressed as

$$\Delta x_a \geq \tau_a U_c = (\tau_m + \tau_f) U_c \tag{4.6}$$

As indicated by equation 4.5, the convective velocity U_c here is dependent on the cut-off wavelength of the real-time filter $\lambda_{x.c}$, as if the filtering delay τ_f, while the mechanical response time of the actuators τ_m is invariant. A typical causal FIR filter to convolve the temporal signals in real-time leads to a filtering delay equal to half of the filter length as,

$$\tau_f = \frac{\lambda_{x.c}}{2U_c} \tag{4.7}$$

When we substitute the functions of U_c (equation 4.5) and τ_f (equation 4.7) into the lower bound expression of the sensor-actuator separation (equation 4.6) and we can obtain the lower bound of δx_a as followed,

$$\frac{\Delta x_a}{\delta} \geq \underbrace{\frac{\tau_m {U_\tau}^2}{\nu} \frac{1}{\mathrm{Re}_\tau} \left[\frac{1}{\kappa} \log\left(\sqrt{15\mathrm{Re}_\tau}\right) + A + \frac{1}{\kappa} \log\left(\frac{\lambda_{x.c}}{\delta}\right) \right]}_{\textbf{Component I}} + \underbrace{\frac{1}{2}\frac{\lambda_{x.c}}{\delta}}_{\textbf{Component II}} \tag{4.8}$$

where the component I and component II are resulted from mechanical delay τ_m and computational delay τ_f, respectively. The existence of Re_τ and U_τ in the above inequality is due to the inner-scaled U_c that appears in equation 4.5. In contrast, as shown in figure 4.6, the sensor will carry no useful information for actuation if the separation is excessively large since the structures at the actuator location will be totally uncorrelated the detected passage of skin-friction footprints as the

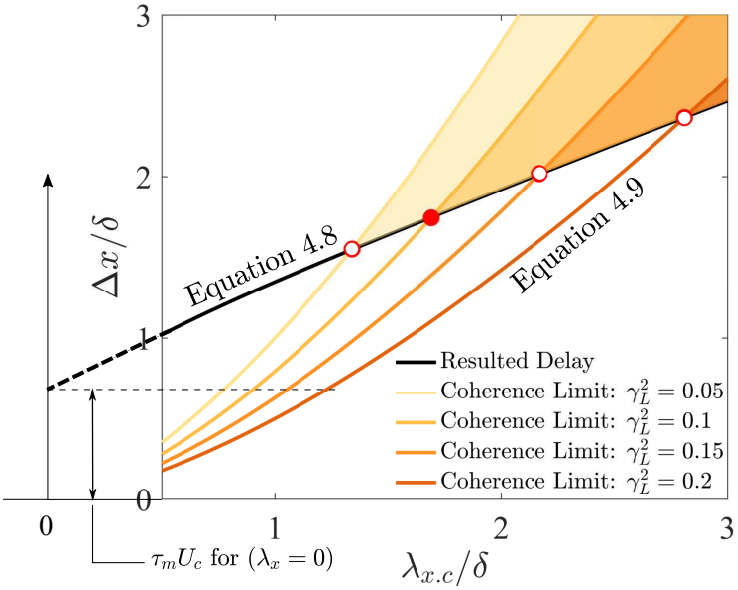

Figure 4.8: Black solid line shows the minimal sensor-actuator separation required to accommodate the temporal actuation delay of the flow control strategy as given by equation 4.8. Colored solid lines are the maximal streamwise wavelength which maintains a selected level of coherence over the streamwise separations as given by equation 4.9. The red dots are the interactions between equation 4.8 and equation 4.9 at a given retained coherence level 0.05, 0.15 and 0.2 (○) and over the separation Δx. For the current study, a coherent level of 0.1 (●) is used for the optimal combinations between the cut-off wavelength of the real-time filter $\lambda_{x.c}$ and the sensor-actuator separation Δx_a.

detection array. This suggests the upper bound of Δx_a, which can be derived from equation 4.3 as,

$$\frac{\Delta x_a}{\delta} \leq \exp\left[-C_2\left(\gamma_L^2, z^+\right)\right]\left(\frac{\lambda_{x.c}}{\delta}\right)^{1.5} \tag{4.9}$$

As discussed previously for equation 4.3, the value of C_2 depends on the value of the chosen spectral coherence level γ_L^2 as also the z location of the traversing hot-wire sensor. Figure 4.8 illustrates the example optimization process for the current active large-scale flow control strategies. As introduced in §3.3, the mechanical delay, which is defined as the latency of actuation from the time a binary "on" control signal (1) is sent from the *Speedgoat* target computer to the solenoid valve, is 22.4ms (600 viscous time units). The friction Reynolds number Re_τ is 14400 with the mean shear velocity $U_\tau = 0.64$m/s. In figure 4.8, the black solid line indicates the minimum Δx_a required to ensure a punctual actuation as given by equation 4.8, whereas the coloured solid lines are the upper bounds of Δx_a that permit the detected LSMs to retain a certain coherence levels

(as given by equation 4.9. A reasonable combination of Δx_a and $\lambda_{x.c}$ should locate in the shaded region of this parameter space with the optimized location being on the intersections between the lines (red dots in figure 4.8). This is because by applying a smaller cut-off wavelength, a higher fraction of eddies in the turbulent boundary layer is manipulated and consequently more turbulence energy is controlled. For the current study, a coherence level of $\gamma_L^2 = 0.1$ is selected, so the favoured sensor-actuator separation is 1.7δ (with almost equal contribution from the component I and component II in equation 4.9) and the targeted events should have streamwise wavelengths greater than 1.6δ.

A typical Fourier low pass filter requires the complete time-series, which is not practical to real-time filtering since it requires future information. Therefore, having determined the desired target scale $\lambda_{x.c}$ of the real-time filter, the next step is shaping the causal FIR filter to capture most of the coherent information from the upstream detected skin-friction velocity signals. This is exercised via an inversed application of the spectral stochastic estimation purposed by Baars et al. (2016), who estimated the fluctuating velocity near the wall from a given observation of velocity fluctuations in the log region. The underpinning idea is to establish the linear transfer function H_L between the upstream detected u_τ signals and the coherent part of the velocity fluctuations u at the actuation position as measured by the traversing hotwire sensor during the *type I* measurements.

$$H_L(z,\Delta x,\lambda_x) = \frac{\langle \mathscr{F}\left[u_\tau(\lambda_x)\right]\mathscr{F}^*\left[u(z,\Delta x,\lambda_x)\right]\rangle}{\langle \mathscr{F}\left[u(z,\Delta x,,\lambda_x)\right]\mathscr{F}^*\left[u(z,\Delta x,\lambda_x)\right]\rangle} \tag{4.10}$$

The complex-valued H_L can be further expressed by its magnitude $|H_L| = \sqrt{\mathrm{Re}(H_L)^2 + \mathrm{Im}(H_L)^2}$ and phase $\angle H_L = \tan^{-1}\left[\frac{\mathrm{Im}(H_L)}{\mathrm{Re}(H_L)}\right]$, which implies the gain of the fluctuations and the spatial shift, respectively as a function of scale λ_x. The jet exit velocity is selected to enable the jet flow to penetrate to the upper bound of the log region and the sensor-actuator separation has been previously optimized at $\Delta x_a = 1.7\delta$ in figure 4.8. Thus, the magnitude and phase shift of H_L at $z^+ = 480$, and $\Delta x/\delta = 1.7$ are presented as gray curves in figure 4.9(a,b), respectively. In figure 4.9(a), the convergence of the linear transfer kernel is increased by fitting its gain using an error function (black solid lines). At the same time, it is observed that the phase shift is linearly proportional to λ_x. To avoid the influence of the uncorrelated structures affecting the estimation accuracy, we employ the modification suggested by Tinney et al. (2006) that manually forces H_L to zero for $\lambda_x \leq 0.6\delta$, which are the structures with negligible coherence. Recall that, for the proposed

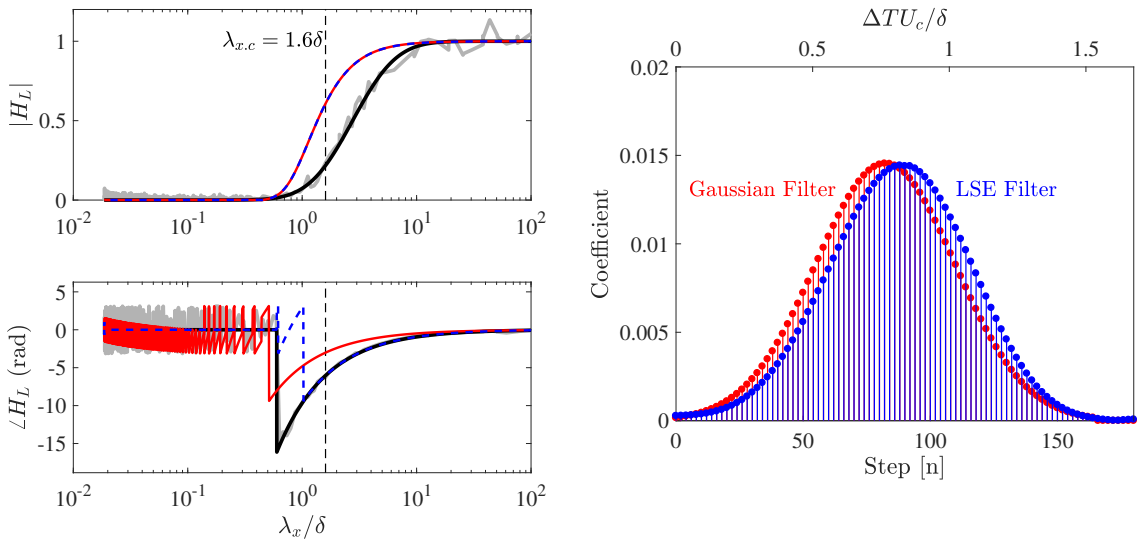

Figure 4.9: (a) Magnitude and (b) phase angle of the linear transfer kernel between the u_τ measured at the detection array and the u acquired at geometric centre of log region with $\Delta x_a = 1.7\delta$ (—). Red solid line (—) and blue dashed line (– –) are the transfer function of the Gaussian and LSE filters, respectively. (c) Coefficients of the Gaussian and LSE filters.

control strategy, the actuation is only discriminated on the sign of the estimated large-scale streamwise skin-friction velocity fluctuations and the magnitude of fluctuation is insignificant. Thus, for demonstration purpose, in figure 4.9(a), we have normalized the gain so that $|H_L|(\lambda_x \to \infty)$ equals to 1. Then time-domain causal FIR filter, whose coefficients are shown as blue stems in 4.9(b), can subsequently be obtained from the inverse Fourier transformation of the fitted H_L. The filter is clipped and dilated to ensure its length does not exceed the designed filter length. In comparison, with a similar configuration, Abbassi et al. (2017) removed the uncorrelated small-scales using a Gaussian filter spanning 1.5δ in the streamwise direction (red stems). It is observed that the peak of LSE filter leads the peak of Gaussian filter by 0.1δ, which makes the LSE filter forward-leaning. The frequency-domain transfer functions of the Gaussian (red solid line) and LSE (blue dashed line) filters in figure 4.9(a,b) offer an illustration on this difference. Despite the identical gains, the phase angle of the LSE filter aligns perfectly with that of H_L, while a clear discrepancy occurs at the phase angle of the Gaussian filter. This is because the traditional Gaussian filter failed to consider the convection velocity difference among the LSMs with different length-scales. The streamwise filter designed here is specifically constructed for the current large-scale active flow control strategy. For other applications, one should accordingly modify the Re_τ, Δx, and z position

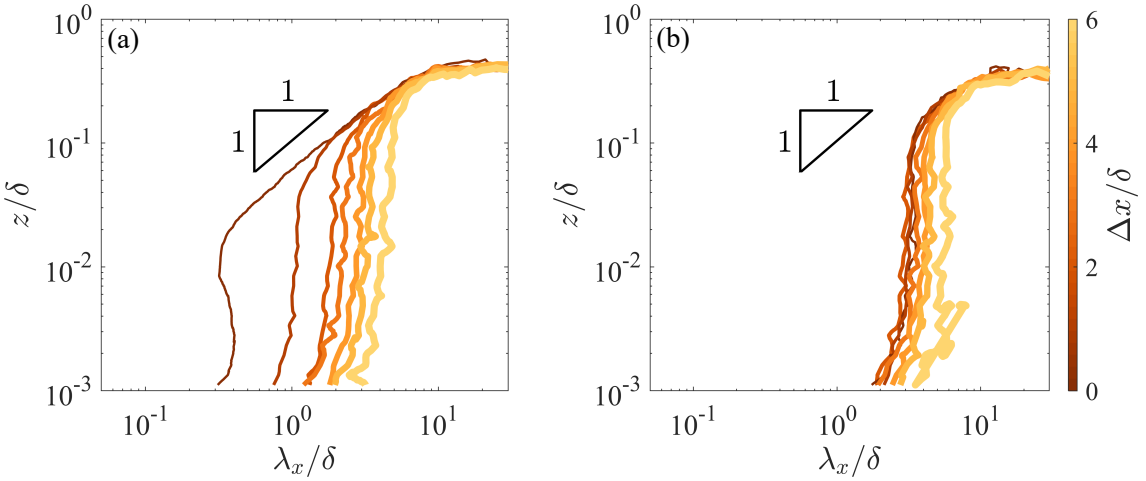

Figure 4.10: Iso-contour lines of 0.1 for the coherence spectrum between HF_5 and the traversing hot-wire probe with Δx equals to 0, 0.3, 0.6, 0.9, 1.2, 1.5, and 2.1 meters (a) with no spanwise offset, (b) with a spanwise offset of Δy equals to 0.075δ

to acquire the H_L corresponding to the control configuration.

The previously assigned streamwise LSE filter only utilizes the u_τ signal acquired by the upstream hot-film without spanwise offset. However, the advantage of applying multiple flow observers in the span is that the neighbouring sensors could also provide information on the targeted structures. In particular, structures longer in the streamwise direction tends to be wider due to the geometric aspect ratio of the coherent structures ($\lambda_x \approx 7\lambda_y$, as suggested by Baidya et al. (2019)). There is a possibility that by filtering out narrower features in y, we might be able to favourably break the approximate constraint that $\tau_f = 0.5\lambda_x/U_c$. This effect is again explored via a similar spectral correlation. The iso-contour lines of γ_L^2 equals to 0.1 are gleaned from the coherent spectrograms between all upstream hot-film sensors and the hot-wire located at all *type I* measurement stations. Especially, the results computed using u_τ without (HF_5) and with a spanwise offset of $\Delta y/\delta = 0.075$ (HF_4 and HF_6) are illustrated in figure 4.10(a,b), respectively. As previously documented, in the absence of a spanwise separation between u_τ and u, the minimum correlating wavelength increases with the streamwise convection of the coherent structure as shown in figure 4.10(a). As concluded by Baidya et al. (2019), when a spanwise offset is employed (as shown in figure 4.10(a)), the $\gamma_L^2 = 0.1$ contour line shifts to a larger λ_x even when the sensors are located at the same streamwise position ($\Delta x = 0$). This is because only the structures with larger streamwise lengthscales (in this case $\lambda_x \geq 2.5\delta$) are able to span across multiple sensors. The values reflect

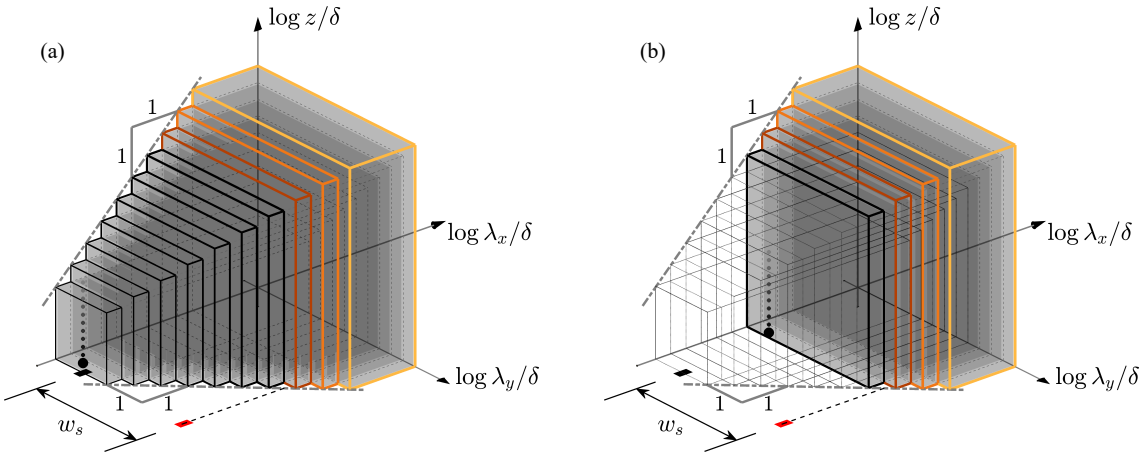

Figure 4.11: Three dimensional hierarchical decomposition of the coherence spectrum (Baidya et al., 2019) between the hot-film array and the hot-wire probe (a) without streamwise separation, (b) with a streamwise separation of 1.7δ. Grey shaded regions show the coherence spectrum with no spanwise separation, while coloured outlines denote surviving coherence when a spanwise separation of w_s is included between the hot-film sensor and the traversing hot-wire probe.

that the streamwise wavelength of the coherent structures $\lambda_x = 28\Delta y$, which agrees with the observation of (Baidya et al., 2019). Furthermore, with the spanwise separation as shown in figure 4.10(b), the spectral correlation contours collapse for $\Delta x \leq 3.3\delta$, since the LSMs with $\lambda_x \geq 2.5\delta$ have lifespans that exceed this threshold. Loss of coherence occurs after $\Delta x \geq 3.3\delta$, beyond which the increase of the minimum correlating length-scale follows that of the iso-contours given in figure 4.10(a) without a spanwise offset Δy. We notice that, for the hot-film located greater than 0.15δ from the centreline, the coherence level is less than 0.1 for all λ_x.

We here adopt the three-dimensional hierarchical decomposition model of the coherence spectrum by Baidya et al. (2019) to further elaborate the implications on the real-time filter design in figure 4.11. Figure 4.11(a) shows the coherence spectrum for the hierarchy with no streamwise separation ($\Delta x = 0$), while plot (b) shows the same for $\Delta x = 1.7\delta$. Each hierarchy is indicated by a cube, with the scale of the $(i+1)^{th}$ block doubling that of the i^{th}. The spectral correlation γ_L^2 at a specific λ_x and λ_y is a linear superposition of all scales in the hierarchy smaller than this scale. Due to the self-similarity, the gradient between λ_y to z also conforms to the one-to-one slope between the streamwise wavelength and the wall-normal extent as previously observed between λ_x and z in figure 4.5. The black rectangle on the wall indicates the hot-film without Δy (i.e. HF_5) and its adjacent hot-film is marked as the red rectangle located at $w_a = 0.075\delta$. The gray shaded regions

indicate the measured contribution from a particular hierarchy level with no spanwise separation between the hot-film (u_τ) and hot-wire (u). The shaded regions with the coloured outlines depict the measured contributions when there is a spanwise separation of $\Delta y = 0.075\delta$. In figure 4.11 (a), the sketched hierarchies correspond to structures with $\lambda_x \geq 0.6\delta$, which are coherent between the centre hot-film (HF_5) and hot-wire probe. However, where there is a spanwise offset between the hot-film and hot-wire, the adjacent hot-film can only simultaneously capture the biggest three hierarchies (colour edged cubics), which contributes to the formation of γ_L^2. When the hot-wire is placed 1.7δ downstream of the hot-film array, smaller-scales vanish from the coherence spectrum during the streamwise convection, which is shown as the departure of the 0.1 contour lines towards larger λ_x in figure 4.10(a). When we consider the case with streamwise and spanwise separation (figure 4.11(b)) we note that, the resolved hierarchies with the coloured outlines remain unchanged from the case with no streamwise separation (figure 4.11(a)) and explaining why the coherence level of u and u_τ with a fixed spanwise offset and varying streamwise separation remains unchanged in figure4.10(b).

In terms of active flow control applications, to provide informative signals for flow estimation, a reasonable spanwise spatial resolution between the sensors should be retained. As a rule of thumb, w_a should not be wider than half of the targeted structure width (i.e. $\lambda_y/4$). According to the geometric aspect ratio of coherent structures suggested by Baidya et al. (2019), this is $1/28$ of the real-time filter cut-off wavelength. If this spanwise resolution of hot-film sensors could be realized (i.e. $w_s \approx 0.055$ for our target $\lambda_x = 1.6\delta$), a spanwise Fourier low pass filter could be directly applied to the series to filter out scales smaller than λ_y without the need for any temporal filter, which would mean that $\tau_f = 0$, and the component II in equation 4.8 could be discarded. This would permit us to operate the control scheme within a wider range of the parameter space shown in figure 4.8 (the black curve corresponding to equation 4.8 would be shifted downwards), permitting the targeting of smaller structures, or with greater correlation. Nevertheless, to only apply the spanwise filtering demands a small spanwise spatial resolution, which in this case was deemed to be unsuitable (requiring more sensors in the spanwise array, or limiting the spanwise domain over which we could actuate). In the future though, it is hoped that spanwise filtering can play an important role to aid the filters in the streamwise direction. For the current control strategy, while the $\lambda_{x.c}$ equals to 1.6δ, the cut-off wavelength in the span is selected as 0.25δ to

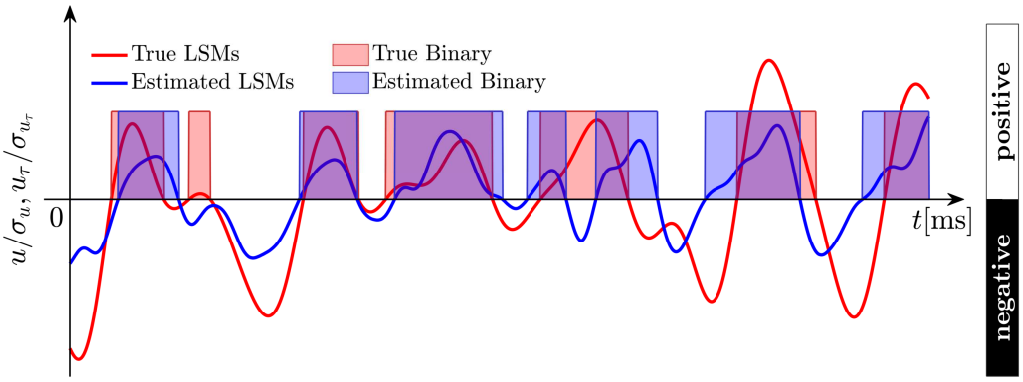

Figure 4.12: A schematic to show the calculation of control accuracy α. Red solid lines (−) are the large-scale streamwise velocity fluctuation acquired at the actuation array. Blue solid lines (−) are the large-scale friction velocity fluctuation filtered from the detection array. Red (■) and blue (■) filled boxes are the binary control signals computed and estimated from streamwise velocity at the actuation array and the friction velocity at the detection array.

comply with the geometric ratio ($\lambda_x : \lambda_y = 7 : 1$) of the LSMs. This, in turn, becomes a low pass filter retaining only Fourier mode 0, 1, and 2 from all nine hot-film sensors.

4.4 Impacts on Control Efficacy

Previous sections elaborate on an optimization procedure for the control architecture, especially the shaping of the real-time filter. To quantitatively assess how the optimized configuration edges the flow estimation, a judging parameter *Control Accuracy (α)* is introduced (Baars et al., 2014). As aforementioned, in the current large-scale flow control strategy, the fluctuating skin-friction velocity signals from the upstream detection array are filtered in real-time to estimate the streamwise velocity fluctuation at the jet position, and the actuators are activated when high-speed events are estimated to occur. Thus, as proposed by Baars et al. (2014), the control accuracy here is defined as the proportion of the high-speed LSMs successfully manipulated by the wall-normal jets. Alternatively, one can also evaluate the control accuracy by assessing the correlation coefficient between the estimated velocity fluctuations and true streamwise velocity signals above the jet position. Since the actuation in the current case is only discriminated on the sign of the estimated velocity fluctuation and the strength of the LSMs is not considered, we adopt the first definition of *Control Accuracy (α)*.

Figure 4.12 shows a schematic of the computation of the control accuracy (α). This requires a pair simultaneously acquired u_τ and u signals, which are measured at the upstream detection array and the center of the log region above the actuation array, respectively. First, the u_τ field is convolved the designed filter off-line to imitate the real-time filtering. The resulting large-scale friction velocity fluctuation, shown as blue solid lines, is regarded as the estimated LSMs. Recall that the real-time filters are shaped to possess a streamwise cut-off wavelength of 1.7δ. For a fair comparison, the u signal acquired over the jet position is Fourier low-pass filtered with a comparable cut-off wavelength to obtain the true LSMs at the desired point of interest. In the second step, we transfer the positive part of the velocity fluctuations to high (1) in control binary signals, whereas low (0) corresponds to the low-speed regions. In figure 4.12 the converted control binary signals from the estimated LSMs and true LSMs are demonstrated as blue and red blocks, respectively. Finally, the control accuracy is calculated as followed.

$$\alpha(\%) = \frac{\Sigma(B_e \cdot B_t)}{\Sigma(B_t)} \times 100\% \tag{4.11}$$

where B_e and B_t are the estimated and true binary control signals, respectively. In the present study, three different filters are inspected, including the streamwise Gaussian filter utilized by Abbassi et al. (2017), the streamwise LSE filter, and a two-dimensional filter composed by streamwise LSE and spanwise low-pass Fourier filters. Their corresponding control accuracies are tabulated

Table 4.2: A summary of implemented control schemes. **Group I** measurements compare the effects of different real-time filter type and measurements in **Group II** compare the actuated structures using the same LSE filter.

	Symbols	**Real-time Filter**	**Control Scheme**	**Control Accuracy** (α)	**Realizations**
	■	—	Uncontrolled	—	90×3-minute
Group II	●	LSE filter	Opposing	70.5%	90×3-minute
	▶	Gaussian filter	Opposing	69.2%	60×3-minute
	■	2-D filter	Opposing	73.1%	60×3-minute
Group I	●	LSE filter	Opposing	70.5%	90×3-minute
	♦	LSE filter	Reinforcing	29.5%	30×3-minute
	△	LSE filter	desynchronized	50%	30×3-minute

in table 4.2, which are 69.2%, 70.5% and 73.1%, respectively. The LSE filter attained from the linear transfer kernel increased α by approximately 1%. This is because only a slight difference is observed between the shape of Gaussian and LSE filters. In comparison, a larger improvement happens when an additional spanwise filter is employed, which manifests the importance of the spanwise information. If the spanwise separation between the hot-film sensors could be further reduced, the resulting control accuracy is likely to be further enhanced.

To further examine the influence of α on the control efficacy, the three filters are all tested independently in real-time active large-scale flow control experiments. A summary of the control schemes and large-scale filters is available in table 4.2. Recognizing that the range of control accuracy is rather limited (i.e. $69.2\% \leq \alpha \leq 73.1\%$) from the three different implemented real-time filters, if the jets are only firing at the estimated high-speed LSMs. Supplementary control schemes have also been implemented to artificially enlarge the scope by activating the jets only on low-speed and random structures as estimated by the streamwise LSE filter. As reviewed in Chapter 2, the high-speed events have natural wall-ward motions, which are opposite to the upward momentum of the jet flow (Hutchins and Marusic, 2007b), so his strategy is termed "opposing control". Manipulation of the low-speed and random structures are hereby referred to as "reinforcing control" and "desynchronized control", respectively. As the high-speed and low-speed events populate the entire estimated LSMs, the α of the "opposing" and "reinforcing" control with identical real-time filter is canonically summed to 100%. It should be noted that the actuation of the "desynchronized" control is not purely random; in this case, the jets are operated based on the control binary signals from the other pre-acquired realizations, so the probability distribution of the duration of the actuation is identical to the opposing and reinforcing control schemes. Since the pre-acquired binary control signal in desynchronized control is independent of the true LSMs, the control accuracy is canonically expected to be 50%, which indeed is confirmed by the results presented in table 4.2.

Control efficacy is statistically investigated by the local drag reduction DR at 1.7δ downstream of the actuation array, where the drag reduction is maximized (Abbassi et al., 2017). The drag reduction here is computed as,

$$DR(\%) = \left(1 - \frac{C_f}{C_{f_{un}}}\right) \times 100\% \tag{4.12}$$

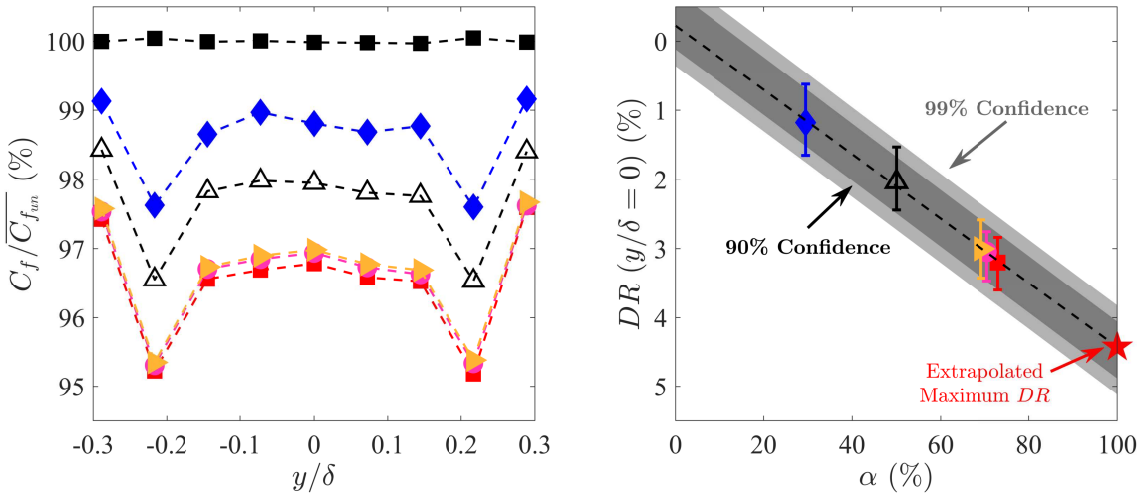

Figure 4.13: (a) Fractional skin-friction coefficient for uncontrolled and all controlled boundary layers at 1.7δ downstream of the actuation. (b) Drag Reduction DR on the centreline against the associated control accuracy α.

where the subscript *un* denotes the quantity obtained in the uncontrolled canonical boundary layer. C_f is the skin-friction coefficient at the streamwise position of interest, which is defined as $C_f \equiv 2\frac{U_\tau^2}{U_\infty^2}$. Two sets of measurements are conducted. As summarized in table 4.2, the first group only considers the impact of real-time filters using sixty 3-minute measurements, which are taken in turn to minimize the temperature drift of the hot-film sensors. In addition, for the second group (**Group II** measurements) a further thirty rounds of realizations are acquired to survey the influence of the control scheme (opposing, reinforcing, and desynchronized) with the same LSE real-time filter.

Figure 4.13(a) presents the fractional skin-friction coefficient, which is the local C_f normalized by the spatial mean of the uncontrolled $C_{f_{un}}$ at 1.7δ downstream of the actuators for all tested cases spanning the entire control plane, -0.3< $\Delta y/\delta$ <0.3. Black filled squares (■) represent the fractional skin-friction coefficient for the uncontrolled boundary layer. It shows a negligibly small variation across the entire span, which implies good convergence of the U_τ measured by the hot-film probes and also spanwise homogeneity in the working section. For the controlled cases, it is observed that all cases achieved a positive drag reduction. Generally, the shape of fractional skin-friction is composed of a central plateau regime flanked by two peaks locating at the $|\Delta y| = 0.21\delta$, which could be attributed to the edge effects (Ruan et al., 2018). We first concentrate

only on the plateau region, where the spatially converged results better reflect the *DR* reached by the active flow control strategy. Clearly, the fractional reduction in the skin friction coefficient for all three opposing controlled cases is greater than that of the reinforcing and desynchronized schemes by 2% and 1% respectively, with the best performance provided by the opposing control scheme employing the 2D filter which yields a reduction in C_f of approximately 3.4%. Since the total actuation input is held constant (jets are on for half of the experimental time) regardless of control strategies or real-time filters, the difference in $DR(\%)$ can be purely ascribed to the control accuracy. The selection of real-time filter results in a less significant effect on the viscous drag reduction. Though the 2D filter performs best, with the LSE filter also outperforming the Gaussian filter used by Abbassi et al. (2017), the difference in *DR* across the three filters is smaller than 0.2%. Clearly, the choice of targeted structures has a much greater influence on the control accuracy and *DR*. The results presented in figure 4.13 suggest that the drag reduction is composed of two major components. First, the jet flow with upwards momentum works as a "virtual wall", which can block or oppose the down-wash of high-velocity large-scale structures from generating local high shear-stress footprints on the wall. Hence, the reduction in C_f is greater for strategies where a larger proportion of high-speed large-scale motions is actuated, the performance of the large-scale control is enhanced. Furthermore, even when the control strategy is reinforcing which will tend to strengthen the high-speed LSMs, a reduction in C_f is still achieved. This implies that a portion of drag reduction is purely due to the injection of low streamwise momentum fluid from the jet actuators (with the implication being that this part of the drag reduction could also be achieved if the jets were just fired continuously or at a fixed frequency). The drag reduction *DR*, as defined in equation 4.12, is computed at the midpoint of the control plane $\Delta y/\delta = 0$ (HF_5) and is presented for all cases in figure 4.13(b). Despite the apparently trivial result that all examined control strategies yield a drag reduction due to the simple injection of low momentum fluid into the near-wall region, the degree of drag reduction is a clear function of the control accuracy. In other words, the drag reduction is linearly related to the efficacy with which we control the targeted large-scale structures with $\lambda_x > 1.6\delta$. By fitting the points with a linear curve (black dashed line in figure 4.13(b)) and extrapolating the line to α =100%, it is hypothesized that the performance of large-scale control with a cut-off wavelength $\lambda_x/\delta = 1.6$ via the current actuation process is bounded by 4.5%, even when we had perfect control accuracy α. For a more conservative

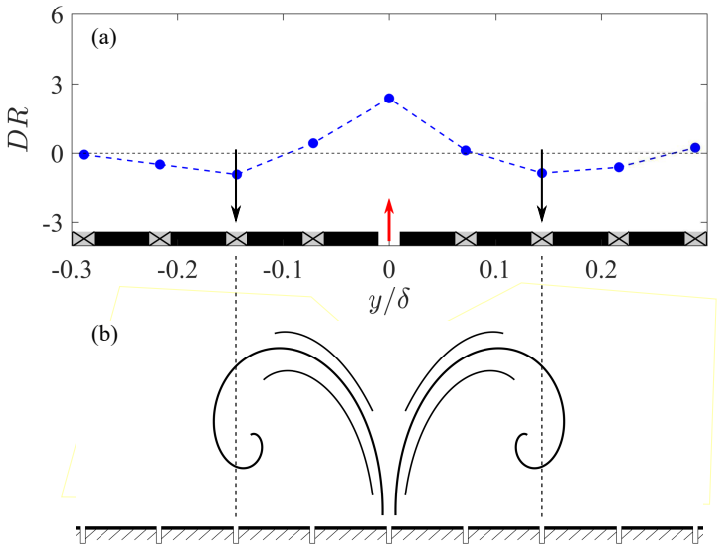

Figure 4.14: (a) Drag reduction at 1.7δ downstream of the actuation due to one jet. (b) A schematic of the counter-rotating vortex pairs induced by the jet.

estimation, error bars are created for *DR* of each case. Then, a 99% confidence band suggests the optimal drag reduction lies between 3.8% to 5%. In addition, figure 4.13(b) shows that the limited degree of drag reduction that we observe here for the optimal opposing case is not greatly restricted by the control accuracy. Even if we successfully achieved $\alpha = 100\%$ (perfect control accuracy under the current definition), we would only attain marginally better drag reduction. Thus the preliminary investigation leads to the following two hypotheses, (i) the actuators lack control authority to successfully mitigate the wall-ward large-scale high momentum sweep events or (ii) that the structures with $\lambda_x > 1.6\delta$ do not actually contribute greatly to the overall turbulent skin friction drag. This will be further elaborated in the hot-wire and PIV studies in Chapter 5 and Chapter 6, respectively

In order to understand the increased *DR* due to the edge effect that has been evidenced in figure 4.13(a), an experiment has been performed where the control plane is narrowed to only one sensor-actuator pair at the centreline of the tunnel. Then, the drag reduction, computed across the entire spanwise width of the measurement array due to this single active wall-normal jet is illustrated in figure 4.14(a). At 1.7δ downstream the actuation, the jet is able to provide a positive drag reduction only within $|\Delta y| \leq 0.08\delta$. At greater spanwise distances from the active jet, there is a slightly increased frictional drag. Based on these measurements, it is proposed that the upwash

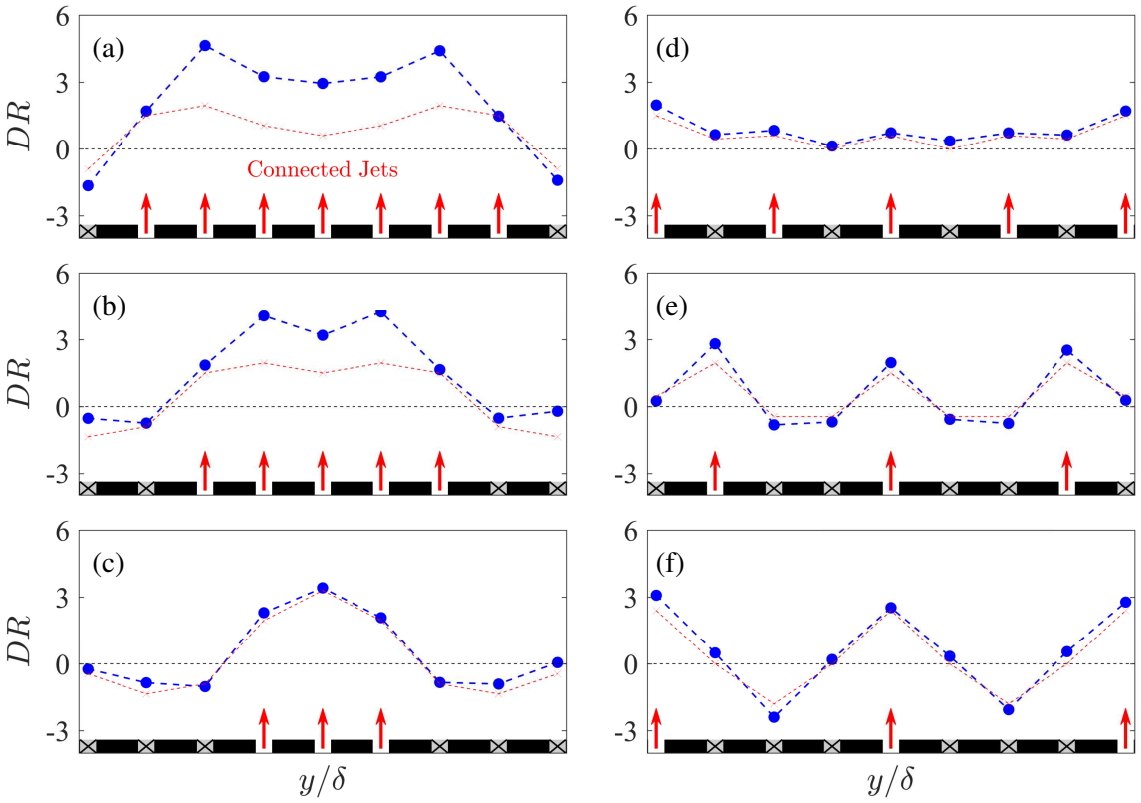

Figure 4.15: Blue dashed lines (−−) are the spanwise drag reduction curves measured when the jets with red arrow labelled are activated under opposing controlled manner. Red dashed lines (−−) are the spanwise drag reduction curves modeled through superimposing the drag reduction curve induced by single operating jet.

due to the single active jet on the centerline sets up a secondary flow in the form of a counter-rotating vortex pair (CVP) as illustrated in the schematic diagram of figure 4.14(b). The CVP seems to lead to a downwash due to the secondary flow at $\Delta y = \pm 0.15\delta$ (at HF_3 and HF_7). The positive drag reduction only seems to be observed in the region where the single active jet is able to provide a net (time-averaged) positive flow away from the wall.

The applicability of the model is assessed via another series of measurements, in which we manually change the spanwise resolution of the jets and the width of the control panel. Only the "opposing" controlled scheme with a streamwise LSE filter is applied in these measurements. The resulting drag reduction curve (blue dashed lines) at 1.7δ downstream of the actuation is shown in figure 4.15. The jets with a red upward arrow are connected to the air supply, and thus are active. All other jets are dormant from figure 4.15(a,b), the edge effect still clearly exists on the position

second nearest to the ends of the control panel. In figure 4.15(e), a dramatic drag increase zone is identified in the middle of two active jets spaced 0.3δ apart. Here, we linearly superimpose the drag reduction in figure 4.14 due to one jet to model the *DR* in all listed cases (red dashed lines). With the exception of figure 4.15(a) and (b), all the other cases with wider spanwise separation between the actuators see good alignments between the observed drag reduction (blue curves) and that predicted from the superimposed drag reduction due to the single jet, which implies the model is valid for the situation where the interaction between the jets is weak. In contrast, the superimposed *DR*, though capturing the salient trends and features, underestimates the actual frictional drag reduction for the jets placed 0.075δ away from each other (the cases shown in figure 4.15(a) and (b)). This indicates that there are additional non-linear interactions between the jets when they are closely located and such interaction seems to further increase the skin-friction drag reduction. This suggests that it may be beneficial to exploit this non-linear interaction by further increasing the spanwise resolution of the actuators so that greater drag reduction could perhaps be achieved. However, increasing the spanwise resolution would require a redesign of the jet actuators (which at the moment each have a spanwise width of 0.075δ which dictates the minimum spacing between jets). This is considered beyond the scope of the current project but could be a useful avenue to pursue in future studies

4.5 Chapter Summary

The streamwise evolution of the coherent structures in the turbulent boundary is studied through simultaneous hot-film and hot-wire anemometry, which further provides information on the optimization of the real-time flow estimation system. Active large-scale flow control is applied to investigate the effect of flow estimation on the outcome of the present real-time flow control strategy. Here, the key findings from the measurements are summarized.

- The minimal correlating scales of the coherent structures tracked by both hot-film and hot-wire sensors increases with the streamwise separations between the probes. The coherent motions with larger streamwise wavelengths remain traceable for a longer streamwise distance during the convection.
- The convection velocity of the coherent motions in the turbulent boundary layer is shown

to increase with their streamwise length-scale. In detail, the structures with streamwise wavelengths greater than a certain threshold is comparable to the mean streamwise velocity at the geometric center of these structures.

- For the real-time flow control configuration, the sensor-actuator separation should not exceed the maximum streamwise traceable distance of the targeted structures. At the same time, the minimum sensor-actuation separation is required to accommodate the time delay due to mechanical delay of the actuators (Component I in equation 4.9) and the real-time flow estimation (Component II in equation 4.9). The combination of these two conditions leads to the optimal selection of the sensor-separation offset and the streamwise wavelength of the targeted structures.

- The friction velocity and streamwise velocity measured with a spanwise offset remain a fixed level of coherence on the LSMs to larger streamwise separations and the wavelength of the correlating structures decreases for a closer spanwise offset. For flow estimation, this implies the possibility of employing the flow observers with a finer spanwise resolution so that only the spanwise real-time filter could be used for flow estimation. In turn, the time delay due to streamwise filters (i.e. component II in equation 4.9) can be eliminated, which shortens the required minimum sensor-actuator separation and eventually provides the opportunity to control the structures with shorter wavelengths

- Skin-friction drag reduction attained from different control schemes is linearly proportional to the accuracy of the flow estimation. However, the maximum potential drag reduction could be achieved by the current control strategy with a perfect flow estimator (i.e. 100% accuracy) is approximately 4.5%.

Chapter 5

Hot-Wire Investigation on the Flow Control Effects

The previous chapter has established that the drag reduction attained from the active large-scale control is positively proportional to the degree of the high-speed events successfully manipulated by the wall-normal jets. In order to examine the underpinning physics, in this chapter, hot-wire anemometry is employed simultaneously with the downstream hot-film array at the same streamwise position to examine the control effects both within the boundary layer and at the wall for each control scenario at $\mathrm{Re}_\tau = 14000$.

Advances in the understanding of high Reynolds number turbulent boundary layers have revealed that the near-wall small-scale structures are amplitude modulated by the LSMs in the log region (Bandyopadhyay and Hussain, 1984). Further, the large-scale velocity fluctuations in the log region superimpose their footprints in the near-wall region (Hutchins and Marusic, 2007a). Mathis et al. (2013) pointed out that the superposition and amplitude modulation effects even extends to the skin-friction stress fluctuations in canonical boundary layers. Here, the influence of the manipulated LSMs on the frictional shear stress and the near-wall turbulence is investigated when the active large-scale control strategy is employed. Comments are made on the applicability of the large-scale amplitude modulation and superposition effects in a perturbed high Reynolds number turbulent boundary layer. Based on the observation, the maximum drag reduction that could be achieved via controlling the targeted large-scale structures is estimated.

Another plausible benefit of the large-scale control is that the persistence of the control effect, which could be inferred from the life-time of the coherent motions discussed in §4.2. By placing the hot-wire probes at different streamwise positions downstream of the actuation array, a general picture of the streamwise evolution of the large-scale control is demonstrated in this chapter.

Finally, some explorations to potentially enhance the control efficacy via manipulating different portions of the detected high-speed events are introduced.

5.1 Large-scale Influence on Skin-friction Drag

Prior to assessing the contribution of the large-scale structures to the mean wall shear stress, the active large-scale control effects on the flow field are demonstrated in figure 5.1(a,b) by comparing the pre-multiplied energy spectrogram ($k_x^+ \phi_{xx}^+$) of the fluctuating streamwise velocities in both uncontrolled and opposing controlled boundary layers at 0.6 meters ($\Delta x_m / \delta = 1.7$) downstream of the actuation array. This measurement location is selected so that the control effect is maximized (Abbassi et al., 2017). Identical with the observation of Abbassi et al. (2017), the canonical (uncontrolled) spectra in figure 5.1(a) clearly exhibits two peaks in the pre-multiplied spectra where the energy of streamwise velocity fluctuations are most energized. The near-wall peak at $z^+ \approx 15$ and $\lambda_x^+ \approx 1000$ (indicated by the $+$) is mainly contributed by the near-wall cycle, while the outer peak at the center of the log region possesses a larger structural wavelength $\lambda_x / \delta = 3 \sim 6$ corresponding to the LSMs and VLSMs with energy that seems to peak close to the geometric mean of the log region (shown by the $+$). The magenta solid line in figure 5.1(a,b) indicates the cut-off wavelength ($\lambda_{x.c} = 1.6\delta$) of the real-time filter determined in the previous chapter. When the opposing large-scale control strategy is activated, which is the case shown in figure 5.1(b), , an evident energy attenuation is observed within the large-scale regime (i.e. $\lambda_x > \lambda_{x.c}$). This implies that the current set-up successfully fulfills the goals to actively reducing the energy content in the low-frequency (large-spatial) turbulent fluctuations.

To better quantify the overall control effects on the large-scale structures, a Fourier decomposition is performed on the fluctuating streamwise velocity signals with a cut off wavelength of 1.6δ, such that the u fluctuations can be expressed as the summation of the large and small-scale velocity fluctuations (u_l and u_s). The turbulent energy of the broadband, large, and small-scale velocity fluctuations in both uncontrolled and opposing controlled cases are demonstrated in figure 5.1(c). Note that the turbulent energy in controlled boundary layers is normalized by a canonical U_τ obtained in the uncontrolled boundary layer at matched Re_τ (as detailed in table 5.1) so that the modifications to large-scale turbulent energy can be more easily discerned. The small-scale turbu-

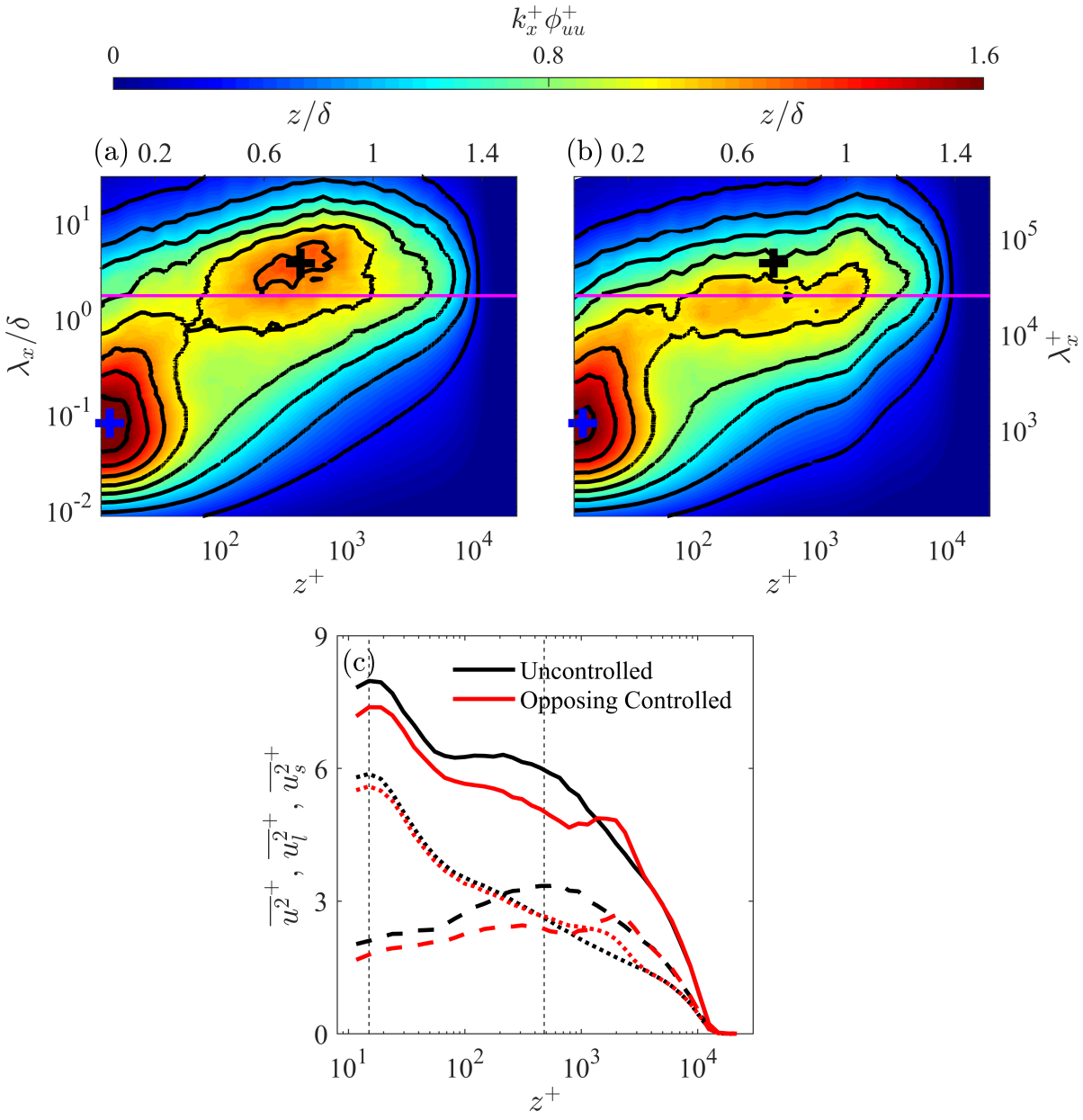

Figure 5.1: Pre-multiplied energy spectrogram of the (a) uncontrolled and (b) opposing controlled boundary layer measured at the $\Delta x_m = 1.7\delta$. Magenta solid lines (−) represents the cut-off wavelength of the Fourier decomposition (with $\lambda_{x.c} = 1.6\delta$). Blue (+) and black (+) markers are the inner and outer peak of the energy spectrogram in the uncontrolled boundary layer. (c) Broadband (solid lines), large-scale (dashed lines), small-scale (dotted lines) variance of streamwise velocity fluctuations for the uncontrolled (black) and opposing controlled (red) cases. The vertical dotted lines highlight the wall-normal position of the inner and outer peaks of the turbulent energy.

lent energy $\overline{u_s^2}^+$ (dotted-line), is the integrated pre-multiplied energy spectrogram with $\lambda_x < 1.6\delta$. This small-scale energy peaks at $z^+ \approx 15$, the location of the inner spectral peak, for both con-

trolled and uncontrolled cases and shows very little difference up to the location of the outer peak ($z^+ \approx 500$). Beyond this height, the small-scale energy exhibits an increased magnitude for the controlled case for $500 < z^+ < 3000$, which is due to the shear layer on the upper part of the injected jet in cross-flow caused by the actuators. Conversely, the large-scale streamwise turbulent energy $\overline{u_l^2}^+$ (dashed line) is the integrated $k_x^+ \phi_{xx}^+$ with $\lambda_x > 1.6\delta$ and for the uncontrolled case exhibits a clear peak at the center of log region. For the opposing controlled case, a clear large-scale energy reduction is observed under the upper bound of the log region (i.e. $z^+ < 0.15\mathrm{Re}_\tau$), which indicates the jet flow penetrates throughout the log region and has successfully attenuated the targeted high-speed large-scale events. The total turbulent energy, shown by the solid lines in figure 5.1(c) are representing the sum of $\overline{u_s^2}^+$ and $\overline{u_l^2}^+$, is reduced under the upper bound of the log region, exhibiting a region of enhanced energy for $2000 < z^+ < 4000$ due to the generated shear layers on the upper part of the jet in crossflow.

To assess how the large-scale turbulent energy impacts the wall-shear stress, the current study simultaneously measures the streamwise and skin-friction velocity fluctuations at $\Delta x_m = 1.7\delta$ in the turbulent boundary layer tailored by different large-scale flow control strategies. In each strategy, the control accuracy, α are artificially varied via changing the real-time filter and control scheme as discussed in Chapter 4 to ensure a consistent level of total control input (time the jet has been activated). As listed in table 5.1, these strategies are divided into two series of measurements

Table 5.1: A summary of all measured control strategies and flow parameters at $\Delta x_m = 0.6$m (1.7δ)

Set	**Symbols**	**Real-time Filter**	**Control Scheme**	Re_τ	U_τ [m/s]	ν/U_τ [μm]	l_{hw}^+	d_{hw}^+
I	□ ▶ ● ■	– Gaussian LSE 2-Dimensional	Uncontrolled Opposing Opposing Opposing	14280	0.645	24.51	21.7	0.1
II	+ ▲ ♦	– LSE LSE	Uncontrolled Desynchronized Reinforcing	14160	0.638	25.12	18.8	0.1
III	▽ ◀	– Gaussian	Uncontrolled Opposing	14400	0.639	24.95	20	0.1

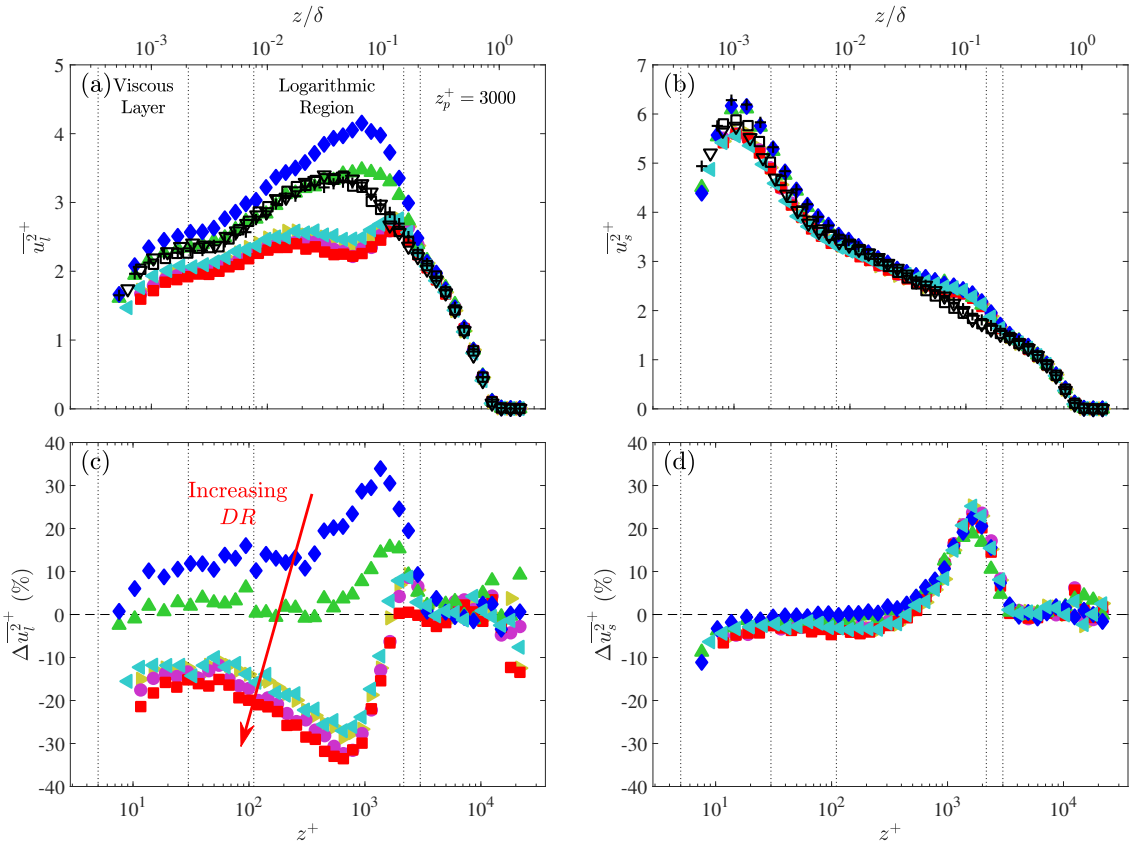

Figure 5.2: (a,b) Large and small-scale turbulent intensity normalized by the corresponding uncontrolled skin-friction velocity for all tested cases in table 5.1. (c,d) Percentage variation of the large and small-scale turbulent intensity for all controlled boundary layers. Symbols are as give in table 5.1.

which respectively consider the variation of the control strategy resulted from real-time filters (set I) and the control schemes (set II). Another opposing controlled database (set III) from Abbassi et al. (2017) is supplemented for validation purposes. To minimize the impacts of the flow conditions on the analysis, each set is benchmarked by its own referencing uncontrolled boundary layer and all measurements are conducted at a canonical Reynolds number of $\mathrm{Re}_\tau \approx 14000$ (i.e. $U_\infty \approx 20$m/s). Their actual Reynolds numbers and mean frictional velocity U_τ listed in table 5.1 are again calculated based on the uncontrolled boundary layer cases. Identical to 5.1(c), the turbulent energy in the perturbed boundary layers is normalized by their corresponding uncontrolled U_τ unless specially nominated in §5.2. More detailed flow parameters in each set of measurement and the symbols of the figures for all tested control strategies in §5.1 and §5.2 are summarized in

table 5.1.

Figure 5.2(a,b) shows the large-scale and small-scale energy of hot-wire measured streamwise velocity fluctuations for all the performed cases. A good agreement is observed among the large-scale turbulent intensity of the reference uncontrolled boundary layers for all three measurement sets. Conversely, small discrepancies occur in their small-scale turbulent intensity, especially within the viscous sub-layer around the inner-peak. These small deviations could be spatial resolution effects due to variations in the viscous-scaled ho-wire length l_{hw}^{+} between measurement set. Hutchins et al. (2009) reported that the inner-scaled near-wall peak of the $\overline{u_s^2}^{+}$ is effectively attenuated by increasing the l_{hw}^{+}, while the large-scale energy attained remains consistent. This is because larger l_{hw}^{+} decreases the spatial resolution of the hot-wire sensing section, which damps out the small-scale energy.

When the control is engaged, the large-scale energy deviates significantly between all control strategies but the small-scale turbulent energy barely changes. To minimize the impact of the hot-wire geometry on the analysis, instead of the absolute energy variation, the percentage change of the large-scale and small-scale energy, $\Delta\overline{u_l^2}^{+}(\%) = \left(\overline{u_l^2}^{+} - \overline{u_{l\text{un}}^2}^{+}\right) / \overline{u_{l\text{un}}^2}^{+} \times 100$ and $\Delta\overline{u_s^2}^{+}(\%) = \left(\overline{u_s^2}^{+} - \overline{u_{s\text{un}}^2}^{+}\right) / \overline{u_{s\text{un}}^2}^{+} \times 100$, are considered in figure 5.2(c,d). Here, $\overline{u_{s\text{un}}^2}^{+}$ and $\overline{u_{l\text{un}}^2}^{+}$ represent the uncontrolled small-scale and large-scale turbulent energy from the canonical reference case for each measurement set. In the viscous region of figure 5.2(c) ($z^{+} < 30$), the four opposing control strategies all achieve approximately 15% large-scale energy attenuation, with the 2-D filter outperforming the others. While the desynchronized control shows a very limited control effect in this region, the reinforcing control energizes the large-scale structures by approximately 10% because the predominantly ejecting negative large-scale streamwise velocity fluctuations are further decelerated and deflected away from the wall by the low-speed jet flow. This tendency is magnified in the log region $110 < z^{+} < 2000$, where the majority of large-scale energy resides and the $\Delta\overline{u_l^2}^{+}$ of both opposing and reinforcing controlled schemes are maximized at approximately $\mp 35\%$, respectively. The maximum change in large-scale energy $\Delta\overline{u_l^2}^{+}$ occurs at a higher wall-normal location ($z^{+} \approx 1500$) for the reinforcing control than for the opposing case ($z^{+} \approx 800$). This is expected since, in the reinforcing control case, the jets are predominantly firing into the ejecting low-speed LSMs, which will tend to reinforce the natural positive wall-normal velocity and push these events further from the wall. Beyond the log region, the curves for all different

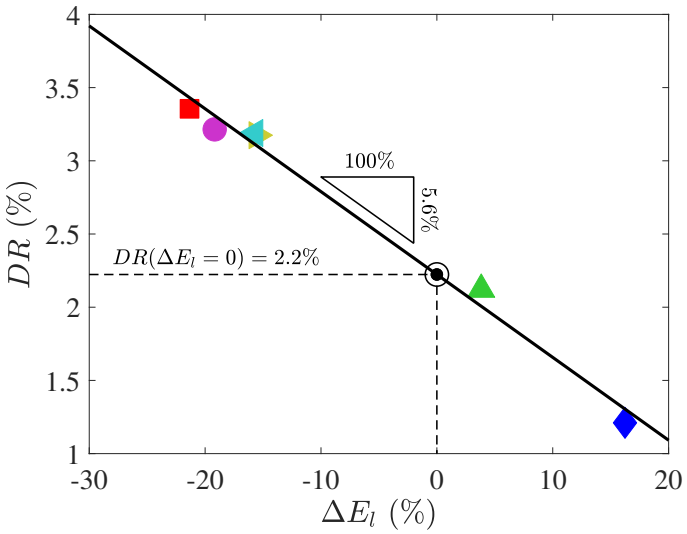

Figure 5.3: Relationship between large-scale energy and the drag reduction for all measured cases. Solid line is the linear fit of the data points for the potential mean wall-shear-stress contribution. Symbols are as give in table 5.1.

control scenarios collapse for $z^+ > 3000$, which is regarded as the effective penetration height z_p^+ of the large-scale control. Finally, recalling the *DR* and control accuracy for each control strategy reported in §4.3, it is can be concluded that the control accuracy enhances the large-scale energy attenuation, which is shown to be positively proportional to the drag reduction.

Figure 5.2(c) shows that all control strategies and real-time filters yield almost identical changes to the small-scale high-frequency velocity fluctuations. In all cases, a mild 2%-5% small-scale energy reduction is obtained in the near-wall region ($z^+ < 100$). At the same time, a dramatic small-scale energy bump, maximized at $\Delta\overline{u_s^2}^+ = 30\%$, occurs around the upper bound of the log region near the penetration height z_p due to the development of the shear layers between the cross flow and the penetrating jet. Though the small-scale energy variation, $\Delta\overline{u_s^2}^+$ shows negligible differences among all control strategies, it is visualized that the opposing controlled boundary layers possess a slightly larger reduction in small-scale energy near the wall than the reinforcing and desynchronized control. Note that the total control input of all cases is maintained consistent (i.e. total time-averaged mass flow rate from the jets) and thus, it can be postulated that the difference between the *DR* and turbulence for each case is exclusively due to the different control strategies (opposing, reinforcing and desynchronized) and to a lesser extent the different real-time filters.

To further quantify the relationship between the mean wall-shear-stress and the change in

the fluctuating large-scale streamwise velocities, the percentage of the mean large-scale energy attenuation ΔE_l is introduced. As expressed in equation 5.1, to include only the direct effect from the large-scale control, ΔE_l considers only the spatially-averaged large-scale energy variation with $\lambda_x \geq 1.6\delta$ under the jet penetration height $z^+ \leq z_p^+ = 3000$

$$\Delta E_l(\%) = \frac{\int_0^{z_p^+} \Delta\overline{u_l^2}^+ dz^+}{z_p^+} \times 100 \tag{5.1}$$

Thus, a negative ΔE_l value indicates large-scale energy reduction, while a positive value means energy gain. Figure 5.3 shows the drag reduction *DR* and the ΔE_l of all control strategies listed in table 5.1. In general, as hypothesized the skin-friction drag reduces proportionally to the ΔE_l, which means a certain percentage of large-scale energy attenuation will lead to a fixed amount of *DR*. Hence, the slope of the linear fit of the data points implies that raising the large-scale energy reduction by 100% has the potential to reduce frictional drag by 5.6%. As defined by the cut-off wavelength of the Fourier decomposition, spatially-averaged large-scale energy variation ΔE_l considers only the energy change for the structure with $\lambda_x > 1.6\delta$. Therefore, in other words, we might hypothesize that the LSMs with streamwise wavelengths $\lambda_x \geq 1.6\delta$ contributes to approximately 5.6% of the total mean-wall-shear stress in a turbulent boundary layer at $\mathrm{Re}_\tau = 14000$. It should be noticed that a uniform weighting of the large-scale energy at all wall-normal positions is assumed by the definition of ΔE_l. However, the deviation of the large-scale energy change is much more significant in the log region than that in the viscous layer. In turn, the slope of the linear regression curve in figure 5.3 will be steeper if only the energy change in the viscous layer is accounted for the calculation of ΔE_l. This might suggest that a larger drag reduction may be achievable by more effectively controlling the large-scale fluctuations within $z^+ < 30$. A more conservative $4\% - 8\%$ drag reduction contribution is then estimated by considering only the ΔE_l in the viscous layer and the log region, respectively. Similar argument is provided by deGiovanetti et al. (2016), who claimed a 5–8% frictional drag reduction when removing structures with λ_y greater than 1.5 channel height (i.e. LSMs and VLSMs) through artificially narrowing of the numerical domain of a turbulent channel flow at $\mathrm{Re} \approx 4000$. The linear fit in figure 5.3 intercepts the vertical $\Delta E_l = 0$ line at $DR = 2.2\%$, which implies that the drag reduction owing to the momentum deficit caused by the jet flow is approximately 2.2%. This value is reflected by the *DR* of the desynchronized control strategy, where a 2.1% drag reduction is achieved with little or no large-

scale energy attenuation. Hence this is the baseline drag reduction due to the low momentum fluid that is injected by the control jets, in the absence of any coherent large-scale control strategy. Any *DR* above or below this value is attributable to either weakening of large-scale high momentum events, or strengthening of large-scale low momentum events respectively. Since the large-scale structures contribute to a larger proportion of the turbulent energy production at higher Reynolds numbers, it is postulated that the LSMs with the same cut-off wavelength (i.e. $\lambda_x > 1.6\delta$) will result in a slightly larger drag reduction in engineering applications at practical Reynolds number ($\mathrm{Re}_\tau \approx O[10^5]$). As this analysis has demonstrated that the LSMs and VLSMs have a convincing impact on the skin-frictional drag, an immediate question after this is by what mechanism the streamwise large-scale fluctuations affect the skin-friction drag and this is discussed in §5.2.

5.2 Large-scale Influence on Near Wall Turbulence

In the past few decades, multiple studies have pointed out the self-sustaining and autonomous characteristics of the near-wall turbulent cycles in a zero-pressure-gradient turbulent boundary layer (Jiménez and Pinelli, 1999, Panton, 2001). However, with the availability of high-fidelity data at high Reynolds numbers, the interactions between the outer-scaled large-scale structures and the small-scale turbulence have become a popular topic in turbulent research. As reviewed in Chapter 2, such interaction was first documented by Rao et al. (1971) in their investigation on the mechanism of the "bursting" process. It is followed by Brown and Thomas (1977) who revealed the amplitude modulation effect between the large and small-scale turbulence. A similar amplitude modulation effect is presented by Bandyopadhyay and Hussain (1984) in a wide range of shear flows via the correlation between the large-scale velocity fluctuations and the envelope of the small-scales. Further, Ganapathisubramani et al. (2012) shows the frequency modulation is also applicable between different scales via detecting the number of small-scale local extrema at high and low-speed large-scale events. In addition to the modulation effect, the LSMs leave the large-scale imprints in the near-wall region via superimposition (Hutchins and Marusic, 2007a). In turn, Metzger and Klewicki (2001) reported that the turbulence intensity at the inner peak (i.e. $z^+ = 15$) increases with the Reynolds number due to the energized large-scale fluctuations. In this section, the underpinning mechanism of the observed relationship between the skin-friction

drag reduction and the large-scale energy attenuation is examined based on the superposition and modulation effects of the LSMs and VLSMs in these perturbed (actively controlled) high Reynolds number boundary layers.

The superposition effects of LSMs in the perturbed boundary layers are first assessed via a three-dimensional conditional analysis of streamwise velocity fluctuations u and friction velocity fluctuations u_τ at $\Delta x_m = 1.7\delta$. These simultaneously measured quantities are both conditioned on the positive zero-crossings of the large-scale skin-friction velocity u_{τ_l} measured by the center hot-film sensors HF_{U5} in the detection array ($u_{\tau_{l5}}$) as expressed in equation 5.2 and 5.3.

$$\langle u_l^+ \rangle (\tau^+, z^+) = \left\langle \left(u^+(t^+ + \tau^+, z^+) \mid u_{\tau_{l5}}(t^+) = 0 \cap \frac{\partial u_{\tau_{l5}}(t^+)}{\partial t^+} > 0 \right) \right\rangle \tag{5.2}$$

$$\langle u_{\tau_l}^+ \rangle (\tau^+) = \left\langle \left(u_\tau^+(t^+ + \tau^+, y/\delta, z^+) \mid u_{\tau_{l5}}(t^+) = 0 \cap \frac{\partial u_{\tau_{l5}}(t^+)}{\partial t^+} > 0 \right) \right\rangle \tag{5.3}$$

Here, $\langle u_l^+ \rangle$ and $\langle u_{\tau_l}^+ \rangle$ are the ensemble average of the qualified u and u_τ signals. τ is the time shift between the ensemble-averaged signal and conditional signals. $\langle A|B \rangle$ indicates the ensemble average of A based on the condition vector defined by B. Since the jets are activated for positive LSMs (large-scale sweep events) in the opposing controlled case, the conditional structures should directly reflect the averaged large-scale control effect on both LSMs and their footprints. It should be mentioned that there is a streamwise separation of $\Delta x_a + \Delta x_m = 3.3\delta$ between the conditional point (detection array) and the signals of interest (measurement array). As introduced in §4.2, the temporal signals are converted into spatial domain using the composite method, which considers time delay τ as a combination of both structural inclination angle $\tau_i(z)$ and streamwise convective motion $(\Delta x_a + \Delta x_m)/U_c$. Consequently, the time delay is converted into spatial shift Δx using $\Delta x = \Delta x_m + \Delta x_a - \tau_i U_c$. Here, U_c is the convection velocity of the targeted structures determined in §4.2. As a reference, the $\langle u_l^+ \rangle$ and $\langle u_{\tau_l}^+ \rangle$ of an uncontrolled boundary layer is presented in figure 5.4(a). Since we are conditioning on a positive zero crossing in the large-scale temporal $u_{\tau_{l5}}$ signal, we see spatially a large-scale inclined (forward leaning) low momentum region located downstream of a high-speed region of similar size and inclination. The strong coherence extends at least up to the top of the log region ($z^+ = 2000$). Since the measurement location of the conditional analysis is located at $\Delta x = 3.3\delta$ downstream of the conditional points, the lifetime of the coherent

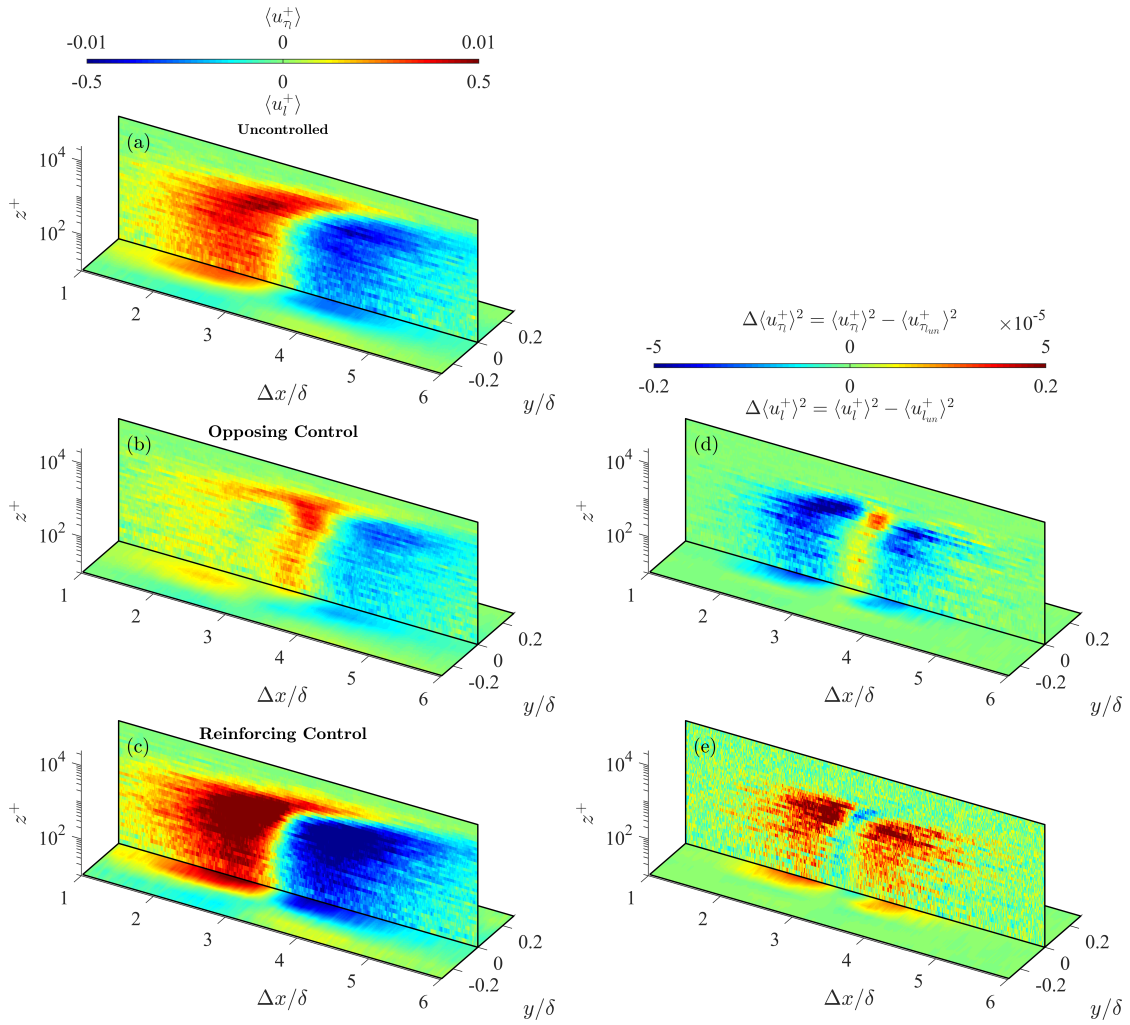

Figure 5.4: Ensemble averaged large-scale events and their footprints at 1.7δ downstream of the actuation array conditioned the positive zero-crossings of the large-scale skin-friction velocity fluctuation acquired by the center hot-film in the detection array (HF_{D5}) within the (a) uncontrolled, (b) opposing controlled and (c) reinforcing controlled boundary layers. Variation of the conditional streamwise velocity energy between the uncontrolled and (d) opposing and (e) reinforcing controlled boundary layers with respect to the uncontrolled case.

motions in equation 4.3 suggests that the LSMs with $\lambda_x \leq 2.3\delta$ is not observable in the conditional structures in figure 5.4(a). Thus, the uncontrolled conditional structure is less energetic than the three-dimensional structures shown by Hutchins et al. (2011), which had $\Delta x = 0$ and would have included these smaller scales, and consequently, the most energetic region of the structure in figure 5.4(a) is located around the center of the log region.

Figure 5.4(b,c) show the conditional large-scale structures manipulated in the opposing control

and reinforcing control strategies, respectively. Since the conditional points are based on the large-scale upstream u_τ with $\lambda_{x.c} > 1.6\delta$, it is expected that the conditionally averaged results in figure 5.4 provide proved conditional view of the structures with a streamwise length-scale larger than the cut-off wavelength, hence providing a useful representation of the manipulation of the active jet actuation on the LSMs without the small-scale disturbance. The conditional high and low-speed events in the opposing controlled boundary layer (figure 5.4(b)) are attenuated in comparison to the uncontrolled case (figure 5.4(a)). The fluctuations of both $\langle u_l^+ \rangle$ and $\langle u_{\tau_l}^+ \rangle$ decrease, as shown on the streamwise/wall-normal and wall-parallel planes respectively in these figures. It is noted that for the opposition control strategy, the jets will only fire during the high-speed positive event (red region) shown in figure 5.4(b). The weakening of the low momentum region is presumably a knock-on effect due to the weakening of the large-scale vortical motions by the opposing control strategy. Conversely, for the reinforcing control strategy, the low-speed LSMs are enhanced by the injected jet flow and the high-speed motion also becomes more energetic. In the reinforcing controlled case, the jets are only fired during the large-scale low momentum region depicted in figure 5.4(c). The strengthening of the low momentum regions is expected. since the positive wall-normal motion of the jets adds to or reinforces these naturally ejecting large-scale events. Strengthening of the high-speed motions, in turn, is the side-effect of energizing the large-scale vortical motions by the reinforcing scheme. The difference of the conditional streamwise velocity energy between the perturbed and uncontrolled conditional structures ($\Delta \left\langle u_l^+ \right\rangle^2 = \left\langle u_{l_{un}}^+ \right\rangle^2 - \left\langle u_l^+ \right\rangle^2$ and $\Delta \left\langle u_{\tau_l}^+ \right\rangle^2 = \left\langle u_{\tau_{l_{un}}}^+ \right\rangle^2 - \left\langle u_{\tau_l}^+ \right\rangle^2$) are shown in figure 5.4(d,e). Figure 5.4(d,e) clearly shows that the opposing control strategy attenuates the energy of the conditional structures while the reinforcing control strategy energizes the structures, which further verifies and explains the variation of large-scale turbulent intensity for these two strategies presented in figure 5.2(a). In addition, a correlation is observed between the control effect on the conditional velocity structures ($\Delta \left\langle u_l^+ \right\rangle^2$) and their footprints on the wall ($\Delta \left\langle u_{\tau_l}^+ \right\rangle^2$). This suggests that the superposition of the large-scale motions from the outer region on the near-wall turbulence is preserved even in the perturbed boundary layers. As a result, the high skin-friction footprints are most effectively alleviated in the opposing controlled case by attenuating the energy of the high-speed motions, which contributes to a higher drag reduction.

The manipulation of the large-scale footprints is further examined by the spanwise two-point

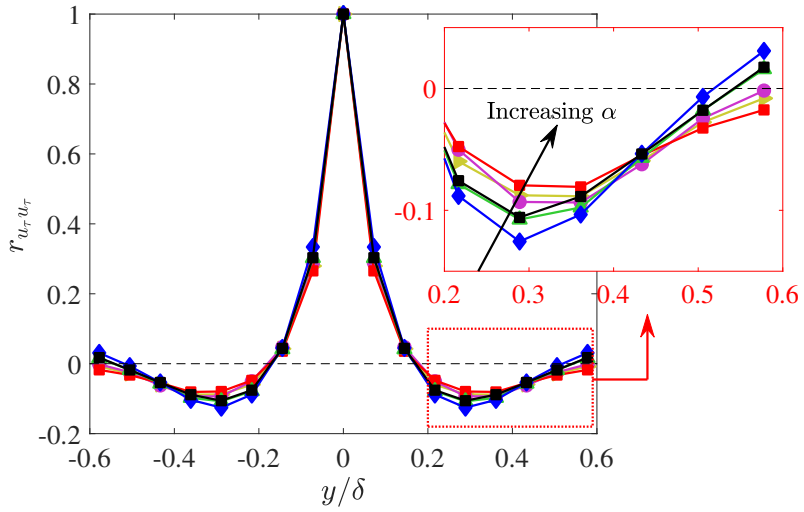

Figure 5.5: Spanwise correlation coefficient between the u_τ signals at $\Delta x_m = 1.7\delta$ with varying spanwise separation for the all control strategies listed in table 5.1. Symbols are as give in table 5.1.

correlation coefficient $r_{u_\tau u_\tau}$ between the u_τ signals acquired at the measurement hot-film array (located $\Delta x_a + \Delta x_m$ downstream of the detection array, in this case, 3.3δ) with different spanwise separations. The $r_{u_\tau u_\tau}$ for both uncontrolled and controlled cases in set 1 and set 2 measurements are shown in figure 5.5. All cases possess a unity auto-correlation coefficient with zero offsets and a positive correlation when the spanwise offset is smaller than 0.2δ. This positive region is flanked by the negative correlations, which agrees with the results of Hutchins and Marusic (2007a). However, small discrepancies are recognizable in the magnified negative correlation region when the control is applied. Compared to the uncontrolled case (black lines), the opposing control weakens the correlation while the reinforcing case enhances it. This indicates that the correlation of the perturbed LSMs is negatively related to the control accuracy. In other words, when a larger portion of the high-speed events is manipulated by the wall-normal jet, the size (length and width) and the strength of the controlled LSMs decreases. Thus, the large-scale superposition of the large-scale structures not only influences their footprints in the x direction, the spanwise dynamic is also affected.

Spectrally, in figure 5.1, the superposition effect can be inferred from the interaction between the log and near-wall regions where $\lambda_x > \lambda_{x.c}$. This superimposed large-scale energy is clearly altered by weakening the large-scale structures in the log region through active opposing control.

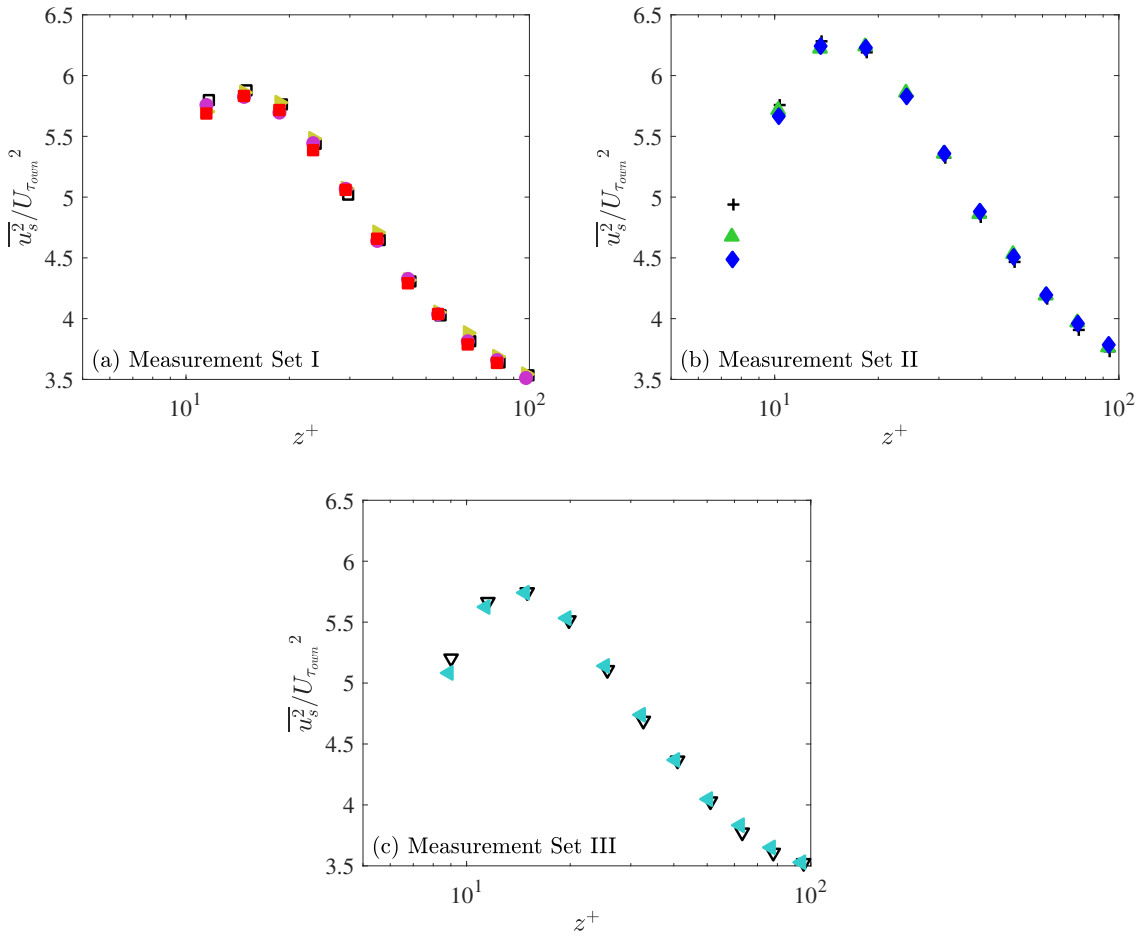

Figure 5.6: Near-wall ($5 \leq z^+ \leq 100$) small-scale turbulent energy normalized by the corresponding local mean friction velocity for the tested cases in (a) Measurement Set I, (b) Measurement Set II, and (c) Measurement Set III. The tested cases and their corresponding symbols are listed in table 5.1.

In contrast, the investigation of the amplitude modulation effect on the near-wall small-scale structures concentrates on the relationship between the large-scale energy in the log region and near-wall small-scale turbulence around the inner peak in the perturbed boundary layers. The classical universality hypothesis depicts that these small-scale structures are universal and independent of the Reynolds number and hence independent of changes in the large-scale structure. Therefore, we might expect the small-scales to exhibit universal behaviour even in the actively perturbed boundary layers. However, in figure 5.2(d), different large-scale flow control strategies result in minor deviations in the small-scale turbulence energy near the wall, because the canonical uncontrolled mean skin-friction velocity is used to normalize the perturbed $\overline{u_s^2}$. Hence, in figure 5.6, the small-

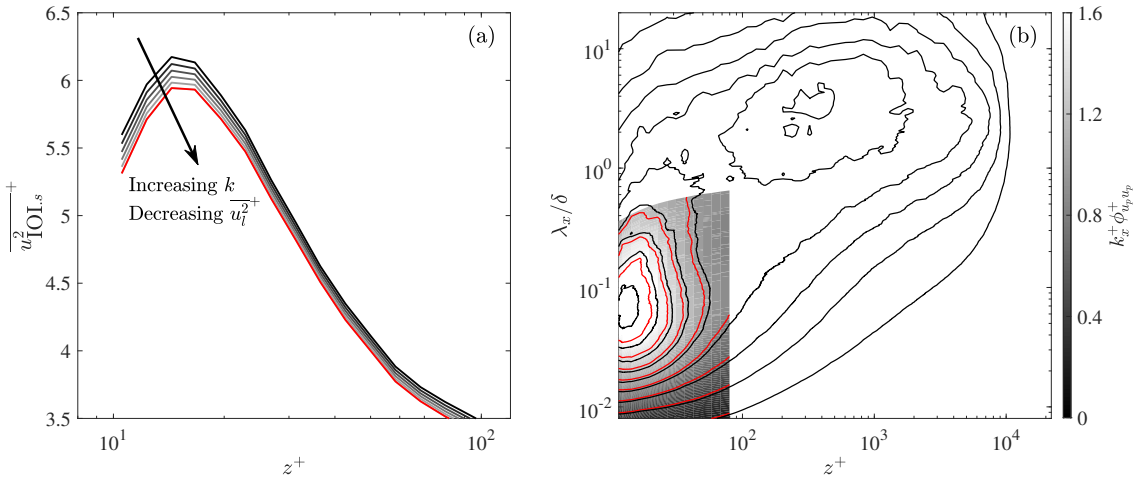

Figure 5.7: (a) Small-scale turbulent energy ($\overline{u^2_{\mathrm{IOI}.s}}^+$) with a cut-off wavelength of approximately 0.5δ predicted based on the IOI model with the large-scale energy of the input signal at the center of log region scaled down by the values of k ranging from 0 to 100% with an increment of 20%. (b) Pre-multiplied spectrogram of u in an uncontrolled boundary layer (black lines). Red lines are the pre-multiplied spectrogram of $u_{\mathrm{IOI}.s}$ predicted from a flattened large-scale velocity component (i.e. $k = 0$).

scale turbulent energy in the controlled cases of all three sets are normalized by their own local U_τ. If we compare, for each set in figure 5.6(a,b,c), the small-scale energy scaled in this manner for the perturbed and the reference uncontrolled case, very good agreement is observed. It reveals that the control effect on small-scale structures near the wall is totally recovered at 1.7δ (25000 wall units) downstream of the actuation array. Such a phenomenon provides another experimental proof to the Quasi-Steady Quasi-Homogeneous (QSQH) hypothesis of Chernyshenko et al. (2012). In the viscous sublayer, the near-wall small-scale turbulence scales with the (temporal and spatial) local fluctuating large-scale skin-friction velocity, which is identical to the observation of Zhang and Chernyshenko (2016) in DNS data at a wide range of Re_τ.

Recently, the IOI model by Marusic et al. (2010) and Mathis et al. (2013) formulated the interactions between the large-scale fluctuations in the log region and the small-scale skin-friction velocity fluctuations near the wall in an uncontrolled boundary layer. Under the QSQH hypothesis of Chernyshenko et al. (2012) and the IOI model of Marusic et al. (2010), it is expected that the universal signal will remain universal even for the perturbed actively controlled boundary layers, but with the degree of amplitude modulation altered as the active control strategy alters the large-

scale energy. Mathis et al. (2009, 2011b) demonstrated that the effect of the amplitude modulation manifests most strongly in the odd moments (i.e. skewness) of the small-scale turbulent signals while the effect of amplitude modulation on the even term (i.e. variance) of the small-scales is limited. Here, attempts are made to quantitatively estimate the potential small-scale energy (variance) attenuation via amplitude modulation effect through controlling the large-scale structures in the outer region via a pseudo-control scheme to mimic the current real-time control strategy. In specific, the unmodified low wavenumber velocity components at the geometric center of the log region are scaled by $\sqrt{k}$, so that $u_{l_k} = \sqrt{k}u_l$. Remember u_l is a zero-mean quantity, in turn, we have $\overline{u_{l_k}^2} = k\overline{u_l^2}$, where k takes a value between 0 and 1. Taking the scaled u_{l_k} as an input of the IOI model, the small-scale streamwise velocity fluctuations $u_{\mathrm{IOI}.s}$ in the near-wall region can be predicted. In figure 5.7, due to the modulation effect, when the large-scale energy of the input u_{l_k} decreases with the k scaling, the small-scale turbulence energy ($\overline{u_{\mathrm{IOI}.s}^2}^+$) of the predicted fluctuating small-scale velocities are also reduced. Note that $\overline{u_{\mathrm{IOI}.s}^2}^+$ in figure 5.7 are normalized by the canonical uncontrolled friction velocity U_τ so that the value of ($\overline{u_{\mathrm{IOI}.s}^2}^+$) does not consider the potential drag reduction resulted from the modified large-scale energy in the log region (in contrast to the results presented in figure 5.6, which used the local modified $U_{\tau_{own}}$). The highlighted red line represents $\overline{u_{\mathrm{IOI}.s}^2}^+$ with a zero k value (de-trended velocity fluctuations, with zero large-scale energy and zero superposition). The red line indicates that when all large-scale fluctuations in the log region are perfectly alleviated the small-scale energy $\overline{u_{\mathrm{IOI}.s}^2}^+$ around the inner peak could be reduced by approximately 4%. The remaining small-scale energy is the universal signal, due to the self-sustaining near-wall turbulence that requires no large-scale input to sustain. For reference, figure 5.7(b) shows the pre-multiplied energy spectrum of an uncontrolled turbulent boundary layer (black solid lines) and that of the perfectly de-trended velocity signals (red solid lines for $k = 0$), which shows a uniform energy reduction for all scales with $\lambda_x \leq 0.5\delta$.

The predictions for the small-scale energy contribution of the LSMs from the pseudo-control strategies is compared against the experimental results of the large-scale control by introducing the mean small-scale energy reduction in the near-wall region of the perturbed boundary layers. Similar to the definition of ΔE_l, the value of ΔE_s is computed as the percentage change of the integrated energy with $\lambda_x < 0.5\delta$ and $z^+ < 80$ between the controlled/pseudo-controlled boundary layer and the uncontrolled cases, which can be expressed as equation 5.4.

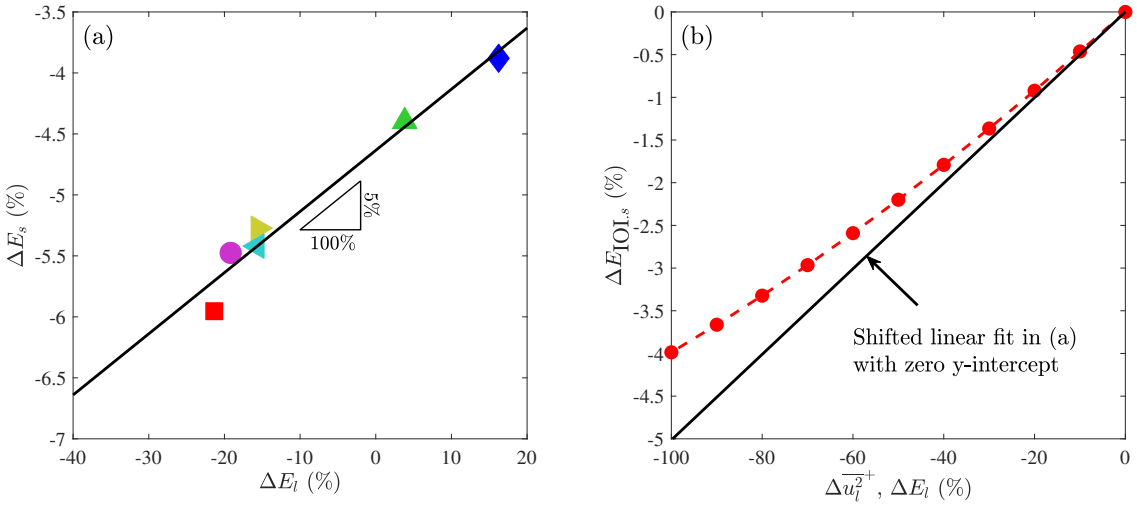

Figure 5.8: (a) Spatial averaged large-scale and small-scale energy reduction under each measurement strategy with the linear fit of the data points shown as black lines. Symbols are as give in table 5.1. (b) Red dashed line is the large-scale energy reduction in the center of the log region against the spatial averaged small-scale energy alleviation in accordance with IOI model. Black solid line is the shifted linear fit in (a) to ensure a zero y-intercept (i.e. no small-scale energy change when $\Delta E_l = 0$).

$$\Delta E_s(\%) = \frac{\int_0^{80}\int_0^{0.5\mathrm{Re}_\tau} \left(\phi_{uu}/\phi_{uu_{un}} - 1\right) d\lambda_x^+ dz^+}{80} \times 100 \tag{5.4}$$

Figure 5.8(a) shows that ΔE_s has a positive linear relationship against ΔE_l for all control schemes and real-time filters tested in table 5.1, which agrees with the predicted relationship from the pseudo-controlled cases in figure 5.7(a). It is useful to also consider the slope of the fitted linear relation between ΔE_s and ΔE_l. With a 100% reduction of the large-scale structures with $\lambda_x > 1.6\delta$, the experimental data in figure 5.8(a) predicts that we would see a 5% reduction of the short-wavelength near-wall turbulence. Such a value agrees with the skin-friction drag contributed by the large-scale energy with the same streamwise wavelengths in figure 5.3, which further suggests that the near-wall small-scale turbulence is an immediate response to the modified local friction velocity referring to the QSQH hypothesis. It is also noted that ΔE_s in actively controlled boundary layers is reduced even by control strategies that cause a large-scale energy increase (e.g. the reinforcing control case in figure 5.8(a)) which is represented by ♦ This offset again is likely due to the net time-averaged mass flux from the jets, and hence net time-averaged positive wall-normal offset imposed near the wall which will tend to lift the viscous sublayer causing an

underlying reduction in small-scale energy. Recall that this time-averaged mass-flux is the same for all control cases. In contrast, for the IOI model predictions (shown as ● in figure 5.8(b)), after virtually damping out all the large-scale energy u_l^2 in the center of the log region, the maximum small-scale energy reduction is approximately 4%, which is slightly smaller than the experimental observation. To better compare the results, the linear fit attained from the experimental result is shifted to remove the net mass-flux effect such that there $\Delta E_s = 0$ when $\Delta E_l = 0$. With this shift in figure 5.8(b), a reasonable alignment is observed between the predicted IOI model behaviour and linear fit to the experimental data, especially within the regime of the experimentally large-scale energy attenuation ($-20\% \leq \Delta E_l \leq 20\%$). This indicates the IOI model is generally applicable in a perturbed boundary layer but only subject to the condition that the near-wall turbulence recovers to the canonical universality (i.e. only at sufficient distances downstream of the actuation). The small discrepancy between the experimental fit and the IOI predictions likely result from experimental error and also from the linear assumption employed in figure 5.8(a). In addition, ΔE_l is the spatially averaged change of large-scale energy below the upper bound of the log region, whereas $\Delta\overline{u_l^2}$ considers only one input z position (at the center of log region i.e. $z^+ = 480$). As aforementioned, ΔE_l depends on the weighting of the large-scale energy at different wall-normal positions. If only the change in $\overline{u_l^2}$ at the geometric center of the log region is considered for the experiments to compute ΔE_l, the slope between ΔE_l and *DR* in figure 5.3 reduces to 4%. which follows the 4% maximum ΔE_s predicted by the IOI model in figure 5.8(b). In conclusion, the results in figure 5.7 and figure 5.8 reinforce the idea that the control of the large-scale structures affects the near-wall small-scale turbulent energy via both an altered superposition and also an altered modulation effect.

5.3 Streamwise Evolution of Control Effects

In previous sections, the mean wall-shear-stress contribution of the LSMs with $\lambda_x > 1.6\delta$ is shown to be limited to approximately 5.6%. However, as discussed in §4.2, the LSMs are capable to maintain correlated for more than 10δ in the streamwise direction. Thus, it is reasonable to presume that the other important feature of large-scale control is long persistence. Here the streamwise evolution of the large-scale control is first investigated by moving the measurement array to different

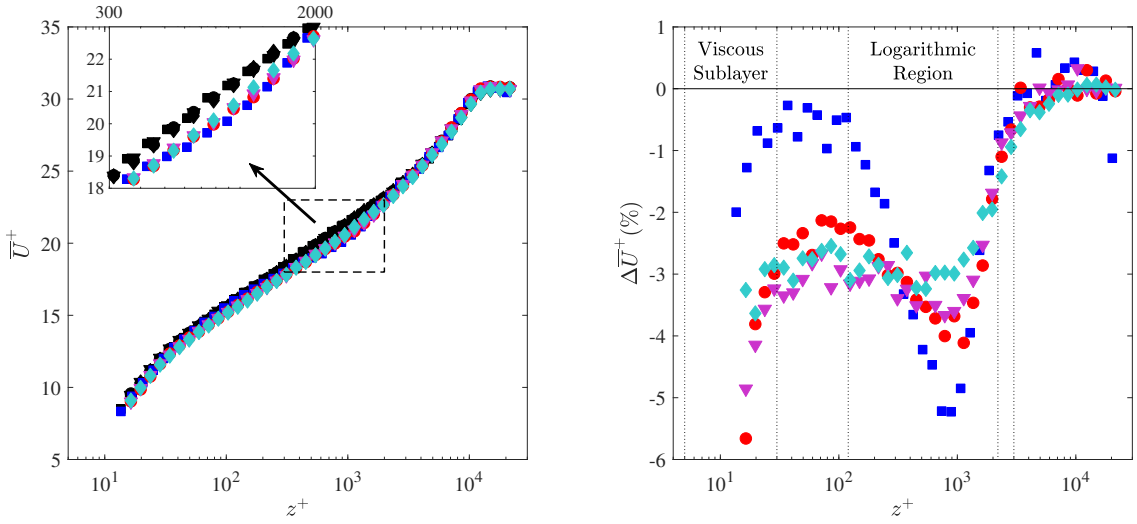

Figure 5.9: (a) Mean streamwise velocity for the uncontrolled and opposing controlled case at all measurement stations (b). Mean streamwise velocity deficit $\Delta\overline{U}\,(\%)$, as defined in equation 5.5, for the opposing controlled case at all measurement stations. Symbols are as given in table 5.2.

positions downstream of the actuation array (i.e. $\Delta x_m = 0.3$m (0.85δ), 0.6m (1.7δ), 0.9m (2.5δ), and 1.5m (4.2δ), respectively). Since the major target of the active control is to achieve skin-friction drag reduction, only the opposing controlled scheme and a referencing uncontrolled case are examined at each measurement station in the current hot-wire investigation on the streamwise evolution of the control effects. Detailed information on the measurement parameters is summarized in table 5.2. As previously mentioned in §4.1, the boundary layer nearly approaches streamwise homogeneity, so that the Reynolds number at each measurement station is approximately equivalent as U_∞ is fixed nominally at 20m/s. This assumption is further validated in figure 5.9(a), which shows a good alignment among the wake regions of the mean velocity profiles of all examined cases.

When the opposing control is applied, streamwise velocity deficits due to the injected jet flow are observed at all measurement stations as highlighted by the zoomed inset in figure 5.9(a), there is a clear streamwise evolution of this effect. This is better explained in figure 5.9(b) where the percentage change of the mean velocity, which is defined below as equation 5.5, is presented to better illustrate the deviation of the opposition control from the canonical case at different streamwise locations.

$$\Delta\overline{U}^{+}(\%) = (\overline{U}^{+}/\overline{U}^{+}_{un} - 1) \times 100(\%) \tag{5.5}$$

In general, $\Delta\overline{U}(\%)$ exhibits two peaks, one in the viscous sublayer and one close to the geometric center of the log region ($z^{+} \approx 800$). The maximum $\Delta\overline{U}(\%)$ in the log region is due to the momentum deficit of the injected low momentum jet flow which has a jet ratio design to ensure penetration of the jet to the top of the log region. This deceleration decays with increasing Δx_m as the low momentum jet fluid mixes and disperses into the targeted large-scale high momentum event. Specifically, figure 5.9(b) indicates that $\Delta\overline{U}^{+}(\%)$ at the log region peak decreases from 5% at $\Delta x_m = 0.85\delta$ to 3% at $\Delta x_m = 4.2\delta$ due to the mixing between momentum of the cross-flow and the jet flow. In addition, close to the jet position, the velocity deficit is more concentrated in the log region between approximately $100 < z^{+} < 2000$ for the upstream location (■), but the streamwise momentum deficit spreads from the log region towards a wider range of wall-normal positions as Δx_m increases. For example, at $\Delta x_m = 4.2\delta$ (♦) in figure 5.9(b), the momentum deficit extends in the range of $0 < z^{+} < 7000$, This behaviour is expected because the conventionally exponential jet trajectory in the crossflow suggests the local penetration height is positively proportional to Δx_m. However, an exact quantification of the penetration height of the jet flow requires a finer streamwise resolution of the flow field, which will be presented in Chapter 6, where PIV data is available. The percentage velocity deficit $\Delta\overline{U}^{+}(\%)$ under the upper bound of viscous sublayer increases from less than 1% at $\Delta x_m = 0.85\delta$, reaching a peak at almost 6% for $\Delta x_m = 1.7\delta$, be-

Table 5.2: A summary of the opposing controlled case at different measurement stations

Δx_m [m]	**Symbols**	**Real-time Filter**	**Control Scheme**	Re_τ	U_τ [m/s]	ν/U_τ [μm]	l^{+}_{hw}	d^{+}_{hw}	δ [m]
0.3 (0.85δ)	■ ■	— LSE	Uncontrolled Opposing	14190	0.635	25.23	18.9	0.1	0.363
0.6 (1.7δ)	● ●	— LSE	Uncontrolled Opposing	14380	0.645	25.03	20.3	0.1	0.362
0.9 (2.5δ)	▼ ▼	— LSE	Uncontrolled Opposing	14570	0.643	25.12	20.2	0.1	0.366
1.5 (4.2δ)	♦ ♦	— LSE	Uncontrolled Opposing	14620	0.652	24.82	20.4	0.1	0.363

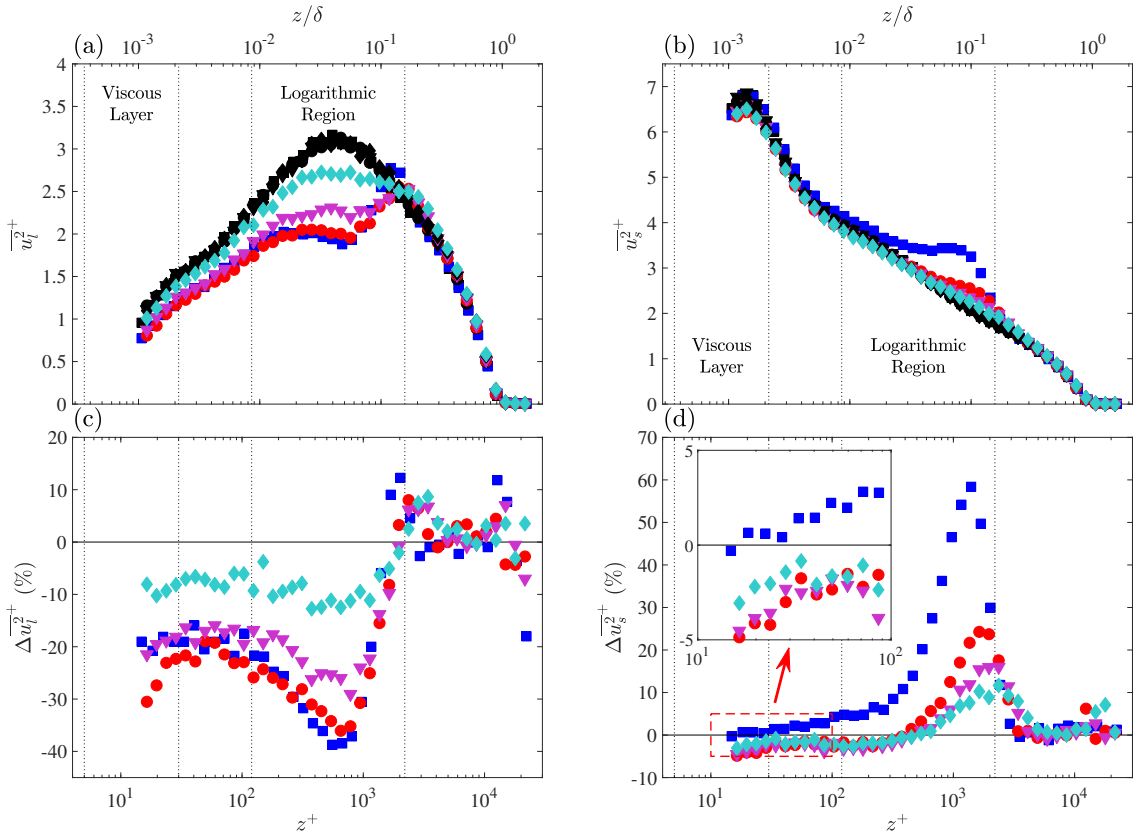

Figure 5.10: (a,b) Large-scale and small-scale turbulent intensity for the uncontrolled and opposing controlled case at all measurement stations. (c,d) Percentage variation of the large-scale and small-scale turbulent energy of the opposing controlled case at all measurement stations. Symbols are as given in table 5.2.

fore relaxing to approximately 3% at the two most downstream locations. This behaviour closely mimics the observed streamwise evolution of drag reduction which is presented in figure 5.11.

The streamwise evolution of the turbulent energy variation caused by the large-scale opposing control is analyzed in the same manner as that in §5.1 using Fourier decomposition. Figure 5.10(a,b) shows the streamwise evolving large and small-scale energy profiles for the opposing controlled case, respectively. The large-scale turbulent energy in figure 5.10(a) at all measurement stations is attenuated under the upper bound of the log region. Here, the large-scale and small-scale turbulent energy in uncontrolled and perturbed boundary layers are both normalized by the uncontrolled referencing U_τ in the same manner as figure 5.2. The percentage change in large-scale energy relative to the uncontrolled case ($\Delta\overline{u_l^2}^+$ as defined previously in §5.1), is pre-

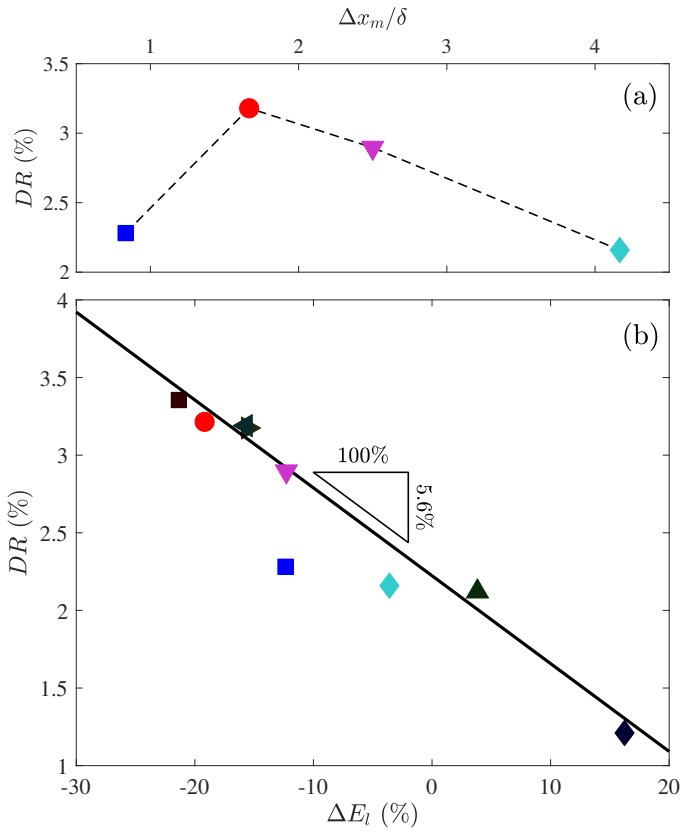

Figure 5.11: (a) Mean skin-friction drag reduction at the centerline of the control plane measured at different streamwise direction. (b) Colored markers are the mean large-scale energy variation and the drag reduction of the opposing controlled boundary layers measured at $\Delta x_m = 0.85\delta$ (■), 1.7δ (●), 2.5δ (▼), 4.2δ (♦), respectively. Black solid line and markers are adapted from the mean large-scale energy variation and the drag reduction for different control strategies in figure 5.3.

sented in figure 5.10(c), which shows that $\Delta\overline{u_l^2}^+(\%)$ is almost identical between 0.85δ and 1.7δ downstream of the actuation, reaching 35-40% in the middle of the log region. Thus, the interaction between the jet flow and the LSMs seems to initiate immediately at $\Delta x_m < 0.85\delta$. However, the deterioration on the large-scale energy reduction initiates after this position, but there is still an approximately 10-15% large-scale energy attenuation in the near-wall and log region at the most downstream measured position (i.e. $\Delta x_m = 4.2\delta$), which confirms that the large-scale control is, to some degree, persistent within the boundary layer. It should be specially noticed that 4.2δ corresponds to 60000 viscous wall units, so this is an extremely persistent control effect in comparison to other opposition control strategies discussed in §2.3.3 that have targeted near-wall viscous-scaled events. Consistent with the observation in figure 5.2, the small-scale energy as

shown in figure 5.10(b) varies insignificantly in the viscous sublayer and increases significantly around the upper bound of the log region, due to the shear layers formed on the upper bound o the injected jet in crossflow. Figure 5.10(d) shows the percentage change of the small-scale energy $\Delta\overline{u_s^2}^+(\%)$ relative to the uncontrolled boundary layer. The small-scale turbulence is energized by the active control for $z^+ > 30$ at $\Delta x_m = 0.85\delta$, but for $\Delta x_m \geq 1.7\delta$ we see an extending region of weakened small-scale energy extending from the wall to close to the geometric midpoint of the log region ($0 < z^+ \lesssim 400$). Figure 5.11(a) shows that the drag reductions measured by the downstream hot-film array at $\Delta x = 0.85\delta$, 1.7δ, 2.4δ and 4.2δ are 2.3%, 3.4$, 2.9% and 2.2%, respectively, so the *DR* is maximized at the 1.7δ downstream of the control. Thus, it is observed that the near-wall small-scale energy attenuation for $\Delta x_m \geq 1.7\delta$ decreases along the x direction in response to the variation of the local skin-friction drag reduction. At the same time, the region of increased small-scale energy (positive $\Delta\overline{u_s^2}^+(\%)$) extends to a higher wall-normal position with increasing Δx_m, which closely follows the streamwise evolution of the jet penetration height at each measurement location.

Results in figure 5.11(a) provide the opportunity to estimate the global power saving (ΔP_g) of the current active large-scale flow control strategy over the entire affected area, and hence, a preliminary estimation on the resulting net power saving (P_{net}). It is worth noting that the estimation of the global power saving still requires many assumptions: (i) Based on the relationship between *DR* and Δx_m in figure 5.11(a), it is assumed that the resulting skin-friction drag reduction deteriorates linearly in the streamwise direction for $\Delta x_m > 1.7\delta$. (ii) The control effect on the skin-friction drag only exists at $|\Delta y < 0.28\delta|$ and the spatial-averaged *DR* in the spanwise direction is assumed to be equivalent to the *DR* at $\Delta y = 0$. (iii) The global power saving due to skin-friction drag reduction is calculated using the equation below, which is numerically computed via the trapezoid method in a discrete manner.

$$\Delta P_g = \Delta D U_\infty = 0.58\delta U_\infty \int_0^{5.8\delta} U_\tau^2 \rho \, DR \, dx \tag{5.6}$$

Here, ΔD is the fractional reduction in the wall-shear stress, and the global power saving over a width of 0.58δ and a length of 5.8δ is estimated to be 21mW. At the same time, the total power input is estimated to be the dynamic energy of the jet flow. It should be mentioned that, in the real world, more electrical energy is required for the air compressor and the control

of the actuation, which is ignored in the calculation (i.e. we assume an ideal compression with 100% efficiency). As mentioned in Chapter 3 the jet exit velocity is 13.6m/s and the jet exit area is $w_j \times l_j = 50\text{mm} \times 2\text{mm}$. The dynamic power input for one normal jet is approximated as $P_{in} = \dot{m}U_{jet}^2 = \rho w_j l_j U_{jet}^3 \approx 0.32\text{W}$. On average, 4.5 jets will be activated simultaneously for the area considered in this calculation, so the total net power input is over 1.4W. There would be additional losses due to the power requirements of the sensors, real-time control, and the solenoid valves. However, even neglecting these it is clear that the net power input substantially overwhelms the global power saving achieved by active control by a factor of more than 66, so the current strategy comes nowhere close to achieving net power savings. however, as mentioned in the introduction and throughout the thesis, the objectives of the current study remain on understanding the potential and mechanism of reducing wall-shear stress by manipulating LSMs.

Figure 5.11(b) combines the drag reduction *DR* and the spatially averaged large-scale energy reduction ΔE_l as defined in equation 5.1, at all four measurement stations (colored markers). Recall that ΔE_l essentially averages $\Delta\overline{u_l^2}^+$ for $0 < z^+ < z_p^+$, where z_p is the jet penetration height taken. Since the evolving jet flow extends to a higher wall-normal position with increasing Δx_m, the penetration height z_p here is defined as the location where $\Delta\overline{U}^+(\%) < 0.1\%$ in figure 5.9, which increases from 3000^+ at $\Delta x_m = 1.7\delta$ to 5000^+ at $\Delta x_m = 4.2\delta$. At the same time, the black markers are the reproduced *DR* and ΔE_l for the different control strategies are presented previously in figure 5.3. It is shown that the *DR* and ΔE_l at $\Delta x_m = 2.4\delta$ and 4.2δ downstream of the actuation agree with the linear relationship obtained in §5.1. The outlier (■) at $\Delta x_m = 0.85\delta$ could be due to the intrusive perturbation induced by the jet flow on the small-scale turbulent energy which has not fully recovered at this position. As evidence of this, in figure 5.10(d), while the near wall ($z^+ < 30$) small-scale turbulent energy at $\Delta x_m \geq 1.7\delta$ are all decreased by 2-4%, the small-scale energy is slightly increased at $\Delta x_m = 0.85\delta$ for $z^+ < 100$. Therefore, the measured drag reduction at this location is a competition between the beneficial (drag reducing) effect of reducing the large-scale energy and the detrimental increase in small-scale near-wall energy. Hence the deviation from the linear curve which seeks to relate *DR* purely to reduction of large-scale energy.

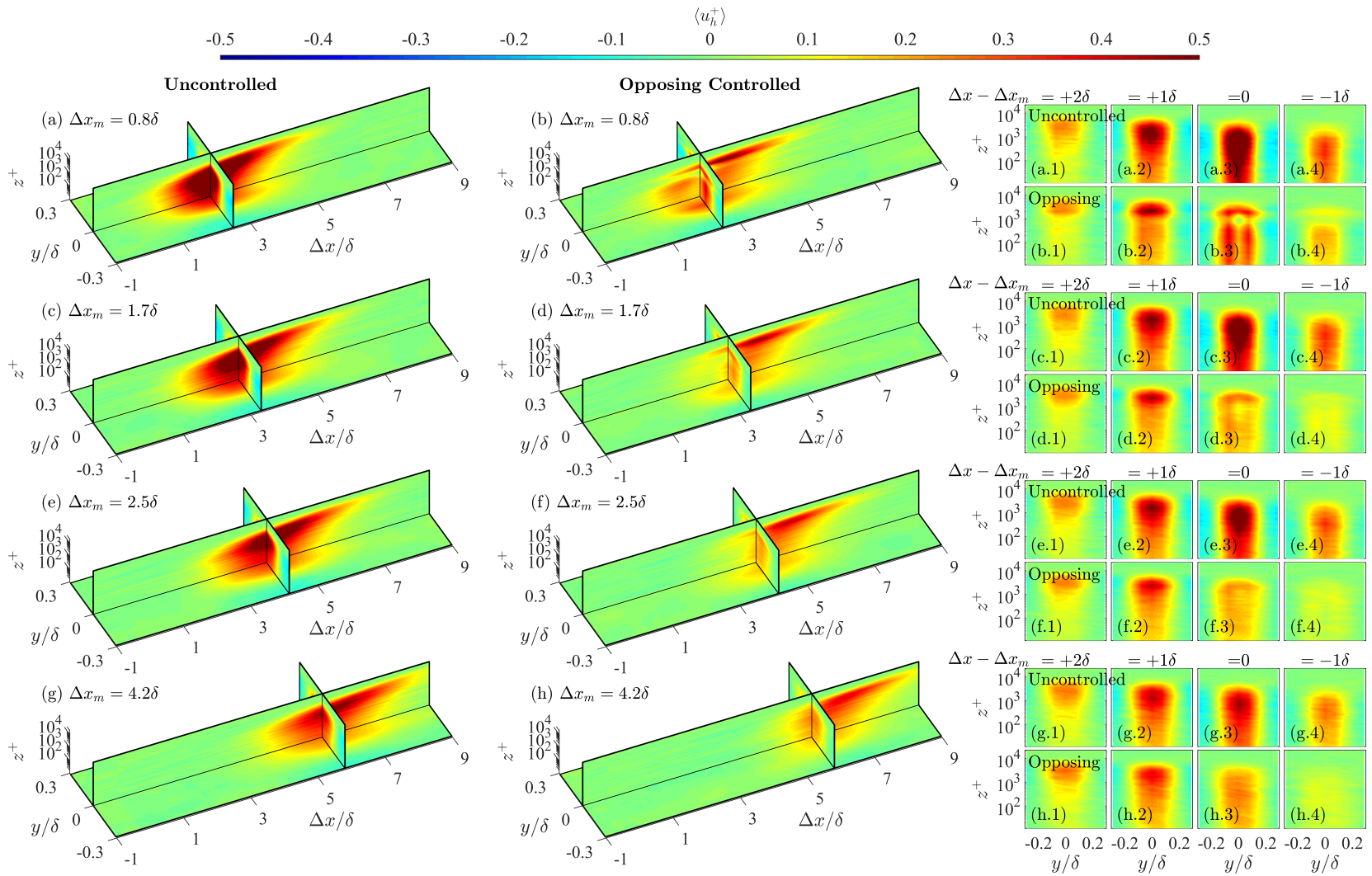

Figure 5.12: Iso-contours of the three-dimensional high-speed large-scale structures conditioned on positive large-scale friction velocity at HF_5 for both uncontrolled and opposing controlled boundary layers at (a,b) $\Delta x_m = 0.85\delta$, (c,d) 1.7δ, (e,f) 2.5δ, and (g,h) 4.2δ downstream of the actuation array. The left-hand column shows the uncontrolled conditional average. The middle column shows the opposing controlled case and the right column shows spanwise/wall-normal slices of the conditional structure upstream and downstream of the condition point at (x.1) $\Delta x = 2\delta + \Delta x_m$, (x.2) $\Delta x = 1\delta + \Delta x_m$, (x.3) $\Delta x = \Delta x_m$, and (x.4) $\Delta x = -1\delta + \Delta x_m$.

Because the opposing control is designed to only manipulate the estimated positive LSMs, the evolution of the control effect is further examined via a 3-dimensional conditional analysis of these events. Since the main focus here is the manipulation of the high-speed events, as expressed in equation 5.7 and 5.8 the conditional points have been changed to all positive u_{τ_l} regions. Different from the conditional averaged quantity in the previous section which was conditioned on positive zero-crossing of the u_{τ_l} estimated from the detection array, these selected condition points ensure a focus purely on the high-speed structures.

$$\langle u_h^+ \rangle (\tau^+) = \langle \Big(u^+(t^+ + \tau^+, z^+) \mid u_{\tau_{l_5}}(t^+) > 0 \Big) \rangle \tag{5.7}$$

$$\langle u_{\tau_h}^+ \rangle (\tau^+) = \langle \Big(u_\tau^+(t^+ + \tau^+, y/\delta, z^+) \mid u_{\tau_{l_5}}(t^+) > 0 \Big) \rangle \tag{5.8}$$

where, $\langle u_h^+ \rangle$ and $\langle u_{\tau_h}^+ \rangle$ are conditional velocity and friction velocity fluctuations conditioned in the presence of a high skin-friction event detected by HF_{U5}. It should be noted that because the condition vector in equations 5.7 and 5.8 are met everywhere throughout the footprint of a positive LSM, these conditional averages will be substantially more phase-jittered than the results conditioned on zero crossings. Figure 5.12(a,c,e,g) are the conditional high-speed structures measured at $\Delta x_m = 0.85\delta$, 1.7δ, 2.5δ, and 4.2δ, while (b,d,f,h) are the opposing controlled high-speed LSMs. Again, the value of Δx is computed from the composite method introduced before. Three additional cross-plane (spanwise/wall-normal) clips locating at -1δ, 1δ, and 2δ away from the measurement points are illustrated for each conditional structure (right column of figure 5.12). In the uncontrolled case, the conditional high-speed events are flanked by two negative streamwise velocity region and the general geometry agrees with the conditional structures reported by Hutchins and Marusic (2007b). Moving further downstream, the conditional structures gradually lose their kinetic energy due to the missing correlation of the high wavenumber velocity components between the condition and measurement points. As a result, maximum $\langle u_h^+ \rangle$ in the cross-plane contours of the uncontrolled structures in figure 5.12(a.3) grows to higher z positions in figure 5.12(c.3,e.3,g.3). In the perturbed structures, figure 5.12(b.3) shows that the control effect is initially concentrated on the centerline ($y/\delta = 0$) of the control plane at $\Delta x_m = 0.85\delta$. With increasing downstream distance the perturbation of the LSM propagates in the spanwise direction,

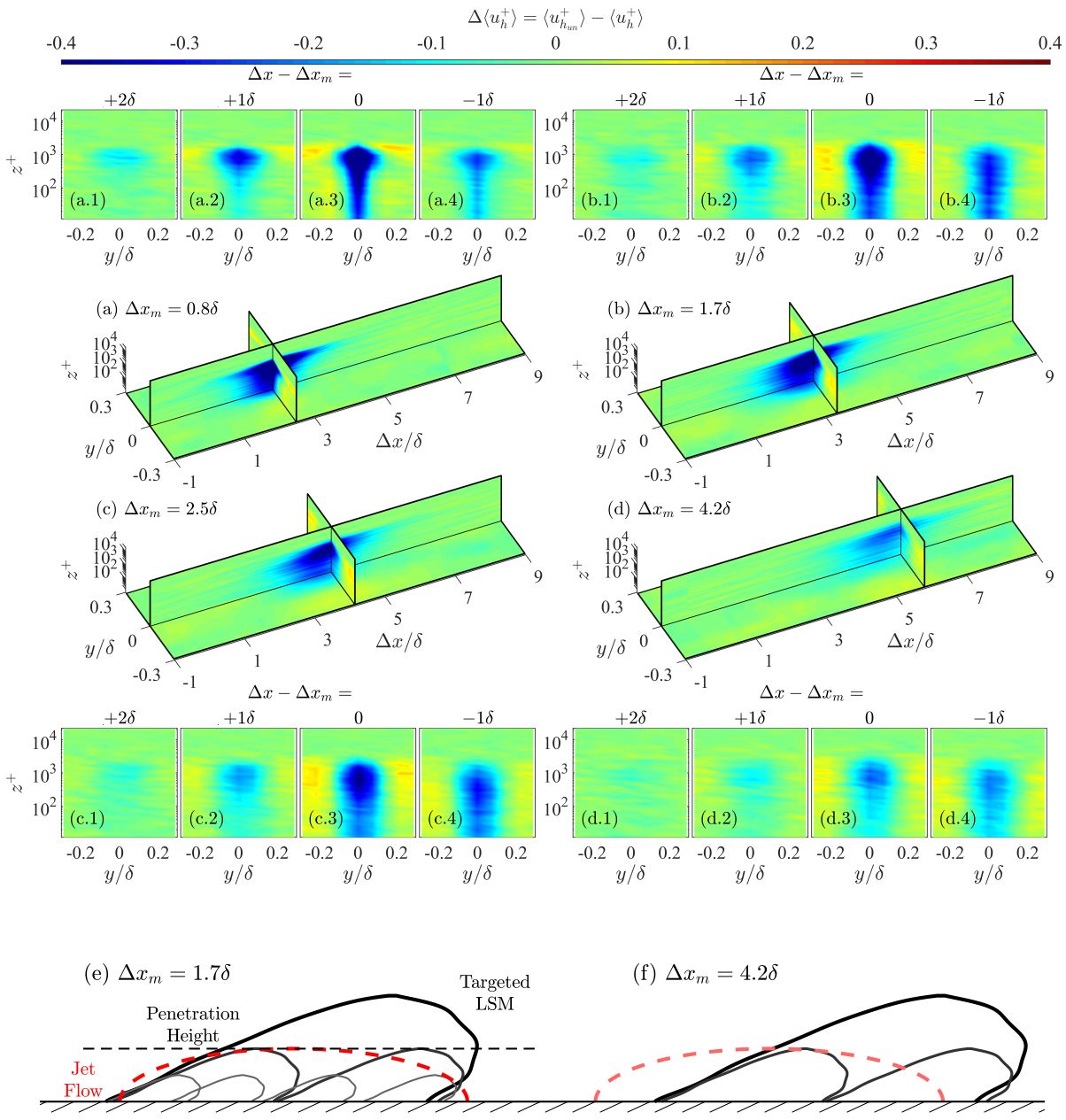

Figure 5.13: Iso-contours of the difference of the three-dimensional high-speed large-scale structures ($\Delta\langle u_l^+\rangle = \langle u_{l_{un}}^+\rangle - \langle u_l^+\rangle$) conditioned on positive large-scale friction velocity at HF_5 for both uncontrolled and opposing controlled boundary layers between the opposing controlled and uncontrolled boundary layers at (a) $\Delta x_m = 0.85\delta$, (b) 1.7δ, (c) 2.5δ, and (d) 4.2δ downstream of the actuation array. The spanwise/wall-normal slices of the conditional structure upstream and downstream of the condition point at (x.1) $\Delta x = 2\delta + \Delta x_m$, (x.2) $\Delta x = 1\delta + \Delta x_m$, (x.3) $\Delta x = \Delta x_m$, and (x.4) $\Delta x = -1\delta + \Delta x_m$. A hypothesized schematic of the streamwise evolving large-scale control model is proposed for the measurement position at (e) $\Delta x_m = 1.7\delta$ and (f) $\Delta x_m = 4.2\delta$.

and eventually in figure 5.12(d.3) the conditional structure across the entire spanwise domain is mitigated by the jet flow at $\Delta x_m = 1.7\delta$.

In figure 5.13, the difference between the conditional high-speed events of the uncontrolled and controlled boundary layers ($\Delta \langle u_l^+ \rangle = \left\langle u_{l_{un}}^+ \right\rangle - \langle u_l^+ \rangle$) is presented to better demonstrate the evolution of the modification. The blue region in figure 5.13 indicates a reduction in the high-speed conditional structures, which clearly decays from $\Delta x_m = 1.7\delta$ to $\Delta x_m = 4.2\delta$ (from plot a to plot d). Therefore, while $\langle u_h^+ \rangle$ in the uncontrolled structure continues to steadily decrease between 1.7δ to 4.2δ downstream of the control, energy attenuation of the opposing controlled coherent structures, in the middle column of figure 5.12, is less obvious. Comparing the spanwise/wall-normal slices positioned at 1δ and -1δ away from Δx_m in figure 5.13(a-d.2) and (a-d.3), the control effect is observed to be more effective at $\Delta x = -\delta + \Delta x_m$ (i.e. the trailing edge of the LSMs). In addition, the deterioration of the control effect is more significant in the cross-plane contours located at $\Delta x = 1\delta + \Delta x_m$ (i.e. the leading edge of the control) in figure 5.13(a.2) to (d.2). Such a phenomenon may be explained by the mismatched convective velocity of the jet flow and the targeted high-speed events. To better elaborate this, figure 5.13(e,f) presents a schematic of the spatially-evolving model of the current large-scale control strategy at two signature measurement positions $\Delta x_m = 1.7\delta$ and $\Delta x_m = 4.2\delta$, respectively. The black solid lines represent the targeted LSMs possessing different length-scales with $\lambda_x > \lambda_{x.c}$. Red dashed lines show the position of the jet flow, which is essentially the effective control zone within the targeted structures. This effective control zone is located beneath the penetration height of the jet flow where a turbulent energy increase is observed due to the shear layer between the LSMs and the jet flow. For the opposing controlled strategy, the energy of the high-speed LSMs is attenuated within this effective control zone. Note that the VLSMs could have a wall-normal extension higher than the penetration height. Thus, in figure 5.4 and 5.12, the highest regions of the conditional structures are not effectively manipulated by the opposing control, and such regions are mostly located at the leading edge of the LSMs due to the forward-inclining feature. This explains why the control effect on the leading edge is less efficient than on the trailing edges. While the targeted LSMs have convected to $\Delta x_m = 4.2\delta$ in figure 5.13(f), the structures with shorter length-scales lose their coherence, which results in the energy deterioration of the uncontrolled conditional structures in the left column of figure 5.12. Since the low streamwise momentum jet flow convects slower than that of the high-

speed structures, the effective control zone in the LSMs gradually slides towards the trailing edge. Hence, the influence of the jet flow on the trailing edge of the targeted structures will be more persistent. This mismatched convective velocity will be further explored using the PIV data in section 6.3.

5.4 Other Factors Influencing Control Efficacy

Previous sections discuss the skin-friction drag reduction mechanism of the active large-scale control strategy and describe the potential maximum control effects which could be achieved by the strategy. Since the potential drag reduction is limited by the mean wall-shear-stress contribution of the LSMs, further exploration is conducted on improving the efficacy of the control strategy via only manipulating the most effectively controlled portion of the detected LSMs. Firstly, we consider the control effects on the structures of different sizes. Specifically, the LSMs are categorized based on their structural width. Instead of length, structural width has the advantage that it could be detected by the detection hot-wire array at each time instance during the real-time control. Thus, the criterion based on the structural width does not introduce any additional actuation delay. Figure 5.14(a) shows an instantaneous fluctuating large-scale skin-friction velocity field detected by the upstream hot-film sensors. It is obvious that the sizes of the detected high skin-friction events differ dramatically from each other. For example, the footprint highlighted by the dashed contour in figure 5.14(a) has a medium length of 2.5δ and width of 0.2δ while a much larger structure is bounded by the solid contour with spanwise width $> 0.4\delta$. At the same time, the larger structure (solid contour) appears to be more energetic than the smaller structures (dashed contour).

To categorize the structures in accordance with their geometric width, the averaged structural width $\mathscr{W}$ along the streamwise direction is introduced. Figure 5.14(b) presents the probability density of $\mathscr{W}$ for all detected high-speed skin-friction fields attained from 40 independent 6-minute u_τ measurements with $\mathrm{Re}_\tau = 14000$ in the uncontrolled boundary layer. A nearly uniform distribution is observed for $\mathscr{W}/\delta < 0.28$, which is equivalent to a streamwise length of 2.0δ owing to the aspect ratio of the coherent structures. This is because of the cut-off wavelength of the streamwise large-scale filter applied to estimate the u_{τ_l} field. With $\mathscr{W}/\delta$ larger than the threshold, a logarith-

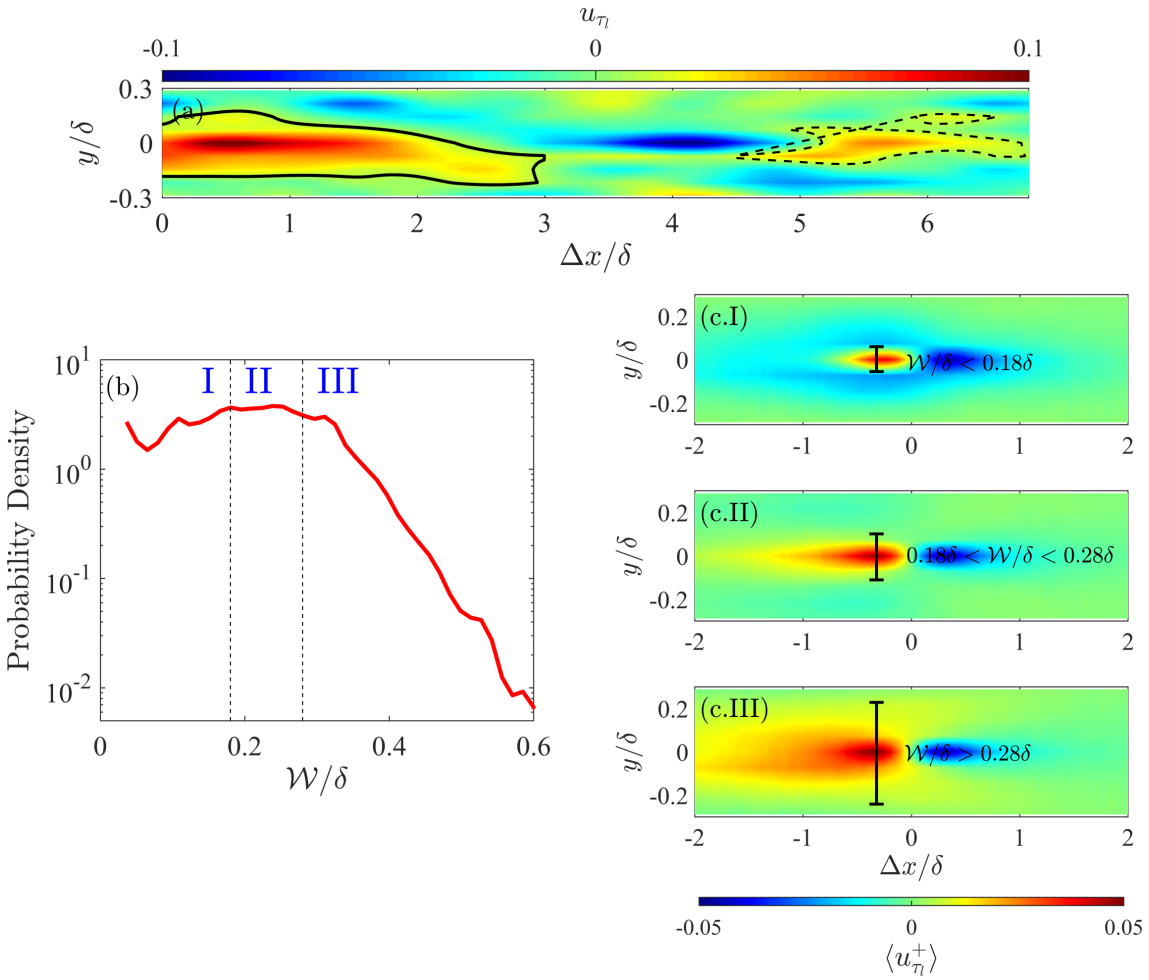

Figure 5.14: (a) A sample of the instantaneous large-scale fluctuating friction velocity field measured by the detection hot-film array in uncontrolled boundary layer. (b) Probability density function of the average structural width $\mathcal{W}$ of the large-scale high shear-stress events. (c) Isocontour of the conditional large-scale friction velocity events for (c.I) very thin structures with $\mathcal{W}/\delta < 0.18\delta$, (c.II) medium structures with $0.18\delta < \mathcal{W}/\delta < 0.28\delta$, and (c.III) very wide structures with $\mathcal{W}/\delta > 0.28\delta$.

mic recession occurs. A similar trend is also documented in Baars et al. (2017a) for the distribution of the streamwise lengths of the large-scale structures. Based on the distribution in figure 5.14(b), the structures are divided into three groups: **Group I**. thin structures - $\mathcal{W}/\delta < 0.18\delta$; **Group II**. Medium structures - $0.18\delta < \mathcal{W}/\delta < 0.28\delta$; and **Group III**. Wide structures - $\mathcal{W}/\delta > 0.28\delta$. These thresholds are selected so that the amount of the qualifying events in each group is identical so that the integrated areas under the curve show in figure 5.14(b) between these limits are equivalent with each other. Validation on the categorization is carried out by evaluating the conditional

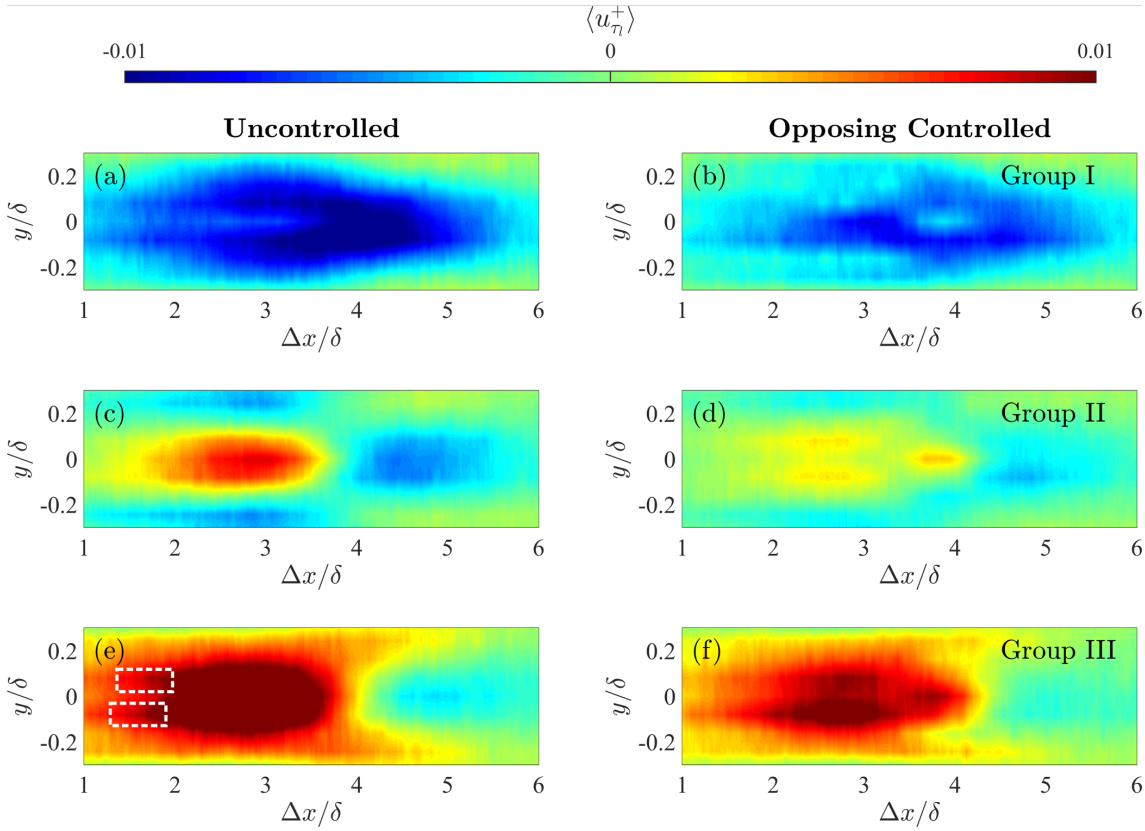

Figure 5.15: Conditional friction velocity measured at $\Delta x_m = 1.7$ and conditioned on the positive zero-crossing of the large-scale friction velocity fluctuation measured by detection array hot-film sensors (HF_5) for (a,b) **Group I** very thin structures with $\mathscr{W}/\delta < 0.18\delta$, (c,d) **Group II** medium structures with $0.18\delta < \mathscr{W}/\delta < 0.28\delta$, and (e,f) **Group III** very wide structures with $\mathscr{W}/\delta > 0.28\delta$. Left-hand plots show uncontrolled and right hand plots show opposing controlled cases. White dashed boxes in (e) highlight the two-tailed feature in very wide **Group III** structures

$\langle u_{\tau_l}^+ \rangle$ for each group in figure 5.14(c). The methodology is similar with 5.3, but the condition and measurement signals are both acquired from the detection array and an additional condition on the structural width $\mathscr{W}$ is imposed. In general, the width of the conditional high skin-friction event in each group meets the defined $\mathscr{W}$ values. A narrow structure from **Group I** tends to be encircled by a much wider low skin-friction field in figure 5.14(c.I). Conversely, for **Group III** in figure 5.14(c.III), a large high skin-friction event conditionally surrounds the adjacent much narrower negative $\langle u_{\tau_l}^+ \rangle$ region.

Note that 5.14(c) shows the conditional footprints measured by the detection hot-film array based on its own u_{τ_l}, which cannot provide any information on the control effects. To compare the manipulation of the structures with different widths, the $\langle u_{\tau_l}^+ \rangle$ acquired by the measurement

hot-film array locating at $\Delta x_m = 1.7\delta$ is computed based on the upstream condition signal. In the uncontrolled boundary layer, figure 5.15(a) shows that by the time the events have convected 3.3δ downstream of the detection array the narrow detected conditional high skin-friction events for **Group I** observed at the detection array in figure 5.14(c.I) are totally overpowered by the surrounding negative u_τ event, which forms a larger low shear-stress region even without any artificial forcing. This indicates the **Group I** structures having streamwise wavelength $\lambda_x < \delta$ are no longer correlated at 3.3δ downstream, which confirms the observation on the life-cycle of the coherent structures in §4.2. In contrast, the wider high-speed structures in the other two groups, in figure 5.14(c,e), remain correlated with high shear-stress regions that survive the downstream convection from the detection to the measurement array. Identical to the observation in 5.14(a) the wider structures seem to remain more energetic than the medium ones. In addition, figure 5.15(e) shows that the wide conditional large-scale friction velocity field has a two-tailed shape (highlighted by the white-dashed boxes in figure 5.15(e)), which implies that the VLSMs in **Group III** may be aggregated by two neighbouring medium structures due to the random spatial distribution of the LSMs. Similar reasoning also explains the ceiling of the scale-dependent convection velocity of the coherent motions in figure 4.7 and the spanwise meandering feature of the VLSMs as reported by Hutchins and Marusic (2007a) or the opposing controlled cases (right-hand plots in figure 5.15, the magnitude of conditional positive skin-friction velocity fluctuations is attenuated by the active control for **Group II** and **Group III**. However, compared to the conditional $\langle u_{\tau_l}^+ \rangle$ fields in the uncontrolled case, the large region of the negative skin-friction velocity fluctuation of the **Group I** structures has been weakened by the opposing control. This means the actuation on such structures conditionally increases the local wall-shear-stress. On the contrary, $\langle u_{\tau_l}^+ \rangle$ in the other two groups decreases as local skin-friction drag reduces due to the manipulation. Especially, by comparing the red contours in the conditional averages between figure 5.15(c,d), the control almost eliminated all the positive skin-friction velocity fluctuations caused by the estimated **Group II** structures. In contrast, 5.15(e,f) show that the power of the perturbation is insufficient to neutralize the positive fluctuations induced by the **Group III** events.

Further, the conditional average analysis is performed on the fluctuating streamwise velocity to understand the control effects across the entire height of the boundary layer for the LSMs with different widths. Figure 5.16 shows conditionally averaged u fluctuations on streamwise/wall-normal

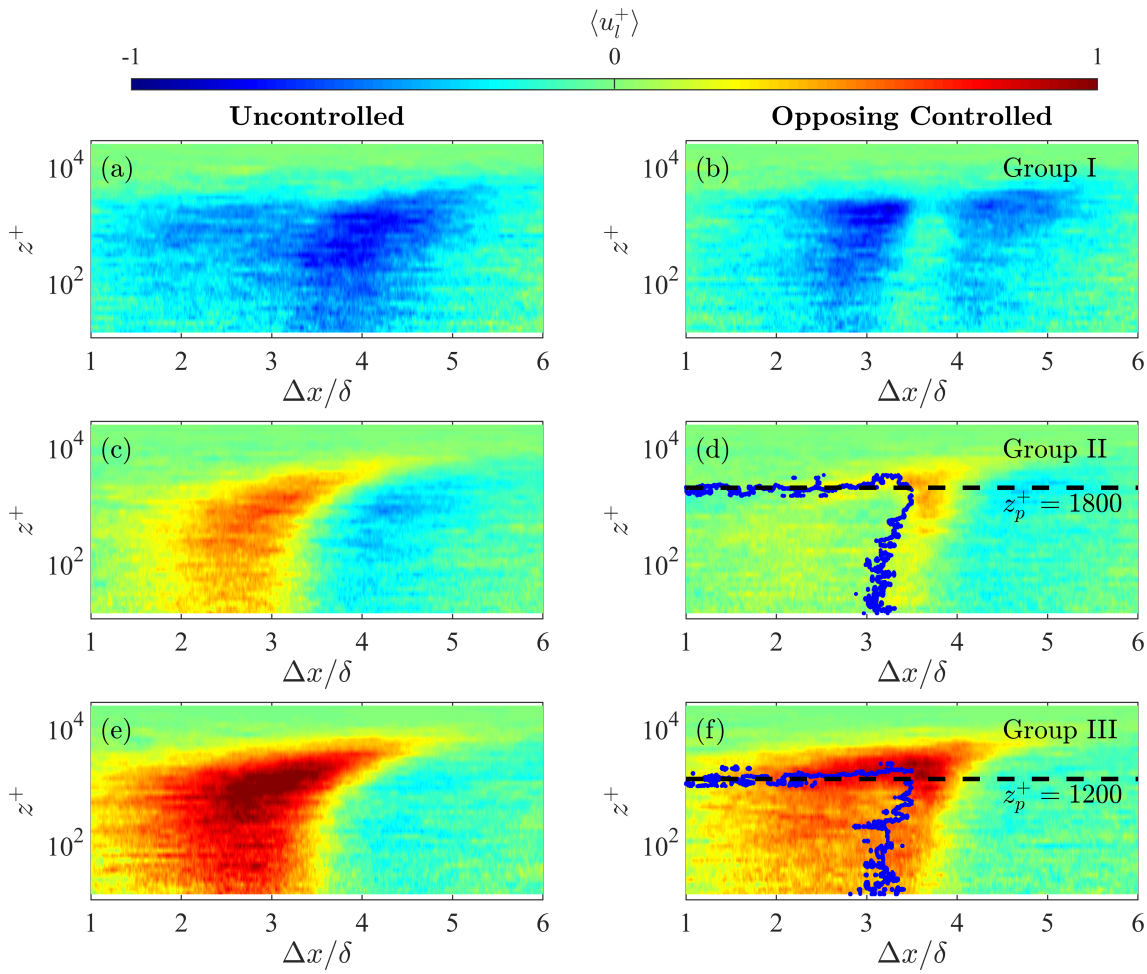

Figure 5.16: Conditional streamwise velocity measured at $\Delta x_m = 1.7$ and conditioned on the positive zero-crossing of the large-scale friction velocity fluctuation measured by detection array hot-film sensors in uncontrolled and opposing controlled boundary layers for (a,b) very thin structures with $\mathscr{W}/\delta < 0.18\delta$, (c,d) medium structures with $0.18\delta < \mathscr{W}/\delta < 0.28\delta$, and (e,f) very wide structures with $\mathscr{W}/\delta > 0.28\delta$. Blue solid lines are the iso-contour line of the difference between uncontrolled and opposing controlled $\langle u_l^+ \rangle$ with a level of -0.05. Black dashed lines are the conditional jet penetration height for the structures with different widths.

planes located at $y = 0$ (i.e. centerline of the control plane aligning with HF_5). In the uncontrolled boundary layers shown in figure 5.16(a,c,e), identical to the observation on the $\langle u_{\tau_l}^+ \rangle$ in figure 5.15, a wider structure (**Group II** and **III** in plots c and e) leads to a stronger positive $\langle u_l^+ \rangle$ fluctuation in the centerline plane. Conversely, the narrower high-speed events initially detected at the upstream array in **Group I** (as shown in figure 5.14(c.I)) disappear, becoming low-speed events at $\Delta x_m = 1.7\delta$ where figure 5.16(a) was acquired. Comparing the opposing controlled $\langle u_l^+ \rangle$ in figure 5.16(b,d,f), it appears that the medium width high-speed structures are the most effectively

controlled since the positive conditional velocity fluctuation is almost completely attenuated by the actuation. Define the difference between the uncontrolled and controlled conditional structures as $\Delta\langle u_l^+\rangle = \left\langle u_{l_{un}}^+ \right\rangle - \langle u_l^+\rangle$, where $\left\langle u_{l_{un}}^+ \right\rangle$ is the uncontrolled conditional average. The blue solid iso-contour shown in figure 5.16(b,d) is $\Delta\langle u_l^+\rangle = -0.05$, which highlights the region that has been effectively controlled by the opposing control. The upper bound of this contour reflects the conditional penetration height of the structures in each group. It is shown that the conditional penetration height of the medium width structures in **Group II** (1800^+) is 50% higher than that of the wide structures in **Group III** (1200^+). This is expected because larger LSMs tends to possess a stronger wall-ward momentum (negative w component) which suppresses the penetration of the upward jet flow (positive w component). Such a phenomenon is also observed using the PIV data in §6.3 with a similar conditional averaging technique. Although the current jet configuration successfully penetrates to the upper bound of the log region in the mean statistics, this proves that the strength of the injected jet flow is not powerful enough to restrain the very large structures ($\mathscr{W} > 0.28\delta$). Moreover, figure 5.16(a,b) reconfirm the previous conclusions that the manipulation on the small structures of **Group I** with $\mathscr{W} < 0.18\delta$ could be redundant or even detrimental because at $\Delta x_m = 1.7\delta$ control of these events reduces the magnitude of negative velocity fluctuations, which would be expected to increase the drag due to these events. Overall, the results seem to suggest two possible refinements of the current control strategy: (i) a proportional jet exit velocity based on the structural instantaneous width might be a way of ensuring consistent jet penetration even where stronger events are targeted and (ii) the above results suggest that actuating on very narrow **Group I** structures may be detrimental and such events should be excluded from the control strategy.

One drawback of the conventional conditional average results shown in figures 5.12-5.16 is that the condition averaged quantities decay rapidly with increasing distance Δx from the conditional point due to phase jitter and the distribution of structural lengths that are detected. Such a problem can be mitigated by applying a VICA. In the same manner, as a conventional conditional average, VICA also requires a condition point, and here we select the positive zero-crossing of the upstream u_{τ_l}. However, for each qualified condition point, the velocity fields between the adjacent negative zero-crossings of the u_{τ_l} will be extracted. In turn, every single conditional event includes an entire pair of high-speed and low-speed events. To find the VICA quantity, every conditional

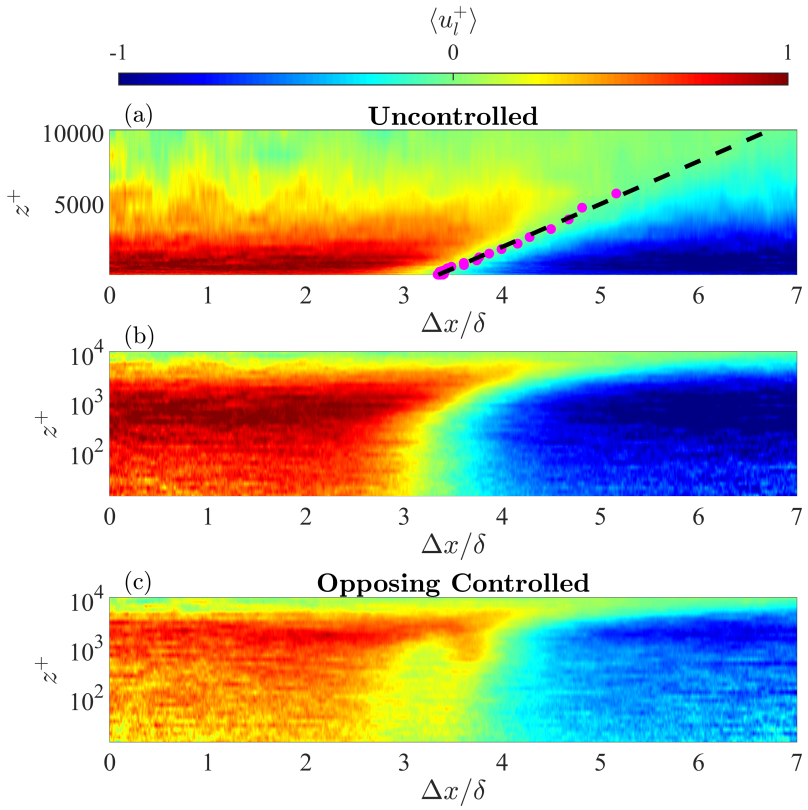

Figure 5.17: Variable interval conditional averaged streamwise velocity fluctuations of the LSMs at $\Delta x_m = 1.7\delta$ based on the positive zero-crossings of the upstream u_{τ_l} in (a,b) the uncontrolled boundary layer and (c) the opposing controlled boundary layer. Magenta markers (•) are the spatial negative zero-crossings of the $\langle u_l^+ \rangle$ and black dashed line (−−) is the linear fit.

event is aligned with respect to the condition point (i.e. the positive zero-crossing) and only the information up to the next negative crossing is considered. Since the lengths of structures are different, the conventional ensemble average is inapplicable, the VICA $\langle u_l^+ \rangle$ is the ratio between the summed quantity and the total number of the conditional events reaching any given location away from the conditional point (see Baars et al. (2016) for further details). Figure 5.17 shows the VICA streamwise velocity fluctuations $\langle u_l^+ \rangle$ for both uncontrolled, in (a,b) and opposing controlled, in (c), cases. In the uncontrolled boundary layer away from the detected zero-crossing, the strength of both low-speed and high-speed structures exhibits very little change in x. By linear fitting, the zero-crossing ($\langle u_l^+ \rangle = 0$) at different wall positions, a clear inclination angle of 11.4 degrees is observed in the linear plot of figure 5.17(a). When the opposing control is engaged as shown in figure 5.17(c), the targeted high-speed events are clearly attenuated throughout the entire stream-

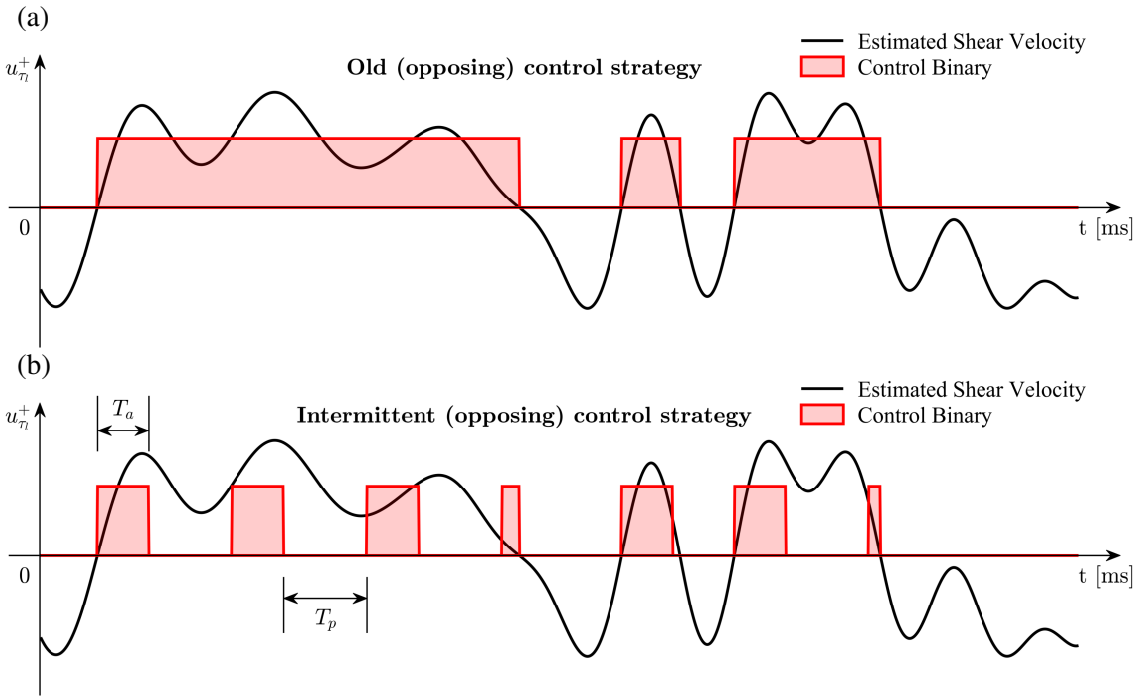

Figure 5.18: Schematic of (a) the original opposing controlled strategy and (b) the intermittent opposing control strategy. Black solid line is the estimated large-scale friction velocity signal and the red solid line is the corresponding binary control signal with an actuation duration T_a and a pause duration T_p.

wise extension. In particular, near the interface of the conditional low and high-speed structures ($3\delta < \Delta x < 3.5\delta$), the positive $\langle u_l^+ \rangle$ is more substantially weakened.

The VICA results reinforce the potential of improving the current control strategy by manipulating only the leading edge of the high-speed large-scale structures. Thus, a series of new control schemes (intermittent and impulsive controls) are proposed to test this hypothesis. The intermittent control periodically activates the jets during one single high-speed event, whose schematic is shown in figure 5.18. The black solid line represents a clip of the estimated large-scale fluctuating shear velocity time series as estimated by the real-time filter. The binary control signal of the intermittent control is determined by two parameters, namely the actuation duration (T_a) and the pause duration (T_p). In specific, the jet is activated immediately after the positive zero-crossings for T_a and switched off for another T_p until the next actuation the estimated fluctuating shear velocity is still positive. Note that the actuation-pause cycle resets at each positive zero-crossing. For $T_p \to \infty$, the jets only actuate on the leading edge of the estimated high-speed events, which leads to a special case of intermittent control called impulsive control.

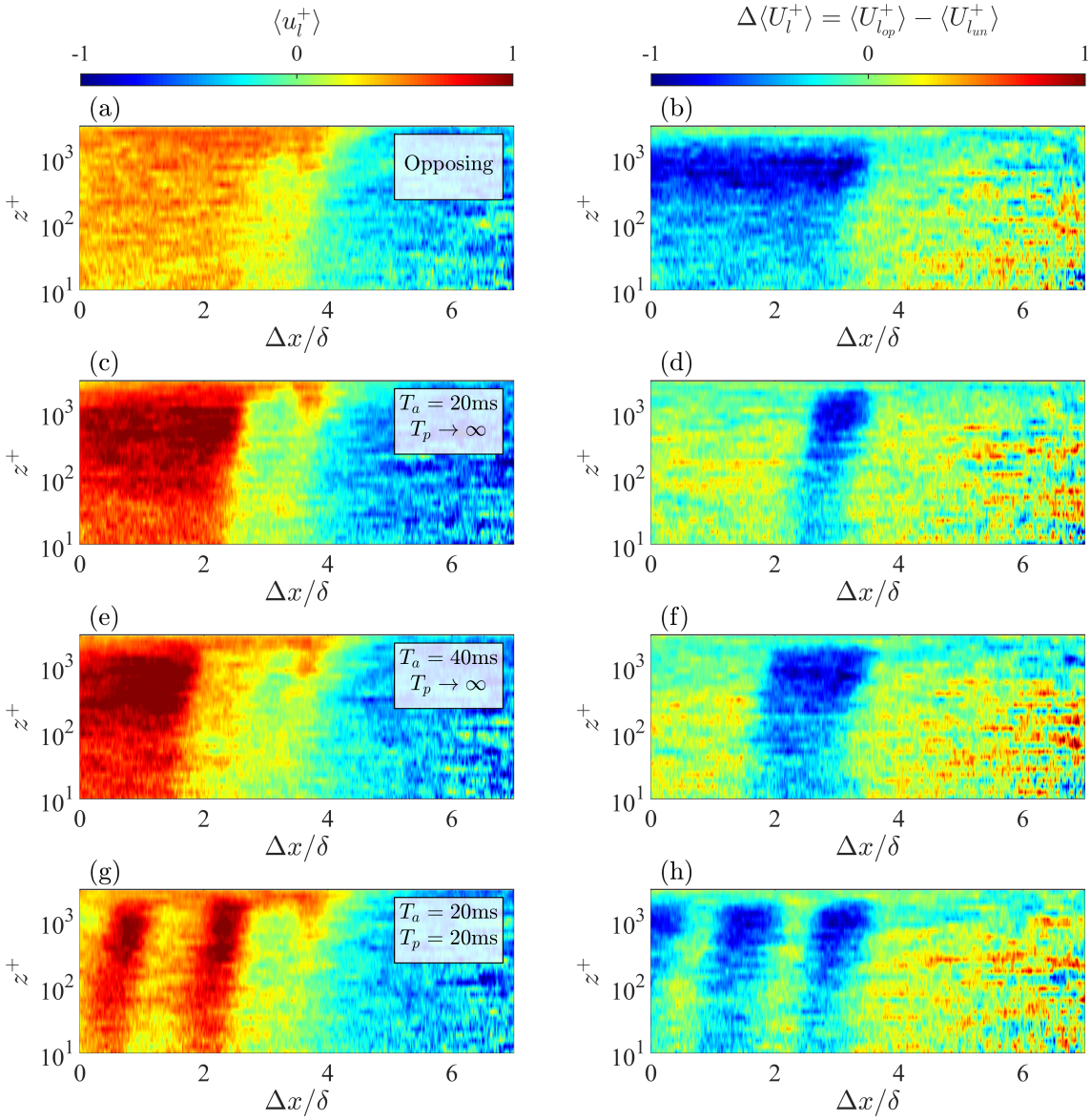

Figure 5.19: Variable interval conditional averaged streamwise velocity fluctuations of the LSMs at $\Delta x_m = 1.7\delta$ based on the positive zero-crossings of the upstream u_{τ_l} in the intermittent controlled boundary layers with (a) $T_a \to \infty$ (i.e. opposing control), (c) $T_a = 20$ms, $T_p \to \infty$, (e) $T_a = 40$ms, $T_p \to \infty$, and (g) $T_a = 20$ms, $T_p = 20$ms. (b,d,f,h) Difference between the total VICA conditional streamwise velocity between the four listed intermittent control strategies and the referencing uncontrolled LSMs.

The intermittent and impulsive control strategies for a range of T_a and T_p values are examined with the measurement array placed at $\Delta x_m = 1.7\delta$. Figure 5.19(c,e,g) illustrates the VICA for three representative impulsive and intermittent opposing control cases, as compared to original

(constant) opposing control scheme as described in figure 5.18(a). In general, it is obvious that the conditional averaged large-scale velocity variation is highly correlated to the firing pattern for all four control schemes in figure 5.19(a,c,e,g). In specific, the reduction of $\langle u_l^+ \rangle$ for the impulsive controlled cases occurs only at the leading edges of the high-speed structures. Similarly, in figure 5.19(g), the intermittent controlled high-speed structure has an apparent high-low pattern that follows the actuation-pause cycle of the jets. However, the conditional averaged velocity fluctuation does not consider the modifications on the mean velocity profile. Since the total jet engagement time changes with the selected T_a and T_p values, $\langle u_l^+ \rangle$ cannot fully represent the control effects on the LSMs. In figure 5.19(b,d,g,h), the problem is resolved by considering the conditional total velocity difference $\Delta\langle U_l^+ \rangle$ between the uncontrolled and the controlled boundary layers. The total velocity deficit only occurs when the jet modification is employed. Although the convection velocity difference shifts the jet flow from the leading edge to the trailing edge of the LSMs during the streamwise evolution, at a fixed location, the control effect of the jet flow is localized in the boundary layer without spreading to a larger streamwise range. These characteristics observed from the VICA high-velocity structures agree with the results of Tardu and Doche (2009), who applied a periodic blowing to the boundary layer and obtained an oscillatory conditional averaged structure.

Focusing on the impulsive control strategies with T_a ranging from 20ms to 80ms, a single-normal hot-wire probe is placed at the center of log region $z^+ \approx 480$ above the downstream hot-film array to investigate the turbulent energy reduction. Figure 5.20(a) shows the pre-multiplied energy spectrum of all tested cases. The large-scale energy with $\lambda_x > 1.6\delta$ in all impulsive controlled boundary layers is upper bounded by that of the uncontrolled case and lower bounded by the opposing controlled case and the large-scale energy reduces for an increasing T_a value. To justify the improvements in control efficacy using the impulsive control, the total control input is considered by defining the ratio between the jet activation time and the measurement duration as firing ratio.

$$\text{Firing Ratio} = \frac{\Sigma B}{f_B T_s} \tag{5.9}$$

where B and f_B are the binary control signal and its sampling frequency, and T_s is the sampling time of each measurement duration. Thus, the firing ratio is linearly proportional to the control

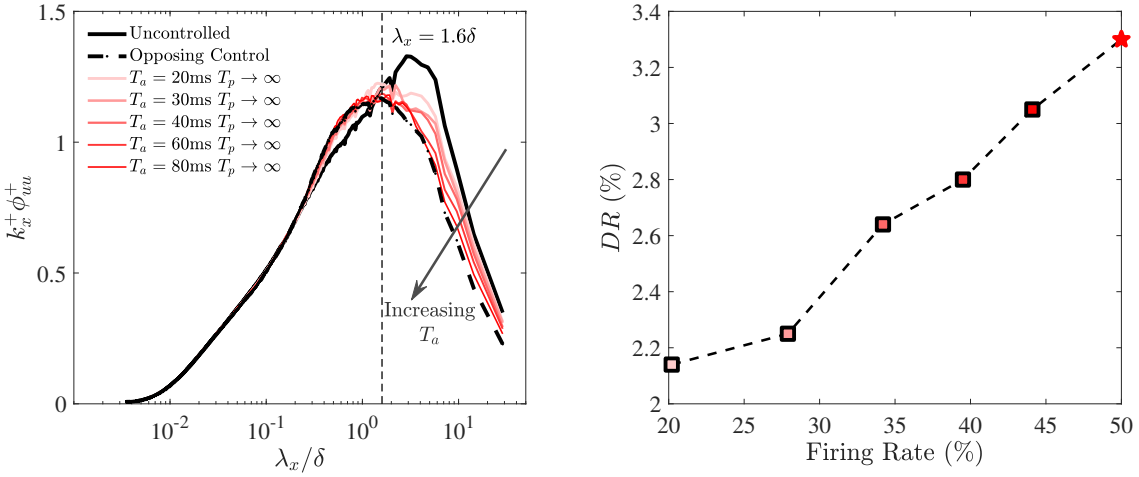

Figure 5.20: (a) Pre-multiplied energy spectrum of the fluctuating streamwise velocity measurement at the center of log region ($z^+ = \sqrt{15\mathrm{Re}_\tau}$) and $\Delta x_m = 1.7\delta$ in the impulsive controlled boundary layers with actuation duration ranging from 20ms to 80ms. Black solid line and black dashed line are the energy spectrum for the uncontrolled (i.e. $T_a = 0$ms) and opposing controlled (i.e. $T_a \to \infty$) cases. Vertical dashed line highlights the cut-off wavelength of the real-time filter in the active control. (b) Firing ratio and local *DR* measured at $\Delta x_m = 1.7\delta$ under all tested intermittent control strategies.

input energy. Ideally, a small firing ratio with a large *DR* value is preferable. Figure 5.20(b) shows that increasing the firing ratio for all impulsive controlled and opposing controlled cases generally improves the resulting *DR*. However, it is worth noting that even with a 20% firing ratio, the drag reduction only decreases from 3.3% to 2.2%. In other words, using 40% of the control input in the opposing controlled case, 66% of its *DR* is attained, which advises an enhancement in the control efficacy of the large-scale control strategy.

5.5 Chapter Summary

Hot-wire and hot-film anemometry is carried out to examine the large-scale flow control effect in high Reynolds number turbulent boundary layers. The results not only reveal the role of the LSMs in the perturbed boundary layers but also suggest further recommendations on improving the efficacy of the large-scale control. The following provides a summary of the key findings in this chapter.

- The current active flow control primarily manipulates the large-scale structures in the tur-

bulent boundary layer. The modified large-scale turbulent energy is proportional to the percentage of high-speed events being successfully actuated. Thus, while the opposing control decreases the large-scale turbulent energy, the reinforcing control energizes the large-scale turbulence.

- The large-scale turbulent energy reduction is shown to be linearly related to the skin-friction drag reduction, which suggests that the LSMs with streamwise wavelengths greater than 1.6δ contribute to approximately 5.6% of the mean-wall-shear stress. In desynchronized control, while the large-scale energy is not modified, the current control set-up achieves a drag reduction of 2.2% due to the momentum deficit induced by the low-speed jet flow

- The primarily controlled LSMs leaves modified large-scale footprints on the wall via superposition. In addition, the near-wall small-scale turbulent energy is varied in response to the local friction velocity, which agrees with the QSQH hypothesis of Chernyshenko et al. (2012). Such a phenomenon is reproduced based on the inner-outer-interaction model, which suggests the possibility of using the IOI model to estimate the potential drag reduction contributed by the LSMs with different length-scales.

- The large-scale energy attenuation and the skin-friction drag reduction are both maximized at 1.7δ downstream of the actuation array (i.e. Δx_m) and the control effect attenuates further downstream. Conditionally averaged high-speed structures show that the control effect is more persistent on the trailing edge of the LSMs due to a mismatched convection velocity between the large-scale structures and the introduced counteracting (or reinforcing) jet flow.

- The flow control best modified the LSMs with medium structural width of $0.18\delta < \mathscr{W}/\delta < 0.28\delta$. In contrast, the perturbation on the wide structures is not strong enough, which suggests the potential of using opposing control with the actuation strength proportional to the structural width.

- From intermittent control strategies, it is observed that the control effect resulting from the jet flow is localized at where the actuation is applied. The control efficacy (i.e. ratio between energy-saving and energy input of the control) increases when the actuation is only activated at the leading edge of the targeted LSMs.

Chapter 6

PIV Investigation on the Flow Control Effects

The hot-wire investigation of the active control strategy in the previous chapter focused on the relationship between the large-scale motions and skin-friction drag reduction in the controlled boundary layers. A coarse evolution of the control effect is investigated by placing the hot-wire probe at different streamwise positions downstream of the actuation array. In this chapter, the streamwise and wall-normal velocity components in the perturbed boundary layers are studied via a planar (streamwise/wall-normal) PIV technique. Specifically, a multi-camera configuration with 8 DSLR commercial cameras is employed to capture the manipulations on the LSMs and the spatial evolution of the control effects in a large field of view. Thousands of realizations of the controlled and uncontrolled boundary layers are obtained. The phase averaged behaviour of the LSMs reveals the control effect of the jet flow on the targeted structures. Simultaneously, the friction velocity downstream of the actuators is acquired by the measurement hot-film array to extend the understanding of the interactions between the LSMs and the near-wall turbulence from the previous chapter.

Details of the experiment set-up, including the data acquisition and PIV configuration, are depicted in §6.1. The mean statistics of the uncontrolled and controlled velocity fields are shown in §6.2, which validates the experimental configuration and assesses how the targeted LSMs could affect the jet trajectory. Furthermore, fields based on the timing of the laser pulses and frictional velocity signals and the series of the conditional and phase averaged flow fields (perturbed and canonical) are shown in §6.3. In §6.4, with the simultaneous measurement of PIV and hot-film anemometry, the impacts of the large-scale turbulent intensity and its associated Reynolds shear stress on the mean wall-shear-stress are analyzed to improve the understanding of the drag-

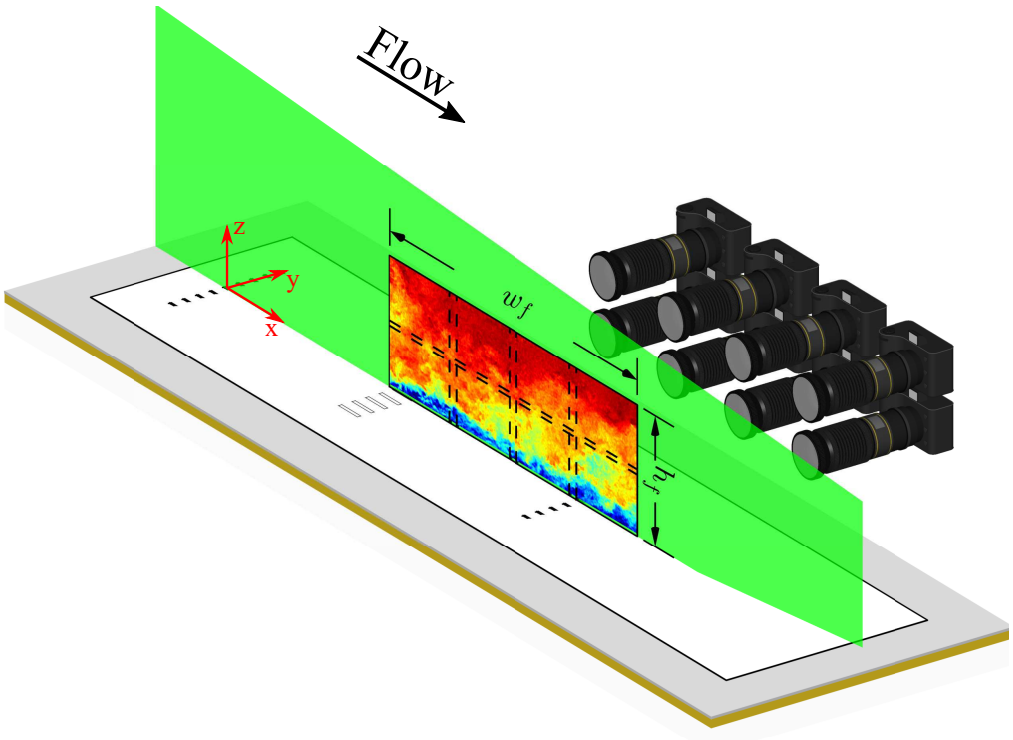

Figure 6.1: Arrangement of the cameras and laser sheets for the PIV measurement, with the FOV highlighted with the large-scale flow control architecture.

reduction mechanism of the present active large-scale control strategy.

6.1 Simultaneous DE-PIV and Hot Film Measurements

The spatial modification of the LSMs under the different control strategies (i.e. reinforcing and opposing control) is observed via a two-dimensional two-component (2D2C) PIV measurement in the streamwise/wall-normal plane (x/z plane). Since the targeted LSMs have streamwise wavelengths $\lambda_x \geq 1.7\delta$, the PIV imaging system must have a large FOV to be able to fully capture the spatial flow features. To fulfill the requirement cost-effectively, specialist PIV cameras are substituted with modern consumer full-frame digital cameras, which are typically available at a fraction of the cost. These cameras are configured to capture double-exposed images (DE-PIV) at a much higher spatial resolution than that available from specialist PIV cameras configured to capture single-exposure images (SE-PIV). Specifically, figure 6.1(a) shows that the imaging system consists of eight Nikon D810 DSLR cameras each with 36-megapixel resolution, which together

offers a combined resolution of ~ 0.3 gigapixels. These cameras are all placed into a two-row-four-column matrix on one side of the wind tunnel. The corresponding FOV spans 0.8m$\times$0.26m ($2.8\delta \times 0.9\delta$) in the streamwise and wall-normal directions, respectively. It should be noted that the operation of the cameras in DE-PIV mode typically leads to direction ambiguity. However, in turbulent boundary layers, flow reversals are rare events restricted to the first five wall units from the surface (Chin et al., 2018), therefore the issue of directional ambiguity is not critical in this case where our first resolvable vector from the wall is at $z^+_{min} \approx 100$. Although the achievable accuracy with DE-PIV is less at matched imaging conditions when compared to SE-PIV (deSilva et al., 2018), the higher sensor resolutions afforded from consumer cameras allow us to use larger interrogation window sizes without compromising spatial resolution. Further, such a FOV is sufficient to visualize the manipulation of the LSMs which primarily reside underneath the upper bound of the log region. Since the FOV does not extend to the edge of the layer in the wall-normal direction, we here assume nominal boundary layer thickness of $\delta = 0.28$m throughout the entire chapter, as indicated from the 99% boundary layer thickness of the hot-wire dataset acquired at comparable U_∞ and streamwise position in Chapter 5.

Laser illumination for the experiments is provided by a 400 mJ/pulse Spectra-Physics PIV-400 Nd:YAG 532nm laser, which is reflected upstream by a 45° front-face mirror mounted on the traversing hot-wire sting of the HRNBLWT located at five meters ($\sim 15\delta$) downstream of the FOV. The thickness of the laser sheet is trimmed to approximately 1mm and it is aligned precisely with the middle wall-normal jet (Jet_5) at the centerline of the control panel. Seeding of the tunnel for both uncontrolled and controlled cases is injected directly into the wind tunnel upstream of the flow conditioning section, which is then recirculated throughout the laboratory. More details on the seeding of the flow in the HRNBLWT facility can be found in deSilva et al. (2014). As shown in figure 6.2(a), the air supply of the center jet is identical to that introduced in §3.2, except that a secondary seeding source is fed directly into the jet plenum after the supplied compressed air is throttled to ~ 0.9bar. With such an arrangement, further pressurization of the fog generator nozzle to inject the seeding particles into the jet cavity is avoided, which minimizes the impact of the seeding on the jet exit velocity. To validate this, a hot-wire probe is placed perpendicularly adjacent to the jet exit slot to test the U_{jet} with and without seeding supply. Figure 6.2(b) shows that the mean U_{jet} at the varying inlet pressure controlled by the pressure regulator

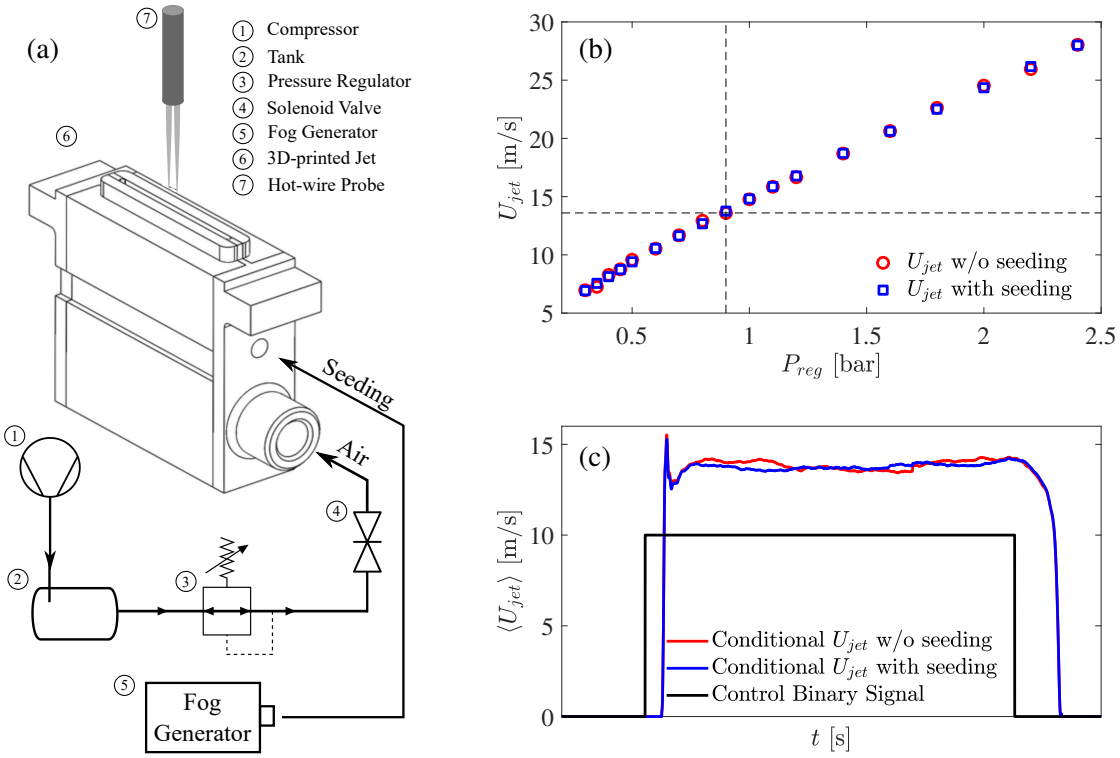

Figure 6.2: (a) A schematic diagram of the air supply and seeding supply for the middle wall-normal jet in the PIV measurements. (b) Jet exit velocity at different inlet pressure of the compressed air as measured by a hot-wire probe with (○) and without (□) seeding supply. (c) Conditional jet exit velocity in responding to a periodic square binary signal (−) acquired with (−) and without (−) seeding supply

agrees closely for the seeded and unseeded cases. The response of the jet is then checked through the conditional jet exit velocity in figure 6.2(c). The black solid line is the binary control signal, which is a periodic square wave. The conditionally averaged jet cycle is consistent between the two cases, giving certainty that any observed differences between the flow fields of the controlled and uncontrolled boundary layer in the following sections are purely contributed by the jet control and not from the addition of seeding particles.

Figure 6.3 illustrates a sample image acquired at 50ms after the middle wall-normal jet is activated. The seeding density of the cross-flow is configured to be sparser than that of the jet flow to separate the flow media in the PIV images. The instantaneous jet trajectory is determined to be at the point where the gradient of the image grayscale in the wall-normal direction exceeds a specified threshold. This is highlighted by the red solid line in figure 6.3. This instantaneous

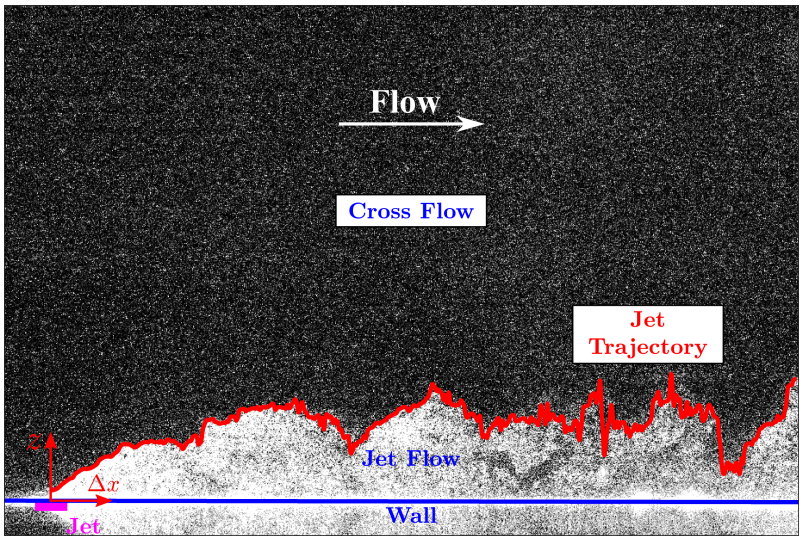

Figure 6.3: A sample PIV picture taken at the moment when the wall-normal jet on the centerline of the control panel is activated in the opposing controlled turbulent boundary layer. Magenta rectangle block illustrates the position of the jet in the wall-normal position. Red solid line (−) is the instantaneous jet trajectory and blue solid line (−) is the wall position

jet trajectory clearly separates the oncoming boundary layer flow (sparser seeding) and the jet flow (denser seeding) regions. The position of the wall-normal jet (magenta rectangle) is carefully identified in a calibration image taken prior to the experiment. The reflection of the jet flow is used to determine the wall position (blue solid line). Table 6.1 summarizes the experimental conditions for the uncontrolled, opposing controlled, and reinforcing controlled boundary layers. Akin to the measurements in Chapter 5, the Reynolds number of the PIV measurements are maintained at $\mathrm{Re}_\tau \approx 14400$ in order to provide a direct comparison between cases. In addition, table 6.2 summarizes the key PIV parameters for each measurement.

The acquisition rate, including the frequency of the laser pulses and the camera triggers, is

Table 6.1: Summary of experimental conditions.

	U_∞ [m/s]	Re_τ	ν/U_τ [μm]	U_τ [m/s]	Field of view ($w_f \times h_f$) [m×m]
Uncontrolled	20.8	15380	23.4	0.671	
Opposing	20.2	14930	24.1	0.642	$0.8 \times 0.26 (2.8\delta \times 0.9\delta)$
Reinforcing	20.2	14980	24.0	0.647	

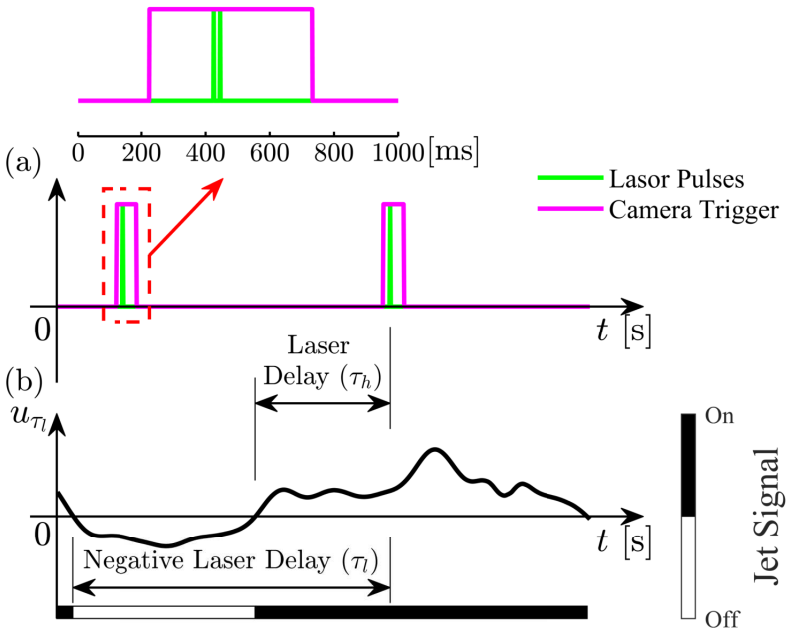

Figure 6.4: An illustration of the (a) laser Q-switch and camera trigger signals together with the (b) shifted real-time large-scale filtered skin-frction velocity fluctuation u_{τ_l} from the up-stream hot-film sensors. Schematic for conditional averaged analysis defining laser delay (τ_h) as the time difference between the opening of the Q-switch and the previous positive zero-crossings of the u_τ signal measured via the center upstream hot-film sensor. The jet signal shown in (b) illustrates an opposing control strategy.

controlled via two SRS DG645 Digital Delay Generators operating at 1Hz. Owing to the moderate acquisition frequency, the wireless remote shutter adapter (SMDV RFN-4s) equipped on all

Table 6.2: Summary of PIV parameters.

	Uncontrolled	**Opposing**	**Reinforcing**
Flow medium	Air (atmo.)	Air (atmo.); (Jet 0.9bar)	
Seeding	Polyamide particles		
Particle size	$\approx 1-2\mu$m		
Total sensor resolution	$\approx 0.3\times10^9$ pixels		
Spatial resolution	$\approx 28\mu$m/pixel (1.1^+)		
$\Delta x \times \Delta z$ (pixels)	96×48 ($105^+\times52^+$)		
Laser sheet thickness	$\approx$ 1mm (40^+)		
Acquisition frequency	1Hz (40 boundary layer turnovers)		
Number of images	2200	2250	2150

eight consumer cameras have sufficient response time, which supplies the external synchronization of the multiple camera system. A schematic of the sampled laser and camera signals along with simultaneously acquired up-stream hot-film signals is shown in figure 6.4. Due to the DE-PIV configuration, the camera shutter remains open for 500ms after being triggered, during which the camera records two laser flashes with a 25µs interval. The acquisition frequency is set to be lower than one image per second and the first laser pulse in each cycle is offset by 200ms against the camera trigger, so that the camera shutter possesses sufficient time to respond to the triggering signal. Detailed discussions associated with synchronizing and triggering of a multi-camera double-exposure system are documented in deSilva et al. (2018). Since the length-scale of the coherent structures in the turbulent boundary layer is inconsistent and randomly distributed in both time and space, the laser flashes, corresponding to the exposure of the images, could occur at any phase of the large-scale structures, or active control cycle. For example, the periodic 1Hz flashing of the laser could happen during either a high-speed or a low-speed event and within these, it could occur at the leading, middle, or trailing section of the LSMs. Thus, we define the time instance of each snapshot based on the temporal difference between the first laser pulse and the previous positive zero-crossing of the u_{τ_l} signal measured at the center sensor in the detection array (HF_{U5}). This quantity is called the laser delay τ_h. Due to the convection of the LSMs along the spatial separation Δx_a between the upstream hot-film probes and actuators (i.e. the leading edge of the FOV), the time series of u_{τ_l} is shifted by $\Delta x_a / U_c$ before calculating the value of τ_h for each image. Thus, effectively, τ_h is the time delay between a detected large-scale positive skin friction event entering the PIV field of view and the time of instantaneous PIV image (small τ_h will have large-scale features entering the FOV, while these features will fill the FOV for larger τ_h). As a consequence, the wall-normal jets are always activated at $\tau_h = 0\,\mathrm{s}$. In addition, because multiple cameras are used here to construct a combined FOV, a calibration procedure is essential and needs to account for distortions within the image plane and also enable stitching of the velocity fields from each camera. Similar to prior multi-camera experiments in the same facility, we employ a large calibration target that spans the entire extent of the FOV (deSilva et al., 2018). The velocity vector evaluation is performed on the LaVision DAVIS 8.4 package based on an auto-correlation algorithm using multi-grid (Willert, 1997) with window deformation applied at the final pass (Scarano, 2001). The databases are processed with 50% overlap and the final interrogation window size for each

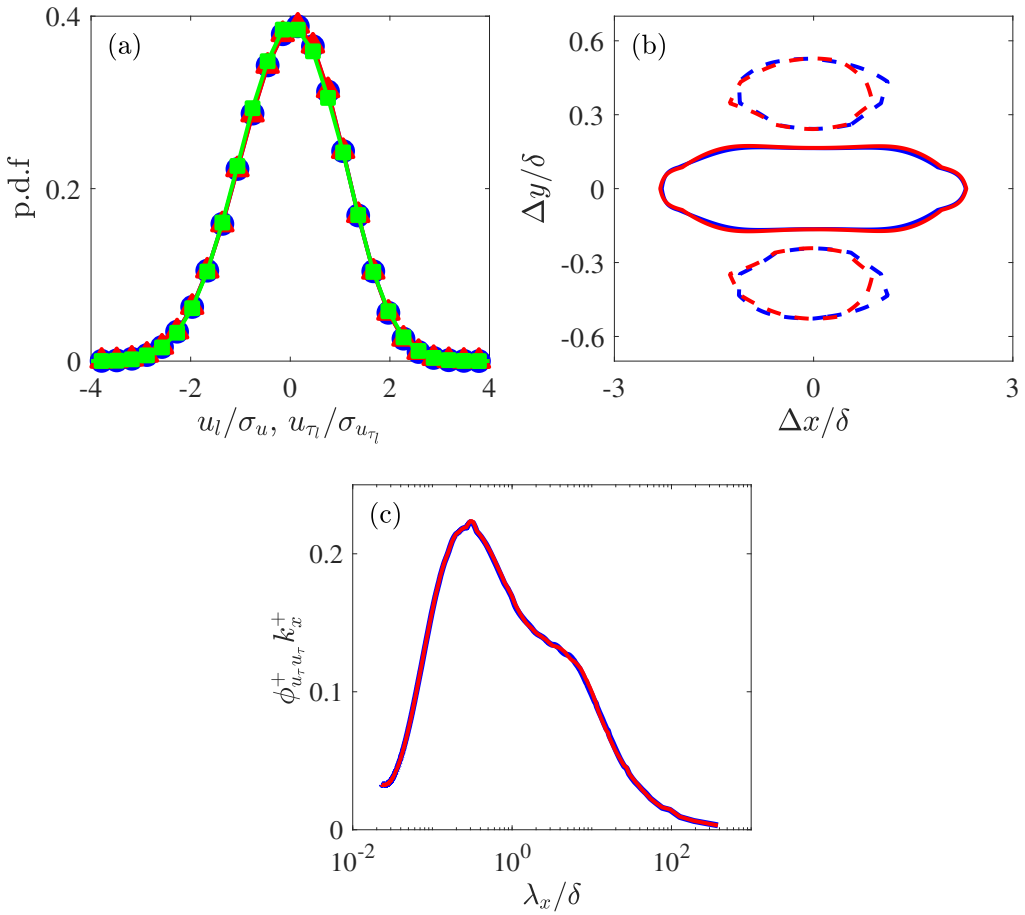

Figure 6.5: (a) Probability density function of the large-scale skin-friction velocity fluctuation normalized by its standard deviation for the measurements with (▲) and without the seeding particles (●), and the standardized large-scale skin-friction velocity acquired by hot-wire at $z^+ = 6$ (■). (b) Iso-contour of two point correlation $r_{u_\tau u_\tau}$ between the u_τ signals at the levels of 0.05 (solid line) and -0.05 (dashed line) and (c) energy spectrogram of the u_τ signals measured by the upstream hot-film sensors with (–) and without seeding particles (–))

dataset is detailed in table 6.2. Further details of processing the DE-PIV images using a similar experimental configuration can be found in deSilva et al. (2018).

The control architecture and the hot-film anemometry utilized in the PIV measurements, as shown in figure 6.1, are maintained to be the same as that described in Chapter 3. However, as the employed Dantec SAFEX fog generator vaporizes the seeding particles via heat addition, the impact of the PIV particles on the precision of the friction velocity signals from the hot-film sensors warrants attention. Since only the large-scale information of the friction velocity signal is of relevance to the present flow control strategy, the accuracy of the u_{τ_l} acquired during the operation

of the fog generator is assessed. The verification is performed via a statistical comparison between the large-scale skin-friction velocity measured by the hot-films, with and without seeding in the flow, and also the large-scale streamwise velocity u_l measured by a hot-wire probe located as close to the wall as possible (at $z^+ = 6$). This is shown in figure 6.5(a), where the green squares (■) depict the probability density function (p.d.f) of u_l as measured by the hot-wire sensor, while the red triangles (▲) and blue circles (●) represent the u_{τ_l} measured with and without the seeding particles injected into the boundary layer, respectively. Our results reveal good alignment among the three cases indicating that the hot-film sensors are capable of accurately measuring the large-scale skin-friction footprint associated with the coherent structures in the boundary layer and that the seeding particles have a negligible influence on the higher-order statistics of the measured u_{τ_l}. In addition, figure 6.5(b) shows the two-point correlation, $r_{u_\tau u_\tau}(\Delta x/\delta, \Delta y/\delta)$, between the u_τ signals measured by the two hot-film sensors with a spanwise offset, Δy, and a streamwise shift Δx computed via Taylor's frozen turbulence hypothesis as indicated in §4.2 (Taylor, 1938). The solid lines, which show iso-contours of $r_{u_\tau u_\tau} = 0.05$ indicate the average length of positively correlated large-scale events exceeds 5δ. These events are flanked by negatively correlated events and are shown by the $r_{u_\tau u_\tau} = -0.05$ contour (dashed lines). The obvious agreement in the correlation contours between the two cases (with and without seeding) implies that the estimated u_{τ_l} from upstream detection array is reliable while a concurrent PIV measurement is in operation. Figure 6.5(c) shows the pre-multiplied energy spectra for the broadband (unfiltered) u_τ signal, indicating that even the high-frequency part of the acquired u_τ fluctuation remains impervious to the effects of seeding, with the energy spectrum of the u_τ signals measured in both scenarios exhibiting good collapse.

6.2 Validation and Mean Statistics

Sample post-processed instantaneous velocity fields in the $x/z-$plane are shown in figure 6.6, where (a,c) show the streamwise velocity U and (b,d) the wall-normal velocity W for the uncontrolled (top row) and opposing controlled cases with $\tau_h = 33.8\,\text{ms}$ (bottom row). Here, U and W are normalized by the free-stream velocity measured by a Pitot-static tube located at five meters downstream of the FOV and at $z = 0.5\text{m}$ $(z/\delta \approx 1.8)$. The large spatial extent of the current 2D2C

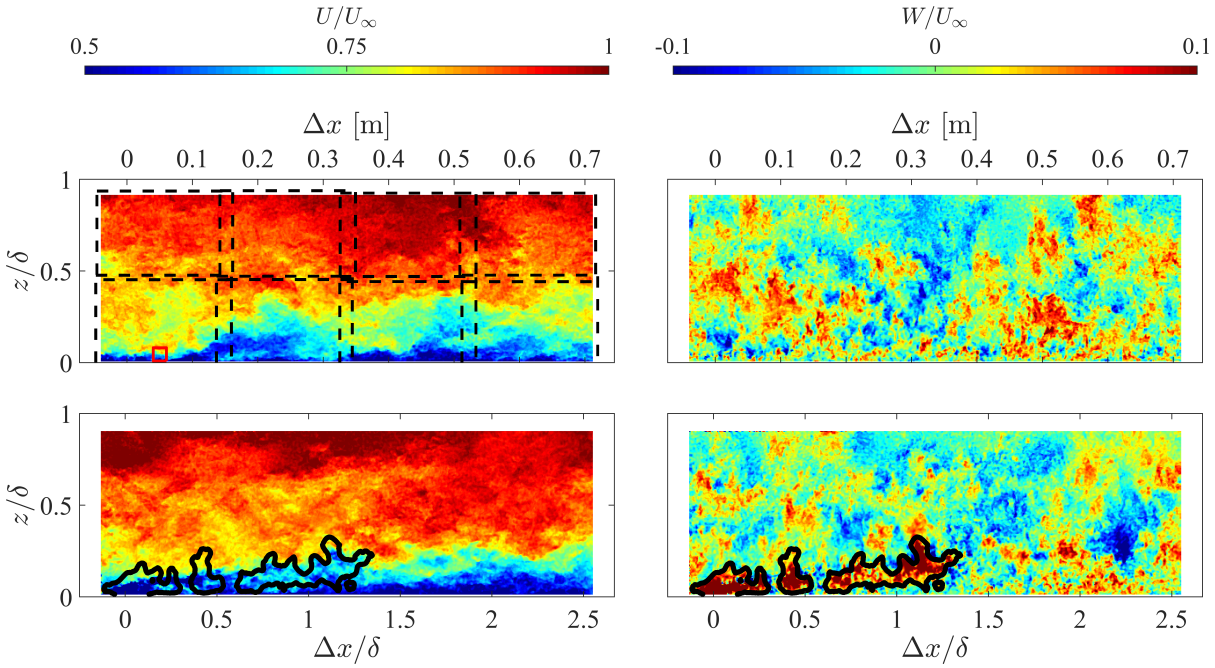

Figure 6.6: An example of the instantaneous velocity vector fields for (a,c) streamwise velocity component and (b,d) wall-normal velocity component for the uncontrolled and controlled boundary layer, respectively. The black dashed lines (− −) indicate the FOV of the individual cameras while the black solid lines (—) highlight an isolated, injected wall-normal jet flow trajectory during a high-speed event for the controlled case (based on filtered $W/U_\infty > 0.05$).

DE-PIV measurement manages to track the motion of the large-scale coherent structures in the turbulent boundary layers at this moderately high Re_τ. The black dash-lines in figure 6.6(a) precisely outline the arrangement of the FOV for each individual camera. Due to the lens distortion on the edges of the pictures, the velocity vectors on the edges are trimmed so that no overlapping regions occur between the FOVs of the adjacent cameras. Additionally, for the analysis in the following sections, the origin of the streamwise distance x is selected to be at the center of the jet outlet, so that Δx is the streamwise separation between the point of interest and the actuation array. The velocity fields shown in figure 6.6 indicate that the FOV successfully captures the entire logarithmic region ($150 \leq z^+ \leq 0.15\mathrm{Re}_\tau$) of the boundary layer, in which the targeted LSMs are most energetic (Mathis et al., 2011a). The timing for the vector fields in figure 6.6 for both uncontrolled and opposing controlled cases are selected so that the laser pulses occur at instantaneous $u_{\tau_l} > 0$. Specifically, for the opposing controlled case, the high-speed event has passed the jet location for 33.8ms (i.e. the jets have been actuated for $\tau_h = 33.8$ms) prior to the acquisition of the PIV snap-

shot. Here, we implement a box filter with $x_b \times z_b = 500^+ \times 500^+$ on the wall-normal velocity fields, and we suggest that the region affected by the jet is bounded by the black solid lines with the criterion that the filtered wall-normal velocity $W_b/U_\infty \geq 0.05$. This region of injected fluid from the jet identified in this way is associated with a defined region of strong positive wall-normal velocity in figure 6.6(d), while no such region is evident in that of uncontrolled wall-normal components in figure 6.6(b). In contrast, injected flow from the jet is rather difficult to discern from the U contours alone in figure 6.6(c). Combining this with the information from the upstream detection u_τ sensors, the instantaneous jet trajectory and its convection velocity within the cross-flow can be estimated. It is clear that the jet flow successfully penetrates up to 0.2δ, which exceeds the upper bound of the log region. Further, by applying Taylor's frozen turbulence hypothesis, we can compute the mean convection velocity of injected flow at this instance is $U_c = 11.6\text{ms}^{-1}$ as it reaches $\Delta x = 1.4\delta$ in 33.8ms.

As shown in table 6.2, over 2000 instantaneous snapshots of the velocity vector fields are acquired in the $xz-$plane for the uncontrolled cases, which provides converged first and second-order flow statistics from the canonical turbulent boundary for validation of the PIV configuration against existing measurements. The uncontrolled mean streamwise velocity, $\overline{U}^+$, and turbulence intensities, $\overline{u^2}^+$ and $\overline{w^2}^+$, are computed and are compared in figure 6.7 with the existing databases at matched Re_τ. Because the single-normal hot-wire data in Chapter 4 has no information on the wall-normal velocity component, flow statistics from cross-wire hot-wire anemometry measurements by Baidya et al. (2017) and prior conventional (single exposed) SE-PIV measurement by deSilva et al. (2014) from the same facility are compared against the present DE-PIV measurements. Figure 6.7(a,b,c) presents this comparison for the mean streamwise velocity and the turbulence intensities of the streamwise and wall-normal components, respectively. Here, the skin-friction velocity U_τ is determined from the upstream hot-film array, and the resulting profile of $\overline{U}^+$ shows a negligible discrepancy with the log-low, with assumed constants of $\kappa = 0.384$ and $A = 4.1$ (Nagib and Chauhan, 2008). The results exhibit good agreement among the current PIV experiments ($\circ$ symbols), the hot-wire experiments ($--$ line) and the SE-PIV experiments ($\triangle$ symbols) (deSilva et al., 2014). The discrepancy in turbulence energy between the PIV and hot-wire measurement is expected, owing to the difference in their spatial resolution. Specifically, the interrogation window and laser thickness of the present DE-PIV suggests a spatial resolution

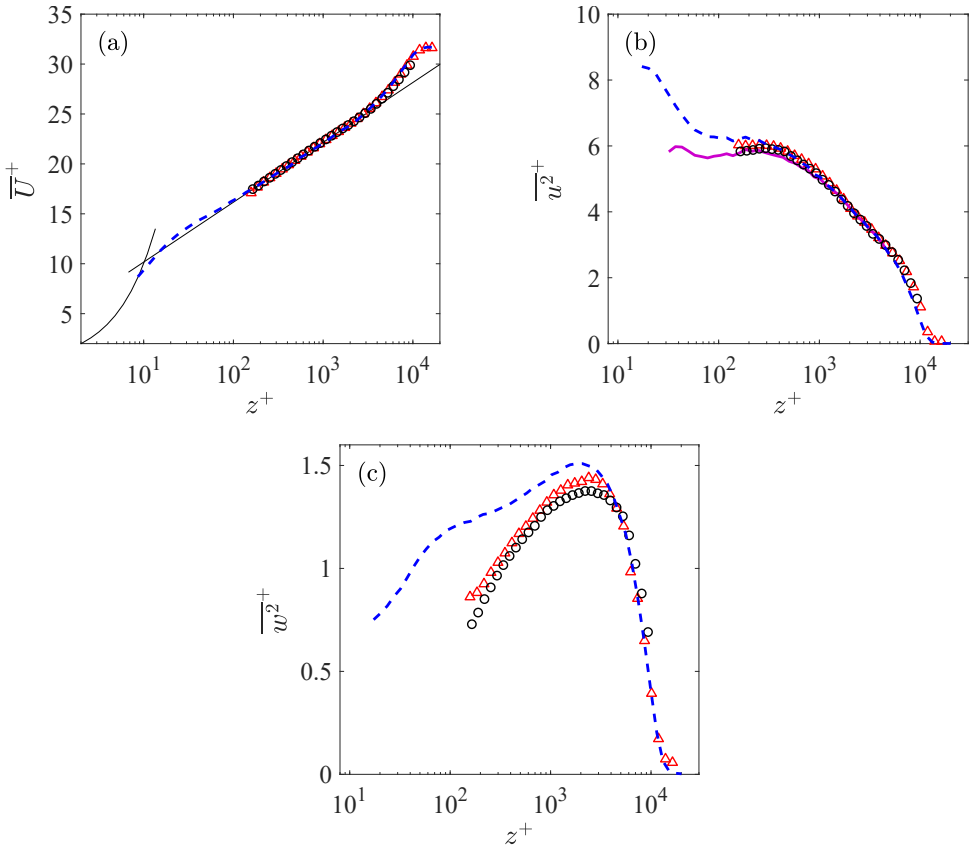

Figure 6.7: (a, b, c) Mean streamwise velocity, $\overline{U}$ and turbulence intensities, $\overline{u^2}^+$, $\overline{w^2}^+$ for the uncontrolled (canonical) turbulent boundary layer. The ∘ symbols correspond to the present DE-PIV experiments, and the blue dashed-line (– –) and △ symbols correspond to measurements by Baidya et al. (2017) and deSilva et al. (2014), respectively. The magenta solid line (—) corresponds to $\overline{u^2}^+$ from the hotwire measurements filtered to the spatial resolution of the present DE-PIV measurements.

of $105 \times 42 \times 52$ viscous units ($\Delta x^+ \times \Delta y^+ \times \Delta z^+ = 105 \times 42 \times 52$, where Δy^+ is the estimated light-sheet thickness), whereas the sensing elements for the x-wire sensor of Baidya et al. (2017) had a volume of $12 \times 6 \times 12$ viscous units. Thus, as shown in figure 6.7(b), due to the effect of spatial averaging, some degree of energy attenuation from the smaller scales near the wall is observed in the streamwise turbulent intensity profiles for the current PIV databases, when compared to the hot-wire data (Lee et al., 2016). Such effect is more obvious for the turbulent energy of the wall-normal velocity fluctuations, where slight deviation even occurs between the two PIV results as the SE-PIV possesses a smaller reported interrogation window ($\Delta x^+ \times \Delta y^+ \times \Delta z^+ = 37 \times 21 \times 37$). Recently, Lee et al. (2016) studied the missing turbulence energy due to the under-resolved PIV

experiments via filtering a well-resolved DNS database with a box filter with varying length-scales to mimic the effect of interrogation window and laser sheet thickness in a PIV measurement. Subsequently, from the energy difference between the raw and box-filtered DNS data, they developed a missing energy estimation toolbox to capture the under-resolved turbulence intensity for PIV experiments. Using this technique, the turbulence intensity for the existing hot-wire measurements is filtered to the same spatial resolution as the current DE-PIV measurements. The magenta solid line (—) shows good agreement with the DE-PIV results, which validates that the discrepancy observed in the near-wall region is primarily due to spatial attenuation. The energy attenuation of the wall-normal velocity components extends to a higher z position ($z^+ \approx 3000$) than that of the streamwise velocity ($z^+ \approx 500$). As a consequence, the toolbox of Lee et al. (2016) established at comparably lower Reynolds numbers is inapplicable to compensate for the energy loss to such a wall position. However, the comparison between the wall-normal turbulent intensity of the SE-PIV and DE-PIV still reflects the acceptable accuracy of the wall-normal velocity fluctuations. In summary, the instantaneous snapshot of the velocity fields in figure 6.6 highlights that the multiple camera double-exposed PIV system captures the LSMs as targeted by the control scheme, and the comparison of the mean statistics of the uncontrolled case against existing HWA and PIV data validates the accuracy of the current PIV configuration.

In terms of the controlled cases, the general evolution of the large-scale flow control effect is considered via comparisons between the converged spatial mean statistics computed from over 2100 realizations for each scenario. Figure 6.8(a,b) demonstrates the change in the mean streamwise and wall-normal velocity fields ($\Delta\overline{U}^+$ and $\Delta\overline{W}^+$) with opposing control, while (c,d) is the corresponding quantities with reinforcing control. In this section, all variations are presented as the difference between the statistics of the controlled and uncontrolled schemes (i.e. $\Delta\overline{U}^+ \equiv \overline{U}^+_{co} - \overline{U}^+_{un}$), so that a positive value indicates that the large-scale control increases the value of the quantity and vice versa for the negative values. The inner-scaled velocities are normalized by the corresponding U_τ attained from the upstream detection array of hot-film probes (uncontrolled U_τ). Thus, the variation of the U_τ along the $x-$direction will not lead to ambiguity in the analysis, since only the unaffected skin-friction velocity is applied. In general, the mean velocity variation due to the opposing and reinforcing control schemes are similar to each other. Figure 6.8(b,d) show that the large-scale flow control results in a strong positive signature on the

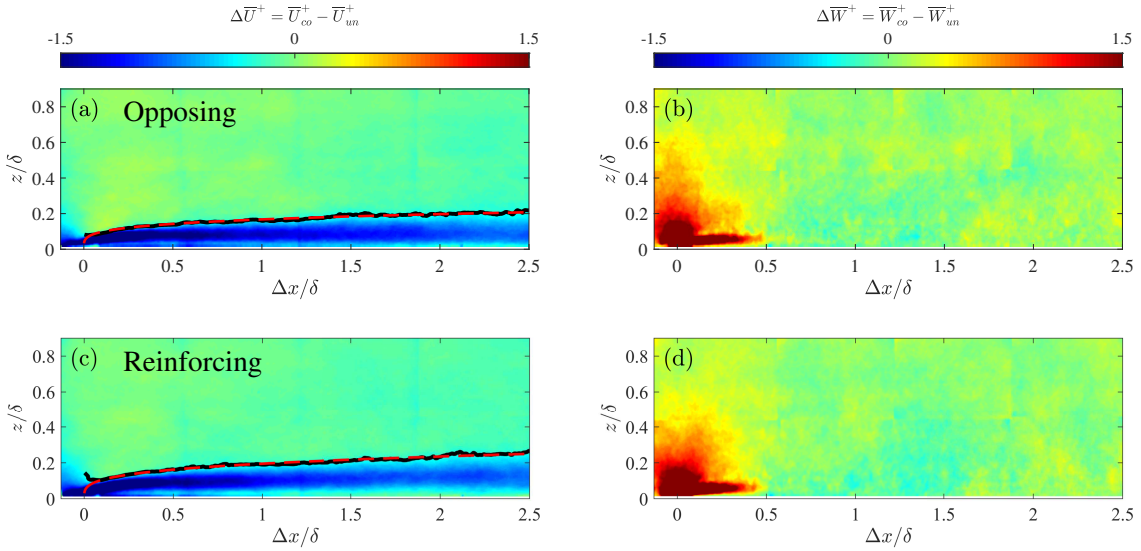

Figure 6.8: Contours of the mean velocity change due to the (a,b) opposing and (c,d) reinforcing control in (a,c) streamwise velocity and (b,d) wall-normal velocity components, respectively. Black solid lines (−) in (a,c) are the iso-contour line at the level of -0.15, and the red-dashed line (−−) is the exponential fit of the iso-contour.

wall-normal velocity component for both control strategies at $\Delta x < 0.5\delta$, and extending up to $z = 0.5\delta$. Because half of the PIV images of the controlled cases are taken while the jets are off, the mean wall-normal velocity near the jet exhaust is less than $0.5U_{jet}$. Furthermore, wall-normal momentum associated with the jet flow decelerates between the jet exit and the minimum z position of the FOV, so the resulting maximum measured velocity in W (~ -5m/s) is less than half of U_{jet}. Due to the rapid decay in the injected wall-normal velocity from the jet for $\Delta x > 0.5\delta$, the streamwise velocity deficit provides a better indication of the jet trajectory. Figure 6.8(a) demonstrate that the injected jet flow for both opposing and reinforcing controlled cases generates a low-momentum band in $\Delta\overline{U}^+$, which extends beyond the PIV FOV ($\Delta x > 2.5\delta$). The velocity deficit regions both reach a wall-normal extension of $z \approx 0.15\delta$ (i.e. the upper bound of log region) for $\Delta x > 0.5\delta$. which validates the selection of U_{jet}, which was made to ensure that the jet flow successfully influences the logarithmic region up to a large streamwise extent downstream of the actuation. For both control strategies, the strength of the jet induced perturbation in ΔU^+ gradually decays with increasing streamwise distance downstream of the actuation.

A careful inspection of the region of negative $\Delta\overline{U}^+$ contours in figure 6.8(a,c) reveals that the velocity deficit region of the reinforcing controlled boundary layer has a slightly more pro-

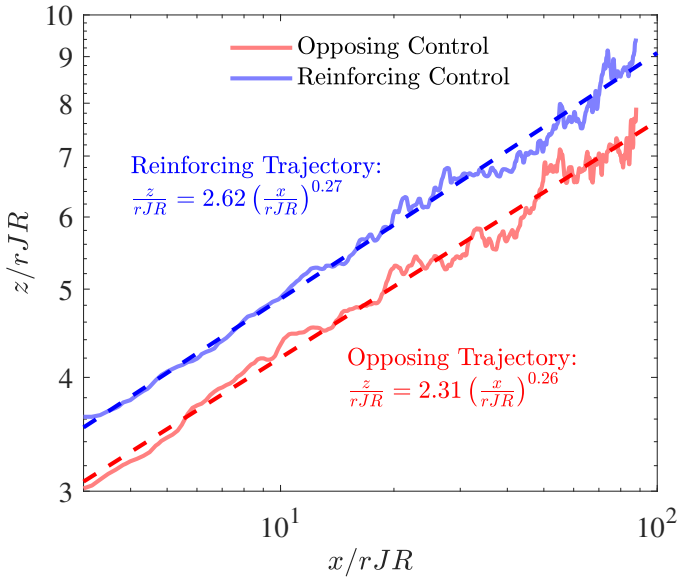

Figure 6.9: Isocontours of the penetration jet trajectories in the opposing (−) and reinforcing (−) controlled boundary layers adapted from figure 6.8(a,c). The dashed lines are corresponding exponential fit for the trajectories.

nounced outwards trajectory (towards the freestream) than that of the opposing controlled case. This might be explained by considering the wall-normal velocities of the targeted structures for the two different strategies. For the opposing control scheme, the actuation is performed on high-speed large-scale structures with natural wall-ward motions. In this case, the higher opportunity of encountering the negative$-w$ events retards the wall-normal momentum of the jet flow, and inevitably suppresses the propagation of the trajectory in the $z-$direction. Conversely, for reinforcing control, the jets are fired during the low-speed events, which are predominantly characterized by flow away from the surface, and hence these large-scale ejection events lift the jet flow further from the wall. To better quantify the difference of the penetration height, we refer to the jet penetration trajectory as the iso-contour of $\Delta\overline{U}^+ = -0.2$ (black solid lines in figure 6.8(a,c)), which is approximately 1% of the mean streamwise velocity at the upper bound of the log region in the uncontrolled boundary layer. Thus, the region above the black solid line has its $\overline{U}^+_{co}$ reaching over 99% of the uncontrolled velocity. Humber et al. (1993) showed that a sharp-edged rectangular jet possesses a similar jet trajectory to the round jet. As studied by Broadwell and Breidenthal (1984) a few decades ago via a similarity analysis, the trajectory of wall-normal jets follows an exponential rule as expressed by equation 6.1.

$$\frac{z}{rJR} = A_{JR}\left(\frac{x}{rJR}\right)^{B_{JR}} \tag{6.1}$$

where $JR = U_{jet}/U_{\infty}$ is the jet exit ratio and $r = \sqrt{l_j \times w_j}$ is the effective jet radius. In figure 6.9, the iso-contour of the penetration trajectory of the opposing controlled (red solid lines) and reinforcing controlled (blue solid lines) cases are shown. Applying these formulas, a good agreement is seen between the experimental results and the fitted trajectories (dashed lines), which implies that the exponential fit may also be applicable to intermittently activated jets. Specifically, due to the more pronounced outwards trajectory for the reinforcing control, its pre-multiplied constant $A_{JR_{re}} = 2.62$ is slightly larger than that of the opposing controlled case $A_{JR_{op}} = 2.31$. In contrast, the exponential constant B_{JR} for the opposing and reinforcing controlled cases almost matches, which best fit the values of 0.26 and 0.27 respectively. Consequently, we see the extracted trajectories for both controlled cases are parallel with each other in the log-scaled diagram. The values of B_{JR} and B_{JR} for both cases satisfy the range summarized by Margason (1993) from a list of experimental results as $1.2 < A_{JR} < 2.6$ and $0.28 < B_{JR} < 0.34$.

The hot-wire results in Chapter 4 showed that the large-scale turbulent energy attenuation plays a key role in the skin-friction drag reduction of the present flow control. Using the PIV dataset, the spatial modification on the large-scale turbulent energy is investigated to better study the evolution of the control effects on different LSMs. In figure 6.10(a,e), the streamwise turbulent intensity variation is presented relative to the uncontrolled boundary layer for both the opposing and reinforcing control strategies, while respective variation in wall-normal turbulent intensity is shown in (b,f). Here, the variation is again defined as the difference between the controlled ($\overline{u^2}^+_{co}$) and uncontrolled ($\overline{u^2}^+_{un}$) turbulent energy (i.e. $\Delta\overline{u^2}^+ = \overline{u^2}^+_{co} - \overline{u^2}^+_{un}$). Yuan et al. (1999) employed LES and reported that a typical round wall-normal jet in cross-flow generates a peak raise in turbulent energy near the jet exit owing to the coherent spanwise rollers, while the interactions between the jet flow and the cross-flow prolong the trend to further downstream. For the current study, as illustrated in figure 6.10(a,e), the jet operates in a semi-periodic on/off mode, which enhances the formation of spanwise roller vortices leading to increased turbulent energy for both control strategies near the jet exit for $\Delta x < 0.25\delta$. Beyond this location, for $\Delta x > 0.25\delta$, the modified turbulent intensity $\Delta\overline{u^2}^+$ shows markedly different behaviour for the two control strategies. For the opposing controlled case, $\Delta\overline{u^2}^+$ downstream of 0.25δ is separated into two regions. The positive

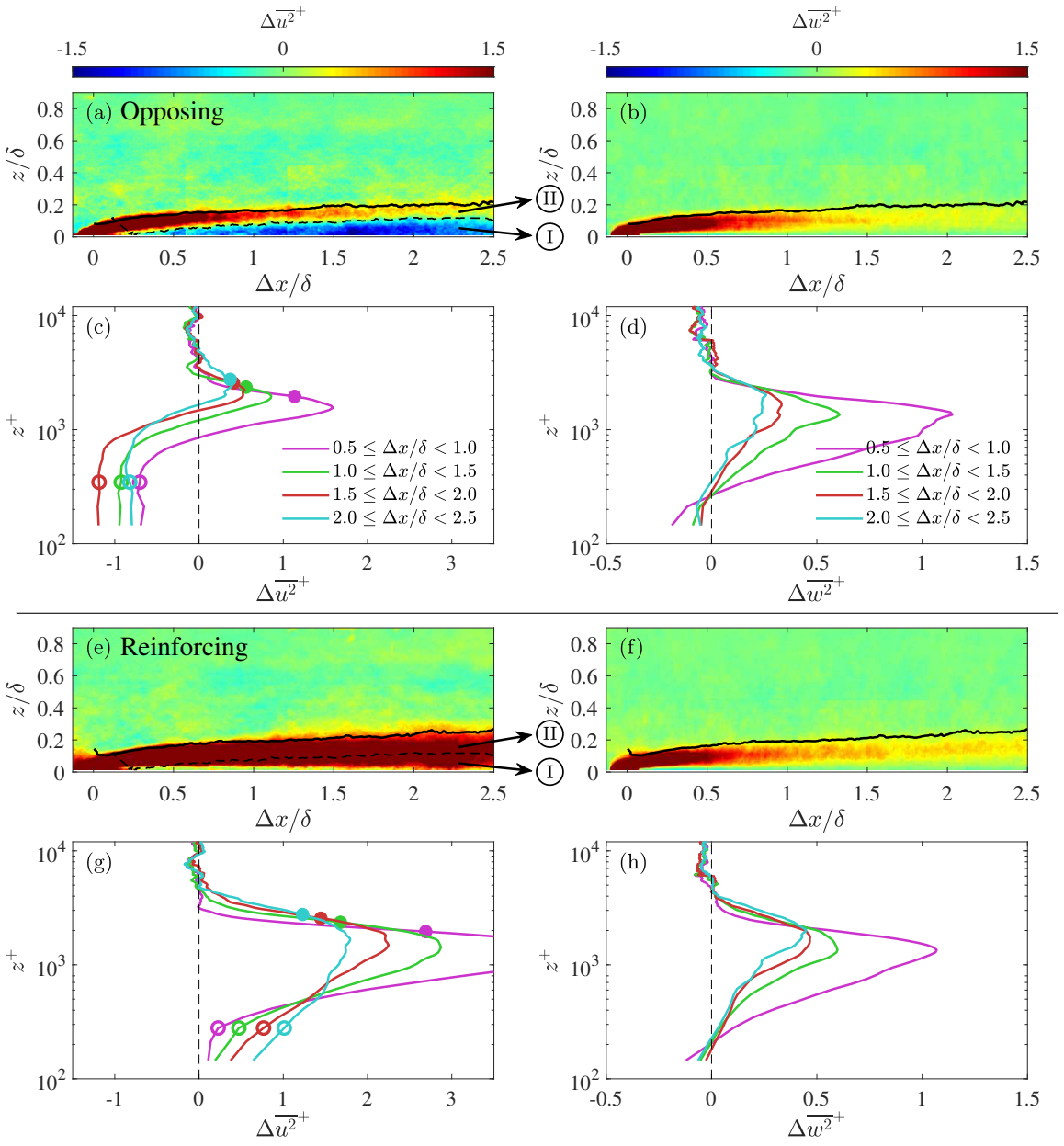

Figure 6.10: Contours of the (a,e) streamwise and (b,f) wall-normal turbulent intensity change for (a,b) opposing and (e,f) reinforcing control strategies. Black solid line (−) is the iso-contour line marking the top of the jet trajectory adapted from figure 6.8(a). (c,g,d,h) Streamwise averaged change in streamwise and wall-normal turbulence energy binned in four equally distributed zones in the $x-$direction. Streamwise turbulent energy change along the jet trajectory and for $z^+ = 350$ (i.e. in the log region) are highlighted by solid (●) and hollow circles (○) in (c,g). Region (I) is the region effectively manipulated by the large-scale control, and region (II) is is the region affected by the shear layer between the jet flow and cross flow.

part locates around the penetration trajectory (region (II)), whereas $\overline{u^2}^+$ attenuates closer to the wall (region (I)). In contrast, for the reinforcing control, there is increased energy in the entire region bounded by the jet trajectory (black solid line) and the wall. Such results agree with the large-scale energy variation obtained from the hot-wire anemometry measurements in §5.1. Figure 6.10(b,f), however, reveal that both control strategies produce more similar behaviour in $\Delta\overline{w^2}^+$ with increased energy for both strategies below the jet penetration trajectory. Unlike the reduced $\overline{u^2}^+$ in the opposing controlled boundary layer, the increased $\overline{w^2}^+$ suggests that the wall-normal velocity of the jet flow fails to suppress the wall-ward motions associated with the targeted LSMs. In order to penetrate the log region, the jet exit velocity is set more excessively than the averaged wall-normal components of the targeted LSMs. Consequently, the jet flow totally overwhelms the wall-ward momentum associated with the high-speed events, converting these to motions away from the wall, especially in the region for $\Delta x < \delta$.

Better visualization of the spatial evolution of the mean control effect can be obtained by streamwise averaging the binned streamwise and wall-normal turbulent intensity variation into four discretized ranges along the x-direction. These results for the opposing controlled case, for both the modification of streamwise and wall-normal intensity, are shown in figure 6.10(c,d) respectively. The first bin covers the range $0.5 < x \leq 1.0$. Figure 6.10(c) shows that, for larger Δx values, a thickened $\Delta\overline{u^2}^+$ reduction zone occurs (larger region of negative $\Delta\overline{u^2}^+$). The solid symbol on each of the binned averages shows the average location of the upper boundary of the jet flow (the average value of the black line shown in figure 6.10(a,b,e,f) over the bin. The peak $\Delta\overline{u^2}^+$ extends to a higher wall position following the observed general trajectory of the jet and is slightly lower than than the local penetration height (solid circle markers). These energy crests are mainly due to the shear layer between injected jet flow and the oncoming boundary layer and are primarily caused by small-scale energy as observed in figure 5.2. The hollow markers on each binned-averaged curve show the variation of $\overline{u^2}^+$ in the log region $z^+ = 350$ for opposing and reinforcing controlled cases. For both control strategies, a similar deterioration of the energy increase due to the interference between the jet flow is observed in figure 6.10(c,g). For opposing controlled case, the reduction in $\overline{u^2}^+$ within the log region (hollow markers in figure 6.10(c)) peaks between 1.5δ and 2δ downstream of the actuation array beyond which the attenuation in energy gradually diminishes. Such phenomenon follows the trend of the skin-friction drag re-

duction measured in §4.4, further illustrating the proportionality between the near-wall reduction in streamwise turbulent energy and the reduction in skin friction drag for the opposing control case. On the contrary, the strengthening on the streamwise turbulent energy in the log region of the reinforcing controlled boundary layer (hollow markers in figure 6.10(g)) increases across the entire FOV. Since the energy variation in the log region is mostly related to the modifications of the LSMs, the large-scale control effect induced by the reinforcing control is more persistent than the opposing control. This suggests that the counteracting dynamics between the jet flow and the high-speed large-scale coherent structures for the opposing control have a damping effect that results in a faster recovery.

6.3 Phase Averaged and Evolution of Control Effects

Following the overall effects of the active flow control strategy illustrated by the temporal average of the first and second-order flow statistics, the tailored LSMs due to the large-scale manipulation are examined by computing conditional quantities from the PIV velocity vectors. Specifically, the results are conditioned based on the upstream skin-friction velocity signal from the center hot-film probe. As mentioned before, though the hot-film signals are acquired simultaneously with the PIV images, the streamwise spatial separation employed between the jet position and u_τ sensors inevitably leads to a time delay τ due to the convection of the coherent motions. For the following analysis, the value of τ and the convection velocity U_c of the large-scale structures are adapted from the measurements in §4.2. Because the leading edge of the FOV is approximately aligned with the actuation array, the convection velocity of the LSMs are determined as $U_c^+ = 20.8$. At first, the conditional analysis considers only those PIV realizations taken while the detected high skin-friction has convected to a location right above the jet to better investigate the initial alteration of the structures due to the jet actuation. The instantaneous PIV vector fields that satisfy this condition are selected based on the acquired laser signal, e_L, and the upstream large-scale skin-friction fluctuation, u_{τ_l}, measured at the same spanwise position of the laser sheet. As an example, in figure 6.4, the second pair of laser pulses ($e_L(t) > 0$) are located within the positive part of the time-shifted upstream large-scale skin-friction fluctuation ($u_{\tau_l}(\Delta y = 0, t - \tau) > 0$), and hence meet this condition. In this case, the jet on the centerline of the control panel will be either on or

off for the opposition or reinforcing control schemes respectively. We define the criteria of this conditional analysis as,

$$\langle\, u_h(x,z)\,\rangle = \langle\, u(x,z) \mid e_L(t) > 0 \cap u_{\tau_l}(\Delta y = 0, t-\tau) > 0\,\rangle \tag{6.2}$$

where u_h is the conditional high-speed velocity fluctuation and u is the fluctuating streamwise velocity from the PIV snapshots. To compute the fluctuating velocity component, the mean velocity for the uncontrolled boundary layer is the spatially averaged mean velocity profile as given in figure 6.7(a). For the controlled boundary layers where there is more pronounced inhomogeneity in x due to the jet actuation, the fluctuating components are obtained by subtracting the temporal averaged fields from all 2100 realizations. The signal u_{τ_l} in equation 6.2 is the real-time filtered large-scale skin-friction velocity fluctuation acquired simultaneously with the PIV snapshots during the measurement. Since the probability of $u_{\tau_l} > 0$ is nominally 50% throughout the entire experiment duration, the conditionally averaged high-speed structures are computed from over 1000 chosen instantaneous velocity fields for all three cases considered (uncontrolled, opposing control, and reinforcing control, see figure 6.11). Note that if all images were included in the averaging calculation, the resulting $\langle u_h^+ \rangle$ would be zero. Hence, the conditional low-speed velocity fluctuations ($\langle u_l^+ \rangle$ and $\langle w_l^+ \rangle$) for all the remaining images (i.e. laser fired during a low-speed events) are the exact opposite values of the $\langle u_h \rangle$ and $\langle w_h \rangle$ in figure 6.11. As expected, in figure 6.11(a,b), the conditionally averaged structures for a positive skin-friction event in the uncontrolled case indicate a large-scale elongated forward-leaning region of positive $\langle u_h^+ \rangle$ which is associated with negative $\langle w_h^+ \rangle$. This validates that in spite of the current streamwise separation between the detection and the actuation arrays, the detection array is capable of accurately estimating the state of the large-scale flow above the actuation array and in the PIV FOV. However, it is noted that the resulting conditionally averaged structure is less energetic than the results of Hutchins et al. (2011), who computed the conditional structures from the hot-wire measurements made at the same x location as the detection array. As discussed in chapter 4, this is because the correlation magnitude between the u_τ and u signals for $\lambda_x > \lambda_{x,c}$ diminishes as the coherent structures lose their coherence or meander while convecting downstream. Thus, increasing energy attenuation occurs with increasing Δx_a.

The conditionally averaged streamwise and wall-normal fluctuations associated with the de-

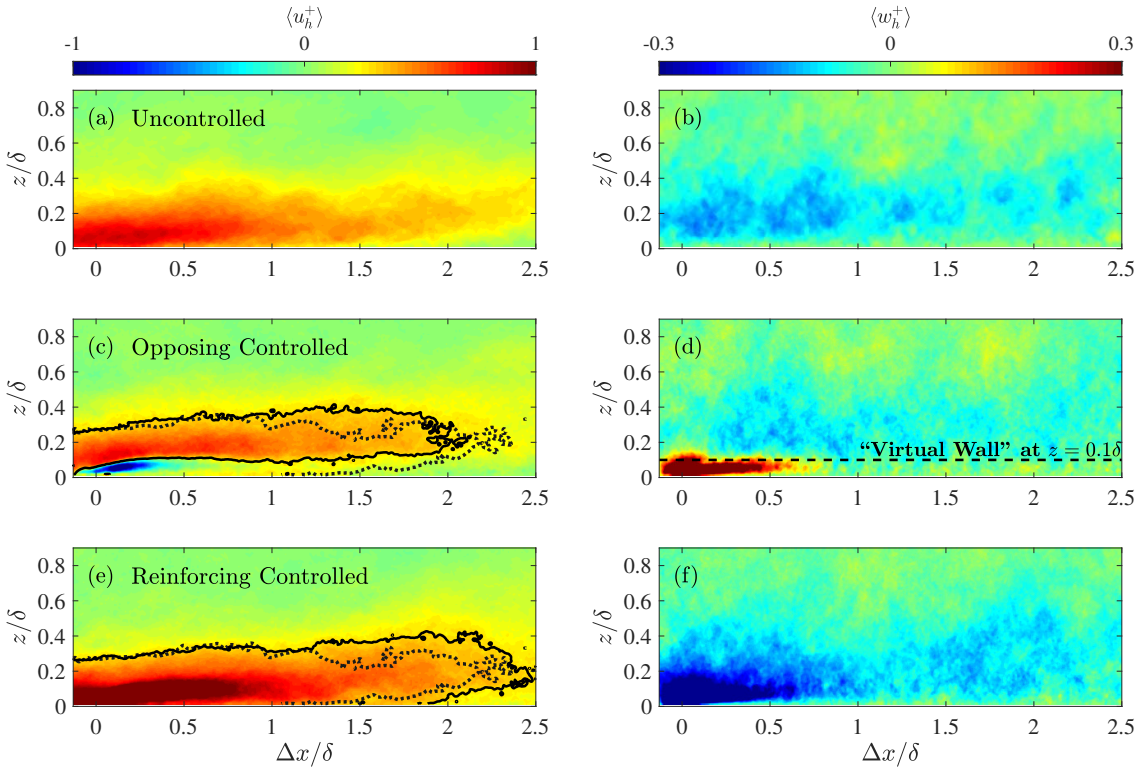

Figure 6.11: Contours of the (a) streamwise, and (b) wall-normal velocity fluctuation fields of the uncontrolled high-speed structures conditioned on the upstream detected high skin-friction event. (c,e) Streamwise and (d,f) wall-normal velocity fluctuation contour of the opposing and reinforcing controlled high-speed structures using identical condition. Black solid and dot-dashed lines in (c,e) are the iso-contour lines of $\langle u_h^+ \rangle = 0.2$ for uncontrolled and controlled cases. Black dashed line in (d) shows the penetration height of jet actuated in opposing controlled case.

tected large-scale structures ($\langle u_h^+ \rangle$ and $\langle w_h^+ \rangle$) are shown in figure 6.11(c,d) and (e,f), for the opposition and reinforcing control cases respectively. A comparison between $\langle u_h^+ \rangle$ in the uncontrolled and opposing controlled boundary layer reveals that the injected jet flow generates a low momentum zone within the conditional high-velocity events. Comparison of the wall-normal component in plots (b,d) reveals that the jet blocks the wall-ward motions associated with the large-scale positive events, creating a "virtual wall" horizontally placed at $z \approx 0.1\delta$ (i.e. upper bound of the log region). The prevention of these down-wash motions associated with the high-speed LSMs mitigates the local high shear stress footprint that occurs via the superposition effect, which ultimately might be expected to yield drag reduction, which agrees with the observation in the conditional averaged results from the hot-wire measurements in §5.2. However, it is noticed that the strong negative $\langle u_h^+ \rangle$ near the jet position does not necessarily lead to a larger drag re-

duction, since the turbulence intensity within the region is significantly raised by the actuation. Dot-dashed and solid line contours in figure 6.11(c,e) mark the boundary of the large-scale high speed event ($\langle u_h^+ \rangle = 0.2$) for the uncontrolled and controlled case respectively. These boundaries demonstrate that the controlled structures are lifted further from the wall under the effect of the active jets for $\Delta x = \delta$. It is also noted in figure 6.11(c), through comparison of these two contours, that the opposing control shortens the length-scale of the structure, which is consistent with the observation that the overall energy of the structure is decreased. In figure 6.11(d), it is observed that a strong positive w accompanies the low streamwise momentum zone near the jet position for $0< \Delta x/\delta < 0.6$, which indicates that the Reynolds shear stress associated with these high-speed structures within this region might be locally amplified in the region of the jet by the opposing control strategy. For comparison, figure 6.11(e,f) show the conditionally averaged streamwise and wall-normal velocity during a detected high-speed event for the reinforcing control case. Note that the jet on the centerline (beneath the plane of the PIV) does not fire during this phase, because the jet at the center of the array is fired only during the low-speed events which will be in the snapshots that do not contribute to this conditional average. It is noted that the reinforcing control increases the strength of the positive events, which have higher positive $\langle u_h^+ \rangle$ and higher negative $\langle w_h^+ \rangle$ and the extents of the conditional structure are also expanded. Consequently, the energized LSMs would be expected to contribute to negative skin-friction drag due to the strengthened high shear stress footprint.

The opposing controlled conditional high-speed structures are further categorized into three groups based on their streamwise length-scale determined from the upstream large-scale skin-friction velocity fluctuations. The resulting conditional averages for short events ($\lambda_x < 1.2\delta$), medium events ($1.2\delta < \lambda_x < 2\delta$), and long events ($\lambda_x > 2\delta$) are shown in figure 6.12(a,b,c), respectively. The selection of the thresholds is corresponding to the categories on the average width of the structures $\mathscr{W}$ determined in figure 5.14. The low-speed region near the wall-position due to the injected jet flow exists for all three lengths of controlled LSMs. However, this low-speed region remains closer to the wall for the longer actuated events, which agrees with the observation from the hot-wire results in figure 5.16. Figure 6.12(d) extracts the zero-contour lines of the conditional streamwise velocity fluctuation in all three types of structures for $\Delta x < 0.4\delta$ (i.e. near the jet position where the low-speed imprints are significant). These contour lines can be regarded

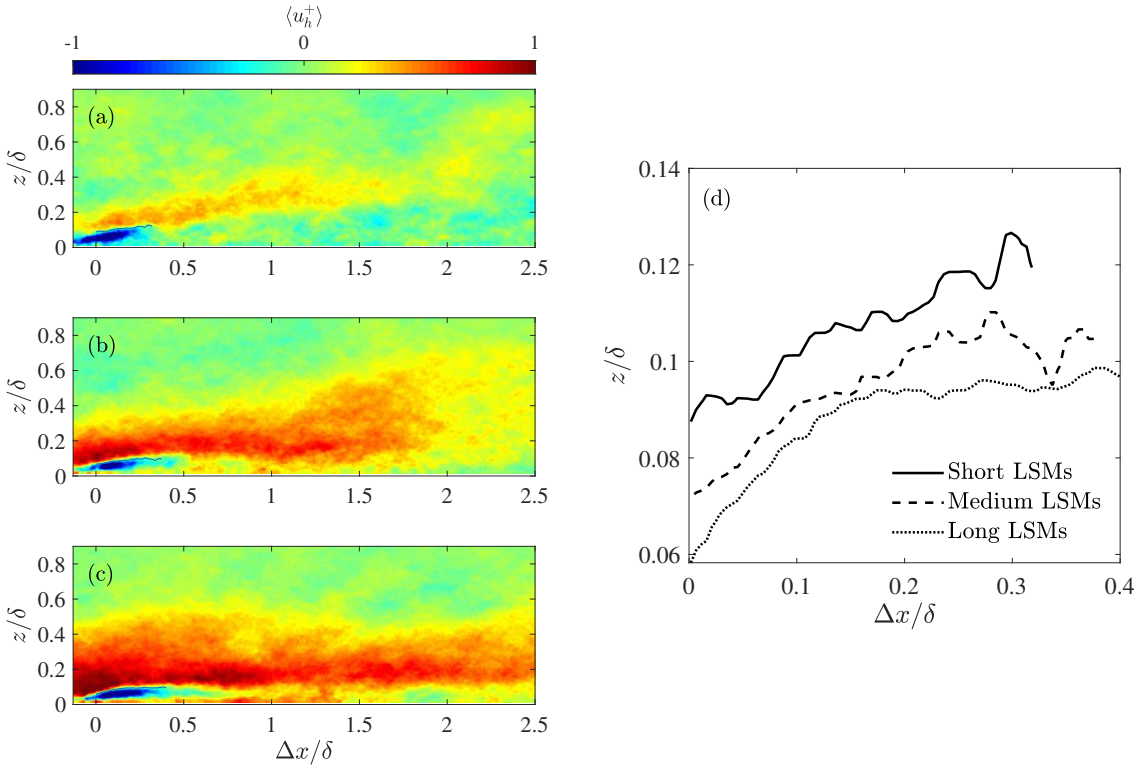

Figure 6.12: Contours of the streamwise velocity fluctuation fields of (a) short ($\lambda_x < 1.2\delta$),(b) medium ($1.2\delta < \lambda_x < 2\delta$), and (c) long ($\lambda_x > 2\delta$) high speed large-scale structures. (d) The zero contour line of $\langle u_h^+ \rangle$ adapted from (a,b,c), respectively.

as the interface between the jet flow and the LSMs in the crossflow. It is clear from figure 6.12(d) that the jet attains a higher wall-normal penetration immediately downstream of injection into a shorter high-speed event than in a longer structure. Similar to figure 5.16, the jet flow penetrates to a much lower $z-$position during the longer structures, because they are associated with a stronger negative wall-normal velocity component.

As shown in figure 6.4, the impulses of the laser signal (e_L) are randomly distributed at any phase of the large-scale friction velocity signal u_{τ_l}, and the conditional averaged results computed from equation 6.2, though specific to the high-speed events, show the ensemble-averaged velocity field acquired at all phases of the high-speed events. This phase-jitter in the ensemble average maps makes it difficult to discern certain features of the large-scale structures, such as the inclined fronts and backs. To address this shortcoming, a phase averaged analysis is carried out to further investigate the spatial evolution of the large-scale structures under the influence of the active control perturbation. In particular, the aim here is to scrutinize the connection between the

skin-friction drag reduction and the manipulation of the LSMs. This analysis is first applied to the opposing controlled case. For this analysis, the PIV snapshots are no longer discriminated based only on the sign of the upstream estimated skin-friction footprint u_{τ_l} but also now on the temporal delay (τ_h) between the impulses of e_L and the corresponding previous positive zero-crossings of the time-shifted u_{τ_l} (see figure 6.4(b)). This temporal delay τ_h corresponds to the time since the upstream edge of a high-speed event passes the jet array, and also the time since the jet has been activated. With the previously determined convection velocity of $U_c^+ = 20.8$, it is computed that 60 ms is required for a large-scale event to pass entirely through the FOV. The PIV snapshots that satisfy the criteria for positive large-scale features are further categorized into bins based on τ_h, with a bin of 10ms and 75% overlap, such that there are approximately 300 instantaneous snapshots in each of the 25 bins. This ensures the opportunity to conditionally analyze the temporally resolved interaction between the jet actuator and the large-scale positive events while retaining an acceptable degree of convergence. The resulting phase averaged velocity fields, which are defined as,

$$\langle\, u_{p.i}(x,z)\,\rangle = \langle\, u(x,z) \mid \mathscr{B}_{i.l} < \tau_h < \mathscr{B}_{i.u}\,\rangle \tag{6.3}$$

In equation 6.3, $\mathscr{B}_{i.u}$ and $\mathscr{B}_{i.l}$ are the upper and lower time limit for the i^{th} bin. Note that the first bin ($\mathscr{B}_1 \in \mathscr{B}_{1.l} < \tau_h < \mathscr{B}_{1.u}$) is selected as $-5 < \tau_h < 5$ms, so that the jet is just about to actuate within this bin in the opposing controlled case. Due to the overlapping, the range for the i^{th} bin can be defined as $(-7.5 + 2.5i < \tau_h < 2.5 + 2.5i)$ms. Figure 6.13(a,b) show the phase-averaged streamwise and wall-normal velocity fields for the first bin of the uncontrolled LSMs. These plots clearly depict an inclined front, with a convecting high-speed event approaching the jet array at $\Delta x = 0$. The detected positive temporal zero-crossings at the wall observed in the upstream detection array is well correlated with an inclined negative spatial zero-crossing that extends up to $z \approx 0.3\delta$. Downstream of the inclined shear layer, a large-scale negative u fluctuation region is evident, and indeed the size of the large-scale coherent structures extends for the entire FOV having a length scale in the order of boundary layer thickness, $\mathscr{O}[\delta]$. Black solid lines in both (a,b) are the zero iso-contour of the phased averaged streamwise velocity field, which defines conditional internal shear layer which clearly separates the high-w and low-w regions in figure 6.13. The red dashed line (−−) is a linear fit of the intersection line for $z < 0.5\delta$, and its gradient

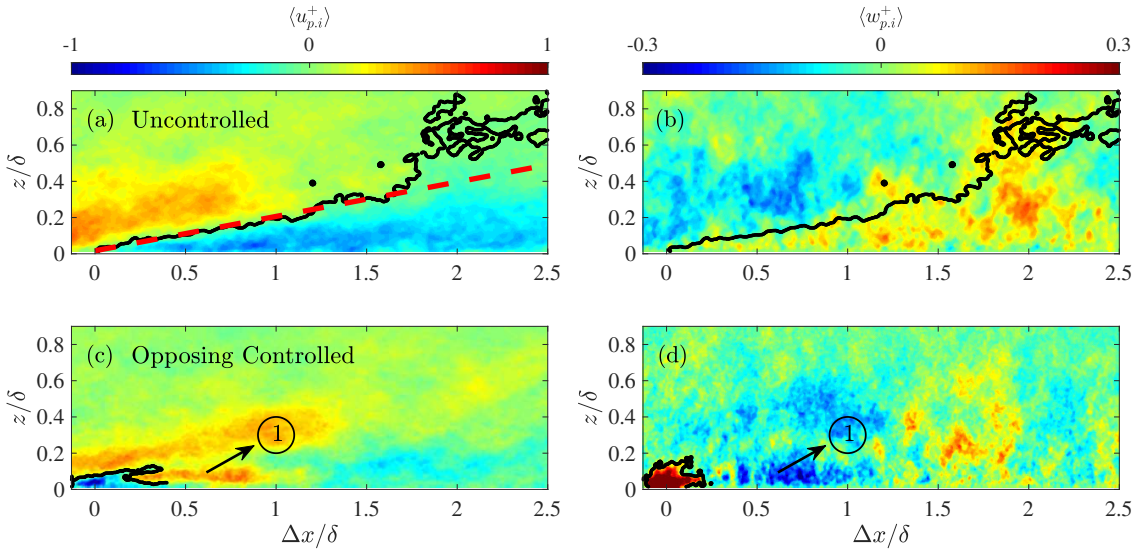

Figure 6.13: Contours of the phase averaged (a) streamwise, and (b) wall normal velocity fluctuation fields of the uncontrolled high-speed structures conditioned within $\mathscr{B}_1$ (i.e. $-5 < \tau_h < 5$ms). Contours of the phase averaged (c) streamwise, and (d) wall normal velocity fluctuation fields of the opposing controlled high-speed structures conditioned within $\mathscr{B}_3$ (i.e. $0 < \tau_h < 10$ms). The black solid lines $(-)$ in (a,c) are the zero iso-contour line of $\langle u^+_{p.i} \rangle = 0$.

implies an inclination angle of $\theta = 11.8^\circ$ for the coherent structures. Such a value is slightly smaller than the typically reported structural inclination angles, which lie between 14.5° and 16° (Hutchins et al., 2012, Marusic and Heuer, 2007, Zhou et al., 1999). The $x-$interception of the intersection line validates that the calculated time delay τ between the detection and actuation array and the estimated convective velocity U_c is sufficiently accurate.

A first glimpse of the effect of the injected jet flow on the high-speed large-scale structures for the opposing controlled case is offered by the phase averaged velocity vector fields within $\mathscr{B}_3$ (i.e. $\overline{\tau_h} = 5$ms) in figure 6.13(c,d), respectively. The black solid lines bound the regions of strong negative streamwise momentum and high wall-normal momentum close to the jet showing the initial penetration of the jet into the layer. It can be observed from figure 6.13(c,d) that the alteration of the oncoming high-speed events is minimal at this phase as the injected fluid from the jet actuation is still in the early stages of penetrating and interacting with these structures. Downstream of the highlighted jet affected region, there is a tail of high-speed streak in the u field in figure 6.13(c), and conversely a negative w region in figure 6.13(d) between $0.3\delta < \Delta x < 1\delta$ (labelled (1) in the plots). This phenomenon is because the subtracted opposing controlled mean

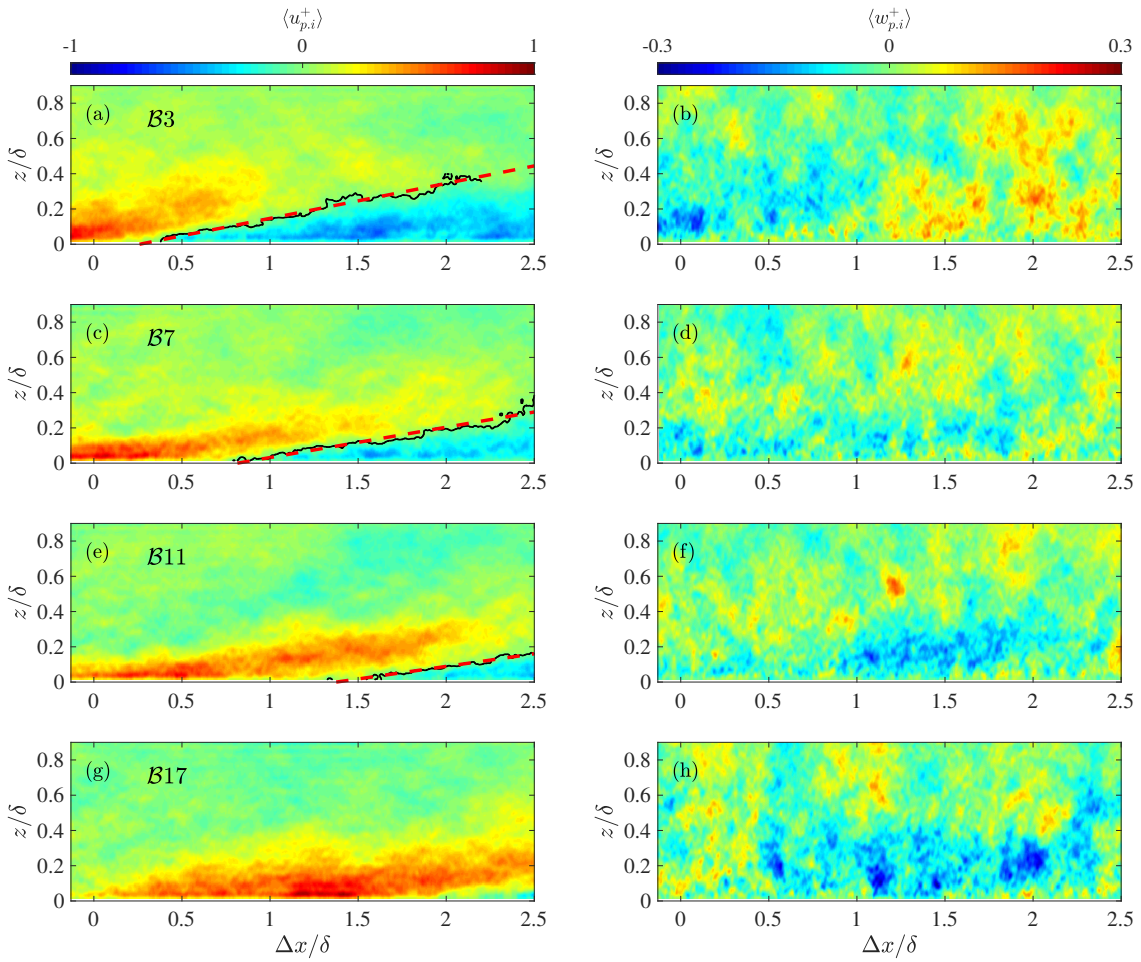

Figure 6.14: Contours of the phase averaged streamwise/wall-normal velocity fluctuation fields of the uncontrolled high-speed structures conditioned within (a,b) $\mathscr{B}_3$, (c,d) $\mathscr{B}_7$, (e,f) $\mathscr{B}_{11}$ and (g,h) $\mathscr{B}_{17}$.

velocity fields have a 50% probability of having the jet affecting this area. However, for the phase averaged results for the early bins, this probability drops to nearly zero due to the conditional criterion. There is always a period prior to the jet switching on where the jet must have been off, and so this region, downstream of $\Delta x \approx U_c \overline{\tau_h}$ will have a higher phase averaged velocity that the time-averaged mean for the controlled case. A similar effect can also still be visualized in the phase averaged streamwise velocity within $\mathscr{B}_5$ illustrated in figure 6.15(a).

Prior to further analyzing the phase-averaged high-speed structures manipulated by the opposing control strategy, the spatial evolution of the phase-averaged high-speed LSMs in the uncontrolled boundary layers are presented in figure 6.14 as a reference. The conditional streamwise

$\left\langle u^+_{p.i} \right\rangle$ and wall-normal $\left\langle w^+_{p.i} \right\rangle$ velocity components in the phase $\mathscr{B}_3$ ($\overline{\tau_h} = 5$ms), $\mathscr{B}_7$ ($\overline{\tau_h} = 15$ms), $\mathscr{B}_{11}$ ($\overline{\tau_h} = 25$ms), and $\mathscr{B}_{17}$($\overline{\tau_h} = 40$ms) are demonstrated in (a,c,e,g) and (b,d,f,h), respectively. From $\left\langle u^+_{p.i} \right\rangle$, forward-inclining features with a streamwise extension over 2δ are clearly observed in figure 6.14(e,g). The black solid lines are the spatial zero-crossings (i.e. the iso-contour of $\left\langle u^+_{p.i} \right\rangle = 0$) separating the adjacent positive and negative coherent structures. With larger $\overline{\tau_h}$ values, the high-speed LSMs convect further downstream such that the positive $\left\langle u^+_{p.i} \right\rangle$ regions appear at an increasing Δx position from figure 6.14(a)to (g). Similar to figure 6.13(a), the red dashed line is the linear fit on the spatial zero-crossings, whose slopes show that the structural inclination angle decreases from 11.3° in $\mathscr{B}_3$ to 8.9° in $\mathscr{B}_{11}$. The observation agrees with the speculations of Lee et al. (2019) that the inclination angle of a tracked coherent structure (detected by the upstream hot-film sensor) gradually decreases while convecting in the x-direction. Additionally, the x-intercepts of the linear x_{int} fitted curve gives information on the convective velocity of the LSMs as $U_c = x_{int}/\overline{\tau_h}$. For the phases in figure 6.14(a,c,e), the convective velocity U_c slightly accelarates from 14.2m/s to 14.4m/s due to the loss of coherence of the structures with smaller wavelengths as indicated in §4.2.

The streamwise spatial development of the opposing controlled high-speed large-scale structures can be qualitatively divided into four stages, as described below. The representative phase averaged streamwise and wall-normal velocity fields ($\left\langle u^+_{p.i} \right\rangle$ and $\left\langle w^+_{p.i} \right\rangle$) for each phase are shown in figure 6.15 are described below.

- **(i). Penetrating stage:** This occurs during the first 200 viscous time scales ($\overline{\tau_h} U_\tau^2/\nu < 200$). The positive wall-normal velocity carries the jet flow into the logarithmic region. Within this stage, the interaction between the jet flow and the targeted structures is minimal. Therefore, the structural geometry of the LSMs, such as the inclination angle and self-similarity, remains almost intact and the wall-normal momentum is barely transferred into the streamwise velocity of the jet flow. Example $\left\langle u^+_{p.3} \right\rangle$ and $\left\langle u^+_{p.5} \right\rangle$ fields of this stage are shown in figure 6.13(c) and 6.15(a) with a mean laser delay of $\overline{\tau_h} = 5$ms ($\mathscr{B}_3$) and 10ms ($\mathscr{B}_5$), respectively. According to the positive region of the $\left\langle w^+_{p.i} \right\rangle$ near the jet position in figure 6.15(b), it can be evaluated that the jet travels approximately 0.34δ in 10ms. Thus, we could calculate that the streamwise convective velocity of the jet flow during this stage is only 9.5m/s ($U^+_{c_{jet}} \approx 14$), which is approximately 65% of the U_c of the large-scale coherent

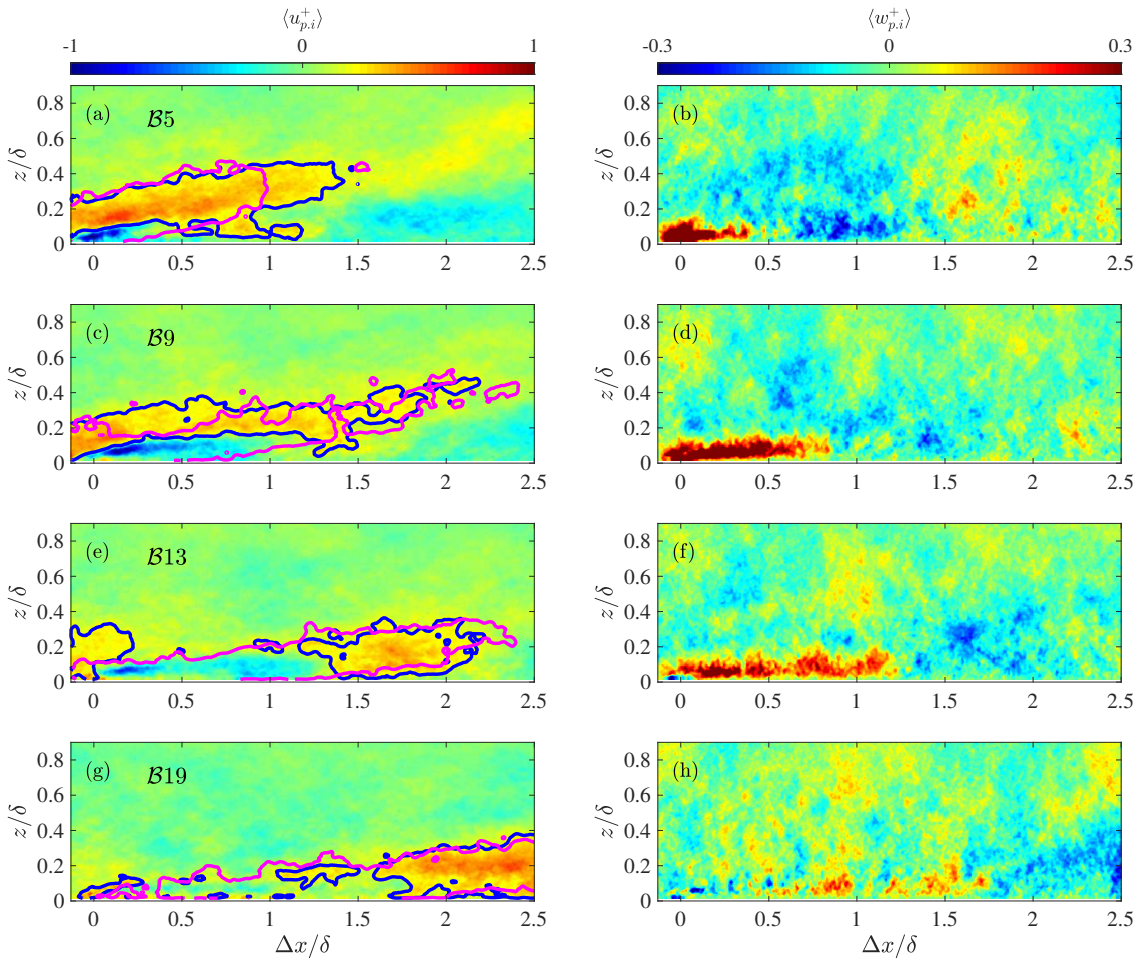

Figure 6.15: Contours of the phase averaged streamwise and wall-normal velocity fluctuation fields of the opposing controlled high-speed structures conditioned within (a,b) $\mathscr{B}_5$, (c,d) $\mathscr{B}_9$, (e,f) $\mathscr{B}_{13}$ and (g,h) $\mathscr{B}_{19}$. Blue and magenta contours are the iso-contour lines of $\left\langle u^+_{p.i} \right\rangle = 0.2$ for the opposing controlled and uncontrolled high-speed LSMs.

structures. As a result, a strong shear layer between the jet flow and the cross flow exists and significantly increases the streamwise turbulent intensity within this region. Owing to the streamwise momentum deficit, the jet flow acts as an obstacle in the boundary layer which contributes to the skin-friction drag reduction during this stage.

- **(ii). Lifting stage:** This stage occurs while the positive large-scale structures travel between 0.5δ to 1δ downstream of the actuation. Sample fields of $\left\langle u^+_{p.9} \right\rangle$ and $\left\langle w^+_{p.9} \right\rangle$ within this phase ($\mathscr{B}_9$) are shown in figure 6.15(c,d). A clear interaction between the jet flow and the high-speed large-scale structures initiates, as the positive w jet flow apparently blocks

the natural wall-ward motions associated with the high-speed events with a clear interface or virtual wall ($w = 0$) seeming to form at $z \approx 0.12\delta$ in figure 6.15(c) (slightly lower than the upper boundary of the log region). This blocking action mitigates the interaction between the large-scale high-speed structures and the wall. The subsequent weakening of the high shear stress footprint at the wall (via superposition) will be expected to yield a local reduction in drag. In addition, though the outline of the large-scale structures with $\left\langle w^+_{p.9} \right\rangle$ equivalent to 0.2 (black solid line) is still recognizable in figure 6.15(c), it is obvious that the targeted high-speed events are deflected and lifted by the jet actuation to higher wall-normal positions than the bounds of the uncontrolled high-speed structures (black dashed line). This is particularly noticeable in figure 6.15(c) for $0 < \Delta x/\delta < 1.0$ where the inclination angle of the LSMs is flattened. The phase averaged region of strong positive, $\left\langle w^+_{p.9} \right\rangle$ observed in figure 6.15(d) shows that the jet flow has convected to a downstream position of $\Delta x = 0.8\delta$ by $\overline{\tau_h} = 20$ms, so the convective velocity of the jet flow $U_{c_{jet}}$ has accelerated now to $0.8\delta/\overline{\tau_h} = 11.2$m/s during this stage, which is still only approximately 80% of the convection velocity of the high-speed event.

- **(iii). Mixing stage:** In this stage, examples of which are given in figure 6.15(e,f), the LSMs mix with the injected low-speed flow. The convective velocity of the high-speed events is much faster than that of jet flow. Therefore, the coherent structures slowly overtake the jet exhaust during this stage of the streamwise evolution. A large region of the high-speed event that has overtaken the actuation seems to have re-emerged, with a region of strong positive $\left\langle u^+_{p.13} \right\rangle$ fluctuation and strong wall-ward $\left\langle w^+_{p.13} \right\rangle$ fluctuation reestablished in the range $1.3 < \Delta x/\delta < 2.2$. Sequentially, during this stage, the turbulence energy associated with the high-speed events has been neutralized to the maximal extent which agrees with the observation in figure 6.10(c) that the streamwise energy reduction is maximized for $1.5 < \Delta x/\delta < 2.0$. The phase averaged streamwise velocity of $\mathscr{B}_{13}$ in figure 6.15(c) demonstrates a clear energy attenuation of the high-speed structures during this stage. It can be calculated via the region of strong positive $\left\langle w^+_{p.13} \right\rangle$ in figure 6.15(f) that the convective velocity of the jet is approximately 11.8m/s ($83\%U_c$) during this stage. Applying the method to all the phases, figure 6.16 shows the change of jet convective velocity in all phases from $\mathscr{B}_3$ to $\mathscr{B}_{19}$. Black square markers (■) are the jet convective velocity $U_{c_{jet}}$ in

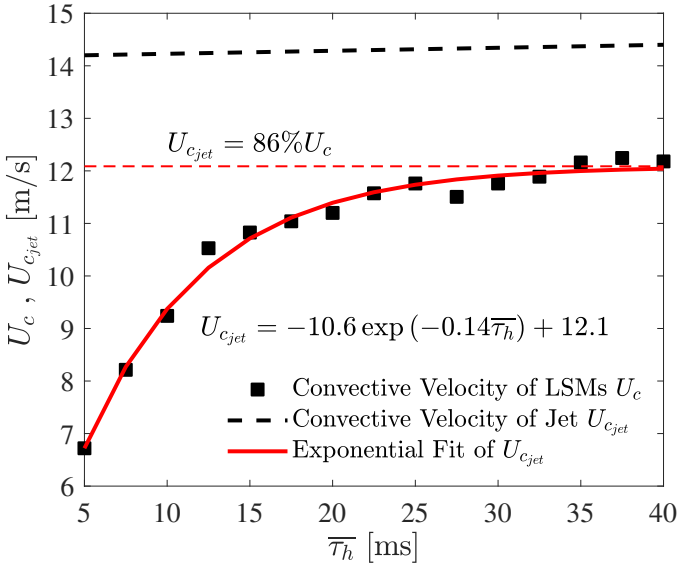

Figure 6.16: Jet convective velocity (■) calculated in the phase-averaged wall-normal velocity fields with different $\overline{\tau_h}$ values. Black dashed line (− −) is the convective velocity of the targeted LSMs and the red solid line (−) is the exponential fit of the $U_{c_{jet}}$ at each phase.

each phase, which shows that $U_{c_{jet}}$ gradually increases with $\overline{\tau_h}$ and exponentially converges to a threshold value. The exponential fit (−) to the measured $U_{c_{jet}}$ infers that the maximum $U_{c_{jet}}$ asymptotes to a velocity slightly lower than the convection velocity of the targeted structure ($U_{c_{jet}} \approx 12.3$m/s$= 88\%U_c$). Most importantly, skin friction drag reduction is typically maximized during this stage due to the large-scale energy attenuation and suppression of the near-wall cycle and small-scale turbulence (as shown from the hot-wire measurements in figure 5.10(d), where the small-scale turbulent energy reduction due to the present control is maximized at $\Delta x_m = 1.7\delta$).

- **(iv). Recovering stage:** The final (recovering) stage in figure 6.15(g,h) occurs after the maximum friction drag reduction for $\overline{\tau_h} > 45$ms (i.e. $\overline{\tau_h}^+ > 1200$ in the current study) and where the spatial negative zero-crossing has convected to approximately 2δ downstream. The low-speed streamwise momentum and positive wall-normal velocity associated with the jet actuation weaken substantially in this stage. Furthermore, due to the difference in U_c shown in figure 6.16, the LSMs entirely overtake the jet flow and start to reform into a feature that closely resembles the uncontrolled large-scale structure for $\Delta x > 2\delta$. Such a process initiates from the leading edge of the LSMs as the energy within the front of the

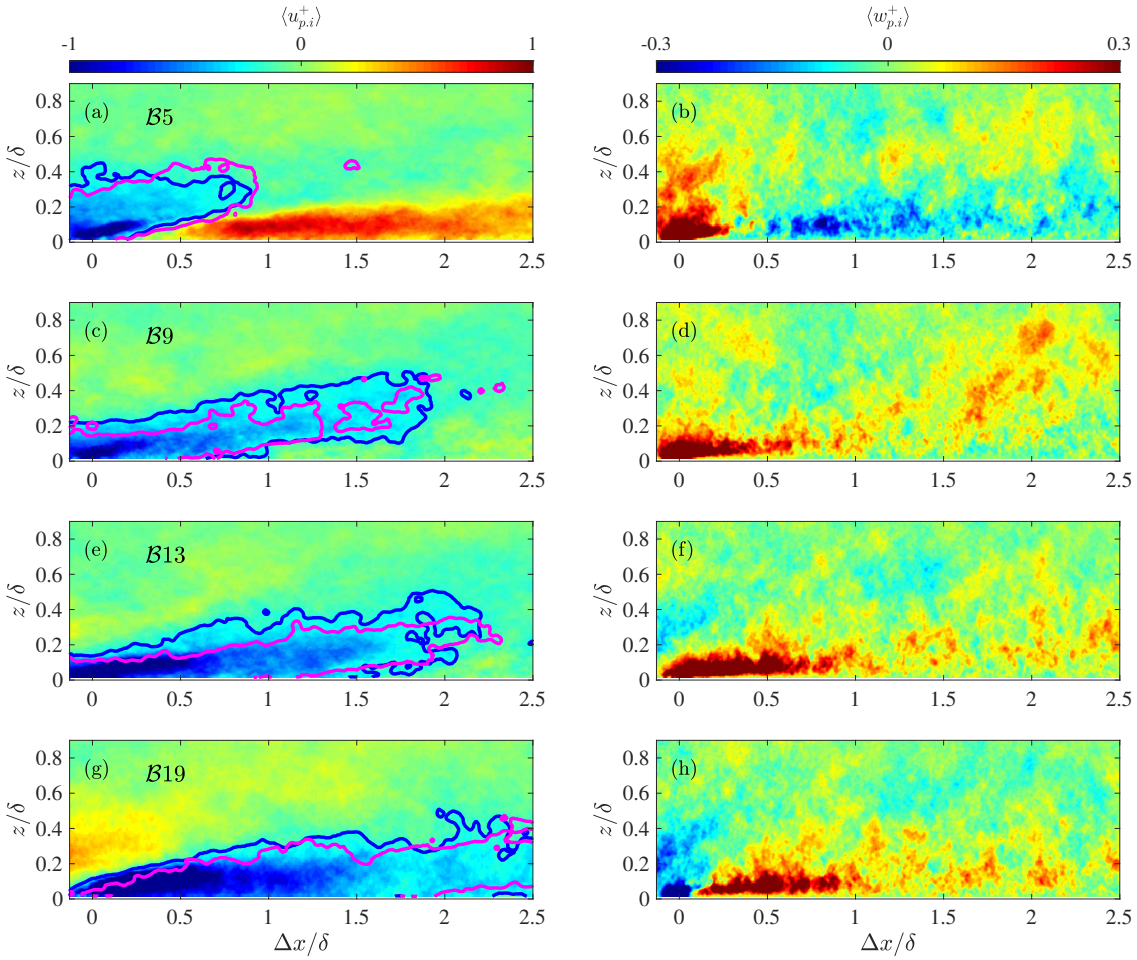

Figure 6.17: Contours of the phase averaged streamwise/wall-normal velocity fluctuation fields of the reinforcing controlled low-speed structures conditioned within (a/b) $\mathscr{B}_5$, (c/d) $\mathscr{B}_9$, (e/f) $\mathscr{B}_{13}$ and (g/h) $\mathscr{B}_{19}$. Blue and magenta contours are the iso-contour lines of $\left\langle u^+_{p.i} \right\rangle = -0.2$ for the reinforcing controlled and uncontrolled low-speed LSMs.

conditional structures overtakes the jets prior to the trailing edge. In the end, at greater Δx, the skin friction will converge to the canonical wall-shear stress within a smooth-wall turbulent boundary layer.

This four-stage evolution process of the opposing controlled Large Scale Motions (LSMs) further validates the spatial-evolving model of the control effect proposed in figure 5.13(e,f), which speculated that the recovery of the control effect is owing to the mismatched convective velocity between the jet flow ($U_{c_{jet}}$) and the targeted LSMs (U_c). Considering the difference between the two is approximately 14% of the convective velocity of the jets in figure 6.16, at $0.5\lambda_{x.c}/0.14\delta \approx$

6δ downstream of the actuation, over half of the targeted LSMs would overtake the jet flow. In this case, 50% of the injected jet is still located within the high-speed large-scale events, but the other half is shifted into the adjacent low-speed structures, which effectively becomes a pseudo-desynchronized control with a 50% control accuracy. In turn, this might indicate that the large-scale control effect could potentially reach 6δ downstream of the control.

In terms of refinements on the flow control strategy, the evolution process implies that only the structures with a sufficient length-scale are likely to be receptive to actuation, as very short structures are likely to only experience the first two stages described above, and so positive outcomes in terms of mitigation of large-scale energy and skin friction reduction are unlikely. Additionally, figure 6.15(e-h) suggest that a re-actuation (a second jet actuation array some distance downstream of the current existing array) after the maximum drag reduction point ($\Delta x = 2\delta$) would be helpful in preserving the control effect over a larger area. Further investigations are required to consider how an actuation or re-actuation could avoid the first two stages to increase the efficacy of control (e.g. the re-actuation could possibly be performed with a lower jet ratio).

For completeness, figure 6.17 shows the phase averages at the same phase, only this time for the low-speed structures actuated by the reinforcing control. Because the actuation is only activated on the estimated negative events, the snapshots are currently binned in accordance with the time difference between the laser impulses and their corresponding previous negative zero crossings of u_{τ_l}, defined as τ_l in figure 6.4 which again refers to the time between the phase average and the triggering of the actuator, or alternatively the time between the phase average and positive spatial zero-crossings arriving at the actuator array. Figure 6.17 illustrates the reinforcing $\left\langle u^+_{p.i} \right\rangle$ and $\left\langle w^+_{p.i} \right\rangle$ with the values of selected τ_l equivalent to the laser delay τ_h in figure 6.17. The conditional low-speed events are energized and expanded by the perturbation but their structural geometry remains intact even with the manipulation of the jet flow during the convection. A stronger correlation between the low streamwise velocity and high wall-normal velocity region than that of the opposing control case is observed for all τ_l instances. Specifically, in figure 6.17(d,f) the positive $\left\langle w^+_{p.i} \right\rangle$ induced by the jet flow reaches over 0.2δ in the z-direction, which is much higher than that in figure 6.15(d,f) for the opposing controlled case. Moreover, because the active jet flow in the reinforcing control case magnifies the amplitude of the large-scale fluctuation, it is observed that the streamwise wavelength of the LSMs grows from 1.5δ in figure 6.17(e)

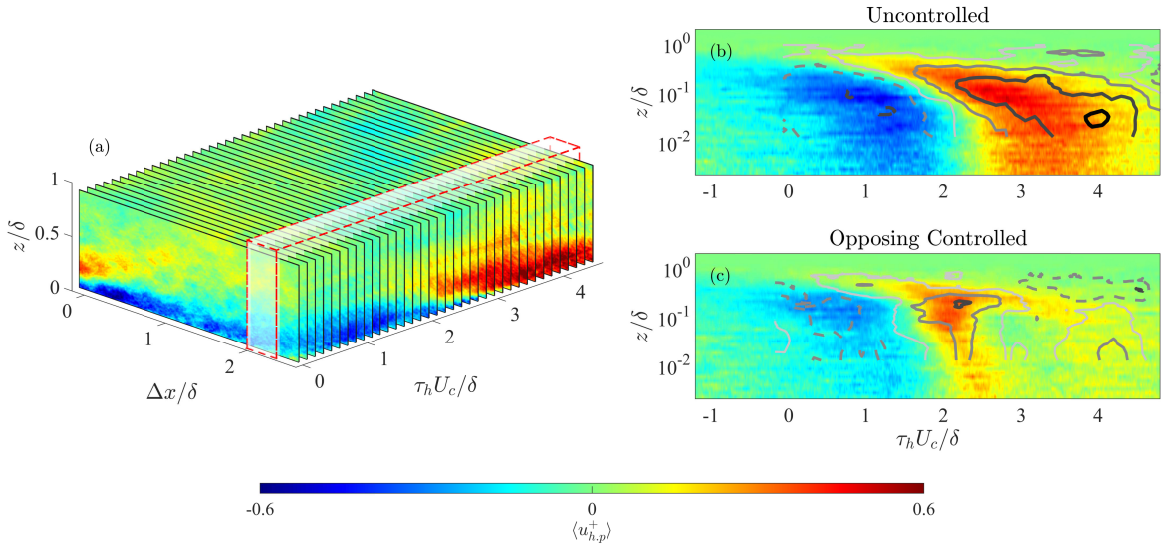

Figure 6.18: (a). A matrix of phased averaged streamwise velocity fluctuation contour ordered with respect to laser delay τ_h. (b,c). Temporal conditional averages contours of streamwise velocity fluctuation field conditioned on positive zero-crossing of the upstream large-scale u_τ signals in uncontrolled and opposing controlled boundary layers. Coloured and gray-scale contours are computed based on previous hot-wire (Abbassi et al. (2016)) and current PIV measurements.

to approximately 2δ in figure 6.17(g) during actuation, indicative of the reinforcement of this structure by the jet actuation. While the recovery phase occurs in $\mathscr{B}_{19}$ in figure 6.15(g), the negative event in 6.17(g) is still larger and more energized than the uncontrolled low-speed events.. This further validates the observation from figure 6.10 that the reinforcing control effect on the low-speed LSMs is more long-lasting than the opposing controlled case.

6.4 Conditional *DR* and Reynolds shear stress

The phased averaged statistics in the previous section characterize the spatial and temporal evolution of the perturbed high-speed large-scale structures within the FOV. The connection between the manipulations of the large-scale structures and the wall-shear stress is considered through analysis of the skin-friction velocity signals acquired by the measurement hot-film array located 2.1δ downstream of the actuation array. However, the quantitative comparison of the time-series data from the skin friction sensors, $U_\tau(t)$, and the spatial velocity fields from the PIV, $U(x,z)$, requires an accurate estimation of the convective velocity, which was shown to vary with respect to the

$x-$position within the controlled boundary layer. Thus, it is unrealistic to directly transfer the spatial velocity fields into the temporal domain via Taylor's frozen turbulence hypothesis, especially in the opposing controlled case. In contrast, the phased averaged analysis, similar to time-resolved PIV, provides the temporal information to conditionally resolve the problem. This transformation is accomplished via first cascading the phase averaged results $\langle u^+_{p.i}(\Delta x, z, \tau_h \in \mathscr{B}_i)\rangle$ with increasing τ_h values , as illustrated pictorially in figure 6.18(a). Then, a temporal velocity field, $\langle u^+_p(z, \tau_h)\rangle$, conditioned on the positive zero-crossings of the u_τ signals at a specific streamwise position can be constructed by slicing the stacked phase -averaged fields at the selected $x-$position as shown by the red dashed lines in figure 6.18(a). Hence, through ordering multiple phase-averaged streamwise velocity fluctuation fields of the uncontrolled canonical boundary layer in terms of the laser delay τ_h, a clear temporal conditional averaged view of the large-scale structures can be observed on the $\Delta x = 2.8\delta$ plane. Note that for this analysis additional bins, up to $\tau_h = 100$ms, have been considered to fully capture the temporal large-scale features. To validate these transferred results, a comparison between the temporal conditional averaged fields obtained from the current DE-PIV measurements and the previous hot-wire anemometry (HWA) database is performed. Colour-contours in figure 6.18(b,c) show the velocity fluctuations from the HWA measurements at $\Delta x = 2.1\delta$, which is previously presented in Chapter 5 conditioned on positive zero-crossings in the upstream large-scale skin-friction velocity fluctuations for the uncontrolled and opposing controlled cases measured, respectively (see figure 5.4). For consistency, the local convective velocity at the $x-$position of the hot-wire measurement ($\Delta x = 2.1\delta$), is applied to convert the laser delay τ_h for the PIV measurement into the spatial domain via Taylor's frozen turbulence hypothesis. These HWA measured conditional averages can be compared with the same result from the DE-PIV by averaging the vector fields within the white shaded inspection window in figure 6.18(a), which ranges $\pm 0.25\delta$ about the hot-wire location $1.85 < \Delta x/\delta < 2.35$. This selected range ensures a sufficient level of convergence level in the computed result. In figure 6.18(b,c), solid lines are the positive iso-contour levels with an increment of 0.2, while the dashed lines show negative values. Generally, the conditional structures attained from the PIV and hot-wire results exhibit good agreement for both cases, which confirms the validity of the spatial-temporal transformation of the PIV phased averaged fields. Specifically, at the selected $x-$position, during the mixing stage, an apparent reduction in u fluctuations is captured in the temporal conditional averaged velocity

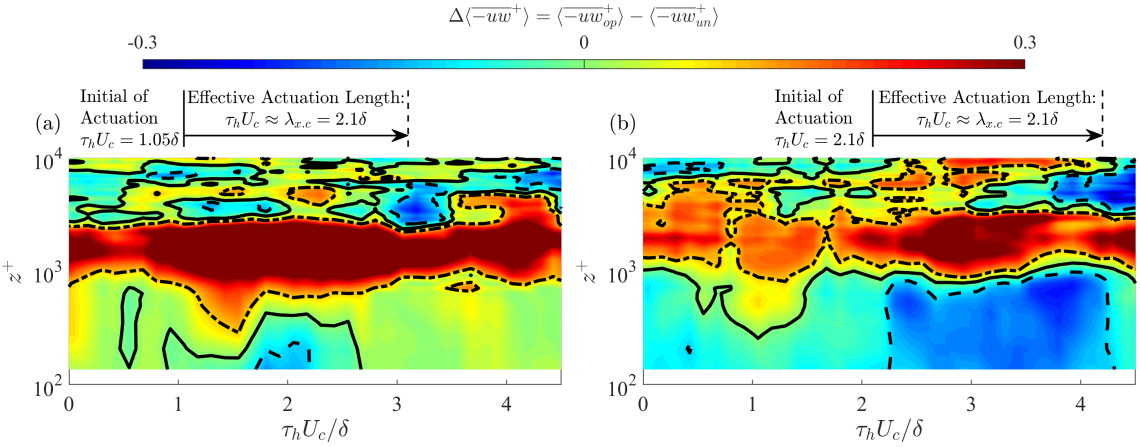

Figure 6.19: (a,b). Conditional Reynolds shear stress change due to flow control extracted from the phase averaged fields at Δx equivalent to 1.05δ and 2.1δ, respectively.

fields, which inevitably leads to an energy attenuation of the LSMs under the upper bound of the logarithmic region and within a range $2.5 < \tau_h U_c/\delta < 4$.

Regarding the drag reduction mechanism, the FIK-identity suggests that the Reynolds shear stress $\overline{-uw}^+$ in a turbulent boundary layer makes a substantial contribution to the wall shear stress production (Fukagata et al., 2002). The current PIV measurement allows the study of the covariance between u and w components. Figure 6.19(a,b) examines the variation of the conditional Reynolds shear stress $\Delta\langle\overline{-uw}^+\rangle = \langle\overline{-uw}^+_{op}\rangle - \langle\overline{-uw}^+_{un}\rangle$ owing to the opposing large-scale active flow control strategy on the planes of $\Delta x = 1.05\delta$ and 2.1δ, respectively. Here, $\langle\overline{-uw}^+_{un}\rangle$ and $\langle\overline{-uw}^+_{op}\rangle$ are the temporal conditional Reynolds shear stress transferred from the PIV phase-averaged velocity fields for both the uncontrolled and opposing controlled cases, respectively. These two planes are selected because the drag reduction at these two streamwise positions is available from previous hot-film studies. Negative values of $\Delta\langle\overline{-uw}^+\rangle$ (blue region) denotes that the opposing control decreases $\overline{-uw}^+$. As a result of the higher drag reduction at $\Delta x = 2.1\delta$, the Reynolds shear stress reduction within the majority of the log region (i.e $z^+ < 1000$) is much greater in this position, as shown in figure 6.19(b), than at $\Delta x = 1.05\delta$, as shown in figure 6.19(a). Note that, due to the selected Δx values, the start of the high-speed motions and the jet actuation in these temporal conditional averages are at $\tau_h U_c = 1.05\delta$ and 2.1δ respectively in figure 6.19(a,b). Clearly, in both fields, the maximized $\overline{-uw}^+$ attenuation initiates after the engagement of control and lasts for a streamwise extension approximately equivalent to the cut-off wavelength

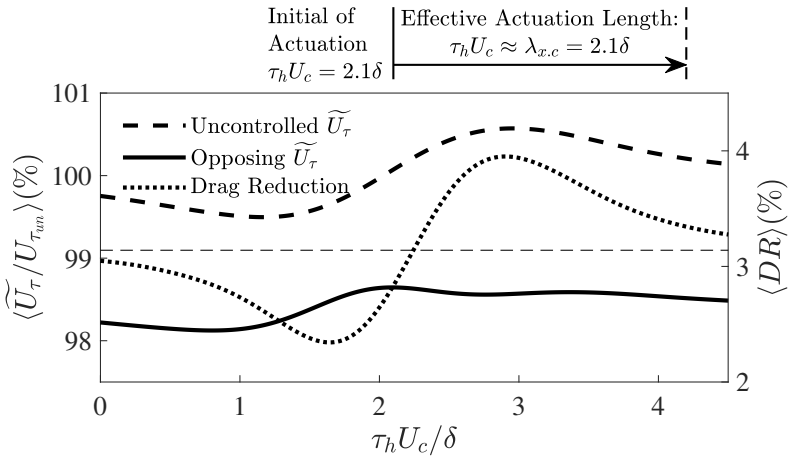

Figure 6.20: Total skin-friction velocity fluctuations $\widetilde{U_\tau}$ measured by the downstream measurement hot-film array conditioned on the positive zero-crossing of the upstream large-scale u_τ signals for uncontrolled (dashed line) and opposing (solid line) controlled cases. Black dot-dashed line is the computed conditional drag reduction $\langle DR \rangle$ curve.

$\lambda_{x.c} = 0.6\text{m} = 2.1\delta$, which indicates that the opposing control jet is able to locally reduce the Reynolds shear stress on the targeted high-speed structures. Such a localized control effect of the jet actuation is consistent with the observation on the VICA streamwise velocity fluctuations of the intermittent-controlled boundary layers in figure 5.19. In contrast, at the same x-position but around the upper bound of the log region where the shear layer between jet flow and cross-flow occurs, significant Reynolds shear stress enhancement is observed. This is because the jet flow intersects with the high-speed motions within this range and gives rise to a shear layer with enhanced small-scale energy shown from HWA measurement results in §5.2.

The conditional averaging analysis is also executed on the total friction velocity fluctuation signals $\widetilde{U_\tau}$ from the measurement hot-film array to relate the alteration of the Reynolds shear stress with the wall signatures of the LSMs. These downstream U_τ signals are conditionally averaged using identical detection criteria as the PIV measurement (positive zero-crossings in the large-scale signal attained from the detection array) and then normalized by the uncontrolled time-averaged frictional velocity for their percentage change. The dashed line $(--)$ in figure 6.20 shows that the fractional $\widetilde{U_\tau}$ within the canonical (uncontrolled) boundary layer exceeds 100% for $\tau_h > 2.1\delta/U_C$. Because the hot-film sensors are positioned at 2.1δ downstream, this indicates that the passage of large-scale structures with high streamwise velocity leaves a large-scale high shear-stress footprint on the wall via the superposition effect (Mathis et al., 2013). The corresponding

fractional change in $\widetilde{U}_\tau$ for the opposing controlled case is shown as by the solid line ($-$) in figure 6.20. The average value of this signal is approximately 98.4%, which reflects the mean drag reduction associated with the current flow control strategy. Moreover, based on the percentage variation of the $\widetilde{U}_\tau$ from the two cases, the conditional drag reduction $\langle DR \rangle$ based on the positive zero-crossing at the upstream detection array u_{τ_l} (black solid line) is computed. This effectively shows the conditionally averaged drag reduction during the passage of an actively controlled large-scale high-speed structure. As the wall-normal jets are designated to actuate during the high-speed events, the conditional drag reduction is amplified within this regime. Conversely, a deterioration of the control effect appears in the low-speed events, which occur prior to the high-speed event from $0 < \tau_h U_c / \delta < 2.1$ in figure 6.20. Evidently, the skin-friction reduction is closely correlated with the reduction in conditional Reynolds shear stress $\Delta\overline{-uw}^+$, which like the hot-film measured drag reduction *DR* (shown by the dot-dashed curve in figure 6.20) is maximized at $2.1\delta < \tau_h U_c < 4.2\delta$ (i.e. initiates at the beginning of jet activation and sustains for a length equivalent to the cut-off wavelength of the targeted LSMs). In summary, the current large-scale flow control strategy influences the wall-shear stress by attenuating the large-scale streamwise velocity fluctuations, which in turn is associated with a reduction of the Reynolds shear stress throughout the logarithmic region (and presumably extending into the near-wall). It should be noticed that the current study considers only the in-plane Reynolds shear stress. However, the jet flow also induces counter-rotating vortex pairs, which could also affect the out-of-plane $\overline{-vw}^+$ component.

6.5 Chapter Summary

The alteration of the LSMs via different active large-scale controls schemes (i.e. opposing and reinforcing control) is visualized by a streamwise/wall-normal multi-camera DE-PIV system and simultaneous hot-film anemometry. As a summary, this novel experiment provides the following insights on the spatial evolution of the control effect as well as the underpinning physics affecting the flow control outcomes.

- The mean velocity deficits resulting from different control schemes show that the wall-normal velocity components associated with the targeted structures have an impact on the jet penetration trajectory. The jet flow penetrates to a higher wall-normal position in the

reinforcing controlled boundary layer than that in the opposing controlled case. Conditional averaged results further demonstrate that the wall-normal penetration of the opposing jets into larger high-speed structures is less than that for smaller high-speed events, which suggests the potential of applying the opposing control with the jet actuation strength proportional to the structure size.

- The large-scale control effect is more persistent on the low-speed structures than that on the high-speed LSMs. While the turbulent energy change due to opposing control is maximized at 2δ downstream of the control with signs of recovery further downstream, the turbulent energy increase in the log region of the reinforcing controlled boundary layer continues to grow with streamwise evolution for the entire streamwise extension of the FOV.

- The streamwise evolution of the LSMs in both uncontrolled and controlled turbulent boundary layers are investigated by phase-average analysis. In the uncontrolled boundary layer, the forward-inclination angle of the LSMs decreases with increasing downstream convection. For the opposing control, the interaction between the jet flow and the targeted high-speed LSMs can be divided into four stages, namely the penetrating, lifting, mixing and recovering stage. The high-speed structures are optimally controlled within the mixing stage at approximately 1.5δ to 2δ downstream of the control. Further downstream, the perturbed LSMs recover to the canonical state mainly due to the difference between the streamwise convection velocity of the jet flow and the targeted structures. This suggests the feasibility of employing another array of wall-normal jets to re-actuate on the recovered high-speed LSMs to prolong the large-scale control effect for higher net energy saving.

- The spatial phased averaged results are transformed into the temporal domain, which shows that the conditionally averaged Reynolds shear stress $\langle\overline{-uw}^{+}\rangle$ is reduced in the log and near-wall regions $z^{+} < 1000$ but increased at the upper edge of the jet penetration ($z^{+} \approx 2000$). The reduction in $\langle\overline{-uw}^{+}\rangle$ corresponds closely with where the conditional skin-friction drag reduction acquired by the hot-film sensors is maximized. Since the flow estimation and jet actuation in the current study are both designed to control only the LSMs, the attenuated Reynolds shear stress at a smaller length-scale is mostly related to the modification on the LSMs. It is hypothesized that the active flow control reduces the large-scale turbulent energy

in the log region, which suppresses the near-wall Reynolds shear stress via the amplitude modulation effect. The subsequent reduction in skin friction drag should be considered a combination of these effects. To further validate this hypothesis, a simultaneous hot-film and cross-wire measurement with the active flow control is proposed as a future work in Chapter 7.

Chapter 7
Conclusion and Future Work

A series of simultaneous hot-film and hot-wire measurements with varying spatial separation are carried out to investigate the streamwise evolution of the LSMs in high Reynolds number turbulent boundary layers at $\mathrm{Re}_\tau = 14000$. Using the results, a systematic approach is proposed to estimate the large-scale structures using non-intrusive flow observers in real-time. The approach is applied to optimize the active large-scale flow control strategy, which utilizes a spanwise array of wall-normal jets as actuators to selectively manipulate the estimated LSMs. Different control schemes are employed to control various sections of the large-scale structures. Furthermore, simultaneous hot-film and hot-wire measurements, together with simultaneous hot-film and PIV measurements are conducted in the perturbed boundary layers to further elucidate (1). the influence of the actively controlled large-scale structures on the mean wall-shear-stress and the near-wall turbulence (2). the streamwise evolution of the large-scale flow control strategies in high Reynolds number turbulent boundary layers. The results not only suggest the potential of reducing frictional drag via controlling the LSMs but also provide recommendations for improving the efficacy of future control strategies. On a fundamental level, this research also improves our understanding of the role of LSMs in both canonical and perturbed turbulent boundary layers.

7.1 Evolution and Estimation of LSMs

From the simultaneous hot-wire and hot-film measurements in the uncontrolled boundary layers, it is observed that the correlation between the fluctuating streamwise velocity and friction velocity signals decays with increasing streamwise separation. The decomposition of the coherence spectrum between the u and u_τ signals supports the view that the large-scale coherent structures are

constructed from a hierarchy of self-similar eddies of different sizes. When tracking the streamwise evolution of a particular coherent motion, the self-similar eddies with shorter wavelengths tend to deteriorate over shorter distances as compared to the larger ones during the streamwise convection. Quantitatively, when tracking the coherent motions over a streamwise distance Δx, only the LSMs with $\lambda_x > \Delta x^{0.67}$ remain correlated. Convective velocities of the LSMs are computed from the temporal shift of the maximum correlation coefficient between the upstream hot-film and downstream hot-wire signals through Taylor's Frozen turbulence Hypothesis. Coherent structures with a longer streamwise length-scale λ_x convect with a higher convection velocity. This indicates the scale-dependence of the convective velocity of the LSMs, which are shown to match the mean streamwise velocity at their geometric center in the wall-normal direction. However, it is noticed that the increase in convection velocity is bounded for the VLSMs with $\lambda_x > 3\delta$. Such phenomenon is postulated to be related to the formation mechanism of the VLSMs which is speculated to be the streamwise alignment of the large-scale structures, and hence, the mean velocity at the geometric center of these very large streaks is capped.

While the traceable distance of the coherent structures informs the minimum wavelength of the estimable LSMs, the convective velocity also suggests the minimum sensor-actuator separation to accommodate the actuation delay. Putting these together, a systematic approach is proposed to optimize the active flow control configurations, which includes the design of a real-time filter to observe coherent structures and the selection of the optimized combination of the real-time filter cut-off wavelength and the sensor-actuator separations. The real-time low-pass filter is shaped via the inverse Fourier transform of the spectral transfer kernel (in the frequency domain) between u_τ acquired at the detection array and u acquired at the actuation array location. Further, a spanwise filter, which utilizes the spanwise information from the friction velocity field is employed, which complements the streamwise filter to extract the coherent information from the upstream detection array to the maximal extent. Compared with the conventional low-pass Gaussian filter, such a two-dimensional filter improves the accuracy of estimating the large-scale structures in the current active flow control strategy by approximately 5%. The optimized combination of the targeted structures and sensor-actuator separation is determined by equating the minimum streamwise distance to accommodate the real-time actuation delay and the maximum streamwise traveling distance of the coherent structures with varying streamwise wavelength. For example, controlling the

turbulent boundary layer with a friction Reynolds number Re = 14000 and a mechanical delay of 83ms, the optimal values of the targeted structural wavelength and sensor-actuator separation are 1.6δ and 1.7δ, respectively. Required modifications to the hardware are discussed later (in future work §7.3) that will permit targeting of shorter wavelengths.

7.2 Active Large-scale Flow Control

7.2.1 Large-scale Influence in the Controlled Boundary Layers

Three different large-scale control schemes, namely opposing, reinforcing, and desynchronized control, are examined in the current project. These control schemes utilize wall-normal jets to actively perturb high-speed, low-speed, and random LSMs estimated in real-time from the friction velocity fields measured by a spanwise array of hot-film probes located 1.6δ upstream of the actuation array. A further spanwise array of hot-film sensors placed at $0.8\delta - 4.3\delta$ downstream of the actuation array reveals that the local skin-friction coefficient is reduced for all three schemes. While the spanwise drag reduction curve is spanwise invariant at $|y| < 0.21\delta$ (where $y = 0$ is the center of the actuation array), an increase in drag reduction is observed on the edges of the control panel (i.e. $|y| = 0.22\delta$) due to the edge effects caused by the jet induced secondary flow. Maximum drag reduction of 3.4% occurs at 1.7δ downstream of the actuation array for the opposing controlled case. This value drops to 2.1% and 1.2% for the desynchronized and reinforcing control schemes, respectively. The resulting drag reduction at this streamwise position is linearly proportional to the ratio of high-speed LSMs (with $\lambda_x > 1.6\delta$) that have been successfully manipulated by the jets (defined as control accuracy α in equation 4.11). With 50% control accuracy, the desynchronized control still achieves 2.1% drag reduction, which is assumed to result from the simple injection of low momentum fluid into the near-wall region. By extrapolating the linear fit, it is observed that the limited degree of drag reduction of the optimal opposing case is not greatly restricted by the control accuracy. Even if we successfully achieved $\alpha = 100\%$ (perfect estimation and control accuracy), only marginally improved drag reduction of approximately 4.5% would be attained.

Simultaneously, hot-wire anemometry is applied to investigate the manipulation of LSMs under different control schemes. The streamwise large-scale ($\lambda_x > 1.6\delta$) energy in the perturbed

boundary layer reduces with an increased control accuracy. By decelerating the high-speed events, opposing control reduces the energy of the conditional large-scale structure and hence attenuates large-scale streamwise turbulent energy by over 35% at the geometric center of the log region ($z^+ = \sqrt{15\mathrm{Re}_\tau}$). Conversely, reinforcing control further strengthens the low-velocity structures and energizes the large-scale turbulence by 20% in the log region. For all tested control schemes, the spatially averaged large-scale energy below the jet penetration height ($z < z_p$) with $\lambda_x \leq 1.6\delta$ is computed to be linearly related to the drag reduction. This relationship suggests that the large-scale energy in the log region with $\lambda_x \leq 1.6\delta$ contributes approximately 5.6% of the mean wall-shear-stress in turbulent boundary layers with $\mathrm{Re}_\tau = 14000$. The large-scale energy is barely modified by the desynchronized control which attains a drag reduction of 2.1%. This is the baseline drag reduction due to the low momentum fluid that is injected by the control jets, in the absence of any coherent large-scale control strategy.

The near-wall small-scale turbulence adjusts to the actively controlled large-scale variations of local skin friction velocity for all examined control strategies for $\Delta x_m > 1.7\delta$. This is in agreement with the Quasi-Steady Quasi-Homogeneous (QSQH) hypothesis of Zhang and Chernyshenko (2016). Via artificially damping out the large-scale energy in the log region, the near-wall small-scale fluctuating streamwise velocity predicted from IOI model experiences a 4% reduction in their variance. This result agrees with the 5% reduction estimated from the linear extrapolation of the experiment outcomes, which indicates the amplitude modulation effect remains valid in the perturbed boundary layer. By comparing the LSMs in both uncontrolled and controlled boundary layers, the variation of the conditional fluctuating large-scale friction velocity is well correlated with that of the conditional streamwise velocity, which infers that the superposition effect is also applicable in the perturbed boundary layers.

7.2.2 Streamwise Evolution of Controlled Structures

Hot-wire anemometry measurements are made at several streamwise locations between 0.8δ to 4.2δ downstream of the actuation array to examine the streamwise evolution of the large-scale flow control effect. The mean streamwise velocity deficit in the opposing controlled boundary layer decays and spreads to a higher wall-normal position along the x-direction. The streamwise large-scale energy reduction is maximized at $\Delta x_m = 1.7\delta$, where the maximum local dag reduction

is attained. Further downstream, the control effect on the large-scale energy decays with the local drag reduction. At $\Delta x_m = 4.2\delta$ (farthest measurement station downstream of the actuation array), the large-scale energy reduction and drag reduction decreases to 5% and 2.2%, respectively. These results on the evolution of the control effect are confirmed by the streamwise/wall-normal plane PIV measurements with a finer spatial resolution. Defining the jet penetration trajectory as the wall-normal position at which the mean streamwise velocity in the controlled boundary layer recovers to 99% of the canonical velocity profile, the PIV data shows a jet penetration trajectory that follows the exponential law for both cases. However, the jet trajectory of the reinforcing controlled boundary layer is slightly higher than the opposing controlled case. This difference is attributed to the different signs of the wall-normal velocity component associated with the high- and low-speed large-scale events for the opposing and reinforcing control cases (which are either counteracted or reinforced by the positive wall-normal momentum of the jet flow). Immediately adjacent to the actuation array ($\Delta x_a < 0.4\delta$), the jet activation significantly raises the streamwise turbulent energy in the controlled boundary layer. Further downstream, for opposing control, energy reduction occurs in the log region due to the large-scale manipulation, while an energy increase is observed at the upper boundary of the jet penetration trajectory because of the shear layer between the jet and crossflow. Conversely, reinforcing control increases the turbulent energy in both regions. This strengthened turbulent energy for the reinforcing control case continues to grow in magnitude with increasing streamwise propagation through the PIV field of view (i.e. $0 < \Delta x_m < 2.5\delta$), which indicates that the control effect on the low-speed structures (for the reinforcing case) is more persistent than control of the high-speed events (opposing control). Due to the positive wall-normal momentum of the jet actuation, both opposing and reinforcing control cases increase the mean wall-normal velocity fields for $\Delta x < 0.5\delta$. The wall-normal turbulent energy is energized along the upper bound of the jet penetration trajectory for both control cases but the effects last over 2δ downstream of the actuation.

7.2.3 Interaction between Jet Flow and Targeted LSMs

The crossflow and jet flow are separately seeded in the PIV measurements, which guarantees that the PIV snapshots are capable of visualizing the interaction between the jet actuation and the targeted LSMs. Phase averaged analysis is applied via categorizing the time difference between the

laser illumination and its preceding positive zero-crossing large-scale friction velocity fluctuation detected by the upstream detection array (τ_h and τ_l). The phase averaged velocity fields in the opposing controlled boundary layer show that the interaction between the jet flow and the high-speed large-scale structures could be described in four stages, which include the initial penetration, lifting, mixing, and recovering stages. The large-scale energy reduction is best mitigated in the mixing stage, while the maximum effect on the momentum deficit occurs in the lifting stage. Based on the streamwise length of the positive wall-normal velocity imprints in the phased averaged results, the local convective velocity of the jet flow increases during the convection. However, the maximum convective velocity is approximately only 86% of the convective velocity of the LSMs. This mismatched convective velocity between the two leads to the recovery of the control effect in the opposing controlled boundary layer, as the targeted structures eventually overtake the injected jet flow. As the high-speed structures convect faster than the low-speed events, the mismatched convective velocity offers a further explanation for why the control will be more persistent in the reinforcing controlled boundary layers.

Temporal conditional averaged structures are attained via cascading the phase averaged velocity fields in the order of laser delay (τ_h). The resulting conditional structures agree with the conditional averaged velocity fields obtained from the hot-wire measurements. Furthermore, it is observed that the phased averaged Reynolds shear stress variation due to the opposing control correlates well with the conditional skin-friction drag reduction. The drag reduction is shown to be maximized when the Reynolds shear stress is best suppressed by the jet flow. Further, the control effect on the Reynolds shear stress is well-aligned (spatially and temporally) with the locations where the jet has modified the LSMs. Overall, the large-scale turbulent energy reduction influences the near-wall small-scale turbulent intensity via a reduced amplitude modulation effect, which decreases the local Reynolds shear stress and skin-friction drag. The large-scale frictional velocity footprints superimposed from the modified LSMs also lead to the alleviation of a high shear-stress region in the opposing controlled boundary layers (superposition effect) which also reduces drag. These factors combined explain the drag reduction mechanism of the present control strategy.

7.2.4 Strategies and Recommendations to Improve Control Efficacy

In order to seek the strategy to improve the overall control efficacy (i.e. net energy reduction), intermittent and impulsive (opposing) control strategies are employed to perturb certain sections of the high-speed LSMs. By comparing the VICA total velocity fluctuation in the uncontrolled and intermittent (opposing) controlled boundary layers, it is revealed that the control effect of the jet flow is uniformly distributed and localized at where the jet injection is activated. The drag reduction and turbulent kinetic energy reduction resulting from the impulsive control increases with the total jet engagement time during the measurement. However, the control efficacy is enhanced for the impulsive control with a 17% firing ratio. This scheme saves two-thirds of the input energy (actuation time is only 1/3 of the original scheme) yet still attains a 2.2% drag reduction. Hence, the resulting control efficacy, defined as the ratio between *DR* and input energy, doubles that of the original opposing control strategy.

In order to seek further improvements, the detected structures have been binned into three groups with respect to their mean structural width. The conditional averaged medium-width structures ($0.18 < W/\delta < 0.28$) are most effectively targeted by the current scheme, exhibiting the highest reduction in turbulent energy. In contrast, the jet actuation appears to be too strong for the thin structures ($W/\delta < 0.18$) and too weak for the widest events ($0.28 < W/\delta$) structures. We also see signs that the thinnest structures do not remain coherent over the distance separating the detection and actuation arrays. Together, these results suggest two possible refinements of the current control strategy: (i) a proportional jet exit velocity based on the structural instantaneous width might be a way of ensuring consistent jet penetration even where stronger events are targeted and (ii) a strategy that excludes very thin high-speed structures from actuation should yield a higher control accuracy (and control efficacy).

7.3 Future Work

The present project addresses an approach to optimize the real-time active flow control configurations and estimate the potential mean wall-shear-stress reduction via manipulating the large-scale structures in high Reynolds number turbulent boundary layers. The connection between the large-scale structures in the log region and the near-wall turbulence and the streamwise evolution of the

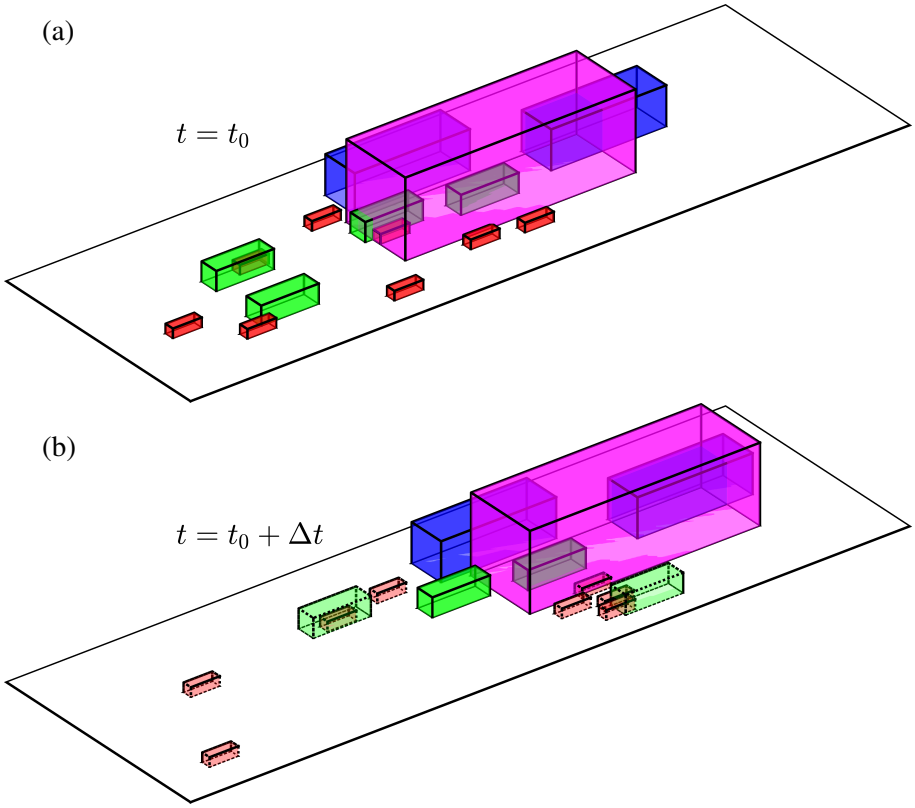

Figure 7.1: A three dimensional schematic based on AEH showing the spatial distribution of the coherent structures with different length scales in the turbulent boundary layer at (a) a reference time instance t_0, and (b) a certain time interval after the reference time $t_0 + \Delta t$.

control effect is investigated. This work leaves some unanswered questions and possible improvements for future academic research, which include both extending the physical understanding of the coherent structures in the turbulent boundary layers and exploring alternative approaches to enhance the control efficacy of the existing control strategy.

Further advancing the understanding of the evolution of coherent structures: The study of the streamwise evolution of the coherent motions through simultaneous hot-film and hot-wire measurements in Chapter 4 is specifically designated to optimize the present large-scale active control strategy. The traceable distance (i.e. lifetime) and convection velocity of the LSMs are investigated to determine the sensor-actuator separation and the low-pass filter cut-off wavelength of the real-time control at a fixed Reynolds number $\mathrm{Re}_\tau \approx 14000$. Looking beyond active control, these results could also provide valuable information for a temporally evolving model of turbulent

motions in wall-bounded turbulence. For example, the AEH indicates that the coherent structures are randomly distributed in the spatial domain of the turbulent boundary layer at a given time instance t_0 as shown in figure 7.1(a). The rectangular cubes represent the LSMs with different wavelengths, which, referring to AEH, is inversely proportional to their population density. With the knowledge on the convective velocity and the traceable distance (i.e. lifetime) of the LSMs, one could evaluate the spatial flow field at a certain interval after the time instance $t = t_0 + \Delta t$ in figure 7.1(b) to attain a time-resolved spatial velocity modeling of the turbulent boundary layer. Such an approach would require a more comprehensive study on the streamwise evolution of the coherent structures at a wider range of Reynolds numbers and length-scales. Furthermore, this study has shown that the convection velocity of the LSMs increases with their geometric size only up to the upper limit $\lambda_x < 3\delta$. Structures beyond this length-scale (VLSMs) seem to convect at a fixed velocity, regardless of length. It is suggested here that this may be due to the fact that VLSMs are formed from agglomerations of LSMs (and hence the convection velocity of the VLSMs is capped at that of the LSMs). By further extending the streamwise separation between the probes used in this study, such that the largest LSMs are incoherent across the probe separation but the VLSMs are still traceable by both probes, one would be able to better investigate this behaviour, and also to answer questions regarding the lifetimes of VLSMs, which is currently unknown.

Improvements to real-time wall-based estimation: Though the current flow estimation system utilizes a spanwise array of nine hot-film sensors, the spectral coherence results suggest that the entire observation array provides limited spanwise information of the targeted coherent structures due to the selected spanwise offsets between the hot-films ($\Delta y = 0.07\delta$). As a consequence, the wavelength of the estimable structures of the current control architecture is limited to a relatively large value under equation 4.9, which leads to a larger **Component II** in equation 4.8 and consequently a larger sensor-actuator separation Δx_a to accommodate the associated computational delay. In order to control the structures with smaller wavelengths and influence a greater amount of turbulent energy, a plausible improvement of the existing estimation configuration is to employ a finer spanwise resolution of the wall-based observers. In turn, one could ideally discard the streamwise filter leading to reductions in the time delay due to the real-time filtering (i.e. **Component II** in equation 4.8). Sequentially, the sensor-actuator separation and the cut-off wavelength of the targeted LSMs can be significantly reduced. In addition, the method of spectral coherence

is a linear flow estimation approach that neglects the non-linear interactions between the structures. Therefore, the inherent error of the linear estimation can also contribute to the limitation on control accuracy. For future flow estimation investigations, attempts could be made to employ non-linear flow prediction methods for estimation purposes, such as the recent advance in predicting wall-bounded turbulence via recurrent and convolutional neural networks based on wall-based quantities Guastoni et al. (2020).

‘

Investigating scale and Reynolds dependence of the drag reduction contribution: The drag reduction contribution estimated in this dissertation is specific for the large-scale structures with $\lambda_x > 1.6\delta$ in wall-bounded boundary layers with $\mathrm{Re}_\tau = 14000$. Such values are selected to optimize the control accuracy of the current control strategy. Extending this picture, one could apply the same methodology with a real-time filter with a shorter cut-off wavelength (following the previous point) to evaluate the drag reduction contributed by the intermediate structures, which are suggested to retain a greater influence on skin-friction drag (deGiovanetti et al., 2016). At the same time, the turbulent kinetic energy contributed by the LSMs increases with Reynolds number, which implies the large-scale energy generated drag reduction might also possess a positive Reynolds dependence. However, for the current facility, higher Reynolds numbers would imply higher freestream velocities meaning that the LSMs travel with a higher convection velocity, which would require a larger sensor-actuator separation due to a larger **Component I** in equation 4.8. As a consequence, the shorter structures would no longer be coherent between the detection and actuation arrays. To resolve the problem, instead of increasing the free-stream velocity to examine the Reynolds dependency, one can decrease the Reynolds number so that the convective velocity of the LSMs decelerates. In these cases, a smaller sensor-actuator separation (due to smaller **Component I** in equation 4.8) is sufficient to accommodate the actuation delay τ_a, which makes the structures with shorter wavelengths a suitable control target. Consequently, the active control with a real-time filter with a shorter cut-off wavelength could be implemented to investigate the scale dependency of the real-time flow control outcomes, but such experiments would need to be conducted at lower Reynolds number (and hence the Reynolds number effect at matched target wavelength $lambda_x$ should first be investigated).

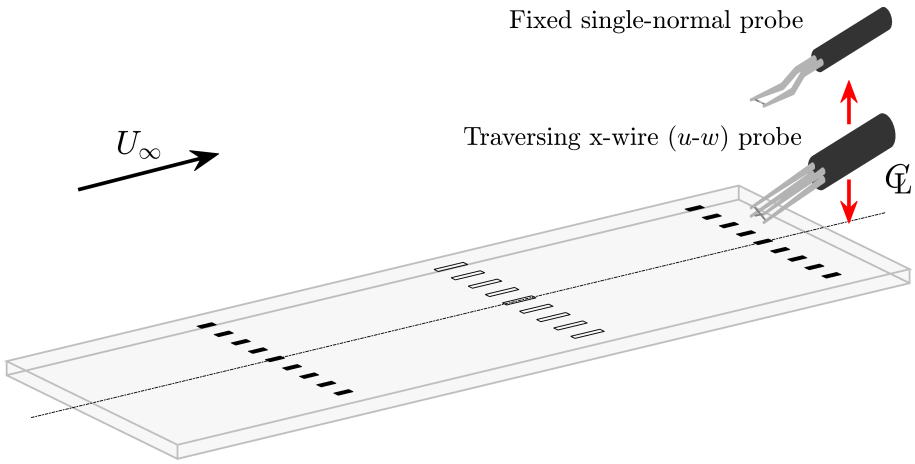
Fixed single-normal probe
Traversing x-wire (u-w) probe
U_∞
$\mathbb{C}\!\!\!

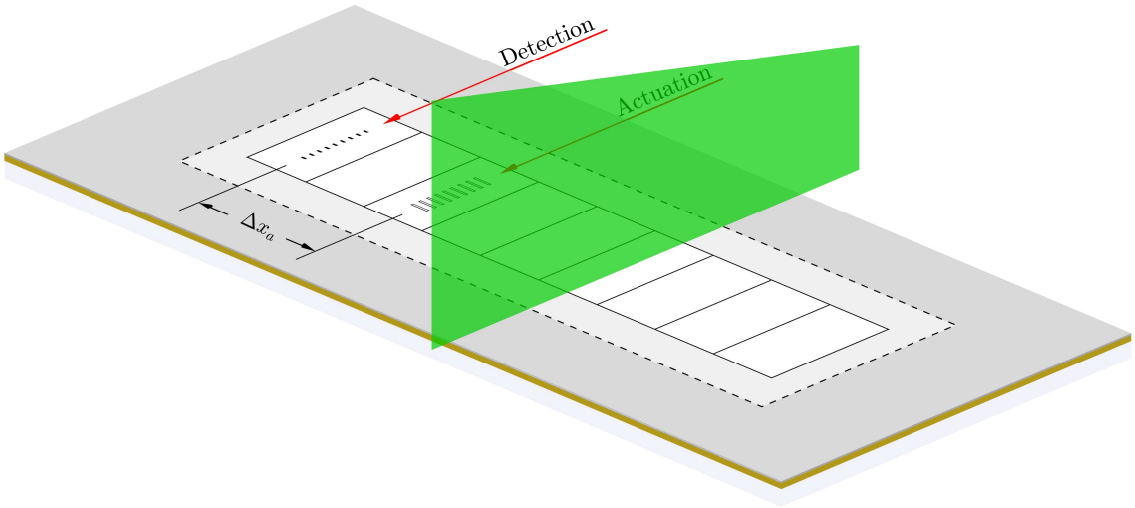

Figure 7.3: A schematic of stereo-PIV measurement set-up to investigate the effect of the secondary flow induced by the actuaotrs

the large-scale turbulent energy variation. At the same time, the conditional *DR* in the controlled boundary layers is closely correlated with the conditional Reynolds shear stress change from PIV measurements, which agrees with the FIK identity (Fukagata et al., 2002). Following this observation, the question remains: how the large-scale fluctuation in the log-region affects the Reynolds shear stress. Since the streamwise extension of the FOV in PIV measurements is only $1.8\lambda_{x.c}$, the fluctuating velocity signals with a wavelength larger than the cut-off frequency are undetectable spectrally. In addition, the spatial resolution of the velocity vector fields is $\sim \mathscr{O}[100]$ wall units so that the existing PIV dataset is insufficient for the nominated problems. A suggested experiment to approach this question is shown in figure 7.2, which consists of a single-normal hot-wire probe fixed in the geometric center of the logarithmic region to measure the large-scale velocity fluctuation simultaneously with a cross-wire hot-wire probe that can be traversed in the wall-normal direction to acquire the Reynolds shear stress in the perturbed boundary layer. Eventually, one could investigate the co-spectra between the streamwise and wall-normal velocity fluctuations to better understand which scale of the Reynolds shear stress is best suppressed by the large-scale control. This information could help to further elucidate the mechanism by which the large-scale control attains drag reduction at practical Reynolds numbers.

Understand the effect of the jet actuation on the large-scale structural topology: The jet flow

induces counter-rotating quasi-streamwise vortex pairs which lead to an increased drag reduction on the edge of the control panel. The counter-rotating secondary flows increase the drag reduction where there is common-flow-down and reduce the drag reduction where there is common-flow-up. In the current study, for the cases where the spanwise separation between the jets exceeds 0.14δ, this phenomenon can be approximated by the linear superposition of the drag reduction curve obtained by a single jet. However, if a spanwise separation is smaller than 0.07δ, the superimposed model underestimates the experimental results since the linear superposition fails to include the non-linear dynamics between the strongly interacting neighbouring jets which seems to lead to increased drag reduction (above the predicted by the linear model). A further investigation of this effect is warranted and could lead to a better understanding of how the secondary flow induced by the jet flow leads to a higher frictional drag reduction which, in turn, may suggest the ideal separation between the actuators or even an improved actuator design. It is suggested that such a study could be conducted via a stereo-PIV measurement on the spanwise/wall-normal plane downstream of the actuation as shown in figure 7.3. By acquiring all three velocity components simultaneously, the induced secondary flow and the associated Reynolds shear stress could be carefully examined. The acquisition of all three velocity components on spanwise/wall-normal planes could provide further opportunity to investigate the modification of the streamwise vorticity and spanwise/wall-normal Reynolds shear stress induced by the jet flow.

Modify the existing control algorithm: Although the current work suggests that the contribution of the large-scale structures with $\lambda_x > 1.6\delta$ on the mean wall-shear-stress is bounded by 5.6%, recognizable skin-friction drag reduction (over 2%) is able to reach over 4.2δ (60000 wall units) downstream of the actuation in the opposing controlled boundary layers. Hence, the modification of the existing large-scale flow control algorithm should focus on two aspects. (i) Prolonging the control evolution, and (ii) increasing the control efficacy. As aforementioned, the maximum skin-friction drag reduction and large-scale energy attenuation are both located at 2δ downstream of the actuation and the control effect decays beyond this point. Therefore, it would be advisable to employ an additional array of actuators further downstream of the existing actuators to prolong the control effect on the perturbed LSMs further downstream as shown in figure 7.4(a). Since a certain level of control effectiveness due to the initial perturbation will remain at the second actuation array, the re-actuation could be operating at a lower strength. The ideal operation level and

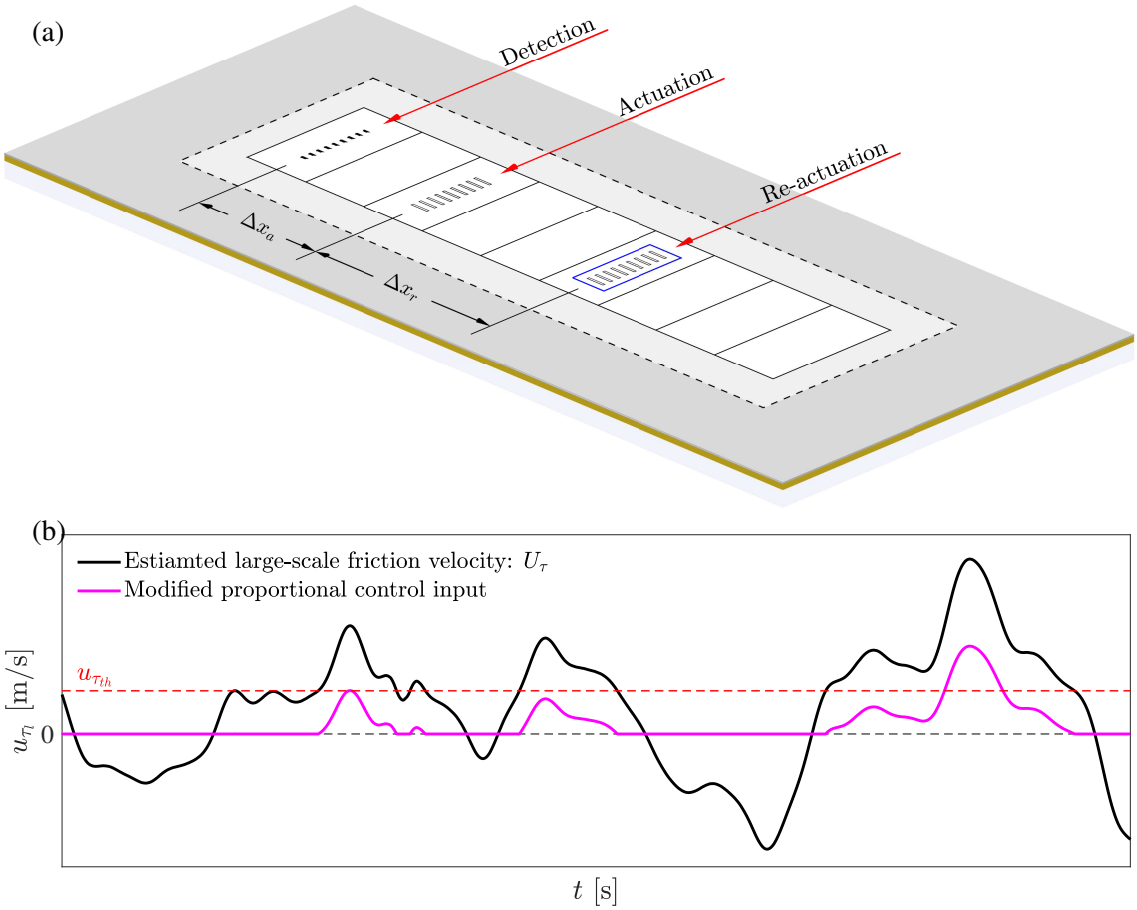

Figure 7.4: (a) Schematic for a modified large-scale flow control strategy employing an additional re-actuation array. (b) A clip of large-scale friction velocity fluctuation estimated from detection array (−) and the corresponding control input signal under modified proportional opposing control strategy.

separation between the actuators should be carefully designed to optimize the global net energy saving. On the other hand, as the maximum outcome by eliminating large-scale turbulent energy is restricted, the control algorithm should aim to distribute the energy input (i.e. the jet actuation) onto the structures which are most effectively manipulated to enlarge the net energy saving. The conditional streamwise velocity fluctuations of the LSMs with different widths show that the narrowest (weakest) high-speed structures are naturally transformed into low-speed events during downstream convection suggesting that they are not effectively controlled in the current control strategy. In addition, the actuation on the widest (strongest) structures is not strong enough to entirely mitigate their associated energy. Thus, a recommended control algorithm should activate

the jets proportionally to the estimated large-scale velocity fluctuation, but only on the instance that u_{τ_l} is greater than a certain threshold value $u_{\tau_{th}}$ as shown in figure 7.4(b)).

Though the realized drag reduction from the control of large-scale structures to date is limited, this study has provided a clear path forward for future investigations. The above recommendations will hopefully provide a useful starting point for continued study, with the goal of retaining the proven practical advantages of the large-scale control (realizable sensor/actuator requirements) but with higher attainable drag reductions.

Bibliography

M.R. Abbassi, W.J. Baars, N. Hutchins, and I. Marusic. Skin-friction drag reduction in a high-Reynolds-number turbulent boundary layer via real-time control of large-scale structures. *Int. J. Heat Fluid Flow*, 67:30–41, 2017.

H. Abe, H. Kawamura, and H. Choi. Very large-scale structures and their effects on the wall shear-stress fluctuations in a turbulent channel flow up to re τ= 640. *J. Fluids Eng.*, 126(5):835–843, 2004.

R.J. Adrian and P. Moin. Stochastic estimation of organized turbulent structure: homogeneous shear flow. *J. Fluid Mech.*, 190:531–559, 1988.

R.J. Adrian, C.D. Meinhart, and C.D. Tomkins. Vortex organization in the outer region of the turbulent boundary layer. *J. Fluid Mech.*, 422:1–54, 2000.

L. Agostini and M. Leschziner. The impact of footprints of large-scale outer structures on the near-wall layer in the presence of drag-reducing spanwise wall motion. *Flow Turbul. Combust.*, 100(4):1037–1061, 2018.

L. Agostini and M. Leschziner. The connection between the spectrum of turbulent scales and the skin-friction statistics in channel flow at $\mathrm{Re}_\tau \approx 1000$. *J. Fluid Mech.*, 871:22–51, 2019.

L. Agostini and M.A. Leschziner. On the influence of outer large-scale structures on near-wall turbulence in channel flow. *Phys. Fluids*, 26(7):075107, 2014.

P.H. Alfredsson, A.V. Johansson, J.H. Haritonidis, and H. Eckelmann. The fluctuating wall-shear stress and the velocity field in the viscous sublayer. *Phys. Fluids*, 31(5):1026–1033, 1988.

J.B. Anders. Outer-layer manipulators for turbulent drag reduction. *Viscous Drag Reduction in Boundary Layers*, 123:263–284, 1990.

R.A. Antonia, L. Fulachier, L.V. Krishnamoorthy, T. Benabid, and F. Anselmet. Influence of wall suction on the organized motion in a turbulent boundary layer. *J. Fluid Mech.*, 190:217–240, 1988.

W.J. Baars and I. Marusic. Data-driven decomposition of the streamwise turbulence kinetic energy in boundary layers. Part 1. Energy spectra. *J. Fluid Mech.*, 882, 2020.

W.J. Baars, K.M. Talluru, B.J. Bishop, N. Hutchins, and I. Marusic. Spanwise inclination and meandering of large-scale structures in a high-Reynolds-number turbulent boundary layer. In *Proc. 19th Australasian Fluid Mech. Conference*, 2014.

W.J. Baars, K.M. Talluru, N. Hutchins, and I. Marusic. Wavelet analysis of wall turbulence to study large-scale modulation of small scales. *Exp. Fluids*, 56(10):188, 2015.

W.J. Baars, N. Hutchins, and I. Marusic. Spectral stochastic estimation of high-Reynolds-number wall-bounded turbulence for a refined inner-outer interaction model. *Phys. Rev. Fluids*, 1(5): 054406, 2016.

W.J. Baars, N. Hutchins, and I Marusic. Reynolds number trend of hierarchies and scale interactions in turbulent boundary layers. *Philos. Trans. R. Soc. A*, 375(2089):20160077, 2017a.

W.J. Baars, N. Hutchins, and I. Marusic. Self-similarity of wall-attached turbulence in boundary layers. *J. Fluid Mech.*, 823, 2017b.

R. Baidya, J. Philip, N. Hutchins, J.P. Monty, and I. Marusic. Distance from the wall scaling of turbulent motions in wall-bounded flows. *Phys. Fluids*, 29(2):020712, 2017.

R. Baidya, W.J. Baars, S. Zimmerman, M. Samie, R.J. Hearst, E. Dogan, L. Mascotelli, X. Zheng, G. Bellani, A. Talamelli, B. Ganapathisubramani, N. Hutchins, I. Marusic, J. Klewicki, and J.P. Monty. Simultaneous skin friction and velocity measurements in high Reynolds number pipe and boundary layer flows. *J. Fluid Mech.*, 871:377–400, 2019.

P.R. Bandyopadhyay and A. Hussain. The coupling between scales in shear flows. *Phys. Fluids*, 27(9):2221–2228, 1984.

A. Baron and M. Quadrio. Turbulent drag reduction by spanwise wall oscillations. *Applied Scientific Research*, 55(4):311–326, 1995.

R.F. Blackwelder and H. Eckelmann. Streamwise vortices associated with the bursting phenomenon. *J. Fluid Mech.*, 94(3):577–594, 1979.

R.F. Blackwelder and R.E. Kaplan. On the wall structure of the turbulent boundary layer. *J. Fluid Mech.*, 76(1):89–112, 1976.

R.F. Blackwelder and L.S. Kovasznay. Time scales and correlations in a turbulent boundary layer. *J. Fluid Mech.*, 15(9):1545–1554, 1972.

J.E. Broadwell and R.E. Breidenthal. Structure and mixing of a transverse jet in incompressible flow. *J. Fluid Mech.*, 148:405–412, 1984.

G.L. Brown and A.S. Thomas. Large structure in a turbulent boundary layer. *Phys. Fluids*, 20 (10):S243–S252, 1977.

S.L. Brunton and B.R. Noack. Closed-loop turbulence control: Progress and challenges. *Appl. Mech. Rev.*, 67(5), 2015.

K.J. Bullock, R.E. Cooper, and F.H. Abernathy. Structural similarity in radial correlations and spectra of longitudinal velocity fluctuations in pipe flow. *J. Fluid Mech.*, 88(3):585–608, 1978.

J. Canton, R. Örlü, C. Chin, and P. Schlatter. Reynolds number dependence of large-scale friction control in turbulent channel flow. *Phys. Rev. Fluids*, 1(8):081501, 2016.

B.J. Cantwell. Organized motion in turbulent flow. *Annu. Rev. Fluid Mech*, 13(1):457–515, 1981.

H.A. Carlson and J.L. Lumley. Active control in the turbulent wall layer of a minimal flow unit. *J. Fluid Mech.*, 329:341–371, 1996.

L.N. Cattafesta III and M. Sheplak. Actuators for active flow control. *Annu. Rev. Fluid Mech*, 43: 247–272, 2011.

D. Chandran, R. Baidya, J.P. Monty, and I. Marusic. Two-dimensional energy spectra in high-Reynolds-number turbulent boundary layers. *J. Fluid Mech.*, 826, 2017.

Y. Chang, S.S. Collis, and S. Ramakrishnan. Viscous effects in control of near-wall turbulence. *Phys. Fluids*, 14(11):4069–4080, 2002.

S.I. Chernyshenko, I. Marusic, and R. Mathis. Quasi-steady description of modulation effects in wall turbulence. *arXiv preprint arXiv:1203.3714*, 2012.

C. Chin, R. Örlü, J.P. Monty, N. Hutchins, A. Ooi, and P. Schlatter. Simulation of a large-eddy-break-up device LEBU in a moderate Reynolds number turbulent boundary layer. *Flow Turbul. Combust.*, 98(2):445–460, 2017.

C. Chin, R. Vinuesa, R. Örlü, J. Cardesa, A. Noorani, P. Schlatter, and M. Chong. Flow topology of rare back flow events and critical points in turbulent channels and toroidal pipes. *J. Phys.: Conf.*, 2018.

H. Choi, P. Moin, and J. Kim. Active turbulence control for drag reduction in wall-bounded flows. *J. Fluid Mech.*, 262:75–110, 1994.

H. Choi, W.P Jeon, and J. Kim. Control of flow over a bluff body. *Annu. Rev. Fluid Mech.*, 40: 113–139, 2008.

K.S. Choi and B.R. Clayton. The mechanism of turbulent drag reduction with wall oscillation. *Int. J. Heat Fluid Flow*, 22(1):1–9, 2001.

K.S. Choi and M. Graham. Drag reduction of turbulent pipe flows by circular-wall oscillation. *Phys. Fluids*, 10(1):7–9, 1998.

K.S. Choi, J.R. DeBisschop, and B.R. Clayton. Turbulent boundary-layer control by means of spanwise-wall oscillation. *AIAA J.*, 36(7):1157–1163, 1998.

K.S. Choi, T. Jukes, and R. Whalley. Turbulent boundary-layer control with plasma actuators. *Philos. Trans. R. Soc. A*, 369(1940):1443–1458, 2011a.

K.S. Choi, T. Jukes, and R. Whalley. Turbulent boundary-layer control with plasma actuators. *Philos. Trans. R. Soc. A*, 369(1940):1443–1458, 2011b.

K.T. Christensen and R.J. Adrian. Statistical evidence of hairpin vortex packets in wall turbulence. *J. Fluid Mech.*, 431:433, 2001.

E.R. Corino and R.S. Brodkey. A visual study of turbulent shear flow. *J. Fluid Mech*, 37(1):30, 1969.

T.C. Corke and F.O. Thomas. Active and passive turbulent boundary-layer drag reduction. *AIAA J.*, 56(10):3835–3847, 2018.

T.C. Corke, Y. Guezennec, and H.M. Nagib. Modification in drag of turbulent boundary layers resulting from manipulation of large-scale structures. 1981.

T.C. Corke, H.M. Nagib, and Y.G. Guezennec. A new view on origin, role and manipulation of large scales in turbulent boundary layers. 1982.

T.C. Corke, C.L. Enloe, and S.P. Wilkinson. Dielectric barrier discharge plasma actuators for flow control. *Annu. Rev. Fluid Mech*, 42:505–529, 2010.

S. Deck, N. Renard, R. Laraufie, and P. Weiss. Large-scale contribution to mean wall shear stress in high-Reynolds-number flat-plate boundary layers up to $\mathrm{Re}_\theta < 13650$. *J. Fluid Mech.*, 743: 202–248, 2014.

M. deGiovanetti, Y. Hwang, and H. Choi. Skin-friction generation by attached eddies in turbulent channel flow. *J. Fluid Mech.*, 808:511–538, 2016.

J.C. del Álamo and J. Jiménez. Estimation of turbulent convection velocities and corrections to Taylor's approximation. *J. Fluid Mech.*, 640:5–26, 2009.

J.C. Del Álamo, J. Jimenez, P. Zandonade, and R. Moser. Self-similar vortex clusters in the turbulent logarithmic region. *J. Fluid Mech.*, 561:329, 2006.

J.C. Del Álamo and J. Jiménez. Spectra of the very large anisotropic scales in turbulent channels. *Phys. Fluids*, 15(6):L41–L44, 2003.

J.C. Del Álamo and J. Jimenez. Linear energy amplification in turbulent channels. *J. Fluid Mech.*, 559:205–213, 2006.

R. Deshpande, J.P. Monty, and I. Marusic. Streamwise inclination angle of large wall-attached structures in turbulent boundary layers. *J. Fluid Mech.*, 877, 2019.

C.M. deSilva, E.P. Gnanamanickam, C. Atkinson, N.A. Buchmann, N. Hutchins, J. Soria, and I. Marusic. High spatial range velocity measurements in a high Reynolds number turbulent boundary layer. *Phys. Fluids*, 26(2):025117, 2014.

C.M. deSilva, K. Kevin, R. Baidya, N. Hutchins, and I. Marusic. Large coherence of spanwise velocity in turbulent boundary layers. *J. Fluid Mech.*, 847:161–185, 2018.

C.M. deSilva, D. Chandran, R. Baidya, N. Hutchins, and I. Marusic. Periodicity of large-scale coherence in turbulent boundary layers. *Int. J. Heat Fluid Flow*, 83:108575, 2020.

M.R. Dhanak and C. Si. On reduction of turbulent wall friction through spanwise wall oscillations. *J. Fluid Mech.*, 383:175–195, 1999.

Y. Du and G.E. Karniadakis. Suppressing wall turbulence by means of a transverse traveling wave. *Science*, 288(5469):1230–1234, 2000.

A. Duong, T. Corke, F. Thomas, and K. Yates. Turbulent boundary layer drag reduction using pulsed-dc plasma actuation. *J. Fluid Mech.*, 2019.

A.H. Duong, T.C Corke, and F.O Thomas. Characteristics of drag-reduced turbulent boundary layers with pulsed-direct-current plasma actuation. *Journal of Fluid Mechanics*, 915, 2021.

H.A. Einstein and H. Li. The viscous sublayer along a smooth boundary. *J. Eng. Mech.*, 82(2): 1–7, 1956.

R.E. Falco. Coherent motions in the outer region of turbulent boundary layers. *J. Fluid Mech.*, 20 (10):S124–S132, 1977.

A. Favre, J. Gaviglio, and R. Dumas. Structure of velocity space-time correlations in a boundary layer. *J. Fluid Mech.*, 10(9):S138–S145, 1967.

K. Fukagata and N. Kasagi. Drag reduction in turbulent pipe flow with feedback control applied partially to wall. *Int. J. Heat Fluid Flow*, 24(4):480–490, 2003.

K. Fukagata, K. Iwamoto, and N. Kasagi. Contribution of Reynolds stress distribution to the skin friction in wall-bounded flows. *Phys. Fluids*, 14(11):L73–L76, 2002.

M. Gad-el Hak. Interactive control of turbulent boundary layers - A futuristic overview. *AIAA J.*, 32(9):1753–1765, 1994.

M. Gad-el Hak. Modern developments in flow control. *Appl. Mech. Rev.*, 49:365–379, 1996.

M. Gad-el Hak and R.F. Blackwelder. Selective suction for controlling bursting events in a boundary layer. *AIAA J.*, 27(3):308–314, 1989.

M. Gad-el Hak and D.M. Bushnell. Separation control. *J. Fluids Eng.*, 113(1):5–30, 1991.

M. Gad-el Hak and A.F. Hussain. Coherent structures in a turbulent boundary layer. Part 1: Generation of artificial bursts. *J. Fluid Mech.*, 29(7):2124–2139, 1986.

B. Ganapathisubramani, E. Longmire, and I. Marusic. Characteristics of vortex packets in turbulent boundary layers. *J. Fluid Mech.*, 478(35-46):35–46, 2003.

B. Ganapathisubramani, N. Hutchins, J.P. Monty, D. Chung, and I. Marusic. Amplitude and frequency modulation in wall turbulence. *J. Fluid Mech.*, 712:61–91, 2012.

D. Gatti and M. Quadrio. Reynolds-number dependence of turbulent skin-friction drag reduction induced by spanwise forcing. *J. Fluid Mech.*, 802:553–582, 2016.

A.S. Ginevsky, Y.V. Vlasov, E.V. Vlasov, and R.K. Karavosov. *Acoustic control of turbulent jets*. Springer Science & Business Media, 2004.

M. Guala, S.E. Hommema, and R.J. Adrian. Large-scale and very-large-scale motions in turbulent pipe flow. *J. Fluid Mech.*, 554:521, 2006.

L. Guastoni, M.P. Encinar, P. Schlatter, H. Azizpour, and R. Vinuesa. Prediction of wall-bounded turbulence from wall quantities using convolutional neural networks. In *J. Phys.: Conf. Ser.*, volume 1522, page 012022. IOP Publishing, 2020.

I. Gursul, Z. Wang, and E. Vardaki. Review of flow control mechanisms of leading-edge vortices. *Prog. Aerosp. Sci.*, 43(7-8):246–270, 2007.

E.P. Hammond, T.R. Bewley, and P. Moin. Observed mechanisms for turbulence attenuation and enhancement in opposition-controlled wall-bounded flows. *Phys. Fluids*, 10(9):2421–2423, 1998.

M.R. Head and P. Bandyopadhyay. New aspects of turbulent boundary-layer structure. *J. Fluid Mech.*, 107:297–338, 1981.

J. Hefner, J. Anders, and D. Bushnell. Alteration of outer flow structures for turbulent drag reduction. In *21st Aerospace Sciences Meeting*, page 293, 1983.

A.J. Humber, E.W. Grandmaison, and A. Pollard. Mixing between a sharp-edged rectangular jet and a transverse cross flow. *Int. J. Heat Mass Transf.*, 36(18):4307–4316, 1993.

A.F. Hussain. Coherent structures and turbulence. *J. Fluid Mech.*, 173:303–356, 1986.

N Hutchins and I Marusic. Evidence of very long meandering features in the logarithmic region of turbulent boundary layers. *J. Fluid Mech.*, 579:1–28, 2007a.

N. Hutchins and I. Marusic. Large-scale influences in near-wall turbulence. *Philos. Trans. R. Soc. A*, 365(1852):647–664, 2007b.

N. Hutchins, B. Ganapathisubramani, and I. Marusic. Spanwise periodicity and the existence of very large scale coherence in turbulent boundary layers. In *4th International Symposium on Turbulence and Shear Flow Phenomena*. Begel House Inc., 2005a.

N. Hutchins, W.T. Hambleton, and I. Marusic. Inclined cross-stream stereo particle image velocimetry measurements in turbulent boundary layers. *J. Fluid Mech.*, 541:21–54, 2005b.

N. Hutchins, T.B. Nickels, I. Marusic, and M.S. Chong. Hot-wire spatial resolution issues in wall-bounded turbulence. *J. Fluid Mech.*, 635:103–136, 2009.

N. Hutchins, J.P. Monty, B. Ganapathisubramani, H.C. Ng, and I. Marusic. Three-dimensional conditional structure of a high-Reynolds-number turbulent boundary layer. *J. Fluid Mech.*, 673: 255–285, 2011.

N. Hutchins, K. Chauhan, I. Marusic, J. Monty, and J. Klewicki. Towards reconciling the large-scale structure of turbulent boundary layers in the atmosphere and laboratory. *Boundary-layer meteorology*, 145(2):273–306, 2012.

J. Hwang and H.J. Sung. Influence of large-scale motions on the frictional drag in a turbulent boundary layer. *J. Fluid Mech.*, 829:751–779, 2017.

Y. Hwang. Statistical structure of self-sustaining attached eddies in turbulent channel flow. *J. Fluid Mech.*, 767:254, 2015.

S. Illingworth, J.P. Monty, and I. Marusic. Estimating large-scale structures in wall turbulence using linear models. *J. Fluid Mech.*, 842:146, 2018.

G. Iuso, M. Onorato, P.G. Spazzini, and G.M. diCicca. Wall turbulence manipulation by large-scale streamwise vortices. *J. Fluid Mech.*, 473:23–58, 2002.

K. Iwamoto, K. Fukagata, N. Kasagi, and Y. Suzuki. Friction drag reduction achievable by near-wall turbulence manipulation at high Reynolds numbers. *Phys. Fluids*, 17(1):011702–011702, 2005.

J. Jiménez and A. Pinelli. The autonomous cycle of near-wall turbulence. *J. Fluid Mech.*, 389: 335–359, 1999.

A.V. Johansson, P.H. Alfredsson, and J. Kim. Evolution and dynamics of shear-layer structures in near-wall turbulence. *J. Fluid Mech.*, 224:579–599, 1991.

R. Joussot, D. Hong, R. Weber-Rozenbaum, and A. Leroy-Chesneau. Modification of the laminar-to-turbulent transition on a flat plate using DBD plasma actuator. In *5th Flow Control Conference*, page 4708, 2010.

T.N. Jukes, K.S. Choi, G.A. Johnson, and S.J. Scott. Characterization of surface plasma-induced wall flows through velocity and temperature measurements. *AIAA J.*, 44(4):764–771, 2006.

W.J. Jung, N. Mangiavacchi, and R. Akhavan. Suppression of turbulence in wall-bounded flows by high-frequency spanwise oscillations. *Phys. Fluids*, 4(8):1605–1607, 1992.

Y. Kametani and K. Fukagata. Direct numerical simulation of spatially developing turbulent boundary layers with uniform blowing or suction. *J. Fluid Mech.*, 681:154–172, 2011.

Y. Kametani, K. Fukagata, R. Örlü, and P. Schlatter. Drag reduction in spatially developing turbulent boundary layers by spatially intermittent blowing at constant mass-flux. *J. Turbul.*, 17(10): 913–929, 2016.

S. Kang and H. Choi. Active wall motions for skin-friction drag reduction. *Phys. Fluids*, 12(12): 3301–3304, 2000.

Y.D. Kang, K.S. Choi, and H.H. Chun. Direct intervention of hairpin structures for turbulent boundary-layer control. *Phys. Fluids*, 20(10):101517, 2008.

H. Kim, S.J. Kline, and W.C. Reynolds. The production of turbulence near a smooth wall in a turbulent boundary layer. *J. Fluid Mech.*, 50(1):133–160, 1971.

J. Kim and P. Moin. Large eddy simulation of turbulent channel flow: ILLIAC 4 calculation. 1979.

K. Kim, H.J. Sung, and M.K. Chung. Assessment of local blowing and suction in a turbulent boundary layer. *AIAA J.*, 40(1):175–177, 2002.

K.C. Kim and R.J. Adrian. Very large-scale motion in the outer layer. *Phys. Fluids*, 11(2):417–422, 1999.

J. Klewicki, P. Fife, T. Wei, and P. McMurtry. A physical model of the turbulent boundary layer consonant with mean momentum balance structure. *Philos. Trans. R. Soc. A*, 365(1852):823–840, 2007.

S.J. Kline. Quasi-coherent structures in the turbulent boundary layer. Part I: Status report on a community-wide summary of the data. In *Proceedings of Zaric Memorial Conference, 1989*. Hemisphere, 1989.

S.J. Kline, W.C. Reynolds, F.A. Schraub, and P.W. Runstadler. The structure of turbulent boundary layers. *J. Fluid Mech.*, 30(4):741–773, 1967.

A.G. Kravchenko, H Choi, and P Moin. On the relation of near-wall streamwise vortices to wall skin friction in turbulent boundary layers. *Phys. Fluids*, 5(12):3307–3309, 1993.

H.P. Kreplin and H. Eckelmann. Behavior of the three fluctuating velocity components in the wall region of a turbulent channel flow. *J. Fluid Mech.*, 22(7):1233–1239, 1979.

D. Krug, W.J. Baars, N. Hutchins, and I. Marusic. Vertical coherence of turbulence in the atmospheric surface layer: connecting the hypotheses of Townsend and Davenport. *Bound.-Layer Meteorol.*, 172(2):199–214, 2019.

J. Kühnen, B. Song, D. Scarselli, N.B. Budanur, M. Riedl, A.P. Willis, M. Avila, and B. Hof. Destabilizing turbulence in pipe flow. *Nat. Phys.*, 14(4):386–390, 2018.

L.D. Landau and E.M. Lifshitz. Fluid mechanics. *Course of theoretical physics*, 6, 1959.

J. Laufer and M.B. Narayanan. Mean period of the turbulent production mechanism in a boundary layer. *J. Fluid Mech.*, 14(1):182–183, 1971.

J. Lee. Opposition control of turbulent wall-bounded flow using upstream sensor. *J. Mech. Sci. Technol.*, 29(11):4729–4735, 2015.

J.H. Lee, J.P. Monty, and N. Hutchins. Validating under-resolved turbulence intensities for PIV experiments in canonical wall-bounded turbulence. *Exp. Fluids*, 57(8):129, 2016.

J.H. Lee, N. Hutchins, J.P. Monty, and M. Kozul. Formation and evolution of shear layers in developing turbulent boundary layer. In *Proc. 11th International Symposium on Turbulence and Shear Flow Phenomena*, 2019.

M.A. Leschziner, H. Choi, and K.S. Choi. Flow-control approaches to drag reduction in aerodynamics: progress and prospects. *Philos. Trans. R. Soc. A*, 369(1940):1349–1351, 2011.

C. Liu and D.F. Gayme. Input-output based analysis of convective velocity in turbulent channels. *J. Fluid Mech.*, 888, 2020.

R.I. Loehrke and H.M. Nagib. Experiments on management of free-stream turbulence. Technical report, ILLINOIS INST OF TECH CHICAGO, 1972.

M. Luhar, A.S. Sharma, and B. McKeon. Opposition control within the resolvent analysis framework. *J. Fluid Mech.*, 749:597–626, 2014.

D.G. MacMynowski and D. Williams. Flow control terminology. *Fundamentals and Applications of Modern Flow Control*, pages 59–71, 2009.

P. Magnier, V. Boucinha, B. Dong, R. Weber, A. Leroy-Chesneau, and D. Hong. Experimental study of the flow induced by a sinusoidal dielectric barrier discharge actuator and its effects on a flat plate natural boundary layer. *J. Fluids Eng.*, 131(1), 2009.

R.J. Margason. Fifty years of jet in crosflow research. *Computational and Experimental Assessment of Jets in Cross Flow*, 1993.

I. Marusic and W.D. Heuer. Reynolds number invariance of the structure inclination angle in wall turbulence. *Phys. Rev. Lett.*, 99(11):114504, 2007.

I. Marusic and G.J. Kunkel. Streamwise turbulence intensity formulation for flat-plate boundary layers. *Phys. Fluids*, 15(8):2461–2464, 2003.

I. Marusic, R. Mathis, and N. Hutchins. Predictive model for wall-bounded turbulent flow. *Science*, 329(5988):193–196, 2010.

I. Marusic, J.P. Monty, M. Hultmark, and A.J. Smits. On the logarithmic region in wall turbulence. *J. Fluid Mech.*, 716, 2013.

I. Marusic, K.M. Talluru, and N. Hutchins. Controlling the large-scale motions in a turbulent boundary layer. In *Fluid structure sound interactions and control*, pages 17–26. Springer, 2014.

R. Mathis, N. Hutchins, and I. Marusic. Large-scale amplitude modulation of the small-scale structures in turbulent boundary layers. *J. Fluid Mech.*, 628:311–337, 2009.

R. Mathis, N. Hutchins, and I. Marusic. A predictive inner–outer model for streamwise turbulence statistics in wall-bounded flows. *J. Fluid Mech.*, 681:537–566, 2011a.

R Mathis, I Marusic, N Hutchins, and K.R. Sreenivasan. The relationship between the velocity skewness and the amplitude modulation of the small scale by the large scale in turbulent boundary layers. *Physics of Fluids*, 23(12):121702, 2011b.

R Mathis, I Marusic, S.I. Chernyshenko, and N. Hutchins. Estimating wall-shear-stress fluctuations given an outer region input. *J. Fluid Mech.*, 715:163–180, 2013.

B.J. McKeon and A.S. Sharma. A critical-layer framework for turbulent pipe flow. *J. Fluid Mech*, 658:336–382, 2010.

J. McLean, D. George-Falvy, and P. Sullivan. Flight-test of turbulent skin-friction reduction by riblets. *Turbulent drag reduction by passive means*, pages 408–424, 1987.

C.D. Meinhart and R.J. Adrian. On the existence of uniform momentum zones in a turbulent boundary layer. *Phys. Fluids*, 7(4):694–696, 1995.

M. Metzger and J. Klewicki. A comparative study of near-wall turbulence in high and low Reynolds number boundary layers. *Phys. Fluids*, 13(3):692–701, 2001.

P. Moin and J. Kim. Numerical investigation of turbulent channel flow. *J. Fluid Mech.*, 118: 341–377, 1982.

P. Moin and J. Kim. The structure of the vorticity field in turbulent channel flow. Part 1. Analysis of instantaneous fields and statistical correlations. *J. Fluid Mech.*, 155:441–464, 1985.

P. Moin, T.H. Shih, D. Driver, and N.N. Mansour. Direct numerical simulation of a three-dimensional turbulent boundary layer. *Phys. Fluids*, 2(10):1846–1853, 1990.

J.P. Monty, J.A. Stewart, R.C. Williams, and M.S. Chong. Large-scale features in turbulent pipe and channel flows. *J. Fluid Mech.*, 589:147, 2007.

H.M. Nagib and K. Chauhan. Variations of von kármán coefficient in canonical flows. *Phys. Fluids*, 20(10):101518, 2008.

H. Nakagawa and I. Nezu. Structure of space-time correlations of bursting phenomena in an open-channel flow. *J. Fluid Mech.*, 104:1–43, 1981.

T.B. Nickels, I. Marusic, S. Hafez, and M.S. Chong. Evidence of the k^{-1} law in a high Reynolds number turbulent boundary layer. *Physical review letters*, 95(7):074501, 2005.

D. Noguchi, K. Fukagata, and N. Tokugawa. Friction drag reduction of a spatially developing boundary layer using a combined uniform suction and blowing. *J. Fluid Sci. Technol.*, 11(1): JFST0004–JFST0004, 2016.

S.G. Nychas, H.C. Hershey, and R.S. Brodkey. A visual study of turbulent shear flow. *J. Fluid Mech.*, 61(3):513–540, 1973.

G.R. Offen and S.J. Kline. Combined dye-streak and hydrogen-bubble visual observations of a turbulent boundary layer. *J. Fluid Mech.*, 62(2):223–239, 1974.

G.R. Offen and S.J. Kline. A proposed model of the bursting process in turbulent boundary layers. *J. Fluid Mech.*, 70(2):209–228, 1975.

M. Pamiès, E. Garnier, A. Merlen, and P. Sagaut. Response of a spatially developing turbulent boundary layer to active control strategies in the framework of opposition control. *Phys. Fluids*, 19(10):108102, 2007.

R. Panton. Overview of the self-sustaining mechanisms of wall turbulence. *Prog. Aerosp. Sci.*, 37 (4):341–383, 2001.

J. Park and H. Choi. Effects of uniform blowing or suction from a spanwise slot on a turbulent boundary layer flow. *Phys. Fluids*, 11(10):3095–3105, 1999.

P.M. Peeters, J. Middel, and A. Hoolhorst. Fuel efficiency of commercial aircraft: an overview of historical and future trends. 2005.

A.E. Perry and M.S. Chong. On the mechanism of wall turbulence. *J. Fluid Mech.*, 119:173–217, 1982.

A.E. Perry, T.T. Lim, and E.W. Teh. A visual study of turbulent spots. *J. Fluid Mech*, 104:387–405, 1981.

A.E. Perry, S. Henbest, and M.S. Chong. A theoretical and experimental study of wall turbulence. *J. Fluid Mech.*, 165:163–199, 1986.

L. Prandtl. Über flussigkeitsbewegung bei sehr kleiner reibung. *Verhandl. III, Internat. Math.-Kong., Heidelberg, Teubner, Leipzig, 1904*, pages 484–491, 1904.

A.K. Praturi and R.S. Brodkey. A stereoscopic visual study of coherent structures in turbulent shear flow. *J. Fluid Mech.*, 89(2):251–272, 1978.

M. Quadrio and P. Ricco. Critical assessment of turbulent drag reduction through spanwise wall oscillations. *J. Fluid Mech.*, 521:251, 2004.

M. Quadrio, J.M. Floryan, and P. Luchini. Effect of streamwise-periodic wall transpiration on turbulent friction drag. *J. Fluid Mech.*, 576(004):425–444, 2007.

M. Quadrio, P. Ricco, and C. Viotti. Streamwise-travelling waves of spanwise wall velocity for turbulent drag reduction. *J. Fluid Mech.*, 627:161–178, 2009.

K.N. Rao, R. Narasimha, and M.A.B. Narayanan. The 'bursting' phenomenon in a turbulent boundary layer. *J. Fluid Mech.*, 48(2):339–352, 1971.

R. Rathnasingham and K.S. Breuer. System identification and control of a turbulent boundary layer. *Phys. Fluids*, 9(7):1867–1869, 1997.

R. Rathnasingham and K.S. Breuer. Active control of turbulent boundary layers. *J. Fluid Mech.*, 495:209, 2003.

H. Rebbeck and K.S. Choi. Opposition control of near-wall turbulence with a piston-type actuator. *Phys. Fluids*, 13(8):2142–2145, 2001.

H. Rebbeck and K.S. Choi. A wind-tunnel experiment on real-time opposition control of turbulence. *Phys. Fluids*, 18(3):035103, 2006.

S.K. Robinson. Coherent motions in the turbulent boundary layer. *Annu. Rev. Fluid Mech*, 23(1): 601–639, 1991.

J.R. Roth, D.M. Sherman, and S.P. Wilkinson. Electrohydrodynamic flow control with a glow-discharge surface plasma. *AIAA J.*, 38(7):1166–1172, 2000.

Z Ruan, W.J. Baars, M.R. Abbassi, N. Hutchins, and I. Marusic. Active control of large-scales in a high-Reynolds-number turbulent boundary layer. In *Proc. 21st Australasian Fluid Mech. Conference*, pages 1–4. Australasian Fluid Mechanics Society, 2018.

A. Sahlin, A.V. Johansson, and P.H. Alfredsson. The possibility of drag reduction by outer layer manipulators in turbulent boundary layers. *J. Fluid Mech.*, 31(10):2814–2820, 1988.

M. Samie, W.J. Baars, A. Rouhi, P. Schaltter, R. Örlü, I. Marusic, and N. Hutchins. Near wall coherence in wall-bounded flows and implications for flow control. *arXiv preprint arXiv:2005.01793*, 2020.

A.M. Savill and J.C. Mumford. Manipulation of turbulent boundary layers by outer-layer devices: skin-friction and flow-visualization results. *J. Fluid Mech.*, 191:389–418, 1988.

F. Scarano. Iterative image deformation methods in PIV. *Meas. Sci. Technol.*, 13(1):R1, 2001.

W. Schoppa and F. Hussain. A large-scale control strategy for drag reduction in turbulent boundary layers. *Phys. Fluids*, 10(5):1049–1051, 1998.

W Schoppa and Fazle Hussain. Coherent structure generation in near-wall turbulence. *Journal of fluid Mechanics*, 453:57, 2002.

A. Seraudie, O. Vermeersch, and D. Arnal. Dbd plasma actuator effect on a 2D model laminar boundary layer. Transition delay under ionic wind effect. In *29th AIAA applied aerodynamics conference*, page 3515, 2011.

J. Sillero, J. Jiménez, R.D. Moser, and N.P. Malaya. Direct simulation of a zero-pressure-gradient turbulent boundary layer up to Re_θ= 6650. In *J. Phys.: Conf. Ser.*, volume 318, page 022023, 2011.

C.R. Smith and S.P. Schwartz. Observation of streamwise rotation in the near-wall region of a turbulent boundary layer. *J. Fluid Mech.*, 26(3):641–652, 1983.

C.R. Smith, J. Walker, A.H. Haidari, and U. Sobrun. On the dynamics of near-wall turbulence. *Philos. Trans. R. Soc. A*, 336(1641):131–175, 1991.

A.J. Smits and I. Marusic. Wall-bounded turbulence. *Phys. Today*, 66(9):25–30, 2013.

A.J. Smits, B.J. McKeon, and I. Marusic. High Reynolds number wall turbulence. *Annu. Rev. Fluid Mech*, 43, 2011.

T.N. Stevenson. A law of the wall for turbulent boundary layers with suction or injection. *College of Aeronautics Report Aero 166*, 1963.

A. Stroh, B. Frohnapfel, P. Schlatter, and Y. Hasegawa. A comparison of opposition control in turbulent boundary layer and turbulent channel flow. *Phys. Fluids*, 27(7):075101, 2015.

Y. Sumitani and N. Kasagi. Direct numerical simulation of turbulent transport with uniform wall injection and suction. *AIAA J.*, 33(7):1220–1228, 1995.

K.M. Talluru, V. Kulandaivelu, N. Hutchins, and I. Marusic. A calibration technique to correct sensor drift issues in hot-wire anemometry. *Meas. Sci. Technol.*, 25(10):105304, 2014.

M.K. Talluru. *Manipulating large-scale structures in a turbulent boundary layer using a wall-normal jet*. PhD thesis, 2013.

S. Tardu. Near wall turbulence control by local time periodical blowing. *Exp. Therm. Fluid Sci.*, 16(1-2):41–53, 1998.

S. Tardu and O. Doche. Active control of the turbulent drag by a localized periodical blowing dissymmetric in time. *Exp. Fluids*, 47(1):19–26, 2009.

G.I. Taylor. The spectrum of turbulence. *Proceedings of the Royal Society of London. Series A-Mathematical and Physical Sciences*, 164(919):476–490, 1938.

T. Theodorsen. Mechanisms of turbulence. In *Proceedings of the 2nd Midwestern Conference on Fluid Mechanics, 1952*, 1952.

F.O. Thomas, T.C. COrke, A Duong, S Midya, and K Yates. Turbulent drag reduction using pulsed-dc plasma actuation. *Journal of Physics D: Applied Physics*, 52(43):434001, 2019.

C.E. Tinney, F. Coiffet, J. Delville, A.M. Hall, P. Jordan, and M.N. Glauser. On spectral linear stochastic estimation. *Exp. Fluids*, 41(5):763–775, 2006.

S.S. Toedtli, M. Luhar, and B. McKeon. Predicting the response of turbulent channel flow to varying-phase opposition control: Resolvent analysis as a tool for flow control design. *Phys. Rev. Fluids*, 4(7):073905, 2019.

C.D. Tomkins and R.J. Adrian. Spanwise structure and scale growth in turbulent boundary layers. *J. Fluid Mech.*, 490:37, 2003.

C.D. Tomkins and R.J. Adrian. Energetic spanwise modes in the logarithmic layer of a turbulent boundary layer. *J. Fluid Mech.*, 545:141, 2005.

A.A. Townsend. The properties of equilibrium boundary layers. *J. Fluid Mech.*, 1(6):561–573, 1956.

A.A. Townsend. The turbulent boundary layer. In *Grenzschichtforschung/Boundary Layer Research*, pages 1–15. Springer, 1958.

A.A. Townsend. Equilibrium layers and wall turbulence. *J. Fluid Mech.*, 11(1):97–120, 1961.

A.A. Townsend. *The structure of turbulent shear flow*. Cambridge university press, 1976.

D.J. Tritton. Some new correlation measurements in a turbulent boundary layer. *J. Fluid Mech.*, 28(3):439–462, 1967.

S. Trujillo, D. Bogard, and K. Ball. Turbulent boundary layer drag reduction using an oscillating wall. In *4th Shear Flow Control Conference*, page 1870, 1997.

J.M. Wallace, H. Eckelmann, and R.S. Brodkey. The wall region in turbulent shear flow. *J. Fluid Mech.*, 54(1):39–48, 1972.

M.J. Walsh and J.B. Anders. Riblet/LEBU research at NASA langley. *Applied Scientific Research*, 46(3):255–262, 1989.

R.D. Whalley and K.S. Choi. Turbulent boundary-layer control with plasma spanwise travelling waves. *Exp. Fluids*, 55(8):1796, 2014.

S.P. Wilkinson. Investigation of an oscillating surface plasma for turbulent drag reduction. 2003.

C. Willert. Stereoscopic digital particle image velocimetry for application in wind tunnel flows. *Meas. Sci. Technol.*, 8(12):1465, 1997.

J.D. Woodcock and I. Marusic. The statistical behaviour of attached eddies. *Phys. Fluids*, 27(1): 015104, 2015.

Q.J. Xia, W.X. Huang, C.X. Xu, and G.X. Cui. Direct numerical simulation of spatially developing turbulent boundary layers with opposition control. *Fluid Dyn. Res.*, 47(2):025503, 2015.

K.S. Yajnik and M. Acharya. Non equilibrium effects in a turbulent boundary layer due to the destruction of large eddies, national aeronautical laboratory, bangalore. Technical report, NAL-BL-7, 1977.

J Yao, X Chen, and F Hussain. Drag control in wall-bounded turbulent flows via spanwise opposed wall-jet forcing. *Journal of Fluid Mechanics*, 852:678–709, 2018.

T. Yoshino, Y. Suzuki, and N. Kasagi. Drag reduction of turbulence air channel flow with distributed micro sensors and actuators. *J. Fluid Sci. Technol.*, 3(1):137–148, 2008.

L.L. Yuan, R.L. Street, and J.H. Ferziger. Large-eddy simulations of a round jet in crossflow. *J. Fluid Mech.*, 379:71–104, 1999.

C. Zhang and S.I. Chernyshenko. Quasisteady quasihomogeneous description of the scale interactions in near-wall turbulence. *Phys. Rev. Fluids*, 1(1):014401, 2016.

S. Zheng and E. Longmire. Perturbing vortex packets in a turbulent boundary layer. *J. Fluid Mech.*, 748:368, 2014.

J. Zhou, R.J. Adrian, S. Balachandar, and T.M. Kendall. Mechanisms for generating coherent packets of hairpin vortices in channel flow. *J. Fluid Mech.*, 387:353–396, 1999.